**TECHNISCHE
UNIVERSITÄT
WIEN**
Vienna University of Technology

Dissertation

Oxide Ion Transport in Donor Doped Lead Zirconate Titanate

ausgeführt zum Zwecke der Erlangung des akademischen Grades eines
Doktor der technischen Wissenschaften

unter der Leitung von

Univ.-Prof. Dipl.-Phys. Dr. Jürgen Fleig

am Institut für chemische Technologien und Analytik

eingereicht an der Technischen Universität Wien
Fakultät für Technischen Chemie

von

Dipl.-Chem. Till Frömling
Matrikelnummer 0728637
Anemonenweg 14
D-51069 Köln

Wien, im Mai 2011

Kurzfassung

Degradations- und Ermüdungsmechanismen in $Pb(Zr_xTi_{1-x})O_3$ (PZT) werden oft mit Prozessen, in denen Sauerstoffleerstellen eine Rolle spielen, in Verbindung gebracht. Um Informationen über Sauerstoffleerstellen in donordotiertem PZT zu erhalten, wurden Isotopenaustauschversuche mit $^{18}O_2$ durchgeführt und mit time-of-flight(ToF) Sekundärionenmassenspektrometrie (SIMS) untersucht. Damit wurden Hinweise auf eine Raumladungsschicht in der Nähe der Oberfläche ermittelt. Bei Temperaturen bis ca. 600°C sind in dieser Schicht Sauerstoffleerstellen angereichert, wodurch sich kastenförmige Konzentrationstiefenprofile des ^{18}O-Isotops entwickeln. Um 650°C verändern sich die Profile stark, was durch eine Abreichung der Leerstellen in der Nähe der Oberfläche beschrieben werden kann. Es wird also von einer Änderung der Polarität der Raumladung bei dieser Temperatur ausgegangen. Es hat sich ebenfalls herausgestellt, dass sich die Profile schon bei geringen Modifikationen der Oberfläche verändern, wie beispielsweise durch Ätzen oder Tempern bei höheren Temperaturen. Die Vorbehandlung des PZT-Materials hat demnach den größten Einfluss auf die Isotopenprofile. Durch Anlegen von Spannung wird an der Kathode und im Oberflächenbereich zwischen den Elektroden der Einbau des Isotops erhöht. Auch wurde erhöhte Korngrenzmigration festgestellt. Es konnte allerdings gezeigt werden, dass der Beitrag des Ionentransports zur Gesamtleitfähigkeit bei Temperaturen um die 400°C vergleichsweise klein ist.

Das untersuchte donordotierte PZT zeigte bei Temperaturen um die 650°C schnelle Korngrenzdiffusion. Dies konnte anhand von ^{18}O-Intensitätsbildern von Tiefenprofilen bewiesen werden. Darin wurde ersichtlich, dass sich Bereiche mit hoher Intensität mit der Korngrenzstruktur decken. Donordotiertes PZT, das mit Ag/Pd-Innenelektroden gesintert wurde, zeigt besonders schnelle Korngrenzdiffusion bei 650°C, die sogar in Querschnittsprofilen sichtbar ist. Die Korngrenzdiffusion erstreckt sich nach 4 h bis zu 150 μm in das Material hinein. Durch einen Vergleich mit Leitfähigkeitsmessungen konnte festgestellt werden, dass der ionische Beitrag zur Leitfähigkeit in diesem Fall sehr hoch ist. Anderes donordotieres Material zeigte aber keine solche schnelle Korngrenzdiffusion. Selbst bei Temperaturen über 800°C konnte keine erhöhte Konzentration entlang von Korngrenzen im Querschliff ermittelt werden. Dies zeigt das Ag-Dotierung von PZT vermutlich einen großen Einfluss auf die Korngrenzdiffusion von Sauerstoff hat.

In ergänzenden Wechselstrom- und Gleichstrommessungen wurden unter anderem auch die Elektrodenmaterialien und -geometrien variiert. Es stellte sich erneut heraus, dass die Vorbehand-

lung, beispielsweise Sinterungsatmosphäre und Kosinterung mit dem Elektrodenmaterial, einen großen Einfluss auf die Leitungseigenschaften und sogar auf die Hochspannungsstabilität des PZT-Materials hat. Die Wahl der Elektroden bei den Messungen selbst beeinflusst die Eigenschaften ebenfalls stark.

Zu Vergleichszwecken wurden schließlich Isotopenauschtauschsexperimente mit (La) donor-dotiertem Bariumtitanat (Mn co-Dotierung) durchgeführt. Dieses Material wird in positive-temperature-coefficient (PTC) Widerständen verwendet, in denen Sauerstoffdiffusion mit hoher Wahrscheinlichkeit eine große Rolle bei Reoxidationsprozessen spielt. Extrem schnelle Korngrenzdiffusion konnte für Temperaturen von 750°C bis 900°C ermittelt werden. Auch hier konnten Hinweise auf eine Raumladungszone an der Oberfläche gefunden werden, da sich zu den PZT-Ergebnissen vergleichbare kastenförmige Tiefenprofile ergaben. Die Sekundärphase, die sich während des Produktionsprozesses bildete, ist titanreich und Isotopenaustausch mit dieser Phase konnte nicht beobachtet werden. Deshalb ist es wahrscheinlich, dass Korngrenzdiffusion keinen Beitrag einer solchen Sekundärphase beinhaltet. Es ist eher wahrscheinlich, dass Diffusion entlang einer Raumladungszone an der Korngrenze stattfindet, was vermutlich auch für PZT der Fall ist.

Abstract

Degradation and fatigue mechanisms in $Pb(Zr_xTi_{1-x})O_3$ (PZT) are often attributed to oxygen vacancy related processes. To obtain further information on oxygen vacancies in donor doped PZT material experiments on the oxygen tracer diffusion in PZT were conducted and investigated by time-of-flight(ToF)-secondary ion mass spectrometry (SIMS). Evidence for a space charge layer near the surface is provided. In this layer an enrichment of oxygen vacancies is found at temperatures up to about 600°C resulting in a box-shaped tracer diffusion profile. At 650°C and above, however, the profile shape is modified and can only be explained by a depletion of oxygen vacancies. Accordingly, a change in surface charge can be assumed at such temperatures. Furthermore, the tracer diffusion profiles are very sensitive to surface modifications due to etching and annealing at higher temperatures. The strongtest effects, however, result from the sintering procedure of the PZT material. An application of an external field during the tracer experiments leads to an increased incorporation of oxygen at the cathode and the free surface area between the electrodes. Additionally, evidence for an enhanced grain boundary tracer migration due to the field was found. However, estimates of the ionic particle flux led to the conclusion that electronic conductivity dominates the PZT conduction properties at temperatures around 400°C.

The PZT shows fast grain boundary diffusion for annealing temperatures around 650°C. ^{18}O intensity images from depth profiles clearly coincide with maps of grain boundaries. For donor doped PZT sintered with Ag/Pd-inner electrodes grain boundary diffusion, which extend deeply into the samples, could be determined at 650°C. Cross section images showed enhanced ^{18}O concentration along the grain boundaries up to 150 μm. A comparison with electrical measurements showed that oxide ion conduction in grain boundaries significantly contributes to the total conductivity of that PZT material at 650°C. Other donor doped PZT did not exhibit this extended grain boundary diffusion even at temperatures above 800°C. It is therefore assumed that Ag-doping of PZT during the sintering process contributes to the enhanced grain boundary diffusion of oxygen.

Alternating current and direct current measurements with different types of electrodes have been carried out on PZT, as well. Again, it could be found that pre-treatment, such as sintering atmosphere or co-sintering with electrode material, has a large impact on the conduction properties and high field stability of the PZT material. Additionally, the choice of electrode material also significantly influences these properties.

For the sake of comparison oxygen tracer diffusion experiments were conducted on (La) donor and (Mn) acceptor co-doped barium titante. This is a material used in positive temperature coefficient (PTC) resistors, in which oxygen diffusion is assumed to play a dominant role in the reoxidation process. Rapid grain boundary diffusion was found for annealing temperatures of 750°C to 900°C. Additionally, box-shaped diffusion profiles were obtained, which are similar to the profiles found for donor doped PZT with a position dependend diffusion coefficient due to a surface space charge layer. The secondary phase developing during the production process is shown to be Ti-rich and hardly any oxygen tracer exchange with this secondary phase could be observed. This suggests that grain boundary diffusion does not take place via such secondary phases. Rather, evidence of diffusion along an oxygen vacancy enriched space charge region is found, which is also a possible mechanism for oxygen diffusion in PZT.

Contents

Chapter 1

Introduction

PbZr$_x$Ti$_{1-x}$O$_3$ (PZT) is probably the most important piezoelectric material and employed in a wide range of applications, such as sensors, ultrasonic transducers and actuators [2–4]. However, PZT-based devices often suffer from fatigue and degradation phenomena [5,6], and despite the importance in numerous applications the mechanisms of microscopic degradation phenomena are not completely understood yet. Frequently, they are partly or completely attributed to point defects and their motion in internal or external fields [6–12]. A major reason for the incomplete understanding is thus the lack of quantitative information on the defect chemistry and charge transport properties of PZT. This is in contrast to related materials such as donor- and acceptor-doped SrTiO$_3$ and BaTiO$_3$ where defect chemical relations are not only understood qualitatively but also quantitatively [12–23]. This shortcoming is not necessarily caused by completely different defect chemistry but is rather related to the high volatility of PbO. It easily evaporates during the sintering process and can lead to a significant but usually unknown non-stoichiometry [5,11]. This is reflected in a presumably large mass action constant K of the SCHOTTKY equilibrium according to [2,24]:

$$K = [V_{Pb}''] \cdot [V_O^{\bullet\bullet}] \cdot p(PbO) \tag{1.1}$$

with $[V_O^{\bullet\bullet}]$ denoting the oxygen vacancy concentration, $[V_{Pb}'']$ the lead vacancy concentration and p(PbO) the partial pressure of PbO. All other defects are expected to be affected as well. Therefore, a straightforward extrapolation of known defect related phenomena from doped SrTiO$_3$ or BaTiO$_3$ to PZT is often not possible. It is even still under debate or unknown whether the charge transport in PZT is predominantly electronic or ionic and how this depends on prepara-

tion, doping, atmosphere and temperature [7,24–26]. Moreover, little information is available on the role played by grain boundaries in mass and charge transport processes [27].

In particular, oxygen vacancies are discussed to be the ionic defect inducing fatigue and degradation by drifting in the applied electrical fields and accumulating at the cathode, at grain boundaries or domain walls [6–10]. Therefore, investigations on the vacancy concentration and mobility are very desirable. ^{18}O tracer experiments with subsequent secondary ion mass spectrometry (SIMS) measurements can give highly valuable information on oxygen vacancies and their transport properties [28–37]. In tracer studies on polycrystalline material, even charge transport properties of bulk and grain boundaries might become distinguishable. Suprisingly, only very few studies were carried out on PZT so far and thus data on the oxygen diffusion behavior and the mobility of oxygen vacancies is scarce for this material [38–42].

Also the choice of electrode material can strongly affect the degradation behavior in PZT based or other electroceramic devices. In PZT thin films, for example, fatigue of the material could be significantly reduced by using oxide electrodes or hybrid oxide platinum electrodes [6,43–45]. In piezoelectric actuators mainly silver based electrodes are used. However, it has been found that that these electrodes reduce the stability towards polarization fatigue and resistance degradation under high field [46–49]. Since now, only few systematic investigations have been conducted on the interplay between electrode material, PZT material and resistance degradation. Hence, no satisfying mechanistic interpretation is available so far.

The aim of this study was thus to obtain further information on the relavance of oxygen vacancies and oxygen transport properties in different types polycrystalline donor doped and undoped PZT by investigating ^{18}O diffusion profiles using time-of-flight (ToF)-SIMS. This technique made it possible not only to get an excellent depth resolution for investigating surface-near profiles within grains. It could also be used to visualize fast diffusion paths along grain boundaries. The influence of temperature, pre-treatment and field dependence of near-surface profiles was analyzed in depth as well as the tracer grain boundary diffusion.

For the sake of comparison, tracer diffusion experiments were also performed on donor (La) and acceptor (Mn) co-doped barium titanate (BT) investigated by ToF-SIMS in order to clarify the role played by oxygen diffusion along the grain boundaries in BaTiO$_3$-based positive temperature coefficient (PTC) resistor ceramics. Additionally, in a first systematic study the influence

of electrode material, electrode geometry and pre-treatment on the electrical properties and degradation behavior of donor doped PZT material under high field was investigated.

Thus, substantial novel information on the oxygen transport in PZT and BT as well as on the resistance degradation of donor doped PZT could be obtained in the cours of this work.

Chapter 2

Theoretical Aspects

2.1 Defects in Solids

In a perfect crystal at absolute 0 K no defects are present in the crystal structure [50]. At higher temperature, however, crystal defects have to occur, which can be mostly attributed to an increase of the configurational entropy ΔS. In the following, there will be a short introduction into the topic of point defects, which is imperfections involving an atom or site. For information on higher dimensional defects like dislocations I refer to textbooks on solid state chemistry [1,50,51].

Throughout this thesis the so called KRÖGER-VINK notation will be used. This is a notation widely employed by researchers in solid state chemistry [52]. It includes not only atoms and ions but also the corresponding vacancies V in the lattice. Furthermore, information on the actual position of the defect is given in the subscript (in case it is not an atom site, i stands for interstitials and s for surface sites). The charge is denoted in the superscript by $'$ for negative, $\bullet$ for positive and $\times$ for zero net charge. A negatively charged vacancy at the Na position in an NaCl crystal would therefore be written as V'_{Na}. Also electrons e' and the corresponding holes $h^\bullet$ are accounted for in this representation.

2.1.1 Intrinsic Disorders

There are two types of intrinsic disorders in ionic materials, which means disorders that occur in a stoichiometric crystal. A SCHOTTKY disorder is a pair of vacancies which means that two ions leave the crystal structure. This is expected to be the case in $Pb(Zr,Ti)O_3$ (PZT), for example. PbO evaporation at higher temperature leads to the creation of oxygen vacancies

$V_O^{\bullet\bullet}$ and metal vacancies $V_{Pb}^{''}$ and may result in an undesired unknown defect chemistry [7]. The relation between the lead vacancies and the oxygen vacancies is given by the SCHOTTKY equilibrium (Eq 1.1) [2, 24].

The FRENKEL disorder describes the case in which an atom is removed from its original position to an interstitial. This is often found in crystals like AgCl, AgBr, or CaF$_2$ [53]. It is assumed that some covalent interactions between the Ag$^+$ and the four tetrahedrally surrounding Cl$^-$ stabilize the Frenkel disorder while in the case of a harder Na$^+$ this is the less preferred situation [50].

2.1.2 Extrinsic Disorders and Non-Stoichiometry in Solids

Non-stoichiometry and doping with aliovalent ions leads to modification of the defect concentration because the introduced charge has to be compensated by a defect of opposite charge. This can be illustrated by the example of donor doped PZT. The generation of h$^\bullet$ is favoured over $V_O^{\bullet\bullet}$ for the PZT at high oxygen partial pressures [54] and this results in an oxygen non-stoichiometry:

$$4h^\bullet + 2O_O^x \rightarrow 2V_O^{\bullet\bullet} + O_2 \uparrow \qquad (2.1)$$

In this work mainly Nd- or Nb-doped samples are used for experiments. The Nb dopant, for example, is expected to be compensated according to the following relation [55]:

$$Nb_2O_5 \rightarrow V_{Pb}^{''} + 2Nb_{Ti}^\bullet + 5O_O^\times \qquad (2.2)$$
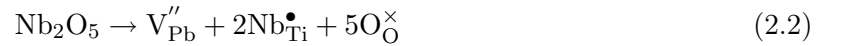
Hence, due to the SCHOTTKY equilibrium the donor dopants cause annihilation of either present $V_O^{\bullet\bullet}$ or h$^\bullet$ while the amount of $V_{Pb}^{''}$ increases [54–56]. As already mentioned in Sec. 2.1.1 the induced intrinsic effects due to sintering of the samples at high temperature results in an unknown defect concentration. Quantitative information about the actual effect of donor doping on the defect chemistry of PZT is yet to be determined.

In applications of PZT oxygen vacancies are only partly undesirable which will be further discussed in Sec. 2.3.3. In oxygen ion conductors, however, the generation of oxygen vacancies is highly necessary as the conductivity of ion conductors depends on the concentration of vacancies therein (Sec. 2.2.2). Those materials are, for example, used in solid oxide fuel cells (SOFCs). As an electrolyte yttrium stabilized zirconia (YSZ) is employed, which obtains an oxygen non-stoichiometry solely due to the yttrium dopant [30]:

$$Y_2O_3 \overset{ZrO_2}{\rightarrow} 2Y'_{Zr} + V_O^{\bullet\bullet} + 3O_O^{\times} \tag{2.3}$$

Promising candidates as cathode materials for SOFCs are compounds with mixed electronic/ionic conductivity like $La_{1-x}Sr_xCoO_{3-\delta}$ (LSC) [57,58]. It has been found that, although the electronic conductivity in LSC is much higher than the ionic conductivity, even higher ionic conductivity values than for the YSZ [59] are possible [60].

2.1.3 Concentration and Relation of Defects

To illustrate the relations between the existing defects in a material, their concentration has to be evaluated as well as the dependence on the surrounding atmosphere. Helpful in this case is that all of the defects shall fulfill the electroneutrality condition [53]

$$z_{dop}c_{dop} + \sum z_{def,i}c_{def,i} = 0 \tag{2.4}$$

where z is the charge number of a dopant or defect and c the corresponding concentration. If the relation is simple and only two majority defects have to be considered in well defined oxygen partial pressure regimes the so called BROUWER or KRÖGER-VINK diagrams can be prepared [1,53]. In these graphs the concentration of the defects are plotted against the oxygen partial pressure (Fig. 2.1).

In the left and the right regime the illustrated model oxide in Fig. 2.1 exhibits oxygen non-stoichiometry while the middle regime is governed by SCHOTTKY disorder. From Fig. 2.1 it is possible to deduce the equilibrium constants of the defect concentrations and the so called power laws, which describe the dependence on the oxygen pressure in one regime. If the BROUWER diagram had been developed yet for PZT Eq. 1.1 could be quantified. But without further knowledge of the defect chemistry of PZT this is not possible.

It can be expected that the real transitions of the regimes are not that abrupt and often further defects or dopants become relevant which increases the complexity of the diagram. Another effect leading to deviations from the ideal behavior is the different activation energy of defect mobility. This induces frozen-in concentration of defects upon fast cooling which inibits reaching the equilibrium state [1]. The other defects are then relaxing according to the frozen-in defect. This
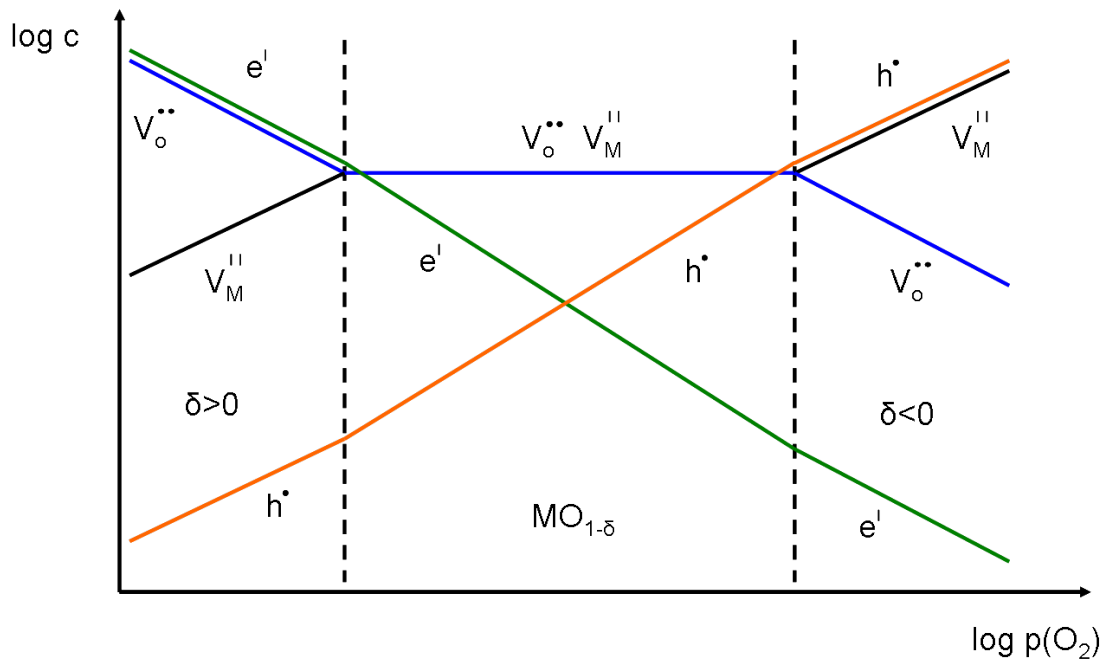
Fig. 2.1: BROUWER diagram of an undoped oxide $MO_{1-\delta}$ according to Ref. [53]

situation, however, is sometimes welcome. In positive temperature coefficient (PTC) resistors based on barium titanate [22,23] such an effect contributes to the desired temperature dependent resistivity of the material [20,61,62]. This topic will be further discussed in the next sections.

2.1.4 Space Charge Layers at Interfaces

Surfaces and grain boundaries are structurally different from the bulk, which can lead to the development of space charge layers [63,64]. In acceptor doped $SrTiO_3$ interface are preferable sites for oxygen vacancies, which results in a segregation of oxygen vacancies and positive charging [65–67]. This causes either a depletion or enrichment of the mobile defects in the space charge region to counter balance the effect of the charged surface. In the case of the acceptor doped $SrTiO_3$ it leads to a depletion of oxygen vacancies and electron holes while the electron concentration increases. This situation can be described as the creation of a single SCHOTTKY barrier at the surface or a double SCHOTTKY barrier at the grain boundary core (Fig. 2.2). Therefore, surface and grain boundary space charge zones become blocking for oxygen diffusion due the depletion of the oxygen vacancies [11,13,64].
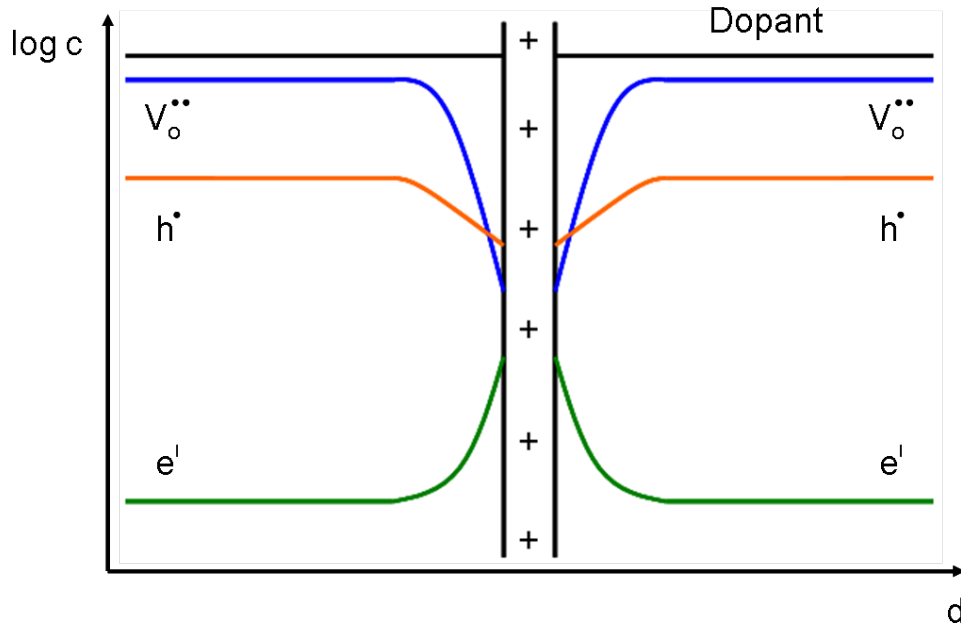
Fig. 2.2: Double SCHOTTKY barriers at the grain boundary in acceptor doped $SrTiO_3$ according to Ref. [65]

Usually, two different cases can be found [1,68]. In the so called MOTT-SCHOTTKY case, one defect concentration or the dopant concentration is frozen while the counter defects are mobile. The GOUY-CHAPMAN case describes the situation in which all defects are mobile and can therefore be depleted or enriched with respect to the bulk concentration. Defect chemical relations being attributed to the MOTT-SCHOTTKY case can often be found in ceramics at lower temperatures when the defect with the highest activation energy is still immobile [68]. Hence, the condition can change to the GOUY-CHAPMAN case at higher temperatures.

In Fig. 2.3 these conditions are illustrated. The vertical line on the right hand side represents the charged interface and the lines 1, 2, and 3 the concentrations of charge carriers in the bulk increasing or decreasing according to their charge. The MOTT-SCHOTTKY condition is depicted in Fig. 2.3 (a). The concentration of the majority defect 3 stays constant while the other with the opposite charge decreases. The mobile minority defect 1 has the same charge as the constant majority defect 3 and increases with respect to the interface charge. Fig. 2.3 (b) and (c) illustrate GOUY-CHAPMAN cases and it can be seen that all majority defects are expected to be mobile. The difference in these two figures regards solely the behavior of the minority charge carrier 1. In Fig. 2.3 (b) 1 has the same charge as 3 while in (c) the opposite is the case. Fig. 2.2 depicts
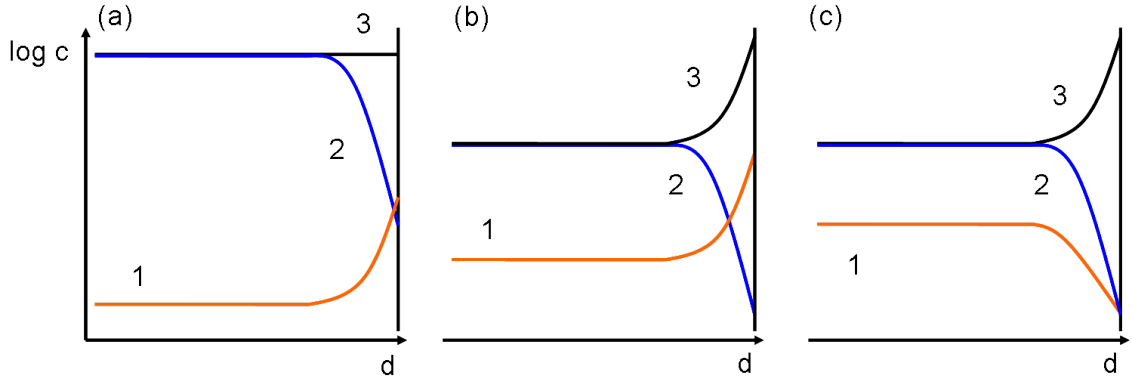
Fig. 2.3: Schematics of (a) Mott-Schottky (b) Gouy-Chapman and (c) modified Gouy-Chapman condition according to Ref. [69]

the Mott-Schottky case for acceptor doped $SrTiO_3$ which has been confirmed by ^{18}O tracer experiments [64].

The concentration of any mobile charge carrier influenced by a space charge can be written as follows [1, 68, 69]

$$\frac{c_j(x)}{c_{j\infty}} = \exp\left(-\frac{z_j e}{k_B T}\Delta\varphi(x)\right) \tag{2.5}$$

where $c_{j\infty}$ is the bulk concentration and $\Delta\varphi(x)$ the electrical potential relative to the bulk and z_j the charge number. The other variables have their established meaning. The difference of the two cases lies in the dependence of the electrical potential on the distance. This can be calculated by solving Poisson´s equation [69]:

$$\frac{\partial^2}{\partial x^2}\varphi = -\frac{Q(x)}{\epsilon} = -\frac{\sum_j z_j e c_{j\infty}}{\epsilon}\exp\left(-\frac{z_j e}{k_B T}\Delta\varphi(x)\right) \tag{2.6}$$

$Q(x)$ denotes the charge density and ϵ is the permittivity. In the Mott-Schottky case the depleted charge carrier is neglected in Poisson´s equation. Therefore, the relationship in Eq. 2.6 can be simplified to [68]:

$$\frac{\partial^2}{\partial x^2}\varphi = -\frac{z_i e c_{i\infty}}{\epsilon} \tag{2.7}$$

.

with z_i and $c_{i\infty}$ denoting charge number and bulk concentration of the immobile charge carrier. Solving this equation and applying the solution to Eq. 2.5 results in

$$\frac{c_j(x)}{c_{j\infty}} = \exp\left(-\frac{z_j e \Delta\varphi_0}{k_B T}\left(\frac{x}{\lambda^*} - 1\right)^2\right) \qquad (2.8)$$

where $\Delta\varphi_0$ is the absolute potential difference between the interface and bulk and λ^* denotes the width of the space charge zone. Eq. 2.8 is valid for $x < \lambda^*$, while $\frac{c_j(x)}{c_{j\infty}} = 1$ for $x > \lambda^*$.

In the GOUY-CHAPMAN case with two mobile species of which the concentrations c_∞ and absolute charge numbers z are equal, POISSON´s equation becomes [1, 68]

$$\frac{\partial^2}{\partial x^2}\varphi = -\frac{z e c_\infty}{\epsilon}\left(\exp\left(-\frac{z e}{k_B T}\Delta\varphi(x)\right) - \exp\left(\frac{z e}{k_B T}\Delta\varphi(x)\right)\right). \qquad (2.9)$$

The solution of Eq. 2.9 results in a concentration distribution of the accumulated charge carrier

$$\frac{c_j(x)}{c_{j\infty}} = \frac{\exp(\xi) + \theta}{\exp(\xi) - \theta} \qquad (2.10)$$

with $\xi = x/\lambda$ where λ is the DEBYE length and

$$\theta = \tanh\left(-\frac{z e |\Delta\varphi_0|}{4 k_B T}\right). \qquad (2.11)$$

The DEBYE length, which is the distance over which the electric field of the boundary is screened by the mobile charge carriers, is given by:

$$\lambda = \left(\frac{\epsilon k_B T}{2 z^2 e^2 c_\infty}\right)^2. \qquad (2.12)$$

These concepts of space charge layers will come across in the next sections in which the diffusion behavior of oxygen tracer ions will be discussed.

2.2 Diffusion and Conductivity in Solids

2.2.1 General Considerations [1]

Before further discussing oxygen transport in PZT it is helpful to first evaluate a few principles on which the further discussion is based. The aim is to get an insight on how transport in a

solid progresses. The relations between concentration gradients, external field gradients and the mobility of a particle are very complex. It is therefore necessary to find conditions in which linear relations can be assumed.

In a system, which is not in equilibrium, fluxes J occur to restore the equilibrium (neglecting chemical reactions for now). From irreversible thermodynamics the relationship between the flux J and the corresponding driving force X can be illustrated by the following progression:

$$J(X) = \alpha + \beta X + \gamma X^2 + ... \tag{2.13}$$

As no flux should be present when the driving force disappears $\alpha = 0$ is required. Close to the equilibrium the terms of higher order should play only a minor role which results in a linear relationship between flux and driving force:

$$J(x) = \beta X \tag{2.14}$$

Prominent and regularly used examples of this condition are FICK´s law in Eq. 2.15 for diffusion and OHM´s law for conduction in Eq. 2.16

$$j = D_S(-\nabla c) \tag{2.15}$$

$$i = \sigma(-\nabla \varphi) \tag{2.16}$$

where D_S is the self-diffusion coefficient, σ the conductivity, j and i the particle flux density and the electrical current density, respectively and c the particle concentration. The two above mentioned laws are related. This becomes obvious when the general relationship between flux of a particle and electrochemical potential (fundamental transport equation) is considered:

$$j = \beta(-\nabla \tilde{\mu}) = j_T + j_E = -\beta \nabla \mu - zF\beta \nabla \phi \tag{2.17}$$

where j_T denotes the the flux density resulting from chemical and j_E the fluxdensity resulting from electric fields. Assuming one of the two driving forces is not present either FICK´s law or OHM´s

law results. If the dilute state is considered then $j_T = -\beta RT \frac{\nabla c}{c}$ is valid. With Eq. 2.15 - 2.17 and $i = zFj_E$ parameter β can be expressed by:

$$\beta = \frac{D_S c}{k_B T} = \frac{\sigma}{q^2}. \tag{2.18}$$

From this the well known NERNST-EINSTEIN equation can be deduced describing the relationship between diffusion and conductivity:

$$D_S = \frac{\sigma k_B T}{q^2 c} \tag{2.19}$$

with q denoting the charge. Note that Eq. 2.19 implies that the conductivity is field independent and proportional to the diffusion coefficient. This clearly illustrates that the assumed linear relationship between driving force and flux is an approximation. It can be expected that the flux of a charged particle in an applied field is not only dependent on the self-diffusion without field. At least, the range in which this condition can be assumed is quite small.

2.2.2 Temperature Dependence of Diffusion and Conductivity in Solids

Another way to approach the subject is regarding the uncorrelated motion of random walkers. The diffusion coefficient in such a case is expressed by the EINSTEIN-SMOLUCHOWSKI relation [70]:

$$D_S = \frac{1}{2d} \Delta x_0^2 \tau \tag{2.20}$$

where d stands for the dimension of the system, Δx_0 the jump distance and τ the jump rate. In a crystal, motion of a defect also depends on the number of neighbouring sites Z it could jump to, which are defined by the crystal structure. With the corresponding jump rate $\Gamma = \tau/Z$ Eq. 2.20 (for d = 3) results in:

$$D_S = \frac{1}{6} Z \Delta x_0^2 \Gamma. \tag{2.21}$$

It is clear, however, that a simple random walk, even if Z is taken into account, can not be attributed to a vacancy diffusion process in a solid material. Generally, the jump-relaxation

model of FUNKE [71] is an appropriate approach to describe ion transport in solids. This model is related to the DEBYE-HÜCKEL-ONSAGER-FALKENHAGEN theory for liquids [72, 73]. The conclusion of the theory is that an ion jump into a neighbouring site is thermally activiated and immediately after the jump the potential well of the former residing place is lower than that of current position. This leads to a high probability of a back jump. To obtain a successful jump the potential well at the current position has to relax with respect to the ion. The temperature dependence of Eq. 2.21 can be expressed by the temperature dependence of Γ

$$D_S = \frac{1}{6}Z\,\Delta x_0^2\,\Gamma_0 c_v \exp\left(-\frac{\Delta G^*}{k_B T}\right) = \frac{1}{6}Z\,\Delta x_0^2\,\Gamma_0 p \qquad (2.22)$$

where Γ_0 is the attempt rate and p the probability of a vacancy site being available for exchange [51, 70]. This probability shows an ARRHENIUS type dependency on the temperature (with ΔG^* as the free activation energy for the hopping process) and a dependency on the site fraction c_v of the corresponding vacancies. It has to be emphasized again that D_S is the self-diffusion coefficient describing the motion of the lattice ions and not the vacancy diffusion coefficient D_v. This coefficient would be described by Eq. 2.22 without the vacancy site fraction dependence [51]. Therefore, the self-diffusion coefficient is naturally much smaller than the diffusion coefficient describing single vacancy motion.

The ionic conductivity can also be expressed by the mobility u of an ion

$$\sigma = c_i q_i u_i \qquad (2.23)$$

The mathematical description of the ion mobility can also be deduced from the motion of a particle described by the jump-relaxation theory [71]:

$$u = \frac{qZ}{6k_B T}\,\Delta x_0^2\,\Gamma_0 \exp\left(-\frac{\Delta G^*}{k_B T}\right) \qquad (2.24)$$

By comparing Eq. 2.22 and Eq. 2.24 it becomes obvious that u and D_v are closely related. Using Eq. 2.23 - 2.24 results in [30]:

$$\sigma = c_i \frac{q^2 Z}{6k_B T}\,\Delta x_0^2\,\Gamma_0 \exp\left(\frac{-\Delta G^*}{k_B T}\right) \qquad (2.25)$$

From this the Nernst-Einstein Equation in Eq. 2.19 can again be deduced. By splitting the free activation energy ΔG^* into its components enthalpy ΔH^* and entropy ΔS^* the factor $\gamma = \exp(\Delta S^*/k_B)$ results [30] and Eq. 2.25 can be simplified to:

$$\sigma = \sigma_0 \exp\left(\frac{-\Delta H^*}{k_B T}\right) \tag{2.26}$$

Hence, the activation enthalpy can be calculated from a logarithmic plof of σ against $1/T$ in which the slope $m = -\Delta H^*/k_B T$. However, in the case of Fig. 2.4 (a) $\sigma_0 \cdot T$ is plotted accounting for the temperature dependence of σ_0 (Eq. 2.25). This dependence is usually assumed to be of minor importance. This is valid in a very large temperature range for ionic conductivity and it has to be kept in mind that for electronic conductivity the temperature dependence of σ_0 is generally much smaller and is not derived in the same way as for the ionic conductivity. Hence, especially in the case of an unknown majority charge carrier, σ_0 is assumed to be temperature independent.
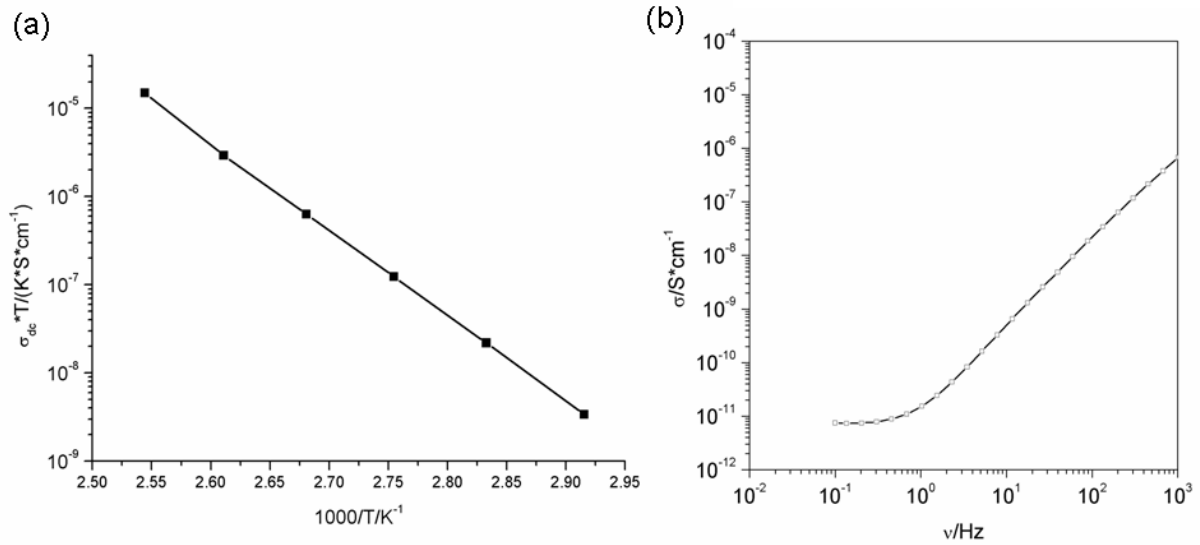
Fig. 2.4: (a) Arrhenius-plot of lithium triflate; (b) conductivity of lithium triflate at 80°C [74]

What has not been discussed so far is the actual time dependence of the conductivity. The evaluation was focussed on the direct current (DC) conductivity but under alternating current (AC) conditions the jump rate dependence of the conductivity becomes pronounced with increasing frequency. The behavior of the conductivity in Fig 2.4 (b) can also be at least phenomeno-

logically explained by the jump-relaxation theory [71]. For a better mathematical description extensions of this concept are used [75, 76]. At a low frequency only successful jumps contribute to the conductivity. However, at higher frequencies the time frame in which a jump can occur becomes smaller. This leads to a contribution to the conductivity value from shifts from the equilibrium position in the potential well (meaning unsuccessful jumps) of a charged particle. Consequently, the conductivity increases and the motion of the ions becomes correlated.

2.2.3 Phenomenological Diffusion Coefficients

In reality, the diffusion coefficients obtained by experiments are different from the self-diffusion coefficient in the previous section. Therefore, the origin of differences and the correlation of the diffusion coefficients will be discussed [1]. Fig. 2.5 illustrates the conditions of experiments resulting in the three different diffusion coefficients for a model oxide.
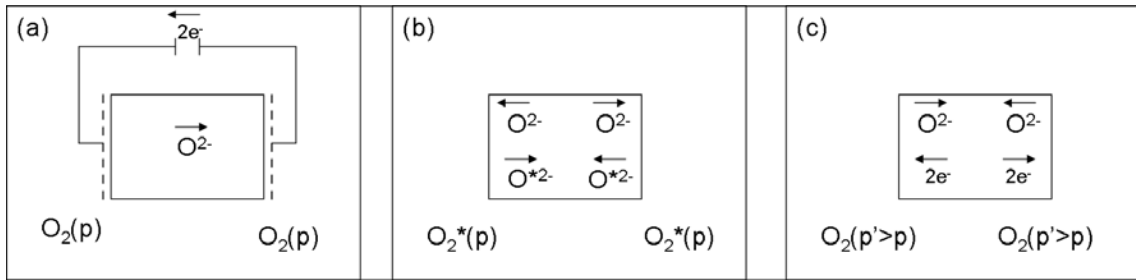
Fig. 2.5: Schemes of (a) conductivity experiment with non-blocking electrodes; (b) tracer experiment; (c) chemical diffusion experiment [1]

In a tracer experiments a diffusant is marked, e.g. in an isotope exchange from the surrounding atmosphere into the sample. The driving force of diffusion is simply the configurational entropy. In this case, the assumption that jumps are uncorrelated is not valid anymore [1, 70]. If a tracer jumps to the next vacancy position the situations before and after the jump are different while in the case of an unlabelled charge carrier this is not the case. As there is a certain probability of a back jump, this would mean that the tracer moves to its original position and the two consecutive jumps have no measureable impact on the tracer diffusion. The tracer diffusion coefficient D is therefore reduced in respect to the self-diffusion coefficient by a correction factor f_D:

$$D = f_D \cdot D_S \tag{2.27}$$

In a conductivity experiment it is extremely necessary that the potential is not too high so that the the linearity condition is not violated. The appearance of defect associates and aggregates leads a further deviation from the self-diffusion coefficient [30]. Hence, also in this case a correction factor f_c has to be introduced for the relation between the diffusion coefficient obtained by conductivity experiments D^σ to the self-diffusion coefficient. If both coefficients are known the following equation can be deduced:

$$\frac{D}{D^\sigma} = \frac{f_D}{f_c} = H_v \tag{2.28}$$

where H_v is the so called Haven ratio. It is quite difficult to determine f_c and very often it is assumed to be close to one for a vacancy related diffusion [70]. Hence, if no evidence supports the generation of defect associates D^σ is directly connected to D over f_D.

The last but most important diffusion coefficient during preparation and equilibration is the chemical diffusion coefficient D_{chem}. The corresponding diffusion mechanism describes the interdiffusion of at least two particles. In ionic compounds it describes the ambipolar diffusion of particles with opposite charge due to a composition change. As depicted in Fig. 2.5 (c), it can be used to evaluate the reaction of a model oxide to a change in partial pressure, which induces oxygen vacancy diffusion and electron transport at the same time. In this case only the change in defect concentration is considered and not the motion of the lattice ions like in Eq. 2.22. Therefore, the chemical diffusion coefficient is at least in the order of magnitude of D_v and much higher than D_S [1]. One possible way to obtain D_{chem} of an oxide is changing the oxygen partial pressure during a DC experiment. From the response in the conductivity signal D_{chem} can be determined [77, 78].

In the next sections, in which it is discussed how diffusion coefficients can be obtained, the focus lies on the tracer diffusion coefficients.

2.2.4 Solution of Diffusion Equations

To obtain the solution of Fick´s laws for a diffusion equation the Laplace transformation can be an excellent mathematical tool [70]. Fick´s second law is basically dependent on the variables space x and time t:

$$\frac{\partial c}{\partial t} = D \frac{\partial^2 c}{\partial x^2} \tag{2.29}$$

LAPLACE transformation can now be used to remove the time variable to obtain a simple differential equation.

$$\int_0^\infty \exp(-pt) \frac{\partial c}{\partial t} dt = D \int_0^\infty \exp(-pt) \frac{\partial^2 c}{\partial x^2} dt \tag{2.30}$$

The solution of this transformation is given by:

$$p\bar{c} = D \frac{\partial^2 \bar{c}}{\partial x^2}. \tag{2.31}$$

With the boundary condition of a constants source on a semi-finite medium $c(x = 0) = c_s$:

$$\bar{c} = \int_0^\infty c_s \exp(-pt) dt = \frac{c_s}{p} \tag{2.32}$$

The solution of Eq. 2.31 satisfying Eq. 2.32 is given by:

$$\bar{c} = \frac{c_s}{p} \exp \left(\sqrt{\frac{p}{D}} \right) x. \tag{2.33}$$

The inverse LAPLACE transformation then results in the analytical solution for the diffusion in a semi-finite medium:

$$c = c_s \left(1 - \mathrm{erf} \right) \left(\frac{x}{2\sqrt{(Dt)}} \right). \tag{2.34}$$

where erf denotes the error function. Eq. 2.34 can now be used to fit diffusion profiles of the corresponding diffusion mechanism by a complex non-linear least square (CNLS) fit. Very often an analytical solution cannot be obtained, especially when the diffusion coefficient is position dependent. In this case information on the diffusion coefficient can be gained from numerical simulations with finite differences (FD) [79] and finite element method (FEM) [80, 81] calculations.

2.2.5 Grain Boundary Diffusion

Evaluation of diffusion coefficients in polycrystalline material is a particularly difficult task. In most cases not only the grain bulk diffusion coefficient D has to be taken into account, but also the grain boundary diffusion coefficient D_{gb}. The diffusion problem illustrated in Fig. 2.6 can be
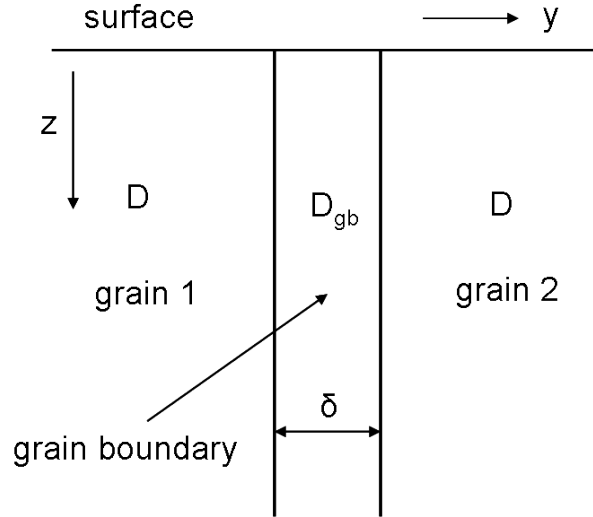
Fig. 2.6: Schematic illustration of an isolated grain boundary with a different diffusion coefficient D_{gb} than for the grain bulk according to FISHER´S model [70, 82].

mathematically described by FICK´S second law [70]:

$$\frac{\partial c}{\partial t} = D \left(\frac{\partial^2 c}{\partial y^2} + \frac{\partial^2 c}{\partial z^2} \right) \text{ for } |y| \geq \delta/2, \tag{2.35}$$

$$\frac{\partial c_{gb}}{\partial t} = D_{gb} \left(\frac{\partial^2 c_{gb}}{\partial y^2} + \frac{\partial^2 c_{gb}}{\partial z^2} \right) \text{ for } |y| < \delta/2 \tag{2.36}$$

with δ denoting the grain boundary thickness. The dependence on x direction is neglected in this model as it is assumed that the xz-plane is the symmetry plane of the grain boundary. With boundary conditions considering the continuity of diffusion fluxes across the grain boundary into the bulk and the assumption that the grain boundary width is small and $D_{gb} >> D$ coupled bulk and grain boundary diffusion equations result:

$$\frac{\partial c}{\partial t} = D \left(\frac{\partial^2 c}{\partial y^2} + \frac{\partial^2 c}{\partial z^2} \right) \text{ for } |y| \geq \delta/2, \tag{2.37}$$

$$\frac{\partial c_{gb}}{\partial t} = D_{gb} \frac{\partial^2 c_{gb}}{\partial z^2} + \frac{2D}{\delta} \frac{\partial^2 c}{\partial y^2} \text{ for } |y| < \delta/2, \tag{2.38}$$

Eq. 2.37 therefore describes diffusion inside the grain boundary while Eq. 2.38 takes the concentration change due to leakage into the grain from the grain boundary into account. The exact solution of such a problem was first obtained by WHIPPLE [83] with the LAPLACE transformation method (see Sec. 2.2.4).
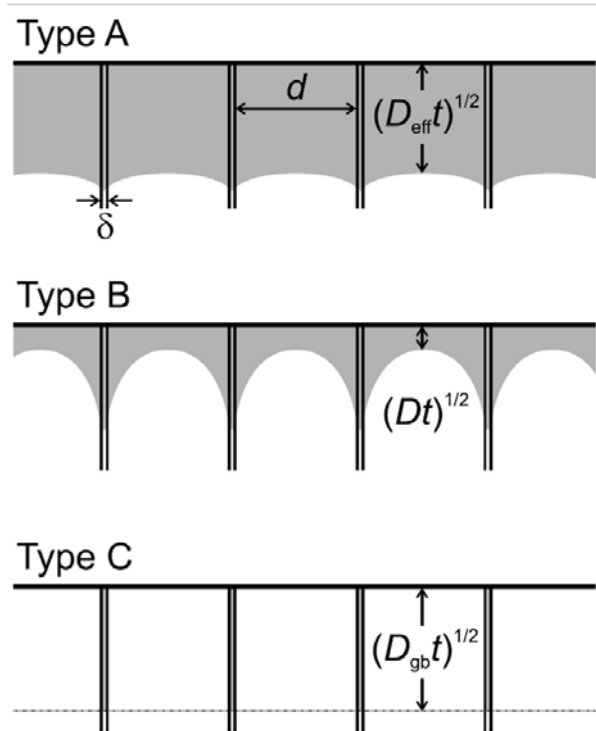
Fig. 2.7: Schematic illustrations of diffusion profiles resulting from different diffusion kinetics according to HARRISON´S classification (adapted from [70]).

A detailed discussion will not be presented in this thesis. However, the results of the solution and the methods for the evaluation of the corresponding diffusion coefficients will be briefly introduced. From the above discussed relations it can be seen that grain boundary diffusion is a very complex process. However, depending on the relation between D and D_{gb} three different regimes of diffusion kinetics can be distinguished [84]. In the so called HARRISON classification [85] the type A diffusion kinetics describe the condition in which the volume diffusion length $\sqrt{Dt}$

is larger than the grain size d. This results when D_{gb} is only slightly larger than D or when grains are filled due to a small grain sizes and/or annealing at high temperature and/or long annealing times. A diffusion profile resulting from these diffusion kinetics is depicted in Fig. 2.7. Depending on the boundary condition (constant source of diffusant or instantaneous source) the diffusion profile can be described by an error (constant source) or gaussian function [70]. However, the diffusion coefficient, which could be deduced from a CNLS fit with the corresponding function is rather an effective diffusion coefficient D_{eff}, which can be seen as an average diffusion coefficient of D and D_{gb}. Many grain boundary diffusion processes can be described with type B diffusion
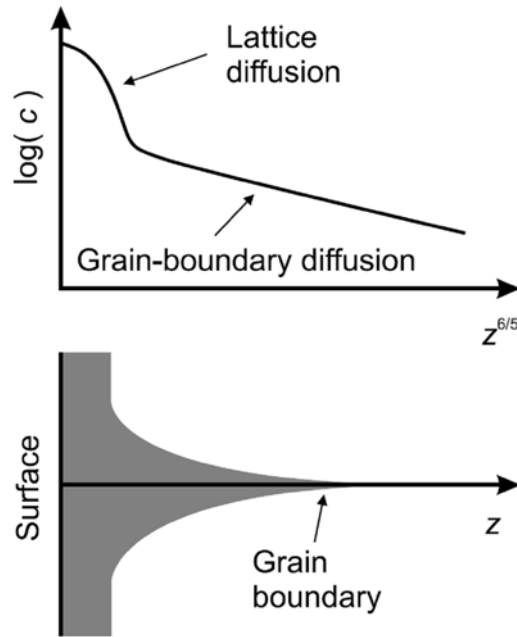
Fig. 2.8: (a) Plot of log c versus $z^{6/5}$ for type B diffusion kinetics (constant source) showing the characteristic grain boundary tail. (b) Corresponding schematic illustration of grain boundary diffusion (adapted from [70]).

kinetics. The conditions which have to be fulfilled in this case are given by [70, 84]:

$$s\delta \ << \ \sqrt{Dt} \ << d \qquad (2.39)$$

where s denotes the segregation coefficient and d the grain thickness. The relation in 2.39 basically describes the situation of a large grain boundary diffusion coefficient compared to the one of the bulk (Fig. 2.7). The segregation coefficient should be included in case the diffusant is foreign in the medium. For ^{18}O tracer experiments in oxide ceramics the diffusant is already part

of the compostion but is labelled. Therefore, the segregation coefficient can be neglected in the tracer experiments conducted in this thesis. The product of grain boundary thickness and grain boundary diffusion can be obtained by a formula given by WHIPPLE [83] and LE CLAIRE [86]:

$$\delta D_{gb} = 1.332 \sqrt{\frac{D}{t}} \left(-\frac{\partial c}{\partial z^{6/5}} \right)^{-5/3} \tag{2.40}$$

where t denotes the diffusion time. Eq. 2.40 was obtained from the solution of Eq. 2.37 and Eq. 2.38 and integrated in y direction. It is valid for a constant source boundary condition but only the proportionality factor changes when an instantaneous source condition is described [70]. The equation is basically an approximation in which the actual amount of diffusant in the grain boundary is neglected and only the concentration leaking from the boundary is taken into account. D_{gb} can now be obtained from a plot of log c versus $z^{6/5}$. This is illustrated in Fig. 2.8. Therein, the concentration profile and the corresponding schematic illustration of the grain boundary diffusion are given. The first part of the concentration profile can be attributed to surface or bulk diffusion and again can be described by an error or gaussian function depending on the boundary conditions. However, the second part is a long tail resulting from grain boundary diffusion. From the slope of this tail D_{gb} can be calculated if the values for δ and D are known.

The last diffusion regime is the so called type C regime. It describes the case when hardly any bulk diffusion occurs and grain boundary diffusion dominates. As the grain boundary thickness is often expected to be very small, investigations of type C diffusion processes can be difficult. It is likely that the concentration of the diffusant is far to low to be detected. However, if the detection of a profile is possible it can be described by an error function (constant source condition) [70, 84]:

$$c(z) \propto \text{erfc} \left(\frac{z}{2\sqrt{D_{gb}t}} \right) \tag{2.41}$$

2.3 Lead Zirconate Titanate (PZT) and Barium Titanate (BT)

In this section the materials, which have been investigated will be introduced in this work. Their usual composition and technical importance in various applications will be discussed as well as mechanisms, which could lead to degradation and fatigue. This should provide information on the importance of the understanding of the microsopic defect situations in PZT and BT, to which this thesis contributes to.

2.3.1 Piezoelectricity, Pyroelectricity, Ferroelectricity

Both materials belong to a class of substances that exhibit piezoelectricity. The piezoelectric effect describes the linear relationship between an applied mechanical stress and a resultant electrical polarization of the material. The opposite situation (development of strain due to an applied field) shows the same proportionality and is called "inverse" piezoelectric effect [87]. Piezoelectricity has to be clearly distinguished from electrostriction, which is found for any dielectric material. It describes the deformation of a material due to an applied field. However, the inverse effect can not be obtained in this case and the relation between field and strain is quadratic, which makes the electrostrictive response independent of field polarity [88]. For
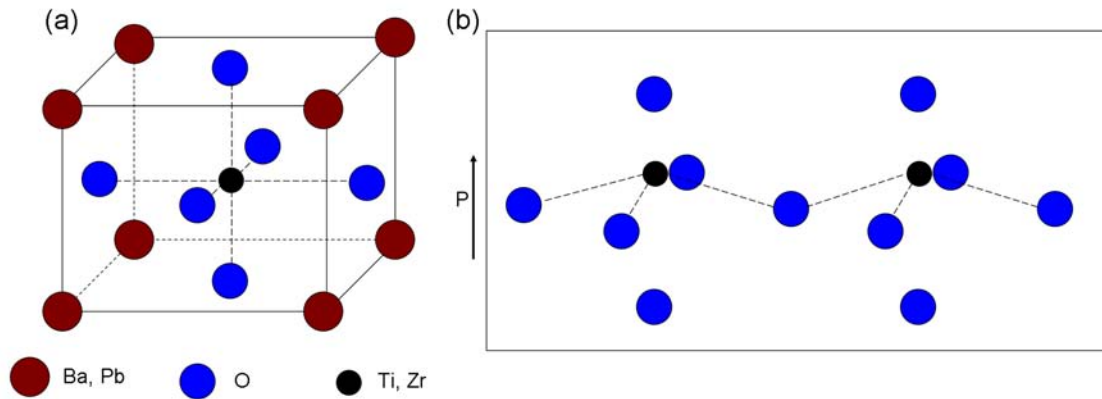
Fig. 2.9: (a) Cubic representation of perovskite crystal structure of PZT/BT. (b) Ti-O bonds favoring angled valencies leading to structural changes (according to [89])

piezoelectricity to occur it should be possible to induce a dipole moment. In a crystalline material this clearly depends on the cystal structure. From the 32 crystal classes 20 are piezoelectric because of the lack of a centre of symmetry. Of these 20 classes 10 result in pyroelectricity, which means the corresponding crystals are spontaneously polarized. The magnitude of the dipole moment is usually temperature dependend, which explains the term "pyro" (latin for fire) [88]. A further subset of pyroelectricity is ferroelectricity. Materials showing ferroelectric behavior polarize spontaneously when going through phase transition but the primary direction of polarization can be influenced by a high electric field [88].

The microscopic origins of these three effects are best explained by referring to the properties of the materials discussed in this thesis. Polycrystalline PZT and BT are both ferroelectric

substances with perovskite crystal structure. In Fig. 2.9 (a) the cubic representation of the crystal structure is illustrated. At high temperature the crystal structure of BT and PZT has this centrosymmetric form, which is paraelectric. That means no polarization is present. Upon lowering the temperature the material undergoes a phase transition at the CURIE-temperature to a tetragonal structure due to movement of the ions [87]. The Ti-ion is removed from its centre position (Fig. 2.9 (b)) leading to polarization and tetragonal distortion. This transition is often attributed to the preferred bonding situations of the involved atoms [89]. Due to homopolar contributions the Ti-O bonds smaller bond lengths and angled valancies are preferred similar to the tendency of water having a 109° angle between the hydrogen atoms. It can be expected from this qualtitative description that parallel orientation is favoured (Fig. 2.9 (b)) and therefore ferroelectric instead of anti-ferroelectric behavior occurs. As a result, single crystalline domains of uniform polarization develop. However, these domains are randomly oriented at first (Fig. 2.10 (a)). Hence, no polarization can be detected macroscopically because the dipoles of the domains cancel each other out [88]. The possible arrangements of the domain walls to one another are 180° and 90° in a tetragonal material. For zirconium rich PZT phases a rhombohedral phase occurs. Therefore, 71° and 109° boundaries are present. Due to a poling step, which means
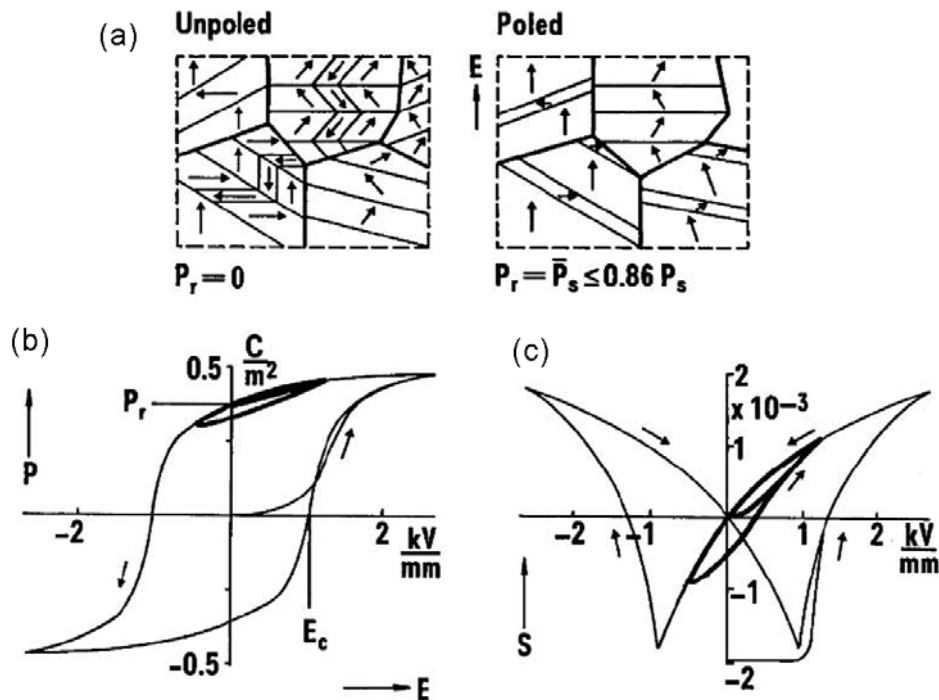
Fig. 2.10: (a) Schematic illustration of poled and unpoled domains. (b) Polarization (with P_r as the remnant polarization) and (c) strain hysterisis loop of tetragonal PZT [89]

application of a high field, it is possible to obtain a preference direction of the polarization. This poling step does not only depend on switching a single crystalline domain (intrinsic response). It is rather a concerted reorientation of domains (extrinsic response)(Fig. 2.10 (a)). Because the field affects the randomly distributed domains differently the electromechanical response is non-linear and results in a hysteretic relation between field and polarization (Fig. 2.10 (b)) as well as field and resultant strain (Fig. 2.10 (c)) [89]. Consequently, the reason why these materials are called ferroelectrics becomes obvious. The similarities to ferromagnetism are large regarding the loss of magnetism/ferroelectricity at the CURIE-temperature, the hysteresis of the magnetic/ferroelectric properties, the remnant polarization/magnetization and the formation of domains. The remnant polarization P_r is the average of all polarized domains and always smaller than the maximum polarization value P_S, which could only be obtained if the domains were all parallel (Fig. 2.10 (a)).

To quantify the piezoelectric properties of a material, parameters derived from thermodynamics are defined [89]. It is expected that the parameters describing a piezoelectric material are temperature T and entropy S, stress T_{ij} and strain S_{ij} and finally electric field E_i and displacement D_i (subscript denoting direction component; see below). From this the GIBBS free energy can be deduced [89]:

$$G = U - TS - S_{ij}T_{ij} - D_iE_i \tag{2.42}$$

$$dG = -SdT - S_{ij}dT_{ij} - D_idE_i. \tag{2.43}$$

If temperature, stress and electric field are seen as independent variables the following equations result:

$$-S = \left(\frac{\partial G}{\partial T}\right)_{T_{ij},E_i}, \quad -S_{ij} = \left(\frac{\partial G}{\partial T_{ij}}\right)_{T,E_i}, \quad -D_i = \left(\frac{\partial G}{\partial E_i}\right)_{T,T_{ij}}. \tag{2.44}$$

It can be expected that either due to applied stress or field processes occur, which lead back to a minimum of the GIBBS free energy. The differential form of Eq. 2.44 can then be expressed by:

$$-\Delta S_{ij} = \left(\frac{\partial S_{ij}}{\partial T}\right)_{T_{ij},E_i} \Delta T + \left(\frac{\partial S_{ij}}{\partial T_{kl}}\right)_{T,E_i} \Delta T_{kl} + \left(\frac{\partial S_{ij}}{\partial E_i}\right)_{T,T_{ij}} \Delta E_i. \tag{2.45}$$

In the isothermal form ($\Delta T = 0$) two of the basic piezoelectric equations can be derived in the non-differential from Eq. 2.44 and Eq. 2.45:

$$S_{ij} = s^E_{ijkl}T_{kl} + d_{kij}E_k \tag{2.46}$$

$$D_i = d_{ikl}T_{kl} + \epsilon^T_{ik}E_k \tag{2.47}$$

with $d_{kij(ikl)}$ the piezoelectric constant, s^E_{ijkl} the elastic compliance (at constant field) and ϵ^T_{ik} the free permittivity (constant stress). To simplify Eq. 2.46 and Eq. 2.47 the so called reduced form is introduced defining stress and strain as first rank instead of second rank tensors:

$$S_j = s^E_{ij}T_j + d_{ij}E_i \tag{2.48}$$

$$D_i = d_{ij}T_j + \epsilon^T_{ii}E_i. \tag{2.49}$$

Finally, we have arrived at the commonly used notation where i is the subscript for the mechanical and j for the electrical direction. The possible direction components are illustrated in Fig. 2.11 (a). The directions 1, 2 and 3 are the normal stress (or strain) directions while 4, 5 and 6 describe shear stresses (or strains). There are more basic piezoelectric equations than de-
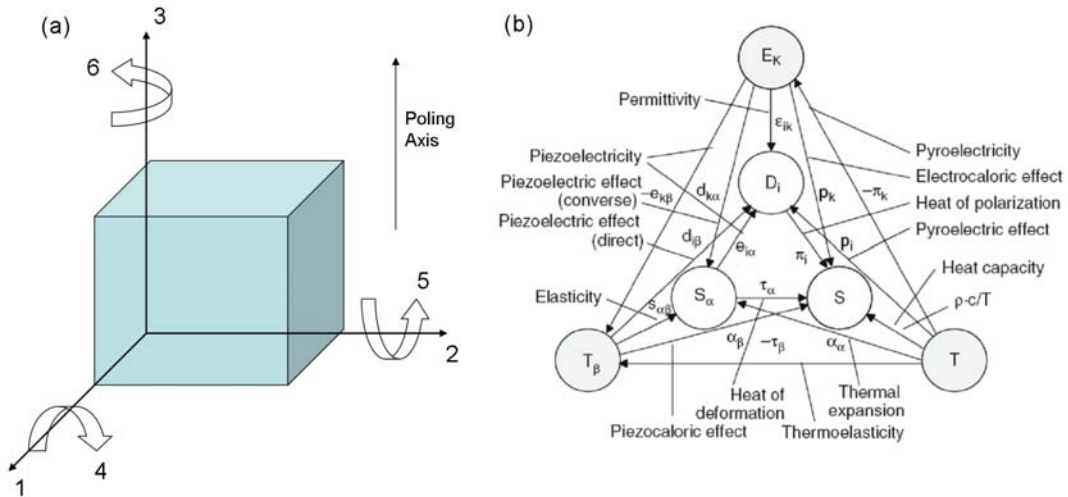
Fig. 2.11: (a) Schematic illustration of direction components of piezoelectric parameters (according to [88]) (b) HECKMANN diagramm showing the relations between the thermodynamic properties expressed by piezoelectric parameters as proportionality constants (adapted from [90])

scribed examplarily in Eq. 2.48 and Eq. 2.49. A further discussion is, however, beyond the scope of this introduction. Nevertheless, all of the relations between the thermodynamic properties in a piezoelectric material can be described by the HECKMANN diagramm (Fig. 2.11 (a)).

2.3.2 Pb(Zr,Ti)O$_3$ PZT

The ferroelectric material PZT is the most widely used material for piezoelectric devices such as sensors, ultrasonic transducers and actuators [2, 3, 88, 91]. The lead content, however, makes it a possible health hazard. Hence, there has been a lot of research concentrating on finding possible lead free substitutes [92, 93]. Due to the excellent and easily modifiable piezoelectric properties of PZT no lead free piezoelectric material investigated so far is a proper replacement. One reason for the superiority of PZT are the properties it obtains when the composition is at the morphotropic phase boundary (MPB). At the Zr/Ti ratio of 53:47 the rhombohedral phase coexists with the tetragonal phase and this condition is almost temperature independent [88] (Fig. 2.12). The dielectric constants and piezoelectric coefficients are greatly enhanced at the MPB. Qualitatively, this is usually explained with the increase of polarization directions, which consequently results in a high piezoelectric response. However, the topic is still part of ongoing research and it can be expected to be more complex than just described. Sometimes, the properties at the MPB are assumed to be associated to monoclinic distortions [94].

The large variety of PZT containing applications results from the opportunity to easily modify the properties by doping with aliovalent ions. PZT is well known for the formation of solid solutions with many chemical compositions. The resulting modifications from doping and the corresponding applications these materials are employed in are given in the following list [4, 88]:

- Donor dopants: Depending on charge and ionic radii the dopants replace Zr^{4+} (e.g. Nb^{5+}) or Pb^{2+} (e.g. La^{3+}) and are expected to lead to an enhancement of domain orientation, remnant field and dielectric constant. Additionally, a low coercitivity results. Donor dopants also counteract the natural p-type conductivity of PZT [2, 7]. However, as already mentioned in Sec. 2.1.2, the defect chemical relations still have to be further investigated. These materials are used in applications, which require a high sensitivity such as loudspeakers, sounders and actuators.

- Acceptor dopants: Additives like Fe^{3+} replacing Zr^{4+} cause poorly developed hysteresis loops and a lower dielectric constant, which is attributed to oxygen vacancy compensation
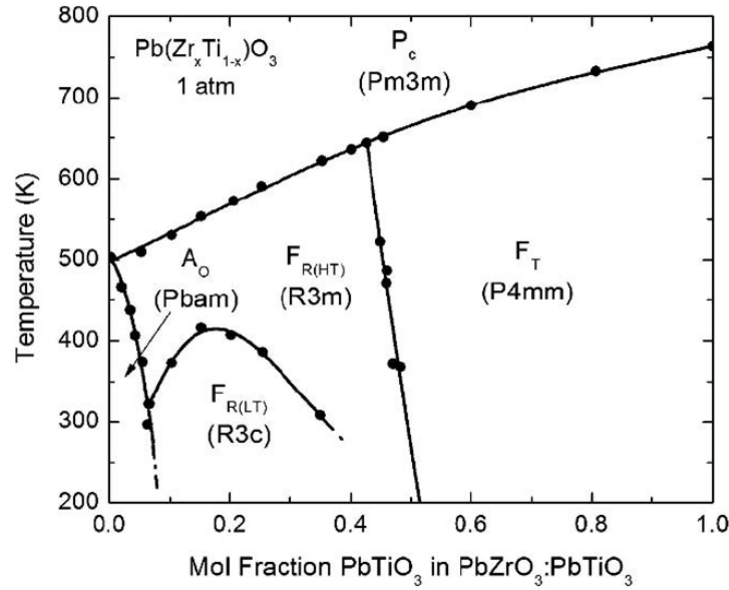
Fig. 2.12: Illustration of the composition-temperature phase diagram of PZT with the MPB between the rombohedral F_R and tetragonal F_T phase (adapted from [2]).

(see also Sec. 2.3.3). The reduction in dielectric loss (energy dissipating as heat in a dielectric material), however, makes acceptor doped materials an excellent choice for high power devices like ultra-sonic transducers.

• Isovalent additives: Substituting a PZT component with an isovalent equivalent can result in a modification of CURIE temperature and also influence the piezoelectric behavior [95].

The concentrations of the dopants are usually in the range of $\leq 3\%$ [4]. This is, of course, a very high concentration from a semi-conductor science point of view, in which doping concentrations in the ppm range are common.

Popular terms to describe a doped piezoelectric material are "soft" and "hard". Donor doped PZT is referred to as "soft" because of the easily switchable domain orientation and low coercivity. Because acceptor doped PZT exhibits quite the opposite properties they are definded as "hard" piezoelectric materials [2, 4, 88].

Despite known doping levels, knowledge on defect concentrations is usually scarce (see also Sec. 2.1.2). One of the reasons why only little information on the defect chemistry is obtained is the circumstance that with impedance spectroscopy it is not possible to simply distinguish between conduction mechanisms in a NYQUIST plot especially if only one semi-circle results (see

Sec. 2.4). There has been research in which a second semi-circle was discussed but it remains unclear why the second one arises in these cases and not in others [24, 25, 96]. Usually, conductivity is attributed to holes and oxygen vacancies with the holes being partly trapped at lead vacancy positions [7, 24]. Whether holes or oxygen vacancies are the primarily conducting defects certainly depends on partial pressure and temperature (see Eq. 1.1). Investigations on conductivity in thin films led to proposed ohmic conduction at low fields and space charge limited currents (SCLC) at high fields [97]. This can be described by a space charge layer developing due to injection of electrons in a resistive material [98]. This layer then inhibits further injection until an equilibrium is reached.

2.3.3 Degradation and Fatigue of PZT

Although PZT is a well known material empoloyed in a lot of applications for over 60 years, for a long time only little attention has been given to degradation and fatigue mechanisms. The role of doping was mostly investigated with respect to the dominant piezoelectric properties and not to the microscopic defect chemical related effects. Recently, this topic got more attention due to new possible applications like ferroelectric random access memories (FeRAMs), in which a high degradation resistance is necessary [43, 99]. The research concerning degradation led to many proposed mechanisms, which have been discussed with hardly any relation to each other, and very often just thin film materials were under investigation [6]. Although, some models suggest that oxygen vacancies induced by PbO evaporation during the sintering step are responsible for some degradation mechanisms [7, 24].

To shed some light on this topic a summary of some possible degradation and fatigue mechanisms will be given in the following. The first priority in the research of degradation of a piezoelectric material is to explain the reduction of remnant polarization and the deformation of the hysteresis curve with increasing cycling number of bipolar loading [5, 6].

One of the most prominent mechanisms suggested is the domain wall pinning mechanism [8, 100–102]. This theory states that the domain movement is hindered by charges at domain boundaries creating a field itself. This is often attributed to electron trapping supported and stabilized by oxygen vacancies. Geneko et al. recently supported this theory [9, 10]. The result of their research was that due to the disorder in the polarizational vectors mobile charges are moving preferably at grain boundaries as an effect of these fields so that local depolarization fields are compensated.
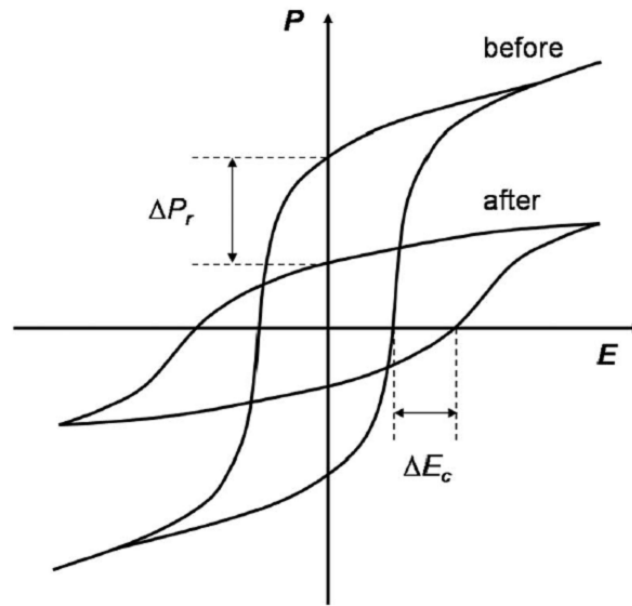
Fig. 2.13: Illustration of the reduced remnant polarization and loop deformation (also change in coercive field E_c) due to degradation after bipolar electrical stressing of the corresponding material (adapted from [6]).

That leads to a development of space charge layers at grain boundaries. Additionally, a state of minimum free enthalpy is reached, which impedes further repolarization. The theory is in good agreement with what is expected from acceptor doping of PZT. The compensation of the dopants by oxygen vacancies results in the "hard" properties because domain movement is inhibited by the charged vacancies. However, some aspects can not be explained sufficiently and although the involvement of oxygen vacancies is often postulated it is still under investigation how large their contribution is [6]. The generation of defect dipoles and clusters which consequently inhibit domain wall movement is also widely discussed [103, 104]. Therefore, domain wall pinning is a plausible, well investigated degradation theory but the defect chemical related effects leading to immobilized domain walls are still rather unclear.

Another microscopic effect, which is attributed to degradation and fatigue is the development of microcracks [5, 105, 106]. Due to the mechanical stress at intersections during domain wall movement cracks might occur. As a result, a higher field is necessary to induce polarization switching. Although it has been found that cracks can occur, it is still not clear if cracking is the cause of fatigue or if it just correlates with it [6].

The third important polarization degradation model is the charge injection model. Lou at al. state that during cycling a phase decompostion can occur due to charge injection [6, 44, 45, 107, 108]. This leads to the development of a pyrochlore like phase with lower permittivity. As a result, the effect of the applied field is reduced (lower permittivity layer). The location of charge injection is where the so called domain nucleation sites reside which in addition is expected to make switching more diffucult. This model can be seen as related to the proposed SCLC conduction mechanism.

The above presented models are mainly used to describe the polarization fatigue. Resistance degradation, which occurs in polycrystalline ceramics used for actuator applications, is still hardly investigated. The term 'resistance degradation' basically means the reduced resistance (sometimes referred to as leakage current) due to application of high voltages [49, 109, 110]. This can lead to a lower polarizability of the ferroelectric material and hence also to a power loss when used in acuators. Usually, the unipolar field applied to these materials has a different impact than bipolar loading [5, 102]. The problem considering the comparison of results is the large variety of parameters which could influence conductivity and degradation mechanisms. Doping is the most obvious example for inducing different conduction mechanisms. Other possibilities are sintering temperature and atmosphere (with respect to PbO evaporation and oxygen vacancy creation), magnitude and frequency of the applied field and choice of electrodes [6]. Considering the electrode choice, mixed electronic/ionic conducting LSC electrodes have been proven to reduce fatigue in PZT samples which might be further evidence for the contributions of oxygen vacancies in degradation mechanisms [44, 111]. In thin film applications these electrodes are discussed to be sinks for oxygen vacancies. Hence, they reduce fatigue mechanisms induced by them. The regularly employed silver based electrodes in actuator materials, however, seem to have a negative effect on the piezoelectric properties [47, 48]. This might be attributed to the silver being very mobile inside the PZT material [112–114] which could also lead to a doping effect [46, 47]. Further contribution to the difference between oxide and metal electrode might result from different contact types. Many metal electrodes, for example, are known for creating SCHOTTKY contacts at the PZT interface [115–117].

This thesis further contributes to the investigations on conduction mechanisms and dominant defects in PZT. Tracer diffusion experiments investigated with time-of-flight(ToF) secondary ion mass spectrometry (SIMS) (see Sec. 2.5) gives further information on the importance and

motion of oxygen vacancies. Additionally, DC/AC measurements have been conducted with different electrodes to investigate the impact of the electrode material on resistance degradation.

2.3.4 BaTiO$_3$ (BT)

As a piezolectric material BT has been almost entirely substituted by PZT. PZT based materials have a higher CURIE point (around 400°C instead of 150°C), possess a range of modifiable piezo-electric constants and obtain an enhancement of dielectric constants and piezoelectric coefficients at the MPB [44]. However, BT is still used in positive temperature coefficient (PTC) [44, 87] resistors and multilayer ceramic capacitors (MLCC) [118]. Before these two applications are introduced the known defect chemical relations in BT will be briefly presented. There is a lot more information available on the defect chemistry than for PZT [18].
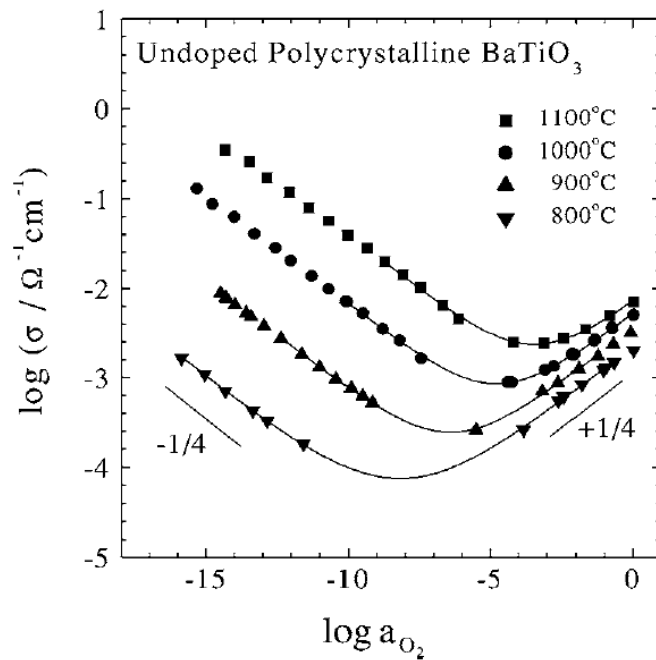
Fig. 2.14: Electrical conductivity isotherms of undoped BaTiO$_3$ (adapted from [18]).

Undoped BT is expected to have at least a small amount of unintentional acceptor doping so that undoped and acceptor doped materials are often discussed equivalently. In this case BT is a mixed electronic/ionic conductor over a large partial pressure range and there is a transition between n- and p-conducting behavior. Fig. 2.14 shows the conductivity isotherms of an undoped BT

where in the low pressure region n-conduction dominates and p-conduction in the high pressure region [16]. This situation can be expressed by a simple equation [18]:

$$[e'] + [A'] = [h^\bullet] + 2[V_O^{\bullet\bullet}] \tag{2.50}$$

where $[A']$ is the acceptor dopant concentration. This way two regimes of disorder can be identified: 1) $(e', V_O^{\bullet\bullet})$ and 2) $(A', V_O^{\bullet\bullet})$ The conductivity in these regimes can be deduced from the defect chemical relations [18]. In the first one the electronic conductivity dominates, which results in:

$$\sigma \approx \sigma_e = eu_e(2K_r)^{1/3}a_{O_2}^{-1/6} \tag{2.51}$$

with u_e the electron mobility, a_{O_2} the oxygen activity and $K_r = [V_O^{\bullet\bullet}]n_e^2 a_{O_2}^{-1/2}$ where n_e denotes the number of electrons. However, in the second regime the total electrical conductivity is dependent on the ionic σ_{ion} and electronic conductivity σ_{el}.

$$\sigma = \sigma_{el}\cosh\left[\frac{1}{4}\ln\frac{a_{O_2}}{a_{O_2}^*}\right] + \sigma_{ion} \tag{2.52}$$

The electronic conductivity consists of the electron and the hole conductivity ($\sigma_{el} = \sigma_n + \sigma_p$). The parameter $a_{O_2}^*$ represents the oxygen activity at which $\sigma_e = \sigma_h$ and is related to the standard oxygen activity $a_{O_2}^0$:

$$a_{O_2}^* = \frac{u_e}{u_h}a_{O_2}^0 \tag{2.53}$$

Highly acceptor doped BT materials are used in MLCC [37,118]. These are sintered in reducing atmosphere to inhibit oxidation of the electrodes. A reduction of the BT, however, should be prevented. Therefore, a high acceptor dopant concentration is necessary [18]. The reason for the need to be careful about reduction is the high n-semiconductivity resulting from it. In contrast to PZT, for which donor doping leads to annihilation of oxygen vacancies and increase of resistance, the BT resistance decreases drastically when it is donor doped. This situation, however, is inverted again for the BT if the dopant concentration is increased even further [17]. In many publications the second increase is attributed to a change from electronic to metal

vacancy compensation [17, 19, 119]. The conductive BT material resulting from donor doping cannot be used for MLCC. However, the described properties of donor doped BT are very useful and employed in PTC resistors.

The PTC behavior describes a sharp increase in conductivity of a donor doped polycrystalline BT material in the vicinity of the CURIE temperature. This situation is often explained by the HEYWANG model [22]. The BT consists of semiconducting grains and a space charge layer at the grain boundaries, which can be characterized as a double SCHOTTKY diode. The relationship between the barrier height $\Delta\varphi_0$ and the depletion layer width d can be deduced from the solution of the one-dimensional POISSON equation [88]:

$$\Delta\varphi_0 = \frac{qc_Dd^2}{2\epsilon_r\epsilon_0} \tag{2.54}$$

where c_D is the bulk donor density. If c_{gb} is defined as the concentration of charge particles per area trapped in boundary acceptor states we obtain:

$$c_{gb} = 2dc_D \tag{2.55}$$

Combining Eq. 2.55 and Eq. 2.54 results:

$$\Delta\varphi_0 = \frac{qc_{gb}^2}{8\epsilon_r\epsilon_0c_D} \tag{2.56}$$

The resistance of the corresponding grain boundary R_{gb} is then given by [120]:

$$R_{gb} = B\exp\left(\frac{e\Delta\varphi_0}{k_BT}\right) \tag{2.57}$$

where B is a more or less temperature independent factor. The dependence of the potential barrier on the permittivity is, however, not sufficiently described by this model. Jonker found out that the permittivity value is not constant but might rely on the ferroelectric behavior of the material [23]. The low resistivity of PTC material below the CURIE temperature can therefore be (at least qualitatively) be attributed to the screening of trapped interfacial charges by the spontaneous polarization of the ferroelectric grains. Above the CURIE temperature the polarization vanishes and the bulk permittivity decreases. Hence, the grain boundaries become

fully resistive. In the case above the origin and the nature of the acceptor states in the grain boundary is not given and leads back to the discussion on the defect chemistry of donor doped BT. What is the origin of the semiconducting behavior? Which mechanisms occur upon slow cooling?

It is be expected that the space charge layer developes due to an already reoxidized grain boundary area. Very often a metal vacancy related oxidation process is assumed [121]:

$$O_2(g) + 4e^{'} \leftrightarrow V_{Ti}^{''''} + 2O_O^x \qquad (2.58)$$

However, contradictory results have been presented considering which metal vacancy actually contributes to the compensation ($V_{Ti}^{''''}$ or $V_{Ba}^{''}$) [20, 120, 122, 123]. Recent research showed that titanium vacancies are most likely to be involved in such a mechanism [62, 121]. It has to be mentioned that the semiconduction behavior does only occur if the corresponding samples are cooled rapidly. Otherwise the resistance is very high. This means that a state is frozen in, which facilitates the semiconductivity. Often, this conductivity is said to be closely related to a correlation between oxygen vacancies and simultaneously created electrons [17, 124, 125]:

$$O_O^x \Rightarrow \frac{1}{2}O_2 + V_O^{\bullet\bullet} + 2e^{'} \qquad (2.59)$$

Morrison et al. suggested that this reaction might even be the whole reason for the semiconduction behavior [17]. The donor dopants on the other hand could simply be compensated by metal vacancies or annihilate oxygen vacancies. The small amount of oxygen vacancies created at higher temperatures due to the relation in 2.59 could then be rapidly frozen in upon fast cooling.

Although the PTC effect is usually attributed to reoxidation via grain boundaries, there is few experimental data available on the oxygen transport along this pathway in donor doped $BaTiO_3$. Most investigations dealing with oxygen diffusion were performed on undoped or acceptor doped BT and $SrTiO_3$ to obtain the chemical diffusion coefficient [13,18,77,78]. Only a few studies of the chemical diffusivity of n-conducting barium titanate have been reported so far [21, 77, 121, 126]. However, ^{18}O tracer diffusion experiments with oxygen exchange rate measurements [125] or subsequent secondary ion mass spectrometry (SIMS) analysis [28] provided first evidence for rapid grain boundary diffusion. In addition, conductivity relaxation experiments on n-type BT

ceramics were interpreted in terms of extremely fast diffusion along the grain boundaries and slow rate-determining diffusion of cation vacancies from the grain boundaries into the grains [127].

In this work we present the results of ^{18}O-tracer experiments on donor (La) and acceptor (Mn) co-doped barium titanate investigated by ToF-SIMS in order to clarify the role played by oxygen diffusion along the grain boundaries in BT-based PTC ceramics.

2.4 Impedance Spectroscopy

To understand the kind of information, which can be obtained by impedance spectroscopy or other conductivity experiments it is necessary to evaluate the mathematical approach used to identify conduction processes in the materials under investigation. In this section a short introduction into alternating current circuits will be given.

The alternating current resistance Z is called impedance [128]. The impedance resulting from inductive or capacitive behavior is called reactance. The current I(t) in a capacitor resulting from a cosine-type alternating voltage $U(t) = U_0 \cos(\omega t)$ is given by:

$$I(t) = C\frac{\partial U(t)}{\partial t} = -\omega C\, U_0 \sin(\omega t). \tag{2.60}$$

C denotes the capacitance and ω the angular frequency. For an inductor with the inductivity L results:

$$U(t) = L\frac{\partial I(t)}{\partial t} \;\Rightarrow\; I(t) = \frac{U_0}{L}\int \cos(\omega t)dt = \frac{U_0}{\omega L}\sin(\omega t). \tag{2.61}$$

Because of the relationship I= U/Z the reactances of an inductor and a capacitor are:

$$|Z_C| = \frac{1}{\omega C} \qquad |Z_L| = \omega L. \tag{2.62}$$

From Eq. 2.60 and Eq. 2.61 it can be deduced that current and voltage of capacitors and inductors are out of phase [129].

Because the reactance is frequency dependent a derivation of the current/voltage relationship with respect to time t is only mathematically simple if the signal depends on one frequency. With alternating currents, which are not cosine- or sine-type or non-periodic, continious time

functions very complicated differential equations result [130]. The calculations can be simplified, however, by conducting a FOURIER transformation:

$$
\begin{aligned}
\hat{U}(\omega) &= \int_{-\infty}^{\infty} U(t) e^{i\omega t} dt \\
\hat{I}(\omega) &= \hat{Z}(\omega)^{-1} \cdot \hat{U}(\omega) \\
I(t) &= \frac{1}{2\pi} \int_{-\infty}^{\infty} \hat{Z}(\omega) \cdot \hat{U}(\omega) e^{i\omega t} dt.
\end{aligned}
\tag{2.63}
$$

Like demonstrated in Eq. 2.63, the time dependent and real function of voltage U(t) is transformed into the complex frequency domain(ˆ denoting a complex value). The frequency dependent current $\hat{I}(\omega)$ can be calculated by dividing $\hat{U}(\omega)$ by the impedance $\hat{Z}(\omega)$. This can be converted again into the time dependent current I(t) by inverse FOURIER transformation. Due to this transformation the differential equations can be expressed by simple products and divisions in the frequency domain. Hence, the mathematical treatment is according to KIRCHHOFF´S rules, which is used to describe the linear voltage/current relations under direct current conditions [128].

The complex variables in the frequency domain can be split into real and imaginary parts [131]. This is illustrated by the example of the impedance:

$$
\hat{Z}(\omega) = \frac{\hat{U}(\omega)}{\hat{I}(\omega)} = Z'(\omega) + iZ''(\omega).
\tag{2.64}
$$

Z' is the real and Z'' the imaginary part of the impedance. The reactance of an inductor and a capacitor contribute mostly to the imaginary part of the impedance. The impedance for a series circuit of a resistor R and a capacitor C can be calculated according to KIRCHHOFF´S mesh rule:

$$
U(\omega) = I(\omega)\hat{Z}(\omega)_1 + I(\omega)\hat{Z}(\omega)_2 \ \Rightarrow \ \hat{Z}(\omega) = R + \frac{1}{i\omega C}.
\tag{2.65}
$$

Other parameters of interest can be deduced from the impedance. The most important ones are the admittance $\hat{Y}$, the permittivity $\hat{\epsilon}$ and the modulus $\hat{M}$:

$$
\hat{Y}(\omega) = \frac{1}{\hat{Z}(\omega)} \qquad \hat{\epsilon}(\omega) = \frac{1}{i\omega C_0 \cdot \hat{Z}(\omega)} \qquad \hat{M}(\omega) = i\omega C_0 \cdot \hat{Z}(\omega).
\tag{2.66}
$$

$C_0 = \epsilon_0 \cdot A/d$ denotes the vacuum capacitance, which depends on the samples geometry (A is the area and d the distance between electrodes). The admittance is closely related to the conductivity.

The conductivity can basically be seen as the specific admittance, which is dependent on the thickness d an the area A of the sample under investigation.

$$\hat{\sigma}(\omega) = \hat{Y}(\omega) \cdot \frac{d}{A}. \tag{2.67}$$

The phase angle between real and imaginary part is usually calculated by:

$$\tan(\delta) = \frac{\epsilon''}{\epsilon'} = \frac{Z'}{Z''}. \tag{2.68}$$

$\tan(\delta)$ is often referred to as dielectric loss function. Because Z' and ϵ'' can be seen as a measure of the energy dissipated as heat and Z'' and ϵ' as a measure of the stored and again available energy $\tan(\delta)$ quantifies the interrelationship.

The simplest illustration of the behavior of conductive material in an alternating current (AC) field is a parallel RC-circuit(Fig. 2.15) [131].
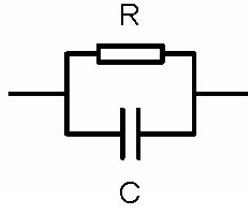
Fig. 2.15: RC-circiut in parallel

In addition to the resistance of the material a capacitance developes due to the polarization of the material. The contribution to the capacitance depends on the permittivity:

$$C = \epsilon_r \epsilon_0 \frac{A}{d} \tag{2.69}$$

ϵ_0 and ϵ are the permittivity of the vacuum and the material respectively.

For a parallel RC-circuit KIRCHHOFF´s junction rule can be applied:

$$\hat{I}(\omega) = \frac{\hat{U}(\omega)}{\hat{Z}_1} + \frac{\hat{U}(\omega)}{\hat{Z}_1} \;\Rightarrow\; \hat{Y}(\omega) = \frac{1}{R} + i\omega C. \tag{2.70}$$

With Eq. 2.66 the following relation results:

$$\hat{Z}(\omega) = \frac{1}{\hat{Y}(\omega)} = \left(\frac{1}{R} + i\omega C\right)^{-1} = \frac{R}{(\omega RC)^2 + 1} - i\frac{\omega R^2 C}{(\omega RC)^2 + 1} \tag{2.71}$$

There are various possible plots from which the frequency dependent information on the just described variables can be obtained. The NYQUIST plot is probably the most common one. In this case the imaginary part Z'' is plotted against the real part Z'. A process, which can be described by a parallel RC-circuit, results in a half circle in a NYQUIST plot (Fig. 2.16) [131].
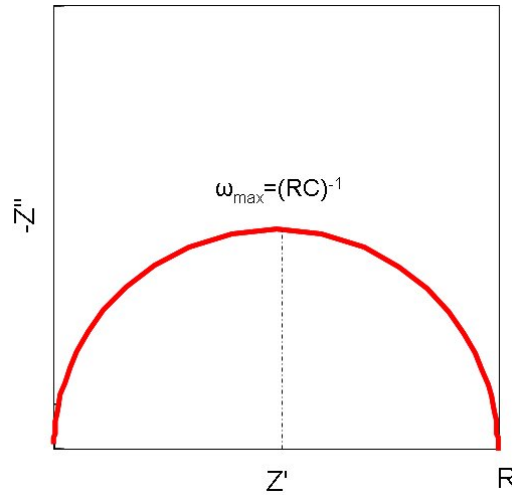
Fig. 2.16: Illustration of electrical properties in the NYQUIST plot of a material described by a RC circuit.

The half circle intersects with the real axis at the value of the resistance R. The frequency is implicit to each point of the semi-circle. The frequency $\omega_{\max}$ at which $-Z''$ obtains its maximum value is given by $\omega_{\max} = 1/RC$. The reciprocal value is the time constant τ. Therefore, not only the value of R but also the value of C can be deduced from a NYQUIST plot which makes it a very powerful tool. The above discussed models describe the ideal behavior of materials. This is usually not the case and the use of ideal resistances or capacitances is often not possible. A deviation from the ideal behavior is sometimes observered for disordered solids or polycrystalline material. In this case the so called constant phase element (CPE) is employed:

$$\hat{Z}_{\mathrm{CPE}}(\omega) = A^{-1}\left(i\omega\right)^{-\alpha}. \tag{2.72}$$

The parameter α can obtain values from 0 to 1 [131]. Eq. 2.72 describes an ideal resistance if the value is 0 and an ideal capacitance in the case the value is 1. With a CPE it is accounted for
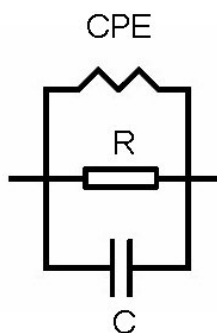
Fig. 2.17: Equivalent circuit with CPE

that the electrical behavior of a material often cannot be described by a single time constant. Sometimes a distribution can be assumed and this has been used by RAISTRICK for the first time to evaluate the behavior of alumosilicates (Fig. 2.17) [132]. A microscopical mechanism, which leads to a time constant distribution, can be deduced from the jump relaxation theory [71]. After a jump into a new potential minimum the surrounding relaxes in respect to the particle. This results in a change of the potential barrier for the return to the original position. Hence, the relaxation leads to a change in the time constant of the hopping process.
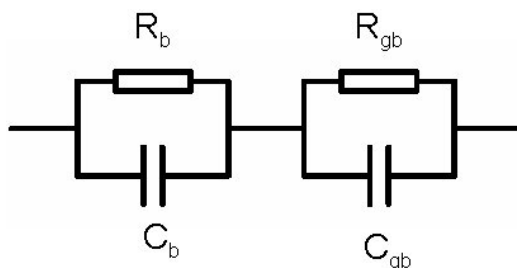
Fig. 2.18: Equivalent circuit according to brick layer theory [131].

The choice of an equivalent circuit does not only depend on the opportunity to fit a spectrum. The elements should be related to physical processes, which sufficiently describe the behavior of a material. This can be complicated due to reactions, which cannot be sufficiently represented by an element [131]. In many cases there are more equivalent circuits applicable for the same spectrum. Is the material of interest a polycrystalline substance the so called brick-layer theory from VAN DIJK and BURGGRAAF is usually employed [133]. This theory states that two processes

contribute to the conductivity. One process concerns the transport inside the bulk of a grain and the other takes the transport across the grain boundary into account. In this case a series of two parallel RC-circuits are used to describe this condition (Fig. 2.18).

R_b and C_b are the contributions from the bulk and R_{gb} and C_{gb} the ones from the grain boundary. The NYQUIST plot of such an equivalent circuit (assuming the valus of the grain boundary are higher than the bulk) is given in Fig. 2.19.
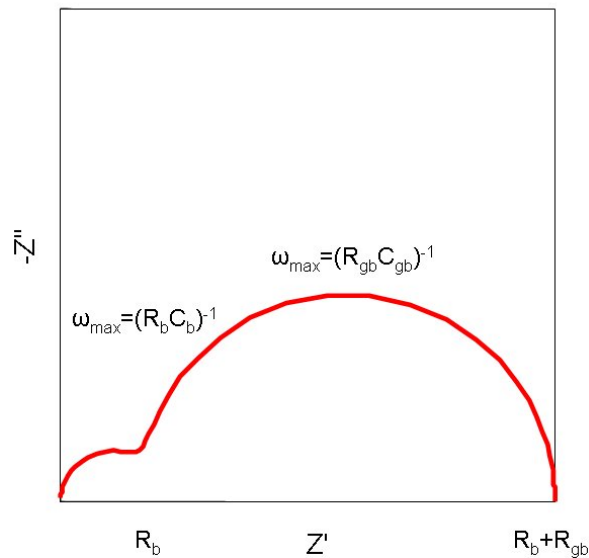
Fig. 2.19: NYQUIST-plot typical for a polycrystalline material.

Again, this is a description of an ideal behavior as grains are assumed to be of the same size and of square shape [134]. Consequently, the expected deviations of this idealization result in a distribution of time constants and the use of a CPE is often preferred [131].

2.5 Time-of-flight(ToF) Secondary Ion Mass Spectrometry (SIMS)

SIMS is a one of the most powerful techniques in surface analysis. The chemical and distributional information of a variaty of materials can be obtained with excellent mass and spacial resolution [135–138]. It has been first discovered by HERZOG and VIEBÖCK that secondary ions are generated from a sample due to an impinging primary ion beam [139]. Although it took a few

decades until this principle could be properly utilized, SIMS is now a well established method and employed in material science [140], polymer science [141–145] and biology [146–149].

Since now a lot of effort has been put into the research of secondary ion generation. However, the mechanisims are not completely understood yet. The generally accepted model regards the impact of the primary ions with the material (with an energy in the range of 250 eV to 30 keV), which leads to an interaction with various sample atoms (Fig. 2.20) [136, 140]. Consequently, the energy dissipates in a so called collision cascade and the primary ion is implanted into the material (penetration depth). Some of the atoms residing in the first few nanometers at the surface obtain a momentum and leave the surface (sputtering process). The layer, which the primary ion penetrates, is altered and that consequently influences further measurements. Differences in the density inside a material lead to preferential sputtering and to roughening of the sample. Such an effect can influence a surface mass spectrum. Areas can develop, that are no more accessible by the primary ion beam incident at a certain angle [150–153]. The beam is basically shadowed by artifacts in the surface topography. The extraction field of the used analyzer is also distorted by these artefacts leading to an additional parameter, which has an impact on the measurement [151,153]. Very often roughening effects can be suppressed by sample rotation [153,154]. However, if the surface should be imaged to obtain the lateral information of surface composition, rotation of the sample is not an option.
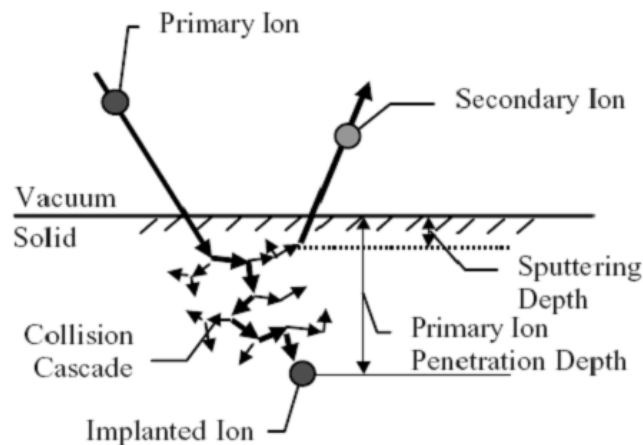
Fig. 2.20: Illustration of collision cascade induced by an primary ion beam (adapted from [140])

The sputtered material mainly consist of neutral atoms and molecules and only a small fraction is ionized ($10^{-6} - 10^{-1}$). The secondary ion current I_m is given by [136]:

$$I_m = I_p Y_m \alpha \; \theta_m \eta \tag{2.73}$$

where I_p denotes the primary ion flux, Y_m the sputter yield, α the ionization probability, θ_m the fractional concentration of species m at the surface and η the transmission of the analysis system. It can be seen in Eq. 2.73 that the secondary ion current strongly depends on the ionization probability and therefore depends also on the chemical state of the emitting surface. This relationship is called matrix effect and results in different secondary ion currents for the atoms or molecules of interest [135, 136, 153]. It can be expected that quantification of the obtained information on the surface composition is therefore quite difficult. To achieve quantification a sample with known concentration and similar or identical matrix is needed. The measurements can then be scaled by the so called relative sensitivity factors (RSF) when the same measurements conditions are applied to the reference and the material under investigation [136, 146].

The mechanism behind the secondary ion generation is also still subject of ongoing research. For many materials it is expected that ionization results from the breaking of a covalent or ionic bond [155]. Depending on the electronegativity of the sputtered and ionized particle it will leave the surface primarily negatively or positively charged. For metals a model of ionization is used based on the interaction between the sputtered particle and the valence band of the material [156–159]. There is a certain probability of charge transfer from or to the surface when the atomic levels of the removed particle cross the electronic levels of the metal. This depends on the work function Φ of the metal, the ionization potential U_I of the sputtered particle, the distance of the particle to the surface z_c and the velocity of the particle (see illustrated in Fig. 2.21).

With the use of a Cs^+ or O_2^+ ion gun it is possible to change the work function of a surface so that the yield of negative or positive secondary ions is enhanced [157, 160]. The Cs^+, for example, leads to an enhancement of the negative ions. With incorporation and neutralisation of the Cs^+ the probability of an electron transfer from the electropositve Cs to a leaving particle increases. This is of course a simplified qualitative view but a further discussion is beyond the scope of this thesis.

Nowadays, it is distingiushed between two kinds of SIMS methods. The first one is the so called dynamic SIMS. The corresponding instruments are equipped with ion guns with very high primary ion flux (μA), which leads to a gradual erosion of the sample in the analysis
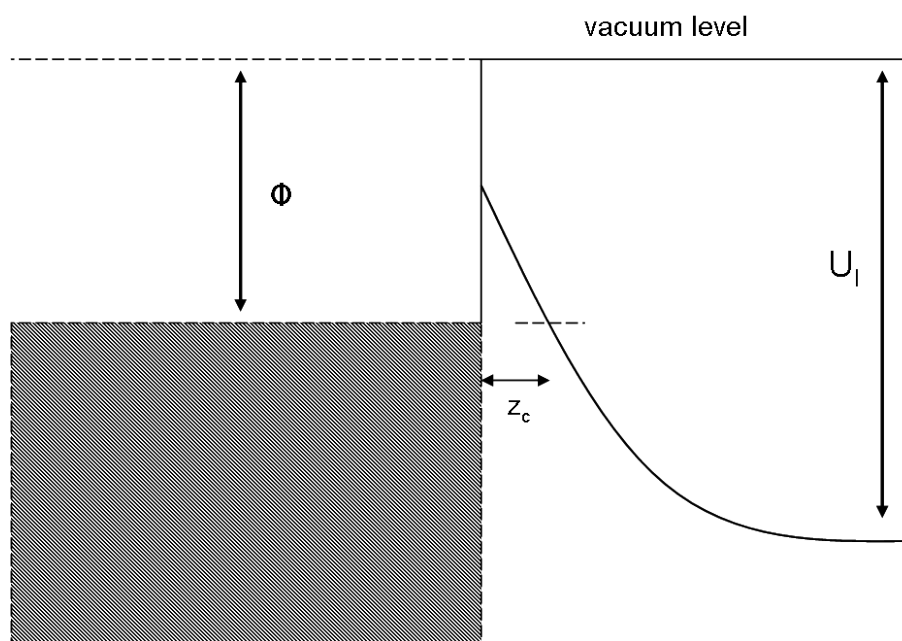
Fig. 2.21: Illustration of an energy diagram for a particle leaving the metal surface (according to [158,159])

area [135]. That way a depth profile of the sample composition is easily obtainable. Together with a magnetic sector field detector dynamic SIMS has been proven to be a good choice for isotope analysis in materials science due to its high mass resolution and secondary ion intensities. However, only a few ions can be detected simultaneously and mainly atomic instead of molecular information can be obtained. This is of course disadvantageous for the analysis of organic or biological material [141]. Additionally, the induced damage in the organic material can be very high.

The other method is called static SIMS. This describes the measurements in which the primary ion beam flux is so low (pA-nA) that less than 1% of the surface is damaged (static regime) [135, 136, 161]. Hence, this method is very surface sensitive and elemental as well as molecular information from the upper most layers is achievable. Monoatomic ion sources (Cs^+ and Ga^+) are successfully employed in ToF-SIMS due to the opportunity to obtain well focussed beam spots [141]. However, considering analysis of organic and biological material monoatomic ions cause similar problems to the already mentioned ones for dynamic SIMS. A high energy impact does not result in an enhancement of secondary ion intensity. It rather leads to a decrease especially for larger molecules. However, experiments with cluster ions (SF_5^+, C_{60} and Bi_n) showed that the use of higher molecular primary ions results in an increased secondary ion intensity and higher

depth resolution for the investigation of organic and biological material [162–165]. Recently, it was shown that an argon cluster beam (with about 1000 atoms per cluster) can ionize an arginine molecule without destroying it [166]. Again the mechanisms on which these effects rely are not completely understood. It is assumed that the energy of a cluster is more or less equally distributed over the atoms and that the impact energy dissipates mainly in the top surface layers as the cluster components hardly penetrate the sample [167]. The by far most widely
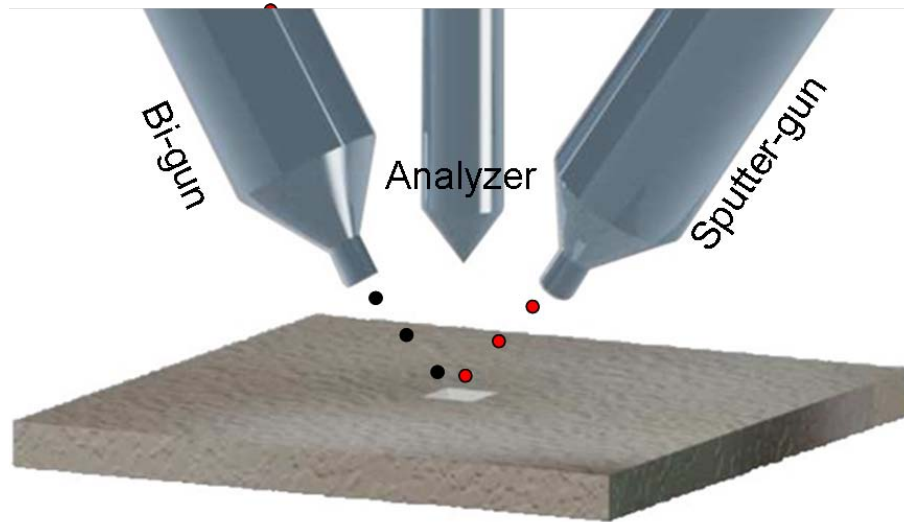
Fig. 2.22: Illustration of a ToF-SIMS dual beam setup.

employed analyzer in static SIMS is the ToF-analyzer. A high transmission and mass resolution can be obtained with it and a wide range of secondary ions can be detected simultaneously. The secondary ions in the analyzer ideally have the same kinetic energy E which leads to different arrival times t at the ion detector [136, 146] after flying a distance x:

$$E = q \cdot U_e = \frac{1}{2}mv^2 \Rightarrow t = L_a \cdot \sqrt{\frac{m}{2qU_e}} \tag{2.74}$$

where v denotes the velocity, m the mass, L_a the length of the analyzer and U_e the accelaration voltage. A consequence from using the ToF-analyzer is that the measurement has to be pulsed. That causes some disadvantages, which will be briefly discussed below. However, during the period in which no secondary ions are extracted it is possible to use an electron gun for charge compensation. Therefore, an investigation on an insulating surface is hardly problematic with ToF-SIMS while charging effects could significantly affect dynamic SIMS measurements because of changes in the extraction field [136]. At first, ToF-SIMS instruments were not able to provide

depth profile measurements. The introduction of a second ion gun, which is solely used to remove surface material made ToF-SIMS instruments versatile tools for many possible applications [168]. In this so called dual beam mode the parameters of the primary ion gun can be optimized for secondary ion generation with excellent mass and lateral resolution while the sputter gun is optimized for material removal. An illustration of the setup is given in Fig. 2.22. In this
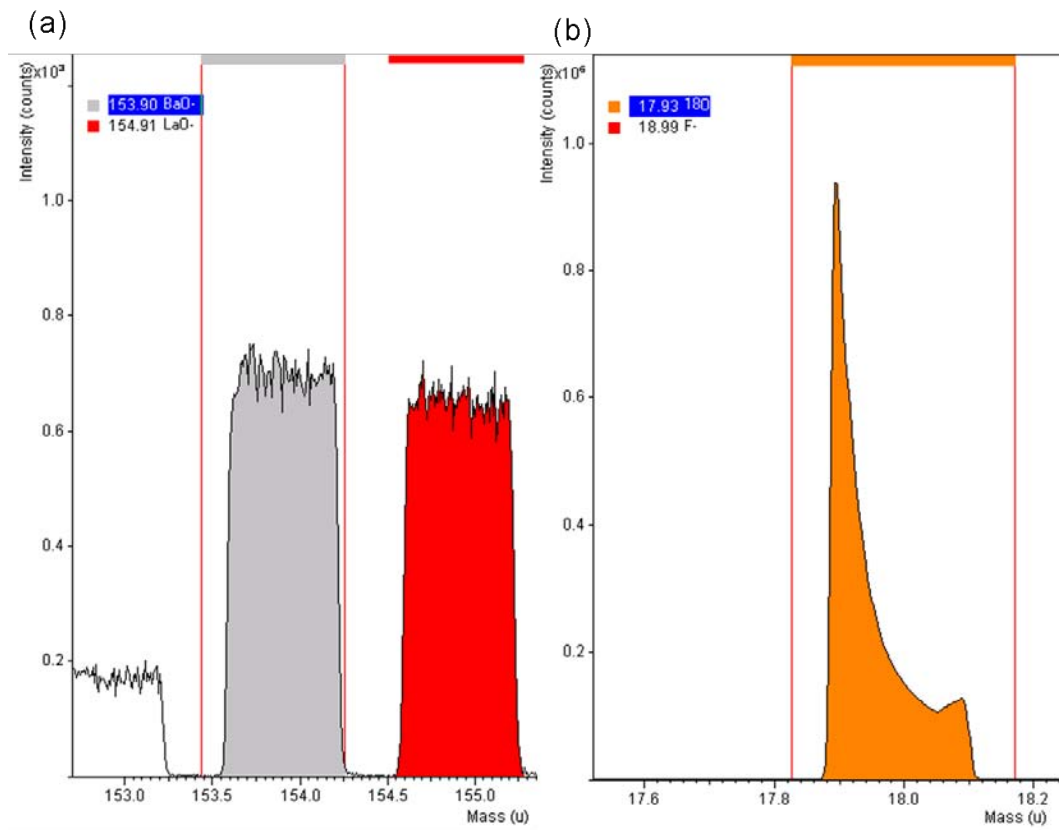
Fig. 2.23: Mass spectra (negative ions) from measurement of $BaTiO_3$ after tracer experiment of (a)BaO and LaO (burst alignment mode); (b) ^{18}O (burst alignment mode).

thesis ToF-SIMS will be used to investigate the ^{18}O tracer diffusion in PZT and BT. A lot of tracer diffusion experiments were investigated with dynamic SIMS [28, 29, 36, 37, 39, 40, 169–177]. However, investigations with ToF-SIMS can be difficult. This is due to the use of a single ion detector. When the detector is hit by a charged particle it cannot detect any further ion coming in for a certain time (dead time). It is expected in static SIMS that the secondary ion yield is low and that not more than one ion of a molecular or atomic species is generated per primary ion pulse. Although, this is often not the case. Therefore, the ions hitting the detector during the dead time are not accounted for and the actual secondary ion intensity can be expected to

be higher than the measured one. To overcome this problem the so called POISSON correction is used for the secondary ion signal. It is still assumed that the secondary ion yield is very low and
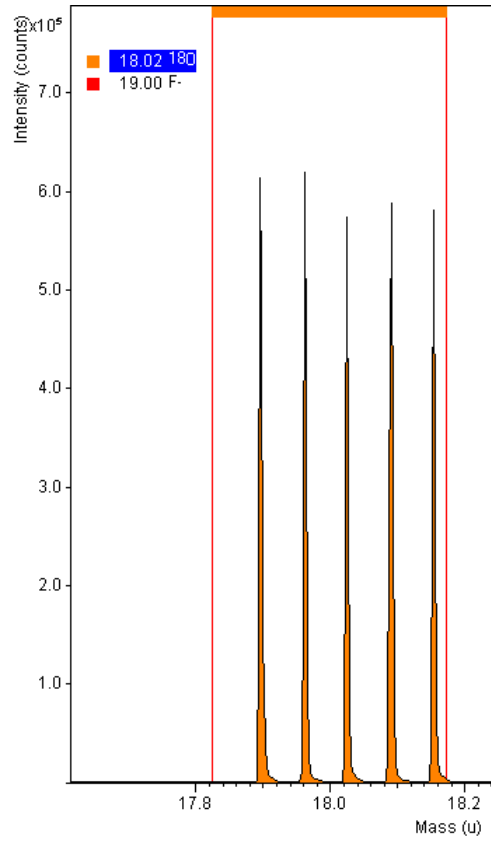
Fig. 2.24: Mass spectrum (negative ions) from measurement of BaTiO$_3$ after tracer experiment of ^{18}O (burst mode).

that the probabilty p$_k$ that k particles out of n are desorbed during the time Δt can be given by the POISSON distribution [178]:

$$p_k = \frac{\lambda_p^k}{k!} e^{\lambda_p} \tag{2.75}$$

where $\lambda_p = p \cdot n$ denotes the arithmetic mean of desorbed particles during Δt with p as the probability that any particle out of n is desorbed. The secondary ion signal can then be calculated with a correction formular:

$$I_{corr} = -N \ln \left(1 - \frac{I_{exp}}{N} \right) \tag{2.76}$$

with N the number of ionization pulses, I$_{corr}$ the corrected intensity and I$_{exp}$ the intensity from the experiment. The mass spectrum of BaO and LaO negative ions (512x512 shots per scan)

from depth profiling of $BaTiO_3$ are depicted in Fig. 2.23 (a). The measurement was conducted in the so called burst alignment mode, which simply means that an unmodified ion pulse is used (no modification of the length and shape of the pulse). It can be seen that there is an equal probability to detect a secondary ion over the length of the pulse. If the intensity of the secondary ion increases even further and the probability to detect an ion in the first few ns becomes high there is an immediate drop in intensity after a high peak due to the dead time of the detector. This situation is illustrated in Fig. 2.23 (b) for the corresponding ^{18}O signal. It can also be seen that the detector recovers again leading to a small increase of intensity at the end of the pulse. The dead time of the detector therefore inhibits quantification and results in a large error for the relative concentration of the tracer. To overcome this problem the so called burst mode was introduced [179]. In this mode the pulse from the signal in the burst alignment mode is chopped into small equi-distant pulses (Fig. 2.24). When, for example, the ^{16}O intensity is very high only the first burst is integrated and the relative concentration $c^*_{18_O}$ can be calculated by:

$$c^*_{18_O} = \frac{\sum\limits_{i}^{k} I_{18_O}}{\sum\limits_{i}^{k} I_{18_O} + k I_{16_O}} \tag{2.77}$$

where k denotes the number of bursts. However, this mode leads to a loss of a large fraction of the primary ion intensity, which consequently increases the noise for low tracer concentrations and lowers the image quality. This is a problem especially when Bi-cluster ion gun instead of a Ga^+ ion gun is used. The primary ion fluxes are generally lower in this case. Additionally, the calculation in Eq. 2.77 has to be changed when I_{18_O} is high. Therefore, it is possible that the calculation of the tracer concentration has to be changed from accounting for high I_{18_O} to high I_{16_O} during the evaluation of a tracer profile. A method introduced by Schintlmeister can be used to boost the performance [180]. Instead of using the burst mode the burst alignment mode is employed but only the first 20 ns are integrated to overcome problems due to dead time effects. This way, measurements with good image qualities can be obtain, which can also be quantified.

Chapter 3

Experimental

3.1 Pb(Zr,Ti)O$_3$ (PZT) Samples

Different types of donor doped and undoped PZT, were analyzed in this study. One series of PZT samples from actuator material with Ag/Pd inner electrodes, supplied by EPCOS OHG (Deutschlandsberg, Austria), was doped with strontium niobate (referred to as PZTSr/Nb) resulting in the composition PZT$_{0.995}$(Sr/Nb)$_{0.005}$, where the Zr/Ti ratio is 52/48 [95]. The other samples were 1.5 mol% Nd doped PZT or undoped samples. In the case of the Nd doped PZT it is distinguished between PZT from actuator stacks (EPCOS) with Ag/Pd inner electrodes, Cu electrodes and material sintered without electrodes (referred to as PZTNd(Ag/Pd), PZTNd(Cu) and PZTNd respectively). The actuator samples (1x1x0.1 cm^3 or 0.7x0.7x0.1 cm^3) were cut from stacks and consisted of plain PZT from the top face of the stacks or of numerous PZT-layers with inner electrodes (80 μm spacing). The PZTNd(Ag/Pd) was sintered in air while the PZTNd(Cu) was sintered in reduced atmosphere to inhibit Cu-electrode oxidation. The PZTNd and the undoped PZT were supplied from the work group of Prof. Dr. Reichmann (Technical University Graz, Austria). These samples were disc shaped with a diameter of 1 cm and 0.1 cm thickness. Grain size evaluation was carried out with the program ImageC (Imtronic GmbH, 2001). The average size of Sr/Nb doped PZT grains was either 15 μm (large grains) or 6 μm (small grains) while the size of Nd doped PZT grains was 4 μm in average. For the polishing procedure (Planopol-3, Pedemax polishing machine, Struers, Germany) diamond suspensions (DiaPro 9 μm and 3 μm, Struers, Germany) were used with MD-disc Largo (Struers, Germany).

Etching of PZT samples was carried out with a 10% HCl-solution (applied for 2 min) or with a 5% HCl-solution with 5 drops of 40% HF-solution per 100 ml (applied for about 10 s).

Tab. 3.1: Summary of PZT samples investigated in this thesis; 'actuator' denotes samples from actuator stack (top face or with inner electrodes).

	dopant	sample type	grain diameter /μm
PZT(Sr/Nb)	Nb [57]	actuator (Ag/Pd)	15 or 6
PZTNd(Ag/Pd)	1.5 mol% Nd	actuator (Ag/Pd)	4
PZTNd(Cu)	1.5 mol% Nd	actuator (Cu)	4
PZTNd	1.5 mol% Nd	cylindrical	4
PZT undoped	/	cylindrical	/

3.2 BaTiO$_3$ (BT) Samples

The BT material was synthesized in the group of Prof. Dr. Werner Sitte and Prof. Dr. Wolfgang Preis (Montanuniversität, Leoben). Donor and acceptor co-doped barium titanate was prepared by means of a modified solid state reaction method. Ti (IV)-isopropoxide (Fluka) was hydrolyzed in deionized water and the resulting aqueous dispersion was mixed thoroughly with appropriate amounts of BaCO$_3$ ($\geq$ 99.0%, Fluka), La$_2$O$_3$ ($\geq$ 99.9%, Fluka), and MnCO$_3$ ($\geq$ 99.99%, Aldrich). After evaporation of water the solid mixture was milled for one hour with zirconia balls in a planetary mill (Pulverisette 7, Fritsch). The calcination was performed at 1100°C for 12 h, yielding barium titanate powder, co-doped by La and Mn, with the nominal composition Ba$_{0.9975}$La$_{0.0025}$Ti$_{1.010}$Mn$_{0.0005}$O$_3$. Powder compacts were obtained by uniaxial pressing (250 MPa) and sintered at 1350°C for two hours. The sintered pellets were cooled down to room temperature with a rate of 8 K/min.

3.3 Conductivity Experiments on PZT

The electrical conductivity of PZT samples used in this study was determined by impedance spectroscopy. Most measurements were carried out in air with an Alpha-A high-performance frequency analyzer and a ZG2 impedance interface (Novocontrol, Germany) in the frequency range from $10^6 - 10^{-1}$ Hz with an amplitude of 1V. This amplitude is still in the linear regime.

A complex non-linear least square fit of the spectra was performed with the software Zview2 (Scribner, USA). A 2611 System SourceMeter (Keithley, USA) was used to perform the high field direct current (DC) measurements. Voltages between 100 V and 200 V were applied and the current value was recorded. The electrode configurations used in this thesis are illustrated in Fig. 3.1.
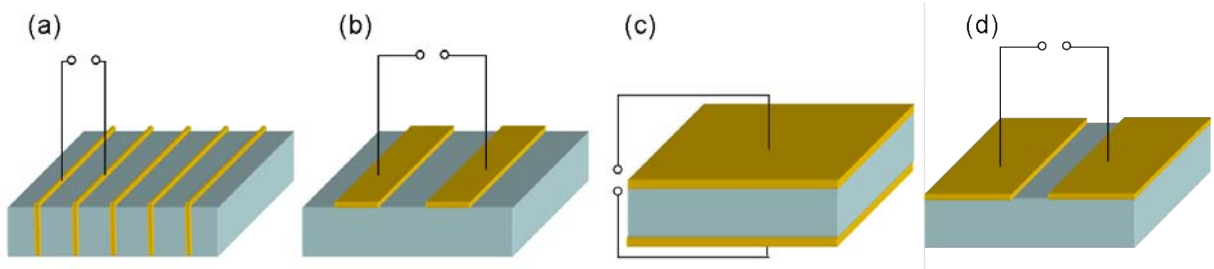
Fig. 3.1: (a) PZT with inner electrodes from actuator stacks (80 μm between each electrode) (b) PZT from top face of a stack, PZTNd samples or undoped PZT with surface electrodes (20 μm wide and 60 μm distance between each electrode). (c) PZT from top face of a stack or PZTNd samples with electrodes on top and bottom. (d) PZT from top face of a stack or PZTNd samples with two large surface electrodes (20 μm distance). Investigations have been carried out in a temperature range of 300°C to 650°C.

In Fig. 3.1 (a) the measurement principle on PZT taken from actuator stacks is given. Electrical contacts to two adjacent electrodes (distance 80 μm) were established by tungsten tips under a microscope (Mitutoyo, Japan) and heating was accomplished with a hot stage (Linkam, UK). Some measurements were conducted under reduced air pressure at about 10^{-2} mbar. In this case the heating stage was positioned in a closed apparatus with a vacuum pump connected to it. To investigate the near-surface properties and the dependence of conductivity and degradation on the electrode material, Ag- and Pt-electrodes were deposited on the surface of the top face of samples without inner electrodes. By a standard photo lithography route (ma-N 1420 negative photoresist and ma-D 533 S developer for photoresist, both: micro resist technology, Germany) using a photomask (Rose, Germany) the preparation of bar shaped surface electrodes as depicted in Fig. 3.1 (b) was possible. The resulting electrodes were about 200-300 nm thick and 20 μm wide with a distance of 60 μm between each electrode over the whole sample length. This way a good comparability between the inner electrode and the surface electrode measurements was obtained.

The simulation of electric field distribution between the surface electrodes was done using the finite element method (FEM) with Comsol Multiphysics (ver. 3.5, Sweden).

3.4 ^{18}O Tracer Diffusion Experiments

The $^{18}O_2$ was purchased from Cambridge Isotope Laboratories, Inc. (97%, chemical purity $\geq$ 99.8%). Exchange experiments were conducted in a furnace with adjustable oxygen partial pressure. Prior to the tracer experiments, the samples were annealed for 1/2 h (or 17 h) in an synthetic O_2 atmosphere at a partial pressure of 200 mbar or in air. The main reason for pre-annealing was not equilibration of PZT by chemical diffusion of oxygen as chemical oxygen diffusion can be assumed to be much faster than tracer diffusion [26]. Different pre-annealing times were rather used to see the effect of other possibly slow processes such as cation diffusion or healing of higher-dimensional defects. After pre-annealing the samples were kept for 4 h in an $^{18}O_2$ atmosphere of the same partial pressure and $^{18}O/^{16}O$ exchange took place. The gas volume was sufficiently large to avoid significant changes of the $^{18}O_2$ partial pressure during the tracer exchange. Even at high exchange rates the estimated ratio of the amount of ^{18}O in the surrounding atmosphere to the exchanged ^{16}O in the sample is well beyond 100:1. The temperatures during diffusion were in the range from 400°C to 850°C and the samples were quenched in ambient atmosphere by immediate positioning on a metal plate at room temperature within less than 20 s after the experiment.

To obtain the relative ^{18}O concentration or isotope fraction, measurements on a TOF.SIMS[5] machine (ION TOF GmbH, Münster, Germany) were performed using a Bi^+ primary ion beam (25 keV in burst alignment mode, 0.2 pA) and a Cs^+ sputter beam (2 keV 170 nA, 300x300 μm^2 raster). To overcome problems due to the dead time of the detector only the first 20 ns were integrated and Poisson corrected for the ^{18}O- and ^{16}O-signal [180] (see Sec. 2.5). Concentration profiles with a diffusion length of a few hundred nanometers were measured by depth profiling. Polished cross sections were prepared for measurements perpendicular to the tracer exchanged face, when the diffusion length was expected to be larger than 5 μm. To determine the length of a depth profile, it was normalized to the sputtering crater depth. This depth - as well as the crater and surface roughness - was measured by means of digital holographic microscopy (DHM) (Lyncée, Switzerland). The profiles of the relative ^{18}O concentration $c^*_{^{18}O}$ could then be calculated from the intensities of the oxygen isotopes [29] (see Eq. 2.77). For the following interpretation of the results the corrected relative concentration $c_{^{18}O}$ was used to account for the initial concentration of ^{18}O in the sample prior to the tracer exchange experiment:

$$c_{18_O} = \frac{c^*_{18_O} - c_b}{c_{gas} - c_b}$$

(3.1)

In Eq. 3.1 c_{gas} is the ^{18}O concentration of the annealing gas and c_b is the boundary concentration, which was always set to the value of the natural abundance (0.21%). Due to the higher concentration of $^{18}O_2$ in many oxygen enriched gases pre-annealing in these gases could already result in a small diffusion profile and might therefore lead to an incorrect analysis of grain boundary diffusion [181]. Such a profile is also found in our case (Fig. 3.2).
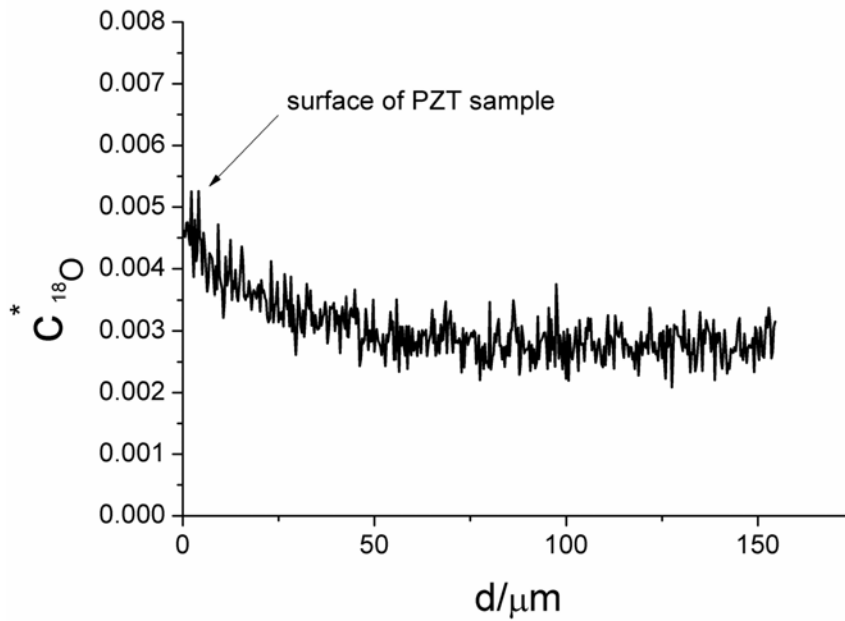
Fig. 3.2: Cross section profile of ^{18}O concentration prior to tracer exchange after pre-annealing a PZTSr/Nb sample for 24 h at 650°C (small diffusion profile due to higher concentration of ^{18}O in the pre-annealing gas than the natural abundance).

However, concentrations are either still very close to the natural abundance or much smaller than the concentrations measured and evaluated after the main diffusion experiment. The error due to neglecting the initial profile when setting $c_b = 0.21\%$ is thus of no importance in our case. Secondary electron (SE) images were also recorded with the TOF.SIMS[5] and this was performed after each ToF-SIMS measurement.

To evaluate the impact of an electric field on the tracer diffusion profile $La_{0.6}Sr_{0.4}CoO_{3-\delta}$ (LSC) electrodes were used. The material was prepared according to Ref. [182] by pulsed laser deposition

and thin films of LSC were deposited on top and bottom of PZT samples from the top face of PZTNd(Ag/Pd) stacks and PZTNd with 50 ns laser pulses supplied by an excimer laser (Lambda Physics, COMPexPro 201) working at 248 nm and a pulse frequency of 5 Hz. The fluence on the target surface was in the range of $1.5 J \cdot cm^2$. The deposition time was 30 min, which resulted in a LSC film thickness of about 200 nm. A constant flow of oxygen was applied during the deposition at a pressure of 0.4 mbar and a substrate temperature of 450°C. The experiments were conducted according to Fig. 3.1 (c). A field of about 130 V/mm was applied to PZT samples during an ^{18}O exchange experiment by a source-measure unit 2611 (Keithley instruments, Inc., Ohio, USA). Electrical contact was accomplished with Pt sheet electrodes inside the tracer exchange apparatus.

Also DC experiments with LSC and Pt surface electrodes and simultaneous ^{18}O tracer experiments were carried out. For these experiments the two deposited surface electrodes basically covered the whole surface (0.4 cm broad and 0.8 cm long for samples from the top face of the stacks) with a distance of about 20 μm between them (Fig. 3.1 (d)). These electrodes were again accomplished by the standard lithography route. This way surface electrode experiments could be conducted inside the tracer exchange apparatus, in which no contact by a microprobe was possible and electrical contact was again accomplished with Pt-sheet electrodes.

The simulations and calculations of diffusion profiles were done using the finite difference approach with MATLAB (ver. 7.5, Mathworks, Inc., Massachusetts, USA) or FEM calculations with Comsol Multiphysics (ver. 3.5, Sweden).

The BT samples were treated similar to the PZT. Prior to the tracer experiments at 600°C-900°C, the samples were annealed for 17 h in air at the same temperature. The samples were then kept for 4 h in $^{18}O_2$ atmosphere with a partial pressure of 200 mbar and $^{18}O/^{16}O$ exchange took place. Quenching was analogues to the experiments on PZT. To obtain the relative ^{18}O concentration or isotope fraction of the BT samples as well as TiO anion signals, measurements were performed with Bi^+ (25 keV in burst alignment mode, 0.2 pA) and Bi_3^{++} (25 keV in burst alignment mode, 0.08 pA) primary ion beams and a Cs^+ sputter beam (2 keV, 170 nA, 300x300 μm^2 raster). For cation signals an O_2^+ sputter beam (1 keV, 250 nA, 300x300 μm^2 raster) was used. Additional scanning electron microscopy (SEM)/energy dispersive x-ray spectroscopy (EDS) measurements were conducted on a Quanta 200 MKII from FEI (Oregon, USA) equipped with an EDAX (New Jersey, USA) EDX detector.

3.5 Analysis of the Chemical Etching Process

For chemical etching analysis a flow injection system coupled to an inductively coupled plasma optical emission spectrometry (ICP-OES) instrument (iCAP 6500 Thermo Scientific, USA) was employed. The PZT sample was put into a teflon cell, which was then filled with water. Together with the start of the ICP-OES measurement, a constant flow of 1.0 ml/min diluted hydrochloric acid (10%) was applied to the cell. The eluate was directly introduced into the detection system. More information on such measurements in the laboratory of Dr. Andreas Limbeck (TU Wien) are given in Ref. [183].

3.6 Conductive Mode Microscopy

A secondary electron microscope can be modified in a way that the current paths of injected electrons can be visualized. The principle this method is based on is depicted in Fig. 3.3.
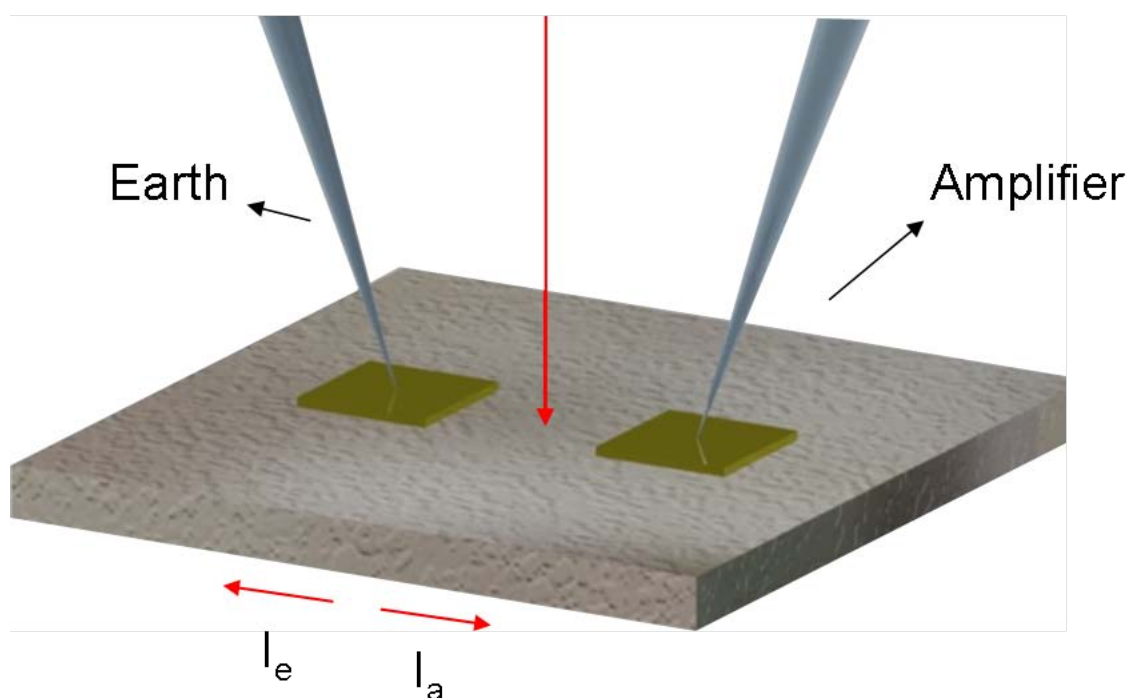
Fig. 3.3: Illustration of conductive mode microscopy in SEM with electron beam and current flow depicted as red arrows.

The red arrows in Fig. 3.3 illustrate the impinging electron beam and the resulting currents. These currents flow either to the surface electrode in contact with earth or the analyzer contact.

Therefore, the surface of the sample between the electrodes acts as a current divider [184]. The current for every electron beam can be detected, which results in a resistive contrast image. For a sample with homogeneous resistivity this leads to a brightness gradient between the electrodes [185]. Any changes in the local resistivity become visible by a pertubation of the image contrast. By applying a voltage bias during the measurement it is also possible to obtain information on high conducting pathways as the local conductivity can be enhanced by the injection of electrons as mobile charge carriers. This is referred to as β-conductivity contrast. Another effect, which can be observed especially at grain boundaries with blocking space charge layers, is the so called electron beam induced current (EBIC) [186, 187]. The electron-hole pairs induced by the electron beam are seperated by the field in the space charge region. This leads to higher currents from this region. Additionally, the charges are accelerated in opposite directions due to the opposite field on either side of the space charge layer at the boundary. Hence, a very dark and a very bright region can be seen in the image for a grain boundary lying between the two contacts (Fig. 3.4).
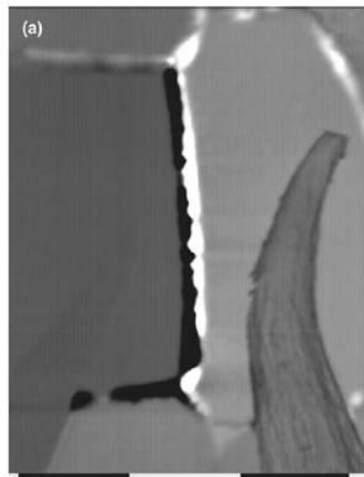
Fig. 3.4: EBIC-image of an varistor grain boundary adapted from [188].

Either circular Au-electrodes (20 μm in diameter and 20 μm distance) or square Pt-electrodes (100x100 μm^2, 50 μm or 100 μm distance) were deposited on PZTSr/Nb and PZTNd(Cu) samples. The experiments were conducted in the work group of Prof. Dr. Leach (University of Manchester, England). These samples were mounted on a Gatan heating stage (350°C and 400°C) in a JEOL SEM (10 kV acceleration voltage, 5 nA to 9 nA beam current) and imaged

using the secondary and conductive modes of operation. Electrical contact was accomplished by tungsten microprobes.

4

Results and Discussion: Conduction Mechanisms of PZT and Degradation by Unipolar Voltage Application

The focus of this thesis lies on the tracer diffusion experiments conducted on donor doped PZT. However, additional conductivity and high field degredation experiments on the donor doped samples were also carried out to obtain information on the electrical properties. Although these are preliminary results, a few interesting aspects are discussed in the next sections.

4.1 Impedance Spectroscopy on Donor Doped PZT with Inner Electrodes

Impedance spectra of PZT generally showed only one semi-circle (see also Sec. 2.3.3). This makes the evaluation and determination of the majority charge carrier and conduction mechanims in PZT quite difficult. However, a comparison of the electrical behavior of different types of PZT could still lead to a better understanding of the present mechanisms. In Fig. 4.1 (a) the impedance spectra of PZTNd(Ag/Pd) and PZTNd(Cu) with inner electrodes at 400°C are given. It can be seen that the impedance of the PZTNd(Cu) is lower than for PZTNd(Ag/Pd). There is also a small shift of the PZTNd(Cu) semi-circle on the real axis, which can be attributed to an electrical contact resistance between the tungsten tips and the Cu-electrodes due to oxidation of the Cu [189]. A parallel RC-circuit was used for the complex non-linear least square (CNLS) fit
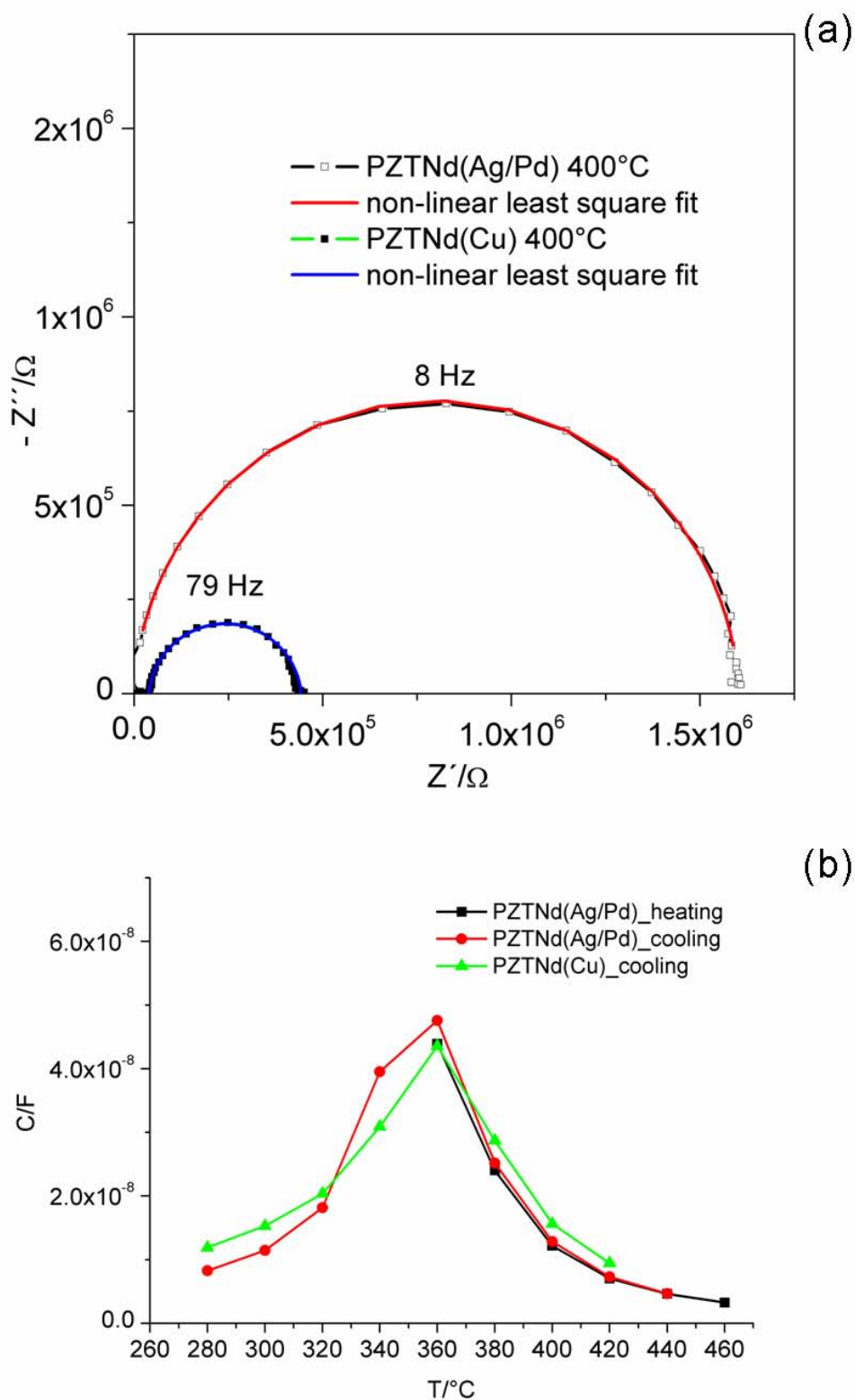
Fig. 4.1: (a) Impedance spectra of PZTNd(Ag/Pd) and PZTNd(Cu) with inner electrodes at 400°C and corresponding non-linear least square fits. (b) Plot of the capacitance evaluated from impedance spectroscopy against temperature for PZTNd(Ag/Pd) and PZTNd(Cu) (heating and cooling cycle).

but instead of a capacitor a CPE was employed. The corresponding capacitances were calculated according to [190]:

$$C = \left(R^{1-\alpha} \cdot A\right)^{1/\alpha} \tag{4.1}$$

where the parameters have the same meaning as in Eq. 2.72. The α values for both types of samples were in the range of 0.95. From impedance spectra of PZTNd(Ag/Pd) and PZTNd(Cu) the capacitances were evaluated and plotted against the corresponding temperature in Fig. 4.1 (b). The impedance measurements were conducted with successive heating (or cooling) steps. Between the increase of temperature and measurement the samples were annealed for 15 min at the given temperature so that the samples were thermally equilibrated. It can be seen in Fig. 4.1 (b) that the capacitances of the samples have their maximum value at 360°C. It is expected that because of the first order transition at the CURIE temperature (T_c) the permittivity ϵ and therefore also C exhibits a maximum [89]. Hence, the CURIE temperature for PZTNd(Ag/Pd) and PZTNd(Cu) are very similar. However, more data should be obtained to draw further conclusions. It has to be mentioned that the difference between the two samples lies not only in the choice of electrodes. Because the Cu is easily oxidized the PZTNd(Cu) is sintered in an atmosphere with a very low oxygen partial pressure.

From the temperature dependent impedance measurements an ARRHENIUS plot of the conductivity can be deduced. This is shown exemplarily for PZTNd(Ag/Pd) and PZTNd(Cu) samples in Fig. 4.2. The CURIE temperature T_c at about 360°C is highlighted. The slope of the plot below T_c is higher than above particularly for the PZTNd(Ag/Pd). It is usually expected that the activation enthalpy and pre-exponential factor change after a phase transition while the extend of the changes may strongly depend on the conduction mechanism [70]. The behavior shown in Fig. 4.2 is in accordance with previous result for PZT [24, 191] but the change in the slope at T_c is not very pronounced for both samples. However, it can be seen that the ARRHENIUS plots of PZTNd(Ag/Pd) and PZTNd(Cu) seem to intersect at the CURIE temperature. The difference of the two samples suggests that the choice of dopant is not the only parameter influencing the conduction mechanism. Not suprisingly, the preparation procedure might have a major impact on these properties as well. This can be even better illustrated by comparing the activation enthalpies and pre-exponential factors calculated from the different slopes in the ARRHENIUS plot for PZTNd(Ag/Pd) and PZTNd(Cu) (see Eq. 2.26) (Tab. 4.1). The activation enthalpy and pre-exponential factors of the PZTNd(Ag/Pd) are significantly lower than the ones
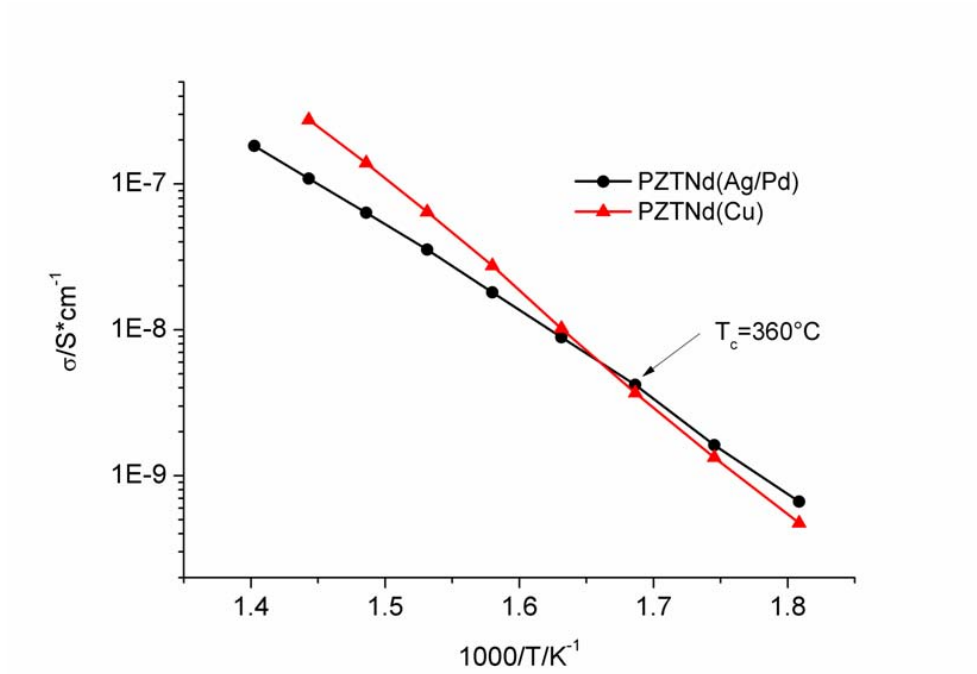
Fig. 4.2: ARRHENIUS plot for PZTNd(Ag/Pd) and PZTNd(Cu).

Tab. 4.1: Activation enthalpies ΔH^* and pre-exponential parameters σ_0 obtained from ARRHENIUS plots of PZTNd(Ag/Pd) and PZTNd(Cu).

	PZTNd(Ag/Pd) below T_c	PZTNd(Ag/Pd) above T_c	PZTNd(Cu) below T_c	PZTNd(Cu) above T_c
$\Delta H^*/eV$	1.25	1.10	1.49	1.45
$\sigma_0/\mathrm{S} \cdot \mathrm{cm}^{-1}$	150	7	1800	990
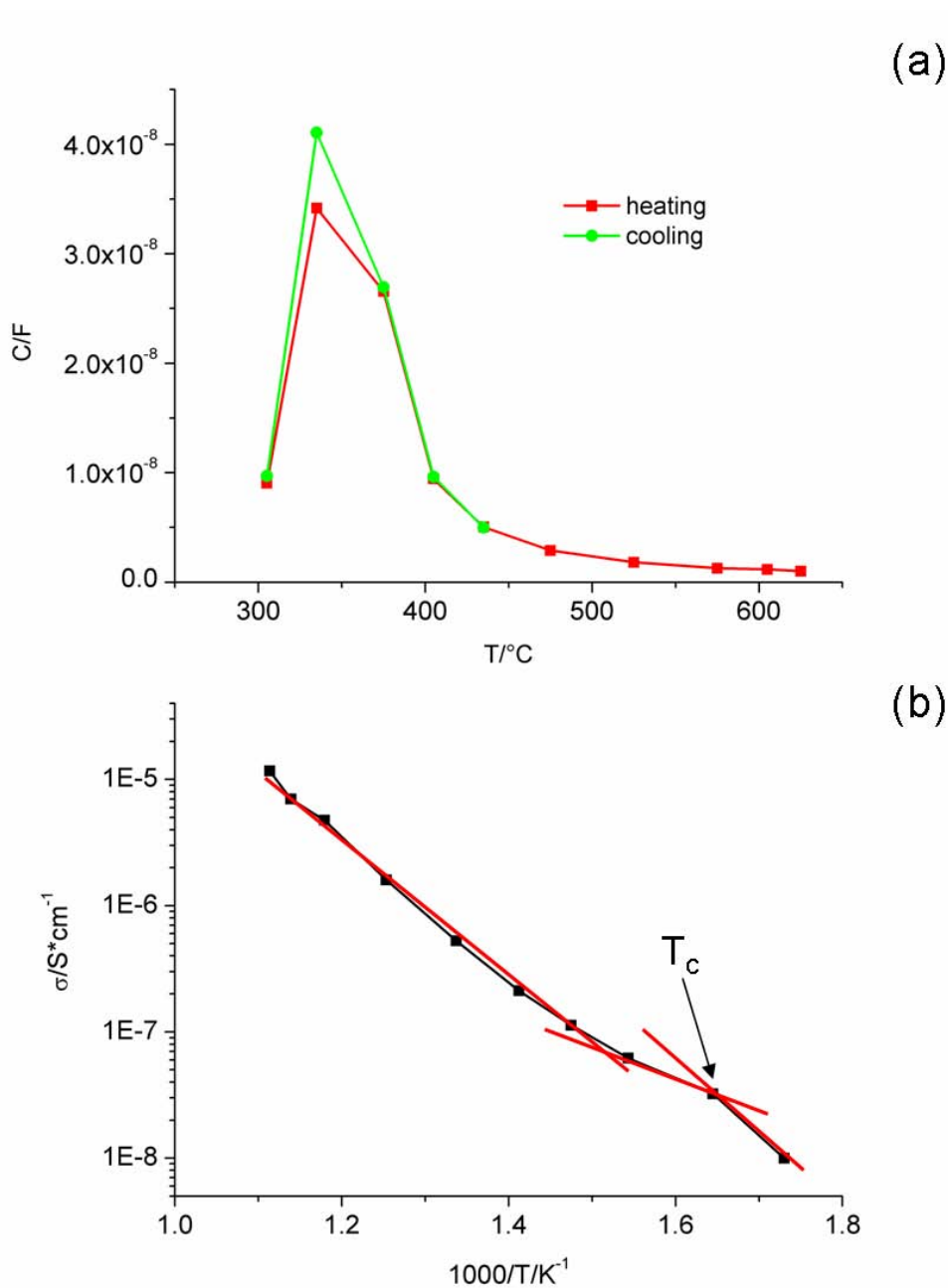
Fig. 4.3: (a) Plot of the capacitance evaluated from impedance spectroscopy against temperature for PZTSr/Nb(heating and cooling cycle). (b) Arrhenius plot for PZTSr/Nb.

for the PZTNd(Cu). It is often found that activation enthalpies around 1 eV result for oxygen vacancy related ionic bulk conductivity [1, 51] which has also been assumed to be the case for PZT [26, 42, 192]. Values for the PZTNd(Ag/Pd) would be well in that range. However, it could be expected that the oxygen vacancy concentration is higher for the PZTNd(Cu) due to sintering in a reducing atmosphere. The activation enthalpy for the conduction process is nevertheless higher than for PZTNd(Ag/Pd). Therefore, it is difficult to draw any conclusion from these results with respect to the conduction process.
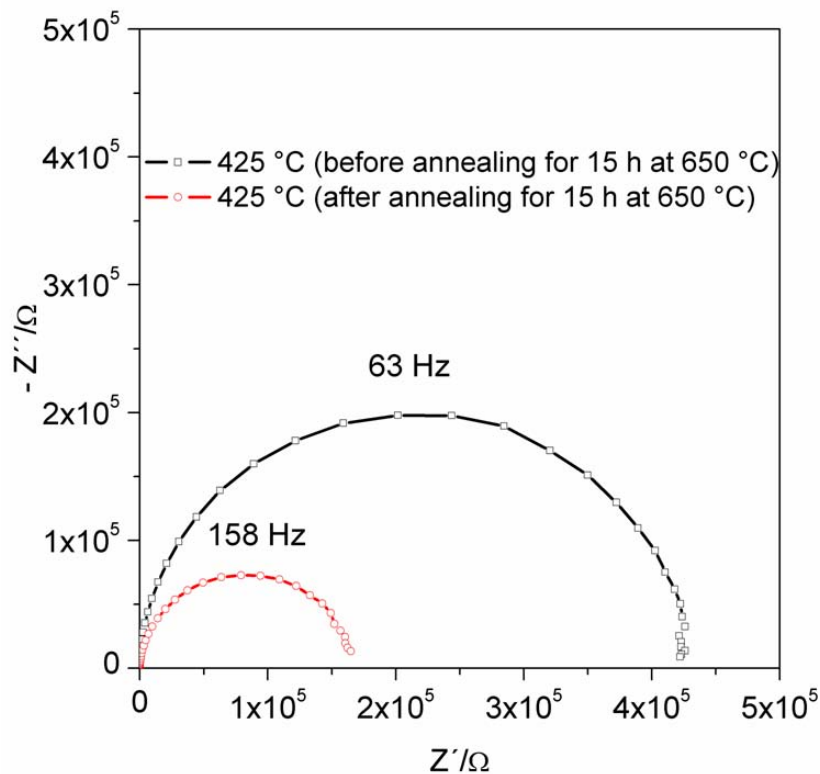
Fig. 4.4: Impedance spectra of PZTSr/Nb at 425°C before and after annealing for 15 h at 650°C in air.

It has also not been determined yet what kind of changes take place with respect to the conduction mechanism at the CURIE temperature. For undoped thin films at lower temperatures [192, 193] as well as for lanthanum doped polycrystalline PZT [25] in a higher temperature range than the one in this thesis a different behavior was presented. In these cases the slope at lower temperature was smaller than the one at higher temperature. A comparison to the results discussed in this thesis is difficult as doping and treatment of the samples are different. However, this illustrates nicely that many parameters influence charge transport in PZT. For the PZTSr/Nb the capacitance
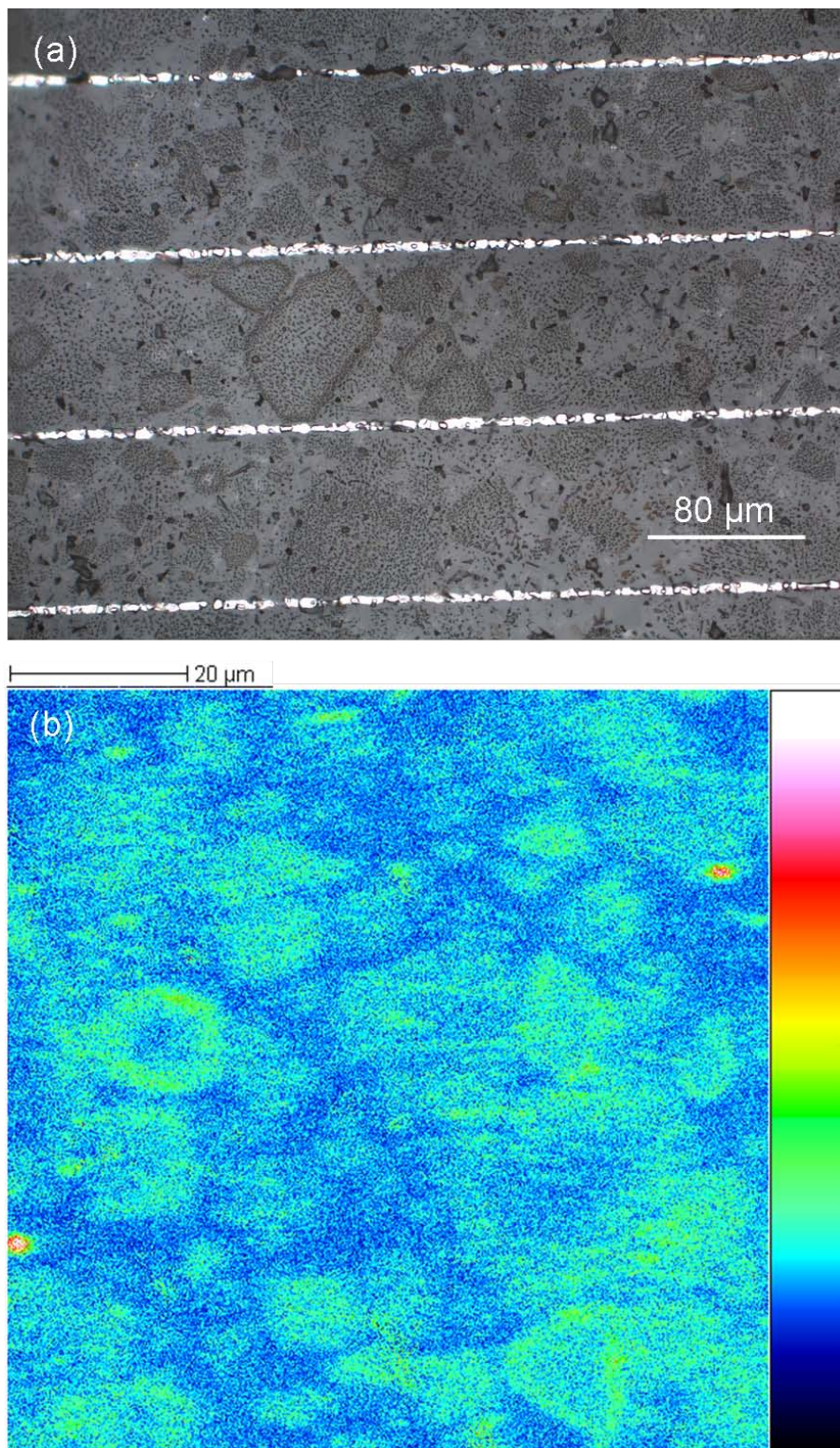
Fig. 4.5: (a) Microscope image of PZTSr/Nb annealed at 650°C for 15 h. (b) SIMS image (Bi$^+$, 0_2^+ sputter gun 500 eV) of the Pb signal normalized by the Zr+Ti signal of the same sample.

of the heating and the cooling procedure is given in Fig. 4.3 (a). The CURIE temperature of the PZTSr/Nb samples seems to be a bit lower than for the PZTNd samples. That is in good agreement with the results from previous research in which it has been found that $T_c = 350°C$. Other than that no difference can be observed in the capacitance plot. The ARRHENIUS plot of the PZTSr/Nb, however, is somewhat changed. Directly above T_c the slope almost seems to change twice. Nevertheless, the activation enthalpie $\Delta H^* = 1.1\ eV$ above the CURIE temperature is the same as for PZTNd(Ag/Pd). From Fig. 4.4 it becomes evident that there are permanent changes if the PZT is annealed at temperatures around 650°C. This also caused deviations form the fit line at the highest temperatures in Fig. 4.3.

To investigate whether the composition is altered by annealing at 650°C or not a SIMS measurement of the corresponding sample was carried out (O_2^+ sputter gun 500 eV). In Fig. 4.5 (a) dark areas are visible, which where not present before annealing for the PZTSr/Nb (not shown). The results of the SIMS measurements are given in in Fig. 4.5 (b). The Pb signal is divided by the sum of the Zr and Ti signal and is therefore normalized. Artefacts arising, for example, from surface roughness should be cancelled out by this procedure. The areas with high lead intensity are similar to the darker areas in Fig. 4.5 (a). This could mean that at 650°C PbO evaporation sets in. However, further extensive investigations on this aspect were not conducted. The measurements with a O_2^+ sputter gun are very difficult as higher charging effects occur compared to the Cs^+ gun (even with a gold layer sputtered on the surface prior to the measurement). Nevertheless, this issue will be addressed again when the ^{18}O tracer diffusion experiments are discussed (Sec. 5.3).

4.2 Direct Current (DC) Experiments on Donor Doped PZT with Inner Electrodes

For actuator piezoelectric materials it is crucial that they withstand long term unipolar field stress. Any process leading to resistance degradation is undesirable. In order to identify the processes, or at least obtain further information on them, DC experiments were conducted on the stack pieces with inner electrodes. Most of the PZTNd(Cu) results mentioned in this thesis were obtained and extensively discussed by HILLEBRAND [189]. In this thesis these results are compared to the ones obtained on PZTNd(Ag/Pd). The PZTNd(Ag/Pd) and the PZTNd(Cu) show a abrupt increase in current after application of 100 V (1.25 kV/mm) at 400°C for a certain
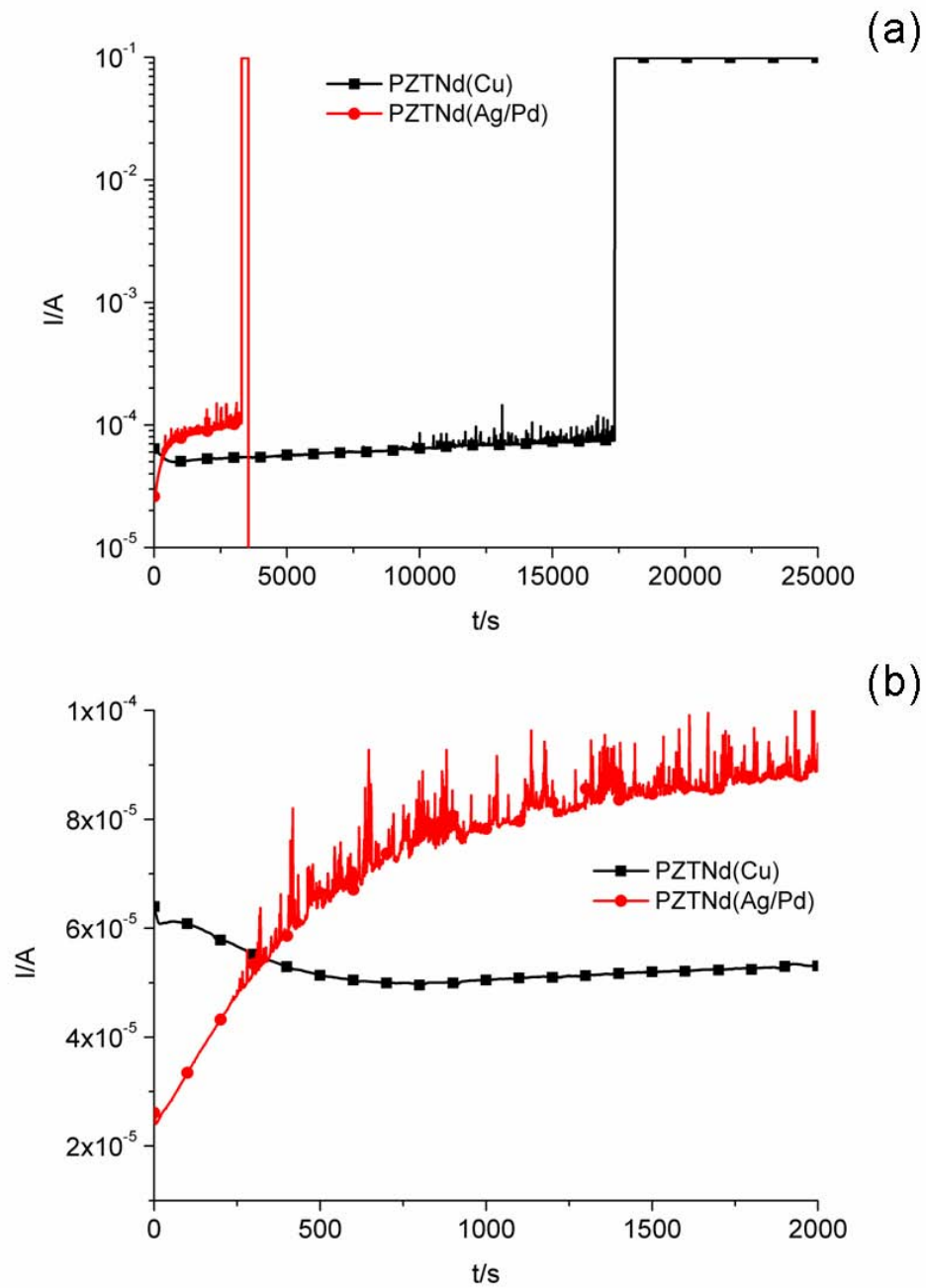
Fig. 4.6: Current plotted against time for DC measurements in air at 400°C and 100 V for PZTNd(Ag/Pd) and PZT(Cu) (a) whole measurents (one symbol every 1000 points) (b) first 2000 s (one symbol every 200 points).

time (Fig. 4.6 (a)). This is usually accompanied with a crater development in the contact region of the tungsten tips and partly with a following drop of the current due to the loss of contact between the tips and the inner electrodes. This just described situation will be referred to as current breakdown or simply breakdown in the course of this thesis. In Fig. 4.6 (a) it can be seen that the changes in the current with progressing measurement time for the PZTNd(Ag/Pd) and PZTNd(Cu) are very different. The breakdown occurs much earlier for the PZTNd(Ag/Pd)
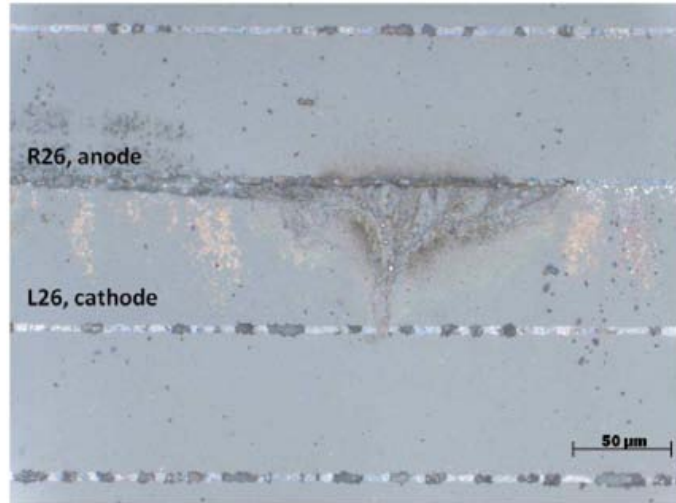
Fig. 4.7: Silver dendrites on PZTNd(Ag/Pd) surface after application of 100 V at 400°C (adapted from [189]).

than for the PZTNd(Cu). At the beginning of the measurements (Fig. 4.6 (b)) the current for the PZTNd(Ag/Pd) increases with time while the current decreases for the PZTNd(Cu). A more detailed investigation of this first decrease for PZTNd(Cu) is given in [194]. This is also important considering the results from the impedance measurements (Fig. 4.1 (a)). These are in accordance with the starting value for the resistance in the DC experiments. However, the conditions are inverted upon high field application in less than 500 s and the DC resistance becomes higher for the PZTNd(Cu) than for the PZTNd(Ag/Pd). Both current plots in Fig. 4.6 (a) show a constant increase of the current after 500 s. Additionally, the noise of the plots becomes larger with progress of time. For the PZTNd(Ag/Pd) this might be related to the development of silver dendrites on the surface between the electrodes, which leads to a high current when these come into contact with the opposite electrodes and subsequently degrade (Fig. 4.7). Interestingly, the dendrites start to occur solely at the anode, which does not make sense from a simple electrochemical point of view, where Ag^+ is transported from the anode through a medium and
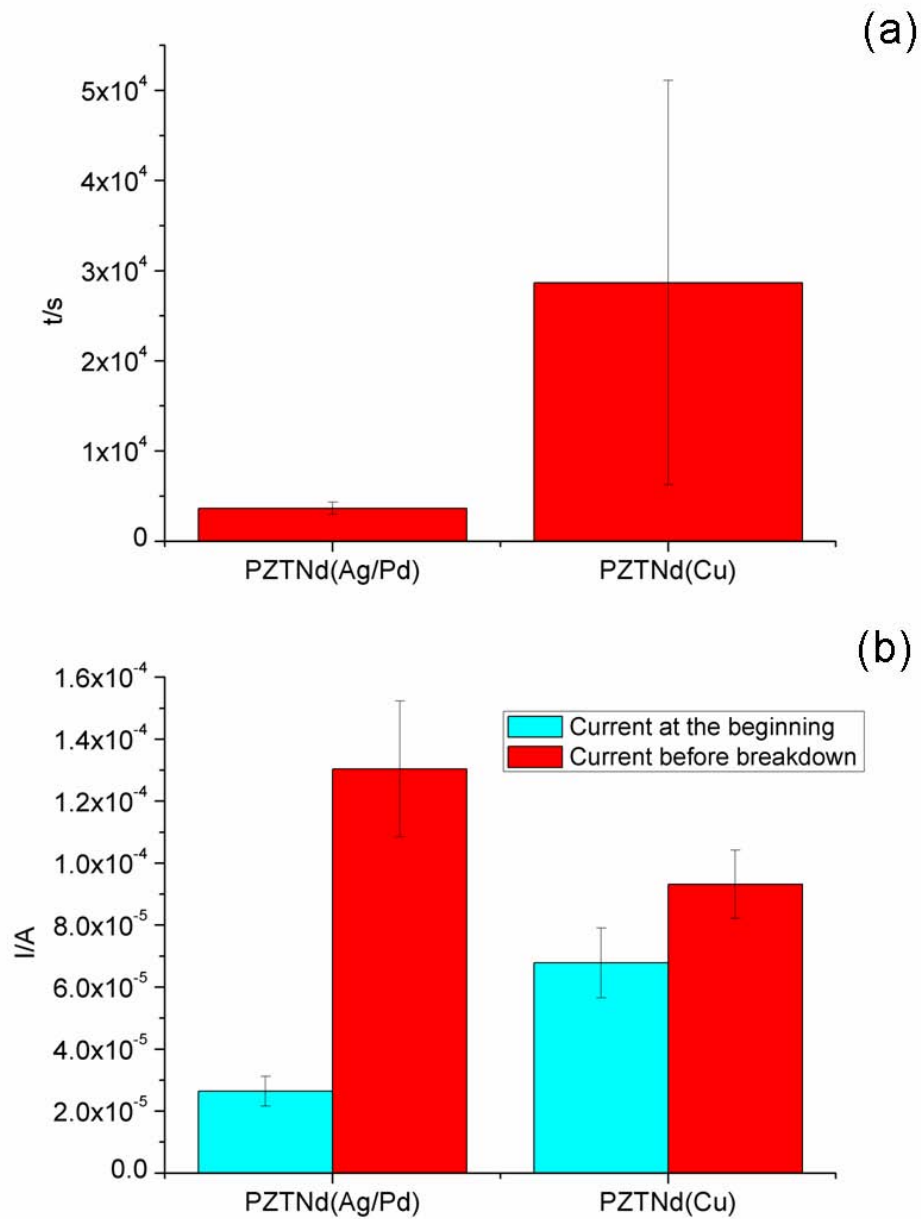
Fig. 4.8: (a) Comparison of times until breakdown for a DC measurement at 400°C and 100 V for PZTNd(Ag/Pd) and PZT(Cu) with inner electrodes, (b) Currents at the beginning of DC measurement (400°C; 100 V) and shortly before breakdown for PZTNd(Ag/Pd) and PZT(Cu). Additional bar represent the confidence interval.

is deposited at the cathode after charge transfer. However, dendrite development cannot be the only reason for the noise as these do not occur for the PZTNd(Cu) [189]. Nevertheless, the noise increases with time for the PZTNd(Cu). Various DC experiments have been conducted for the PZTNd(Ag/Pd) and PZTNd(Cu) to check for reproducibility. The results are compared in Fig. 4.8. The average values of the breakdown times are given in Fig. 4.8 (a) together with the confidence interval for the measurements. This interval is a parameter for the range, in which the values for the different measurements lie and is given by [195]:

$$\bar{x} \pm t_{n-1} \cdot {}^s\sigma/\sqrt{n} \tag{4.2}$$

where $\bar{x}$ denotes the average value, n the samples size, ${}^s\sigma$ the standard deviation and t_{n-1} a statistical factor depending on the $n-1$ degrees of freedom. This factor also depends on the confidence interval range (e.g. 95% or 99%) and the values have been adopted from Ref. [195]. A high standard deviation leads of course to a large confidence interval for the measurements.
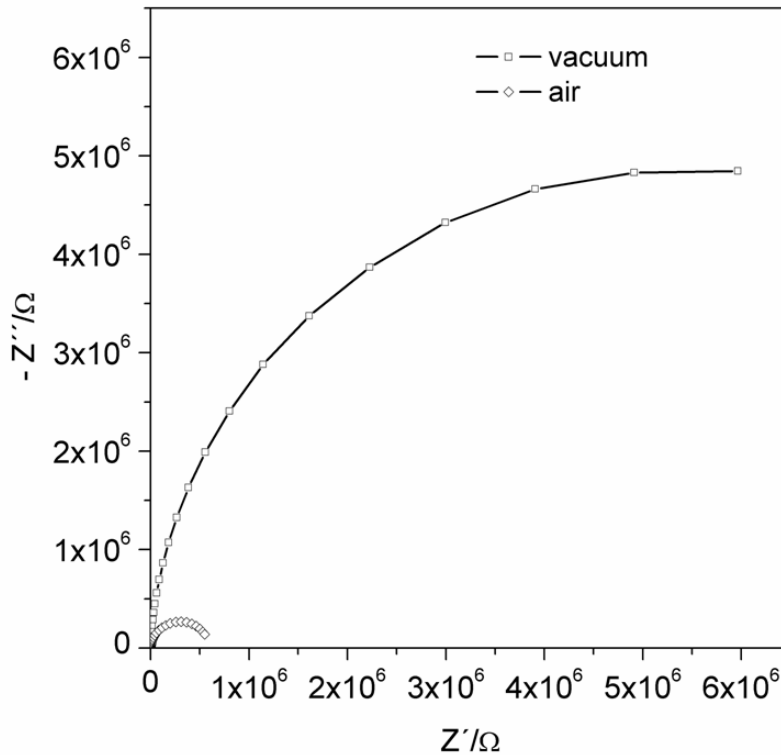
Fig. 4.9: Impedance spectra of PZTSr/Nb at 400°C in ambient atmosphere and in vacuum (10^{-2} mbar).

The breakdown times of PZTNd(Ag/Pd) in Fig. 4.8 (a) are very small compared to PZTNd(Cu),

which means that the PZTNd(Cu) material is more stable with respect to the application of a high field (1.25 kV/mm). However, the confidence interval of the PZTNd(Cu) values is very large, which means that although breakdown times are high in average they cannot be easily predicted. In Fig. 4.8 (b) the average currents at the beginning and shortly before breakdown are given. A rather large difference between these currents results for the PZTNd(Ag/Pd). This can be explained with the current plots in Fig. 4.6. The current increases during the whole measurement for the PZTNd(Ag/Pd). At first there is a sharp and afterwards a slow but constant increase of the current. For the PZTNd(Cu), however, the current decreases at first and then constantly increases. This leads to the rather minor differences between the current at the beginning and before the breakdown.

Not many measurements were carried out on the PZTSr/Nb but some interesting features could be observed, which suggest further investigations. In this case measurements in ambient atmosphere and at low air pressure (ca. 10^{-2} mbar) were conducted. During the measurement in air at 400°C (100 V) the current increases rapidly with high noise (Fig. 4.10 (a)). The breakdown does not lead to the development of a crater. The current reaches such a high value so that it always stays in the current limit of the instrument. In the impedance spectra in Fig. 4.9 it can already be seen that the spectra in air show a much lower resistance than the ones in vacuum. The corresponding DC measurements at 400°C (100 V) (Fig. 4.10 (a) and (b)) show a much higher stability for the PZTSr/Nb in vacuum. No breakdown can be seen even after 60000 s. Additionally, the noise is very high. However, in the case of vacuum measurements it is not entirely verified that the heating stage could reach the same temperature as in air. Therefore, no further conclusion can be drawn from this. Nevertheless, this motivates an in-depth analysis of the partial pressure dependence of the degradation behaviour of donor doped PZT.

4.3 Experiments on Donor Doped PZT with Ag-Surface Electrodes

The surface electrode configuration illustrated Fig. 3.1 (b) was used to be able to investigate the influence of different electrode materials and the electrical properties close to the surface of the samples. In this case the actuator material from the top face of the stacks and PZTNd samples were used with Ag- or Pt-electrodes deposited on them by the photolithography route. First, the focus lies on the results for the different PZT samples with Ag-surface electrodes. The differences
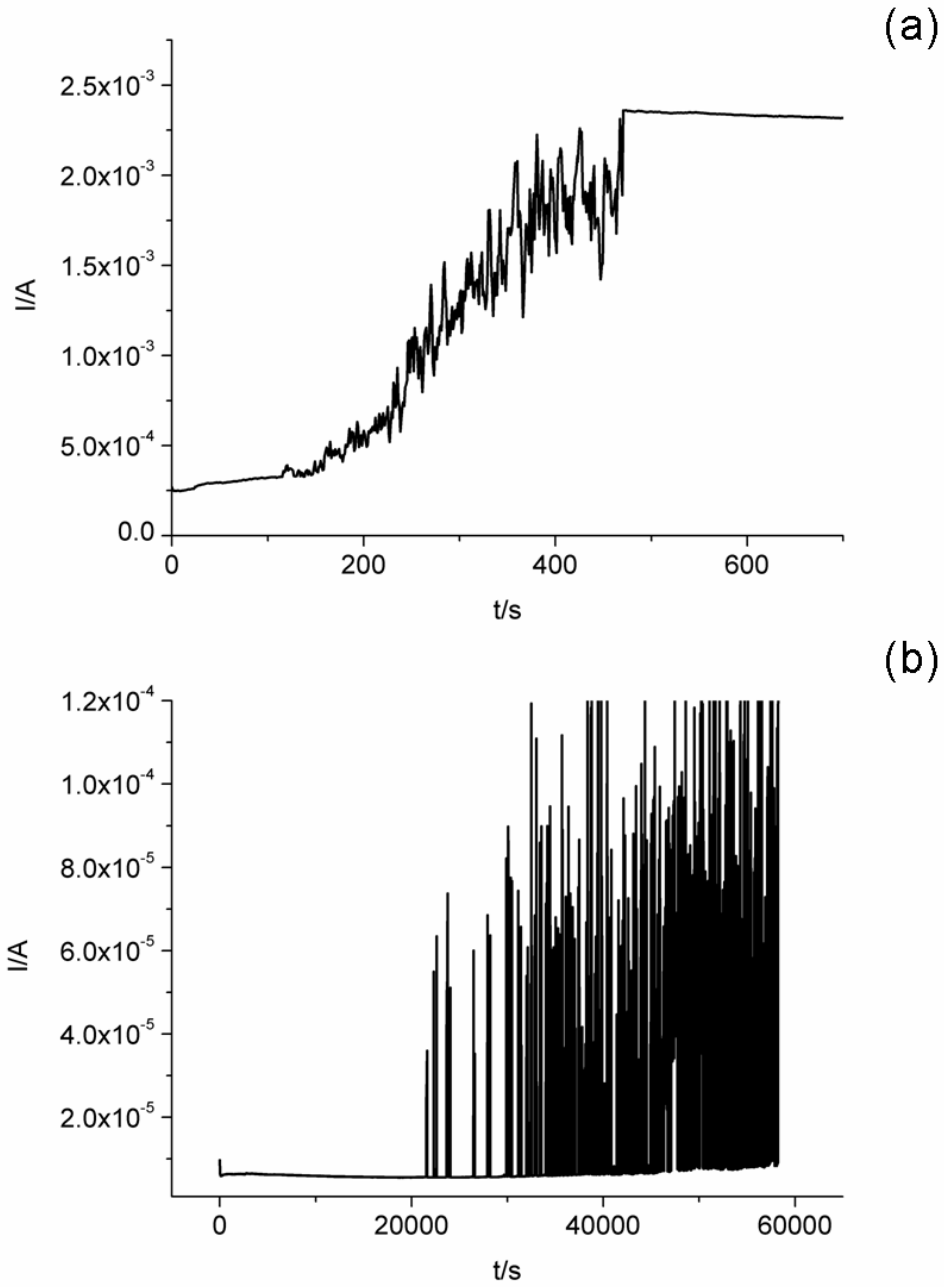
Fig. 4.10: DC measurements of PZT(Sr/Nb) at 400°C (100 V) (a) in ambient atmosphere and (b) in vacuum (10^{-2} mbar established after 10 min prior to measurement).
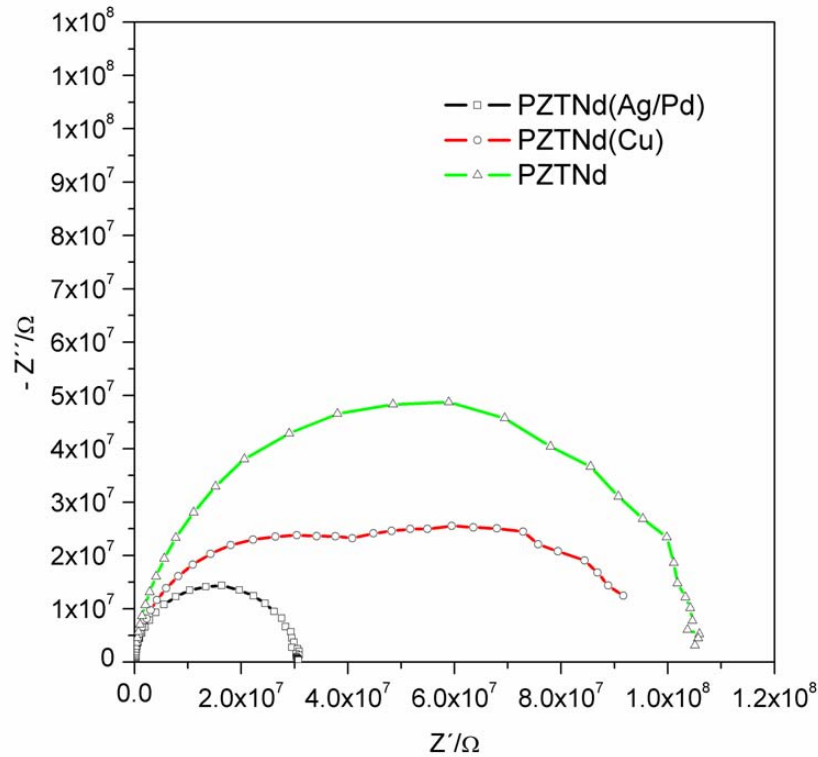
Fig. 4.11: Impedance spectra of PZTNd(Ag/Pd), PZTNd(Cu) and PZTNd with Ag-surface electrodes at 400°C in air.

in the electrical response observed in the measurements should therefore be solely dependent on the PZT material properties. The impedance spectra obtained at 400°C are given in Fig. 4.11. This time the PZTNd(Ag/Pd) sample has the lowest resistance of all samples while the PZTNd shows the highest. For both samples a single semi-circle developes in the Nyquist plot. The plot of the data from the PZTNd(Cu) sample, however, is rather distorted and it seems that there are two semi-circles overlapping each other. An equivalent circuit with two parallel R-CPE in series has been used to fit theses spectra with a CNLS fit. The resulting two ohmic resistances are of the same order of magnitude ($R1 = 7 \cdot 10^7 \Omega$, $R2 = 6 \cdot 10^7 \Omega$). The quality and length of the surface electrodes were mostly similar (on the circular PZTNd samples minor differences could occur) so that the measurements should be quantitatively comparable. Nevertheless, this could have been the source of some errors.

The corresponding DC measurements at 400°C (100 V) (Fig. 4.12) show that the resistance and the stability of the PZTNd(Ag/Pd) samples is by far the lowest. The breakdown occurs very early
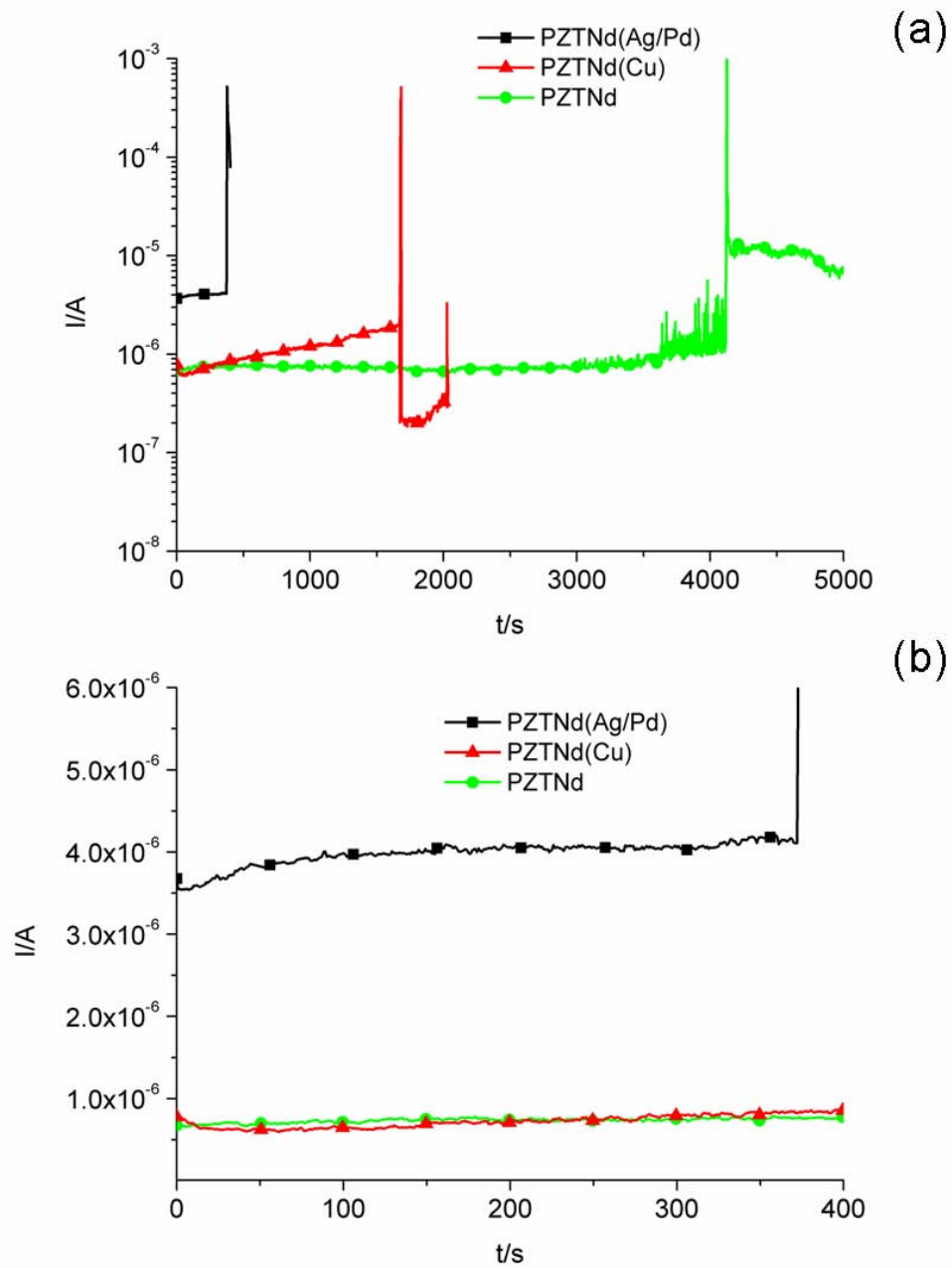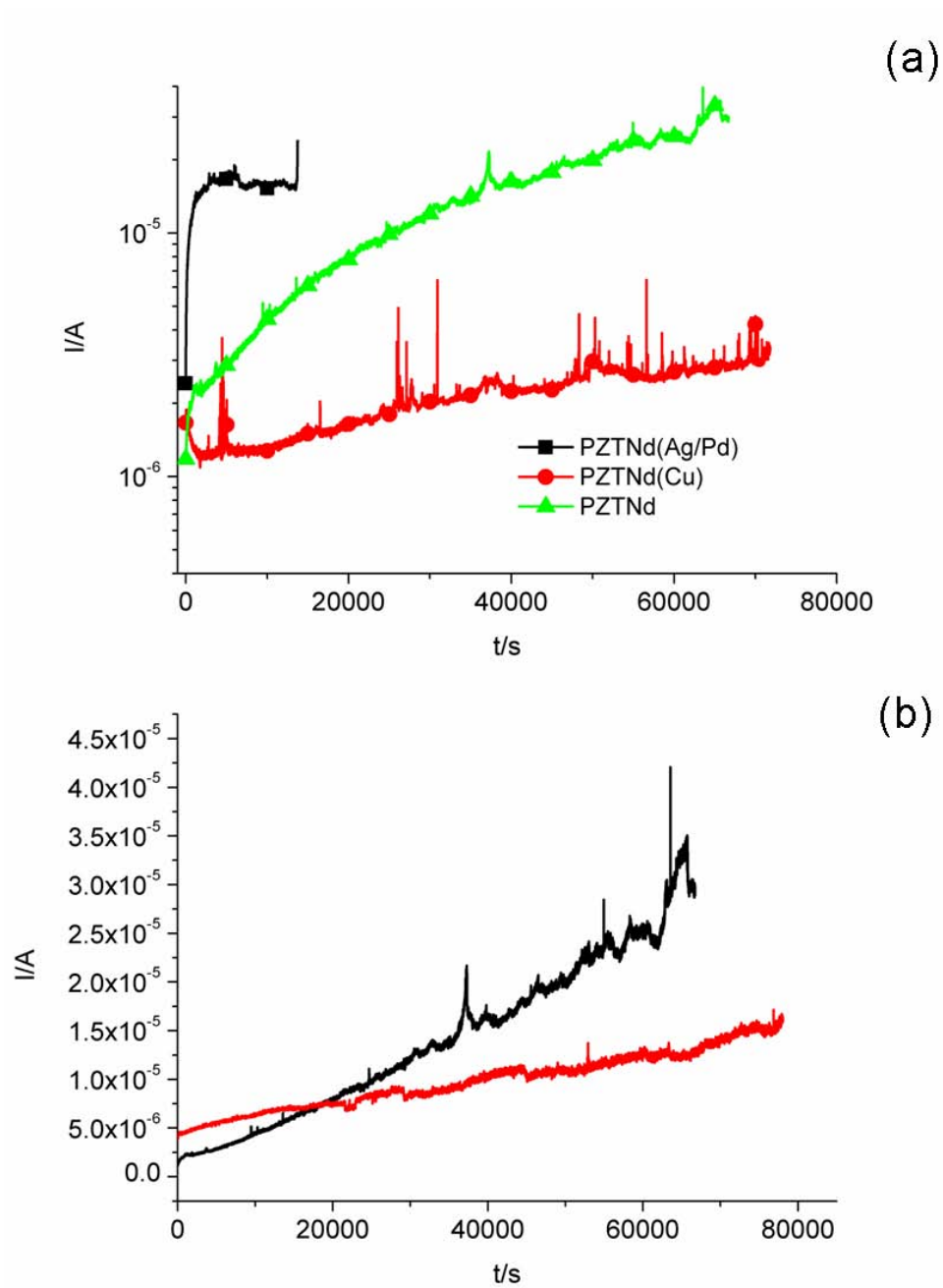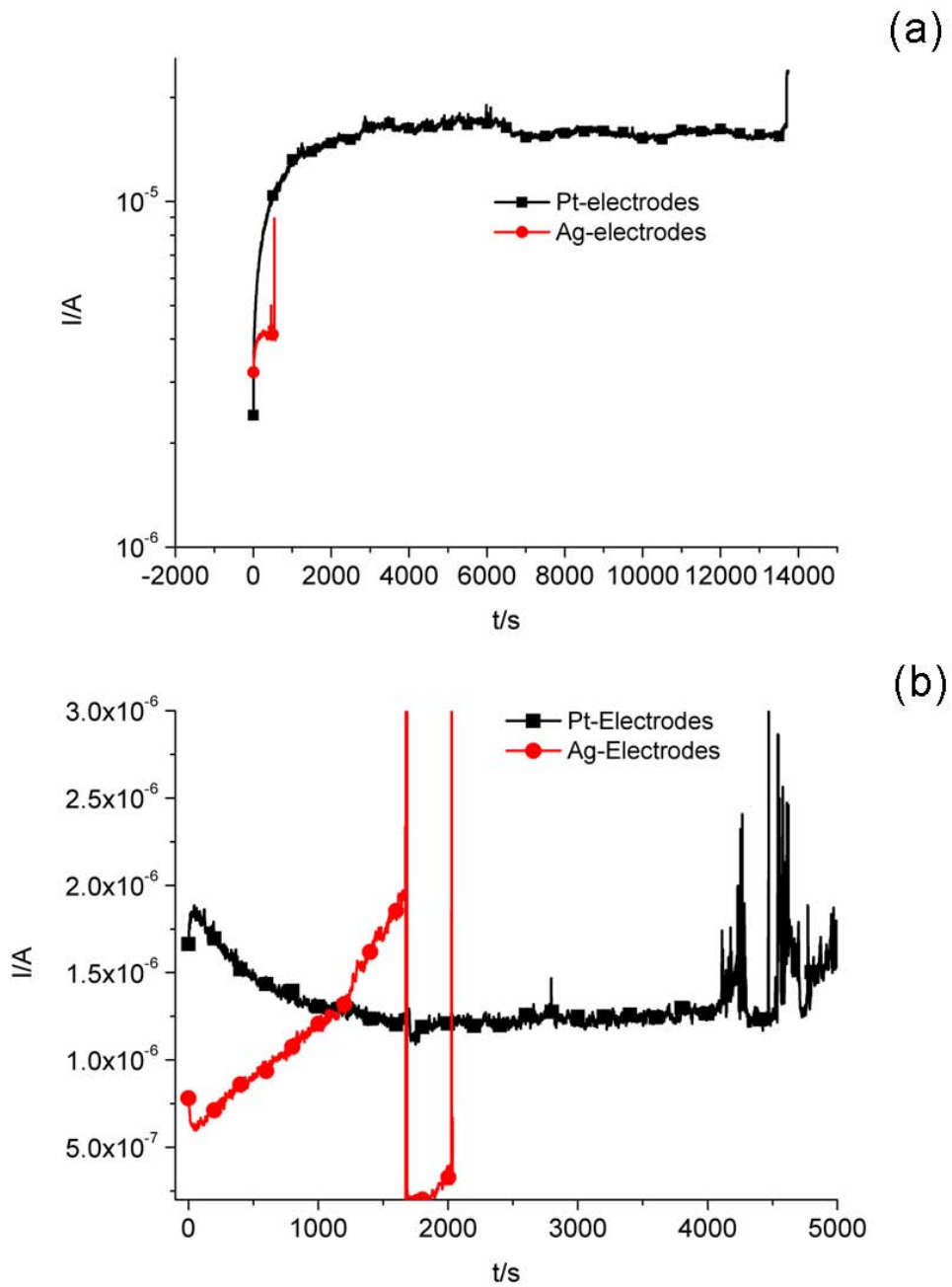
Fig. 4.12: DC measurements of PZTNd(Ag/Pd), PZT(Cu) and PZTNd with Ag-surface electrodes at 400°C (100 V) in air (one symbol every 200 points).

compared to the other samples. For the PZTNd(Cu) and the PZTNd(Ag/Pd) the current at the beginning progresses similarly to the behavior observed for the measurements of the samples with inner electrodes. The current increases in the PZTNd(Ag/Pd) measurement while it decreases in the mesurement of PZTNd(Cu). In the behavior of the PZTNd there is hardly any change in the current until the noise starts to become pronounced. The current increase until breakdown is the highest for the PZTNd(Cu) while also for the PZTNd(Ag/Pd) none is observable except the one at the beginning of the measurement. Noise does not necessarily occur in the measurements of PZTNd(Cu) and PZTNd(Ag/Pd) before breakdown but it sometimes does (not shown). With
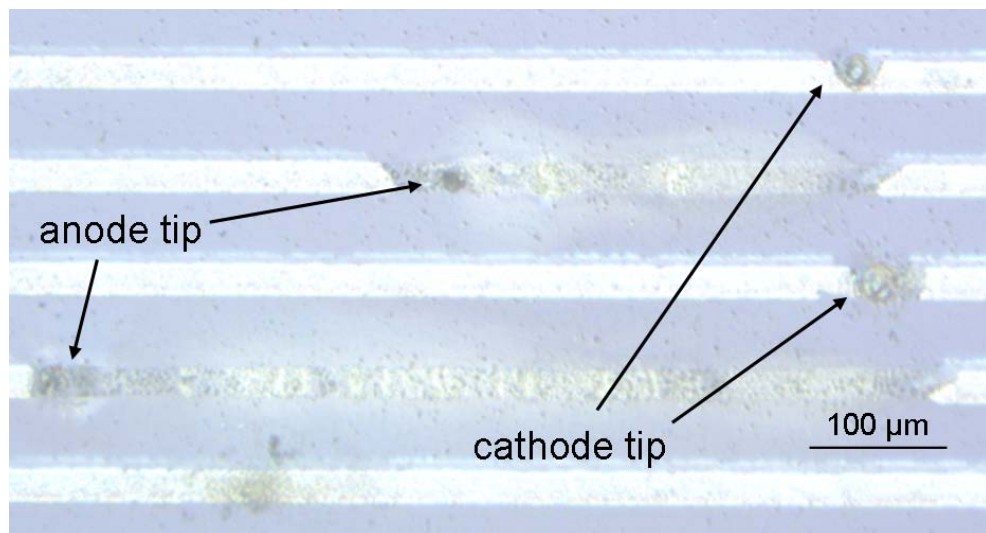
Fig. 4.13: PZTNd(Ag/Pd) with Ag-surface electrodes after breakdown from DC measurements at 300°C and 200 V.

the surface electrodes it is now possible to better determine what happens at the electrodes during a breakdown. In the microscope image of PZTNd(Ag/Pd) with Ag-surface electrodes after a breakdown at 300°C (Fig. 4.13) it can be seen that there is a black degraded spot in the region where the tungsten tip contacted the cathode. However, the anode region seems to be much more damaged. In the whole anode area between the two contacts the silver is basically removed from the surface. These results are in accordance with the measurements by HILLEBRAND on stack pieces with inner electrodes [189]. The area between the two tip contacts really seems to be degraded the most although it could be expected that the electrode is affected homogeneously by the applied voltage due to the high conductvity of the metal electrodes.

One possible origin of noise is again the Ag-dendrite development. In long term measurements of PZTNd(Ag/Pd) with Ag-surface electrodes at 150°C and 100 V dendrites occured at the
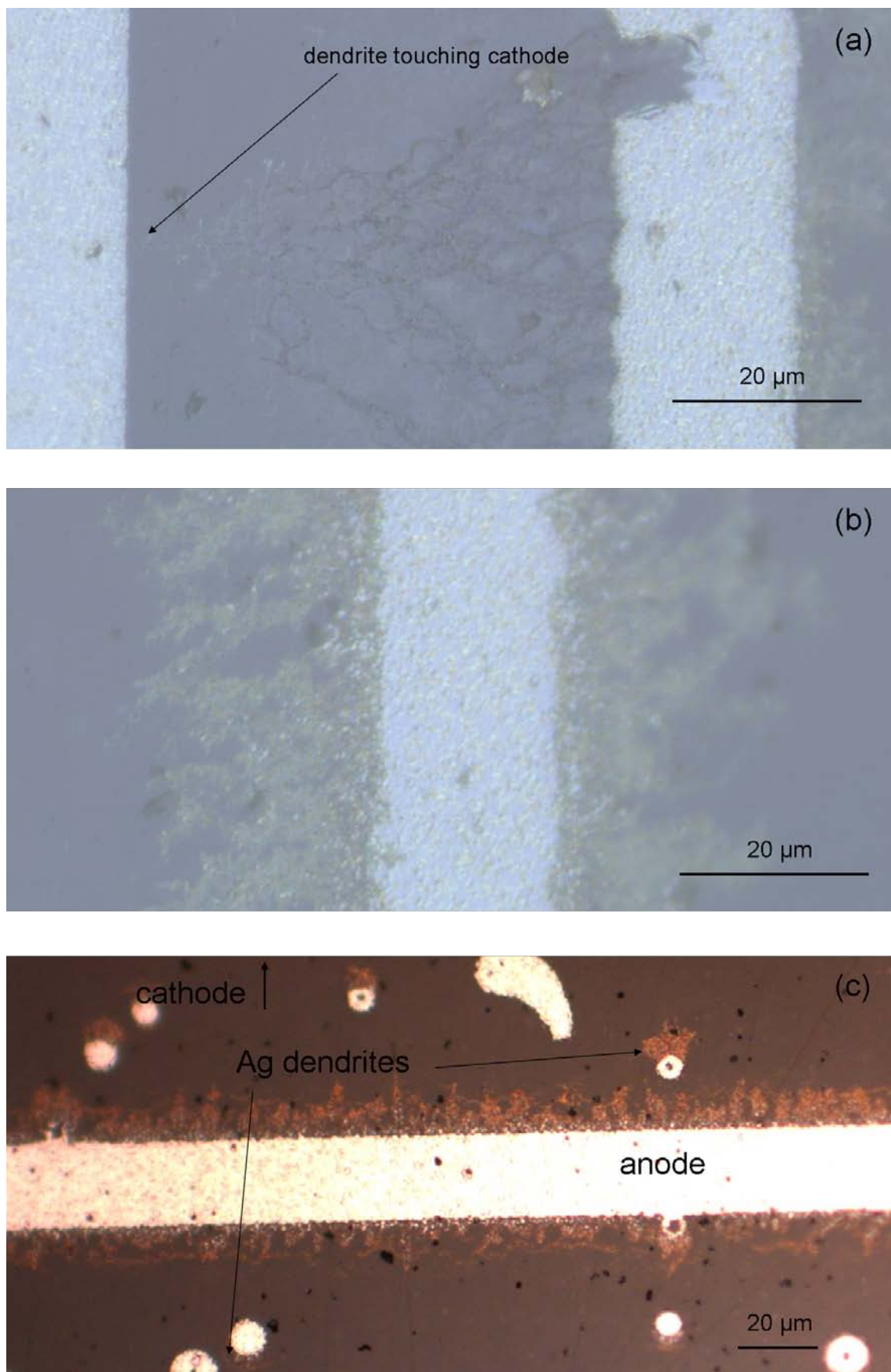
Fig. 4.14: PZTNd(Ag/Pd) with Ag-surface electrodes after breakdown from DC measurements at 150°C and 100 V. (a) Degraded dendrite with connection to cathode. (b) Undegraded metal dendrite. (c) Microscope image after DC experiment on PZTNd with Ag-surface electrodes (400°C, 100 V).

anode. Fig. 4.14 (a) shows dendrites which have already connected to the cathode. These dendrites have created a pathway for the current and degraded due to the high current flow, which subsequently lead to a blackening of the dendrite area. The undegraded metal dendrites are shown in Fig. 4.14 (b). It can also be seen in these images that dendrite development is not exclusively limited to the region between the anode and the cathode but progresses to either side of the anode. In Fig. 4.14 (c) Ag spots are shown, which have been deposited due to an incomplete lithography process. Dendrites also occured on the spots close to both sides of the anode. However, the degraded (blackened) dendrites are again exclusively limited to the area
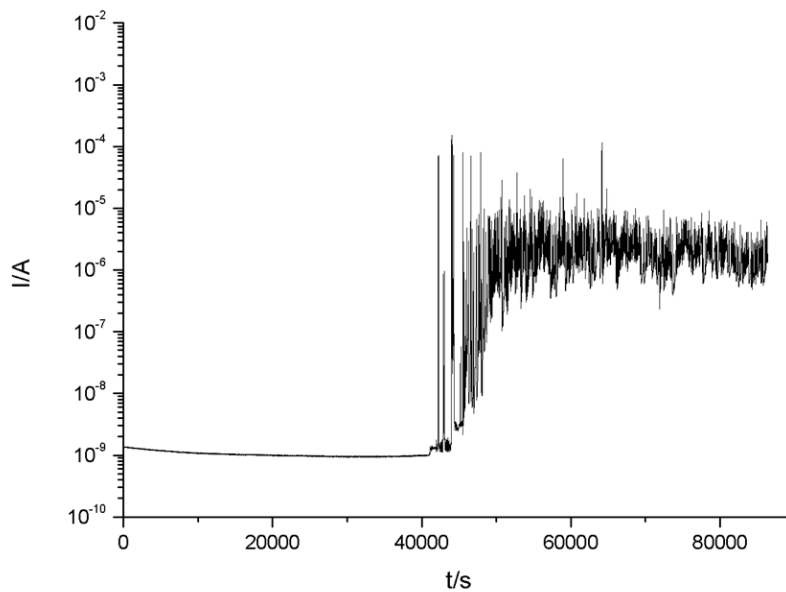
Fig. 4.15: DC measurement on PZTNd(Ag/Pd) with Ag-surface electrodes at 150°C and 100 V.

between the tip contacts which is further evidence for inhomogeneities caused by the tips. The corresponding current plot of this measurement (Fig. 4.15) shows that the current stays constant for almost 11 h. Afterwards, it increases by three orders of magnitude with strong noise development, which can be seen as a sort of breakdown without electrode removal. It is unclear in this case how much the dendrites contribute to the noise.

To prove that the dendrites consist of silver ToF-SIMS measurements have been conducted on PZTNd(Cu) with Ag-surface electrodes. In Fig. 4.16 it is clearly shown that the silver covers a large part of the surface, which can be attributed to the dendrites. Unfortunately, ToF-

SIMS could not be used to measure small silver concentrations because of the mass overlap with many Zr species. Therefore, investigations on Ag residing in the bulk or grain boundaries did not lead to satisfying results. Only the pure metal dendrites at the surface could be clearly distinguished from the PZT material. But, it cannot be ruled out that silver bulk migration plays an important role and investigations with microprobe or laser ablation inductive coupled plasma mass spectrometry might offer better opportunities to obtain information on the silver transport in PZT. Nevertheless, the circumstance that these dendrites also occur on PZTNd(Cu) and PZTNd (Fig. 4.14 (c) with Ag-surface electrodes, leads to the conclusion that an initial Ag-concentration in the PZT material is not needed for dendrite development. The reason for the anodic Ag dendrites is still unclear. However, a further discussion follows in Sec. 4.6 and Sec. 5.10.
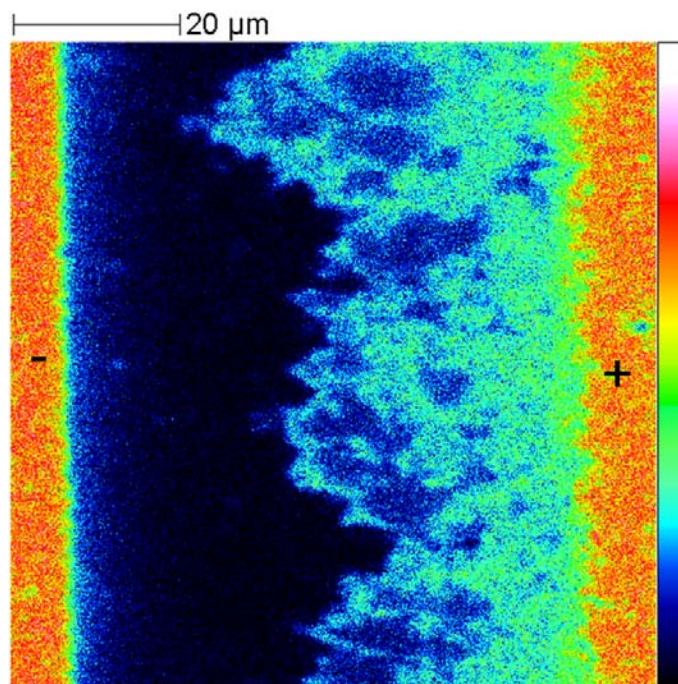
Fig. 4.16: SIMS image of ^{109}Ag, ^{92}ZrOH, ^{91}ZrH$_2$O in dendrite region between anode (+) and cathode (-) after DC experiment on PZTNd(Cu) (400°C, 100 V).

Considering the breakdown times with Ag-surface electrodes PZTNd(Ag/Pd) is again the most instable material (Fig. 4.17) and the breakdown times are by a factor of four lower than for the other samples. PZTNd and PZTNd(Cu) show similar average breakdown times but the confidence interval is very high meaning there is a large spread in the values, which have been taken into account. Nevertheless, it becomes clear that PZTNd and PZTNd(Cu), which have
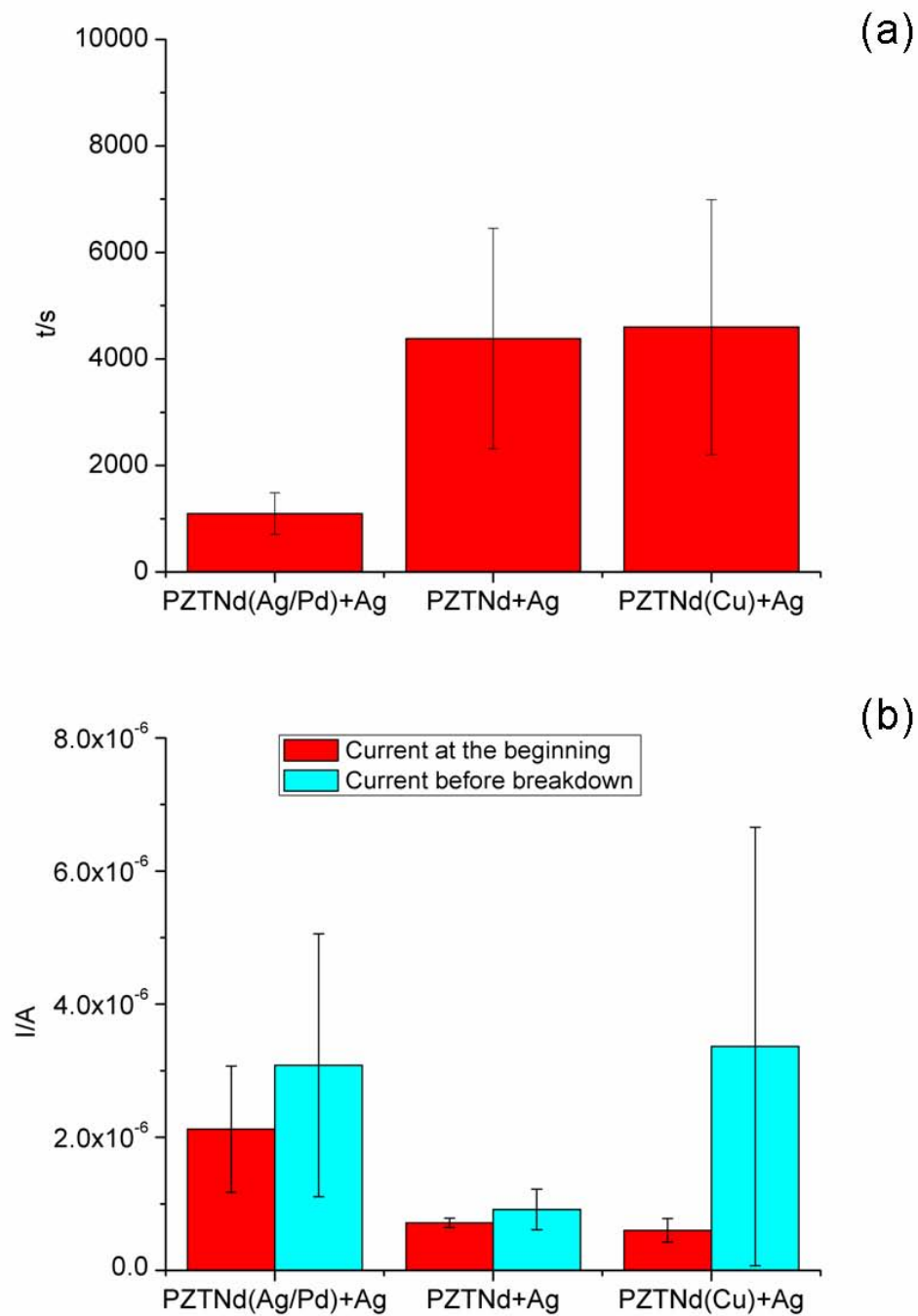
Fig. 4.17: (a) Comparison of times until breakdown for a DC measurement at 400°C and 100 V for PZTNd(Ag/Pd), PZT(Cu) and PZTNd with Ag-surface electrodes, (b) Currents at the beginning of DC measurement (400°C; 100 V) and shortly before breakdown for for PZTNd(Ag/Pd), PZT(Cu) and PZTNd with Ag-surface electrodes. Additional bar represent the confidence interval.

been pre-treated quite differently with respect to sintering, show rather similar behavior while the behavior of PZTNd(Ag/Pd) deviates significantly from the other samples. As a result, the different PZTNd(Ag/Pd) behavior might be attributed to Ag-doping during preparation. Basically, the main parameter which the PZTNd and the PZTNd(Ag/Pd) do not have in common is the fact that the PZTNd(Ag/Pd) has been sintered with the inner electrodes. As it has already been found that silver is transported easily through the material it could very well affect the material properties [112–114]. The surface electrode measurements also showed that the time until breakdown is much shorter than for the inner electrode measurements (Fig. 4.8 (a)). This could mean that the surface region is more prone to degradation than the bulk. In the comparison between the current at the beginning of the measurements and the current shortly before breakdown it can be seen that the PZTNd current is the lowest at all times and does not change significantly (Fig. 4.17 (b)). Although the PZTNd(Cu) is almost as stable with respect to breakdown times as the PZTNd the change in current during the measurement is even larger than for the PZTNd(Ag/Pd). The current values before breakdown for the PZTNd(Cu), however, are widely spread so that it might not be possible to judge the behavior just by the average value.

4.4 Experiments on Donor Doped PZT with Pt-Surface Electrodes

Similar experiments to the ones with Ag-surface electrodes were conducted with Pt-electrodes. In the NYQUIST plots (Fig. 4.18) for measurements at 400°C it can be seen that the shape of these plots are very similar to the ones obtained with Ag-surface electrodes (Fig. 4.11). However, the resistance is slightly higher for all measurements despite the same geometry. The corresponding DC experiments at 400°C (100 V) (Fig. 4.19) show a different behavior than measurements with Ag-electrodes (Fig. 4.12). First of all, the measurements show a much better stability towards breakdown than the Ag-surface electrode measurements. Experiments with the PZTNd(Ag/Pd) material still lead to the earliest breakdowns but the progression of the current plots for the other materials is quite different (Fig. 4.19 (a)). For the PZTNd there is a strong increase in current over time. It becomes even higher than the one of the PZTNd(Ag/Pd) before breakdown. In the end, the PZTNd with Pt-electrodes has the highest current and almost no breakdown could be observed for PZTNd and PZTNd(Cu). Nevertheless, there is still the typical decrease in the current at the beginning for the PZTNd(Cu) and a following slow increase. The high stability is
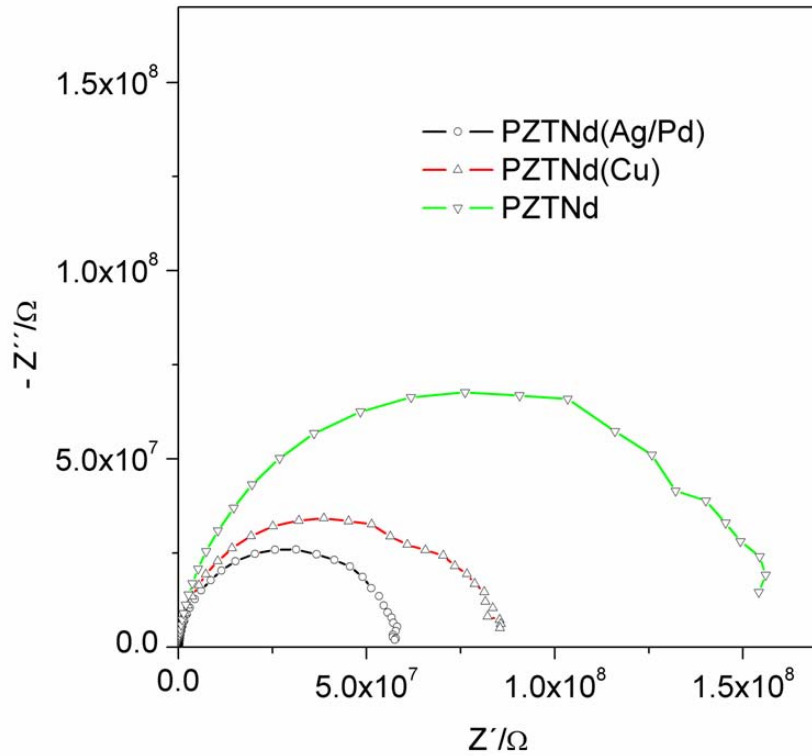
Fig. 4.18: Impedance spectra of PZTNd(Ag/Pd), PZT(Cu) and PZTNd with Pt-surface electrodes at 400°C in air.

the reason why less measurements have been conducted with Pt-surface electrodes. Therefore, no statistical evaluation is possible in this case. In Fig. 4.19 (b) it can be seen that the measurements are also not as well reproducible. That means further investigations are still needed to clearly establish and quantify the trends found here. However, an interesting observation can be discussed from the direct comparison of DC measurements at 400°C (100 V) between Pt- and Ag-surface electrodes on PZTNd(Cu) and PZTNd(Ag/Pd) (Fig. 4.20). It has already been mentioned that the Ag-electrodes lead to a lower stability but here it becomes obvious that the current plots of the measurements of PZTNd(Ag/Pd) with Pt- or Ag-surface electrodes show the same plot shape. It almost seems that the Pt-electrode measurement is a retarded version considering current changes and breakdown time (Fig. 4.20 (a)). The differences are much more pronounced for the PZTNd(Cu) (Fig. 4.20 (b)). For PZTNd(Cu) with Ag-surface electrodes there is a strong current increase with time while with Pt-electrodes the current decreases over the first 1000 s. Possibly, the process causing the initial current decrease for all PZTNd(Cu) measurements continues and is superimposed by a second process leading to an increase of the current. However,

Fig. 4.19: (a) DC measurements of PZTNd(Ag/Pd), PZT(Cu) and PZTNd with Pt-surface electrodes
at 400°C (100 V) in air(one symbol every 5000 points). (b) Comparison between two DC
measurements on PZTNd under identical conditions (400°C, 100 V).

Fig. 4.20: (a) DC measurements of PZTNd(Ag/Pd) with Ag- and Pt-surface electrodes at 400°C (100 V) in air (one symbol every 500 points). (b) DC measurements of PZTNd(Cu) with Ag- and Pt-surface electrodes at 400°C (100 V) in air (one symbol every 200 points).

compared to the results with surface electrodes on PZTNd(Ag/Pd) (Fig. 4.20 (a)) it could be expected that extended decrease for the PZTNd(Cu) with Pt-surface electrodes is a retarded version of the short decrease at the beginning of the Ag-electrode measurement. This would mean that the time over which the current changes is increased by two orders of magnitude.

4.5 Influence of Annealing at Higher Temperatures on Electrical Properties

So far it has been assumed that without field the impedance spectra of a sample stay constant during the time under investigation and that the differences in the DC experiments are solely dependent on the applied field. However, this is not the case and in the following it will be shown that an annealing effect also has to be considered in these studies. This further complicates evaluation of the conduction mechanisms. In Fig. 4.21 the NYQUIST plot of impedance spectra
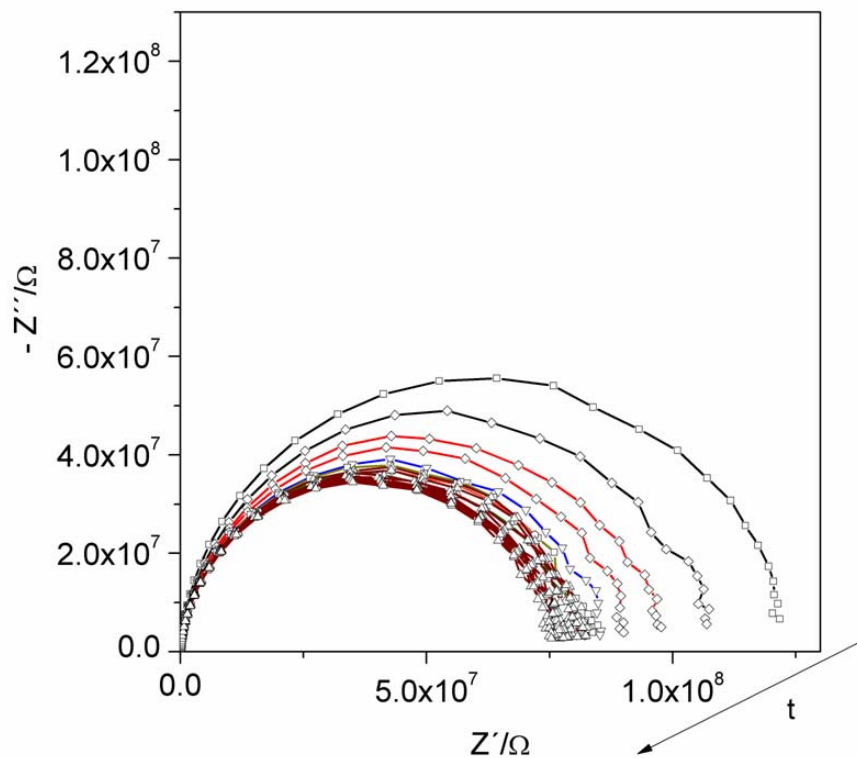
Fig. 4.21: Change in impedance spectra of PZTNd(Ag/Pd) with Ag-surface electrodes at 400°C in air (spectra taken every 15 min).

of PZTNd(Ag/Pd) with Ag-surface electrodes at 400°C are given. After annealing for 15 min an impedance measurement was conducted. The change in the plots with time is illustrated by the arrow in Fig. 4.21. Obviously, a decrease of the resistance is found for the PZTNd(Ag/Pd) with Ag-surface electrodes. It can also be seen that the starting impedance is larger than the value for the measurement shown in Fig. 4.11 which again exemplifies the difficulties to obtain comparable conditions. However, the results depicted in Fig. 4.21 are no coincidence and similar data could be obtain for PZTNd and PZTNd(Ag/Pd) with Pt-surface electrodes. The change in the DC resistance obtained from the impedance measurements is illustrated in Fig. 4.22. There
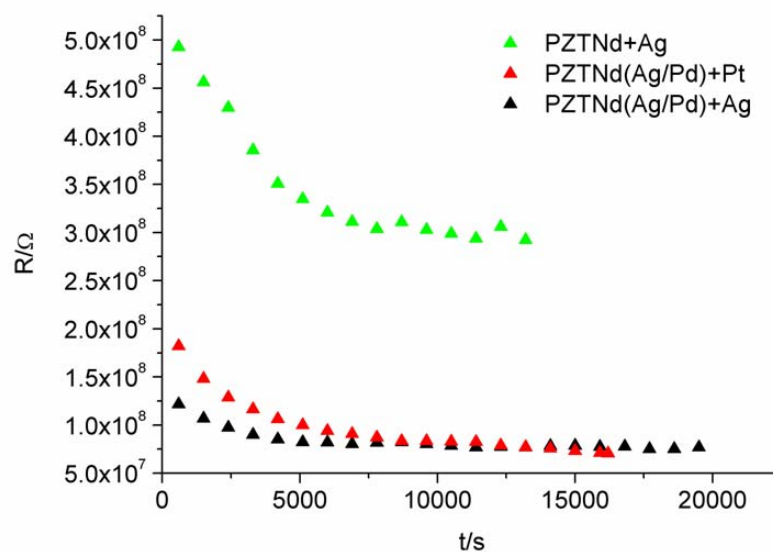
Fig. 4.22: Change in DC resistance values obtained by impedance spectrocopy on PZTNd(Ag/Pd) with Ag- and Pt- surface electrodes and on PZTNd with Ag-surface electrodes at 400°C in air.

is always a decrease in resistance until a constant value is obtained for the measurements on PZTNd and PZTNd(Ag/Pd). For the PZTNd with Ag-surface electrodes the strongest decrease could be observed but the resistance is still the highest in all cases. Interestingly, despite different absolute values the time scale of the resistance decrease is very similar for these configurations. For the PZTNd(Cu) a completely different situation is found. From the NYQUIST plot given in Fig. 4.23 it becomes obvious that the resistance of the PZTNd(Cu) with Ag-surface electrodes increases with time (illustrated by the arrow). The same condition can also be observed with Pt-electrodes (not shown). This is evidence that an annealing procedure has a significant impact on the electrical properties.

However, it can still not be resolved how the degradation behavior is affected. Moreover, it is likely that there is a strong relationship between the pre-treatment of the PZT material and the influence of further annealing in air. In comparison with the DC experiments (Fig. 4.19 and Fig. 4.12) there might be a correlation between the changes occuring due to annealing and the current change at the beginning of a DC measurement. However, the time frame in which these changes happen are different, which could be due to the additional influence of the applied field. What is contradictory to this hypothesis is the resistance change for the PZTNd with Ag-surface electrodes upon annealing. There is a large decrease in the resistance, which, however, can
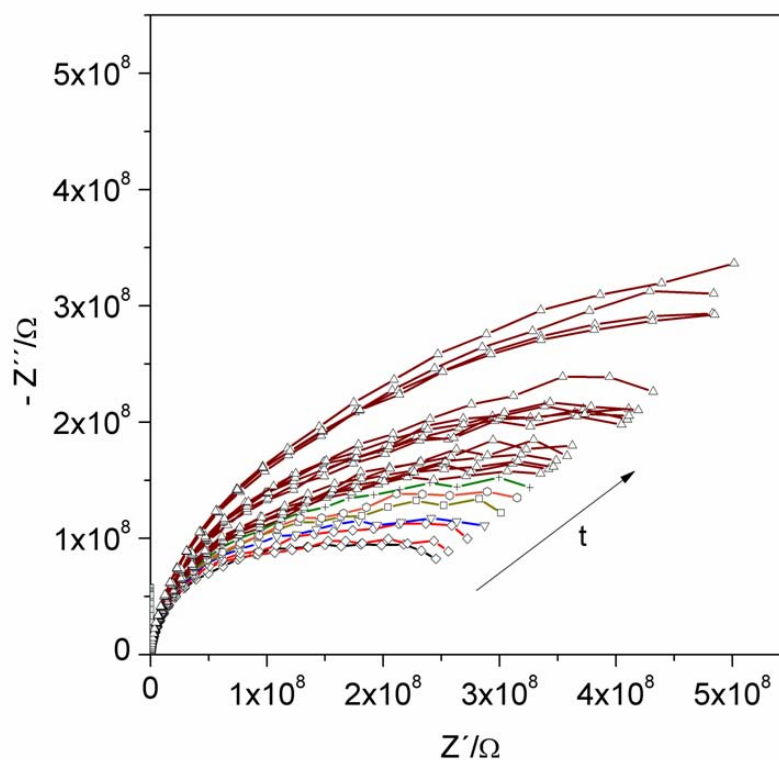
Fig. 4.23: Change in Impedance spectra of PZTNd(Cu) with Ag-surface electrodes at 400°C in air.

only be seen in the DC experiment with Pt-electrodes. The DC experiments on PZTNd with Ag-surface electrodes show the steadiest current at the beginning for all samples (Fig. 4.12). Nevertheless, a field induced effect could be responsible for cancelling out the current decrease due to annealing. In conclusion, it is likely that the current progession at the beginning of a measurement is influenced by field and annealing at higher temperatures. This has also been

nicely illustrated by HILLEBRAND for the PZTNd(Cu) samples with inner electrodes [189]. He was able to show that the starting current behavior in DC-experiments is significantly altered by annealing at higher temperatures. The current decrease was diminished after successive annealing steps. Together with a short application of field the behavior could even be inverted so that it resembled the behavior of PZTNd(Ag/Pd).

A further feature that has to be evaluated is the second semi-circle arising only for the PZTNd(Cu) with Ag- and Pt-surface electrodes. The spectra could be fitted with a CNLS fit taking two processes into account and is modelled by two parallel R-CPE in series. The changes in resistance and capacitance with time is plotted for Ag-electrodes in Fig. 4.24 and for the Pt-electrodes in Fig. 4.25. One of the processes is rather independent of time in resistance and capacitance for both samples while the other changes significantly. For the PZTNd(Cu) with Pt-electrodes the values are scattered for the changing process and no clear trend could be observed most probably due to the limited frequency range in the impedance spectra. The results for the PZTNd(Cu) with Ag-electrodes, however, show that there is a large increase in resistance and decrease in the capacitance of the low frequency process. No constant resistance value could be obtained for the measurements with Ag-electrodes, which means that even after a day the sample resistance of one process changes due to annealing. It is unfortunate that these results cannot be compared to the data obtained from PZTNd and PZTNd(Ag/Pd) as only one semi-circle is visible in the NYQUIST plot. Nevertheless, it would not be suprising that also in this case more than one conduction process contributes to the impedance spectra and therefore one of these processes is affected by the annealing procedure.

The mechanisms behind the different behavior are still unclear. However, one of the processes, which has been evaluated for the PZTNd(Cu) experiments with surface electrodes might be attributed to a gas/electrode reaction or electrode related process. This would fit to the fact that only one semi-circle is obtained in the NYQUIST plot with Cu-inner electrodes. With Ag- and Pt-surface electrodes this condition changes for the exact same material. However, if it is expected that there is a change in material properties originating from the surface a second semi-circle could also arise from altered and unaltered near-surface PZT layers with different properties. In the measurements with inner electrodes this effect might not be very pronounced. The findings may also be discussed in the light of other research in which also two semi-circles have been observed. In the study by BOUKAMP et al. and DONNELLY et al. the semi-circles
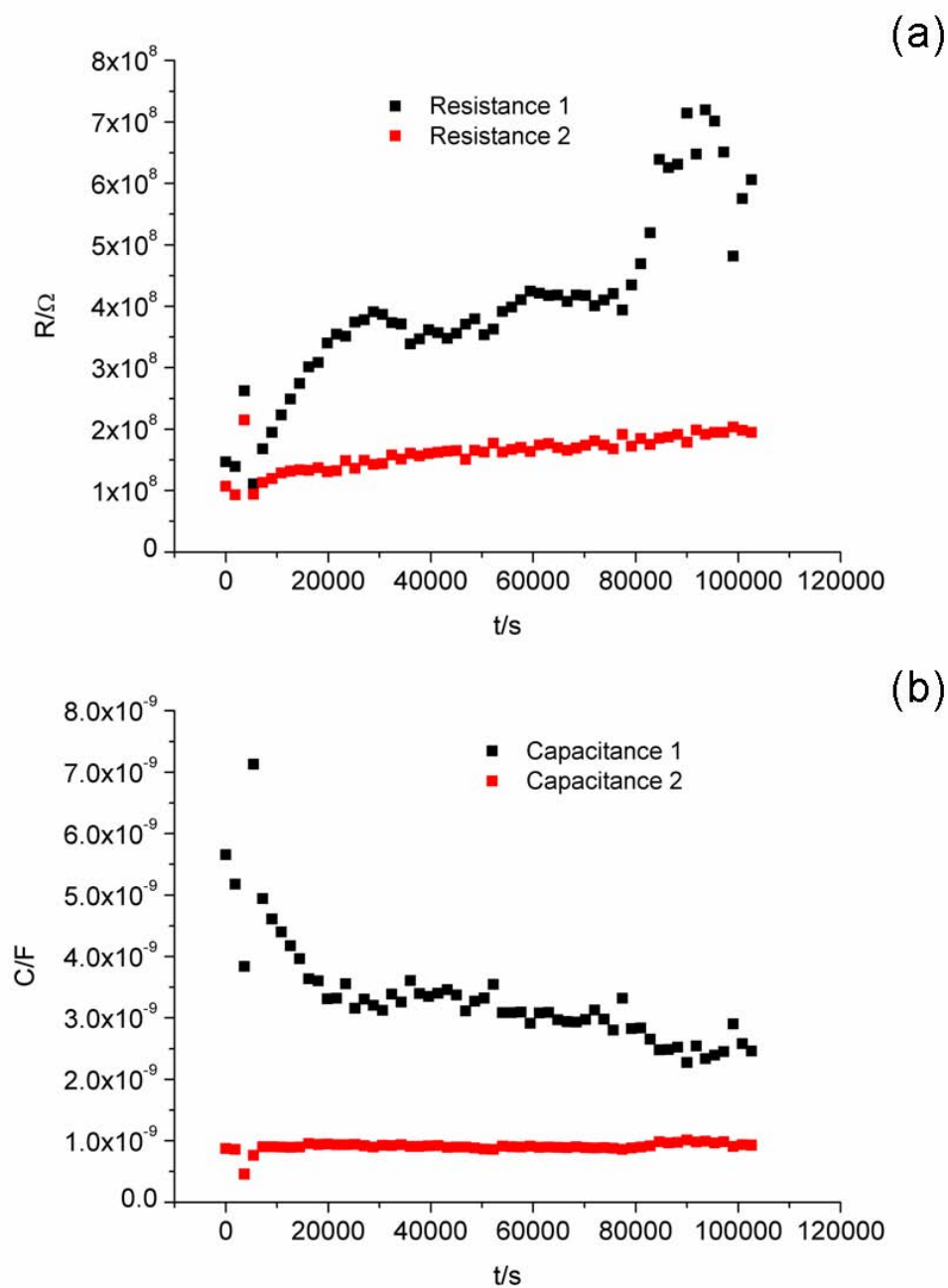
Fig. 4.24: Evaluation of DC resistances from CNLS fit (two proccess modelled by two parallel R-CPE) of Impedance spectra of PZTNd(Cu) with Ag-surface electrodes at 400°C in air.
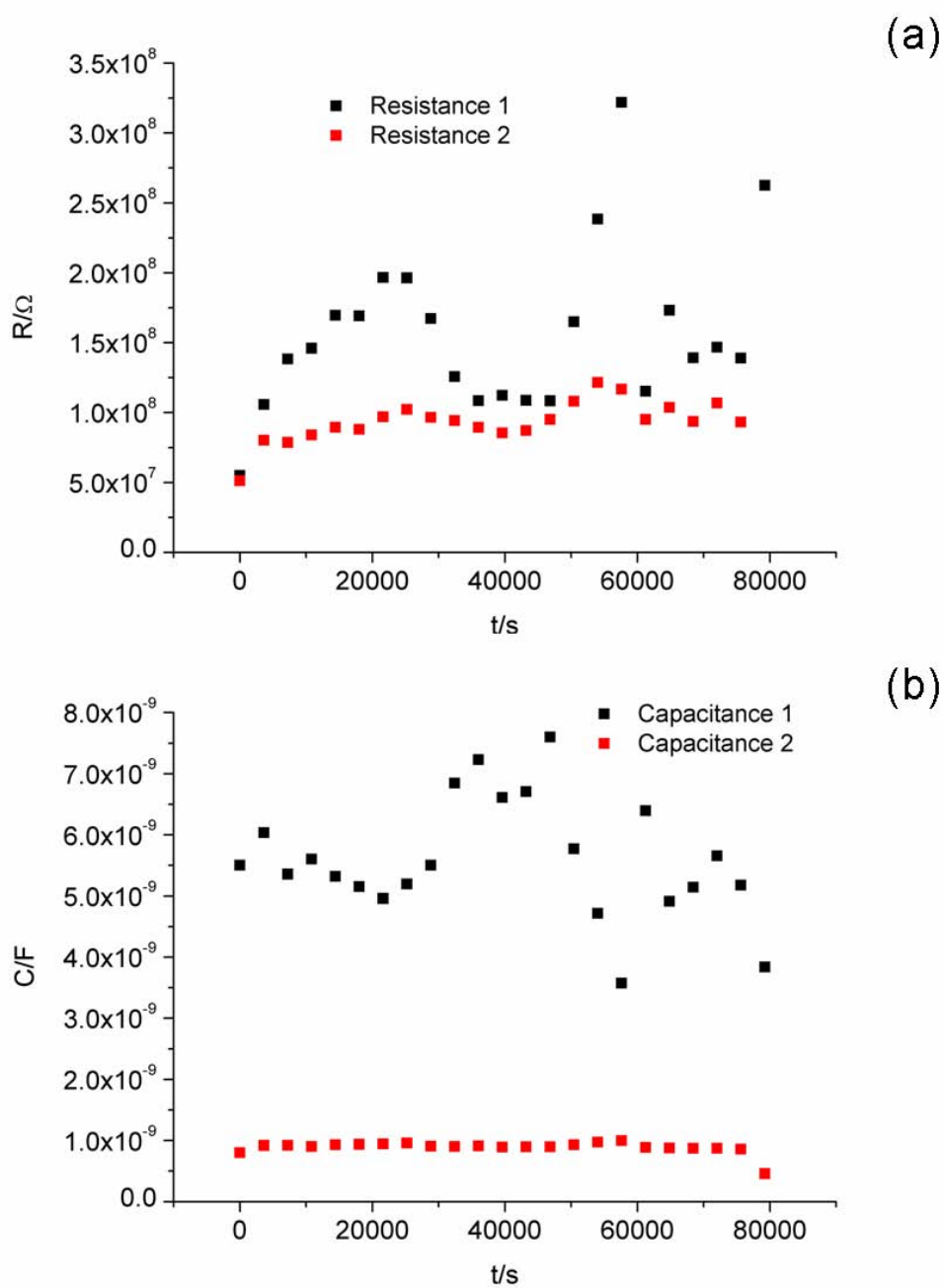
Fig. 4.25: Evaluation of DC resistances from CNLS fit (two proccess modelled by two parallel R-CPE) of Impedance spectra of PZTNd(Cu) with Pt-surface electrodes at 400°C in air.

arising for undoped PZT have been attributed to electronic (polaron) conductivity and ionic (oxygen vacancy) conductivity [24, 96]. Due to the dense metal electrodes, which had been used the ionic conductivity was expected to be blocked. Therefore, the blocked ionic pathway results in a second semicircle. The equivalent circuits employed in that research was hardly applicable to fit the results in this thesis. Boukamp and Donnelly naturally expected parallel ionic and electronic pathways. The data in our research, however, was better fitted with two R-CPE circuits in series suggesting that the corresponding processes are in series. From the present state of knowledge about PZT it might therefore not be wise to attribute the obtained semi-circles from a Nyquist plot to a distinct conduction mechanism. There are still far too many open questions concerning their origin and the comparison with the above discussed research might not be valid due to different pre-treatment (Donnelly) and doping (Boukamp) of the PZT samples. Unfortunately, experiments with Cu-surface electrodes have not been conducted yet because the Cu oxidizes far too quickly in the atmospheres, which were used so far.

4.6 Comparision of Conductivity for Surface and Inner Electrode Measurements

An evaluation of the conductvity from the surface electrode measurements is not straightforward. The usual approach (Eq. 2.67), which can also be employed in the case of inner electrodes is not possible for surface electrodes. The field distribution should be homogeneous over the whole distance between the electrodes and this is not valid for surface electrodes (Fig. 3.1). FEM calculations were conducted to evaluate this field distribution similar to the calculations of surface electrodes by Gerstl [196]. To simplify the calculation only one electrode was simulated while at half distance between two electrodes the boundary was set to ground thereby modelling the electrical response of half of the model system (Fig. 4.26). The normal current density i_n integrated along the ground electrode from the FEM calculations (Fig. 4.26) results in the current per electrode length I_L. Together with the known voltage U the resistance per electrode length R_L can be evaluated:

$$R_L = \frac{U}{I_L}.$$

(4.3)
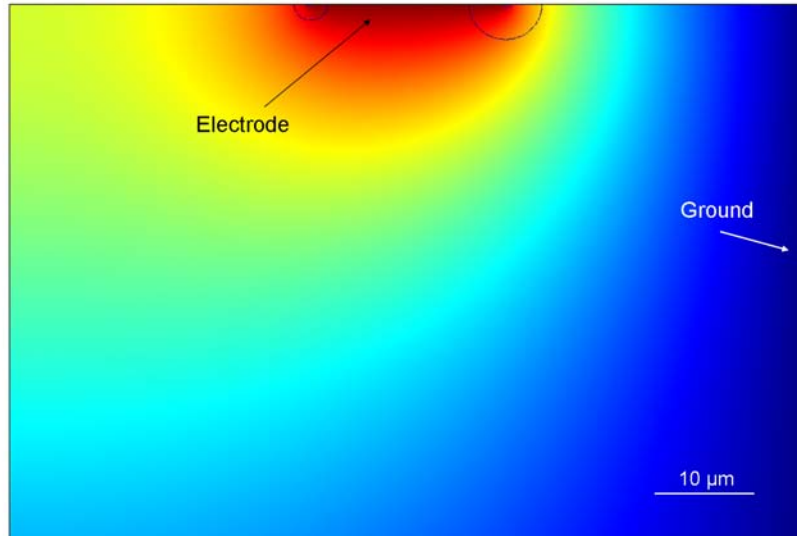
Fig. 4.26: Potential distribution in FEM simulation of surface electrodes. The value of the electrical potential increases from blue to red. The black semi-circles illustrate the distribution of the normal current density.

The geometrical factor f_{geo} is used to describe the relationship between conductivity σ and the resistance of the surface electrodes and can be determined by:

$$R_L = R \cdot L_e = \frac{f_{geo}}{\sigma} \Rightarrow \sigma = \frac{f_{geo}}{R \cdot L_e} \tag{4.4}$$

with L_e denoting the electrode length. For the 20 μm wide electrodes with a 60 μm distance a geometrical factor $f_{geo} = 1.80$ results. Another interesting feature, which can be observed in Fig. 4.26 is that the normal current density is the highest at the end of the electrodes, which corresponds to the triple phase boundary between air, electrode and PZT. The current density is of course unsymmetrical but there is still a high value of i_n at the left end of the electrode, which does not face the second electrode. It can also be deduced from the potential distribution that the voltage does not drop entirely in the region between the electrodes. In respect to the Ag-dendrite development at both sides of the anode depicted in Fig. 4.14 (b) this could mean that the generation of dendrites dependends on the local current density at the triple phase boundary. The most interesting conductivity evaluation, which is now possible, is the comparison of the DC experiments on PZTNd(Ag/Pd) with Ag-surface and Ag/Pd-inner electrodes. In Fig. 4.27 the results from the corresponding conductivity plots are given. It can again be seen that the Ag-inner electrodes are more stable. However, the shapes of the conductivity/time
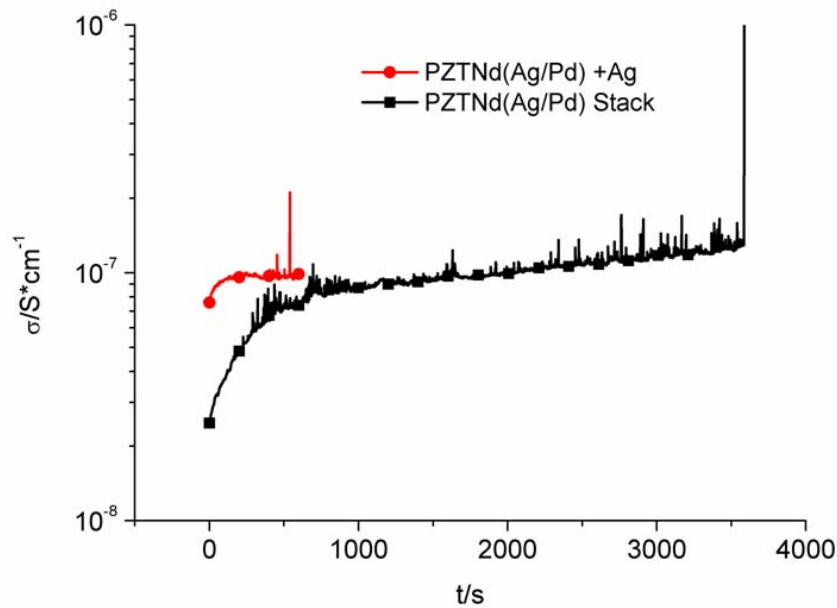
Fig. 4.27: Comparison of conductivity from DC experiments on PZTNd(Ag/Pd) with Ag-surface and Ag/Pd-inner electrodes at 400°C in air.

plots are similar although changes are much more pronounced for the experiments with inner electrodes. Interestingly, conductivities are rather different in the beginning but very similar after the first current increase. These results lead to the conclusion that the changes obtained from DC experiments with Ag-surface electrodes occur in a much shorter time frame but might lead to the same final state. This could mean that either the region close to the surface is more prone to degradation or that the mechanism responsible for degradation originates from the surface.

4.7 Conductive Mode Microscopy (CM) on PZT

The conductive mode microscopy image for PZTNd(Cu) with 20 μm circular Au-surface electrodes at 350°C is given in Fig. 4.28. Contrast steps, which can be attributed to resistive interfaces can be seen. These are similar results as obtained for BT samples from PTC material above the CURIE temperature [184]. In this case the resistance steps was not only attributed to the PTCR effect because clusters of grains were involved. It was assumed that this is also linked to microstructural features from powder agglomeration. Application of voltage leads to a
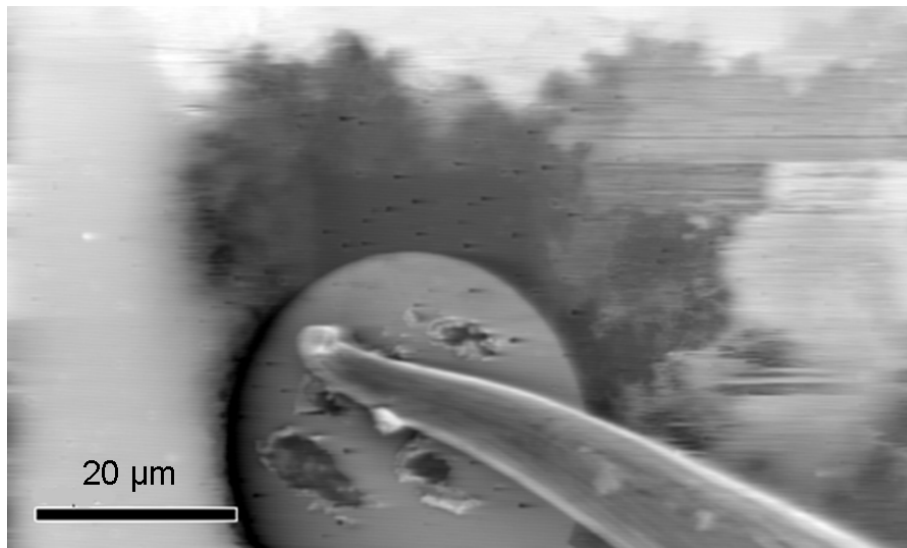
Fig. 4.28: Conductive mode microscopy (15 kV accelaration voltage, 10nA) on PZTNd(Cu) with 20 μm Au electrodes (350°C, $5 \cdot 10^{-5}$ mbar)

change in the contrast steps. The dark contrast on the upper electrode in Fig. 4.29 (a) is reduced in Fig. 4.29 (b) due to the application of 10 V for 40 min. The surface resistivity of the sample seems to be homogenized due to the applied field prior to the next CM measurement. There is, however, still a black ring around that electrode, which can be attributed to a SCHOTTKY contact at the electrode because in this case the current flow is most definitely directed towards the corresponding electrode. However, due to the limited surface quality a more detailed interpretation of these very surface sensitive measurements is not meaningful. To better understand what the origin of the contrast steps might be CM measurements were conducted on HF-etched PZTSr/Nb with square Pt-surface electrodes (100x100 μm^2) at 400°C. Fig. 4.30 (a) depicts the CM image for measurements with an electrode distance of 100 μm. In this image and the corresponding SEM image in Fig. 4.30 (b) the grain boundary structure is clearly visible. It can also be seen that the highest resistance contrast steps occur at grain boundaries. To the author´s knowledge this is the first time that good qualitative information on the conduction behavior perpendicluar to the grain boundaries has been obtained for PZT.

Investigations on the influence of an electric field on the resistance contrast have also been carried out. The CM images of the same area of interest as in Fig. 4.30 after repeated application of 30 V are given in Fig. 4.31 (b), (d) and (f). The corresponding current plots are also depicted next to the CM images. After application of voltage brighter areas occur, which means that the current
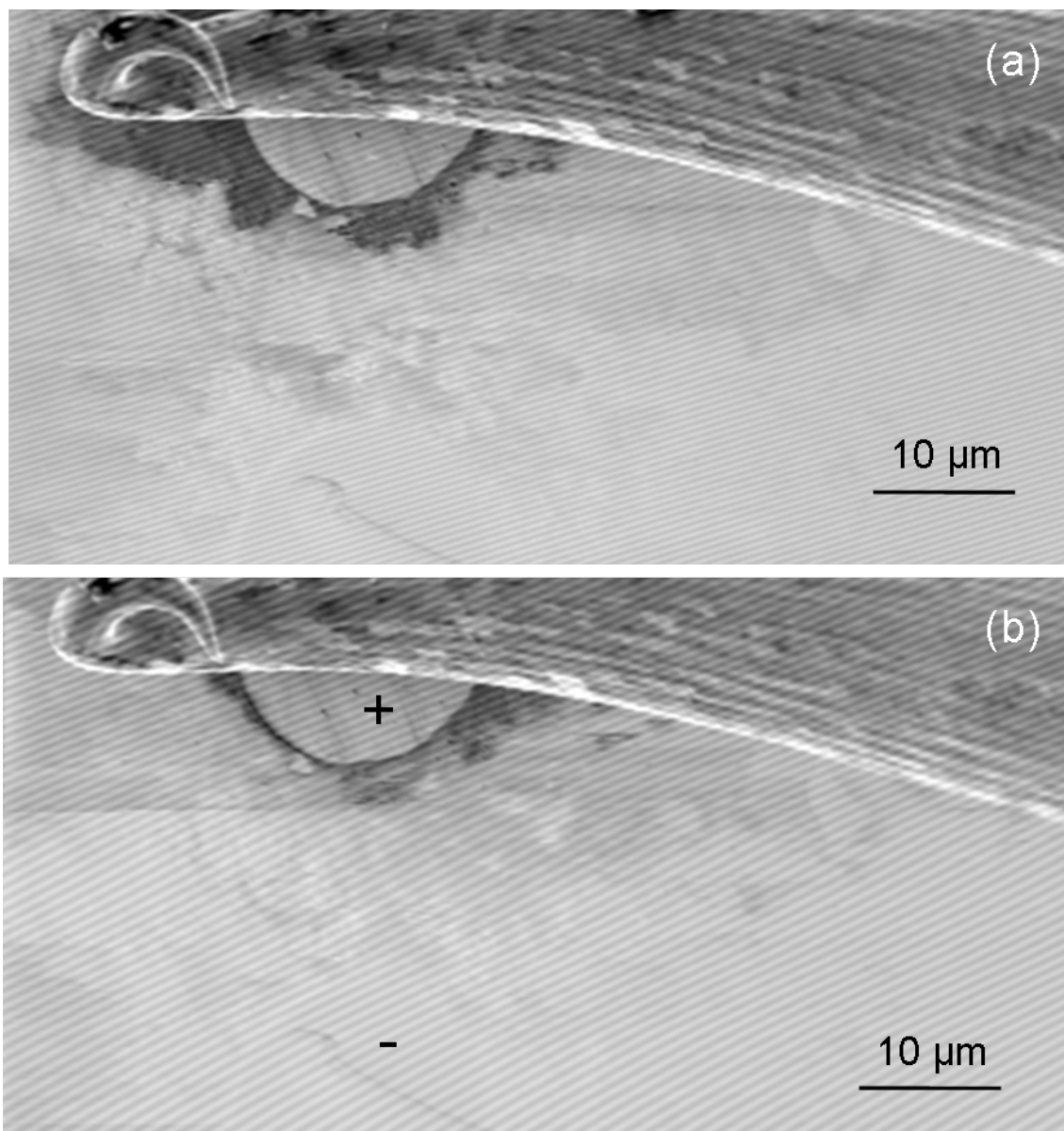
Fig. 4.29: Conductive mode microscopy (10 kV accelaration voltage, 5nA) on PZTNd(Cu) with 20 μm Au electrodes (350°C, $5 \cdot 10^{-5}$ mbar) (a) before (b) and after application of 10 V for 40 min.
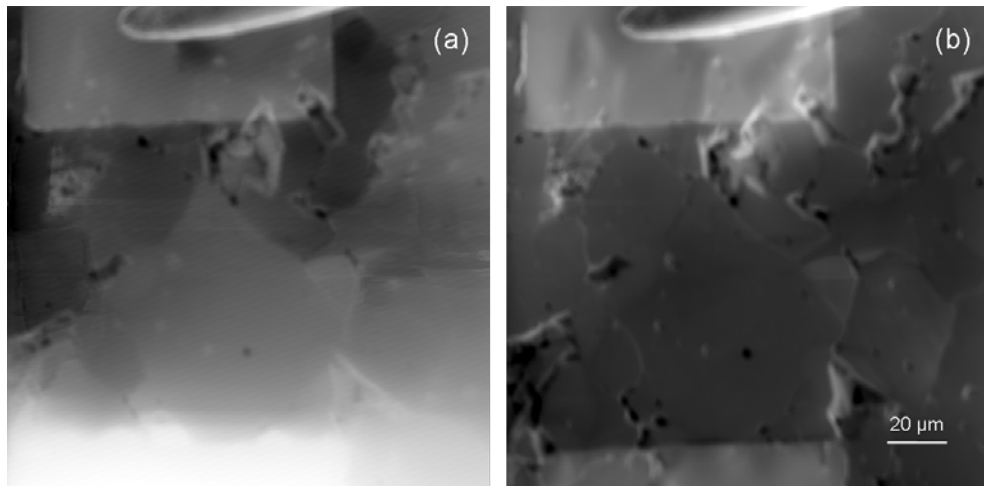
Fig. 4.30: (a) Conductive mode microscopy (10 kV accelaration voltage, 9 nA) on PZTSr/Nb with 100x100 μm^2 Pt electrodes (distance 100 μm, 400°C, $5 \cdot 10^{-4}$ mbar) (b) SEM of the corresponding area.

flow resulting from the electrode beam is now mainly directed to the lower electrode in these areas. Additionally, the resistive contrast becomes more pronounced at some grain boundaries. This process progresses with time and it can be seen that more and more grains become involved. Hence, the resistive barriers at the grain boundaries are breached and no difference between the grain and grain boundary behavior can be determined after field stress. This is best visible for the grain boundary marked by an arrow in Fig. 4.31. After the second field stress it can hardly be seen anymore indicating negligible resistance between the two grains. This breakdown could either be related to a vanishing of the SCHOTTKY barrier due to defect chemical changes or to a short-circuiting path between grains not visible at the surface. It might therefore be no coincidence that peaks occur in the current plots. They might very well be related to a grain boundary breakdown resulting in a temporary increase of current. As a result such a mechanism could be responsible for additional noise in the regular DC experiments.

How the potential is distributed between the electrodes can be also made visible by SEM measurements during voltage application. The application of 30 V at 400°C to Pt-electrodes on HF-etched PZTSr/Nb leads to a change in the material properties and influences the secondary electron formation (Fig. 4.32). The brighter areas in Fig. 4.32 are therefore regions, which are influenced by the cathode potential. Again, it can clearly be seen in these images that grain boundaries are resistive borders, which break down upon voltage application. The progression of property changes on the grain surface can also be observed in Fig. 4.32 (a). These are certainly
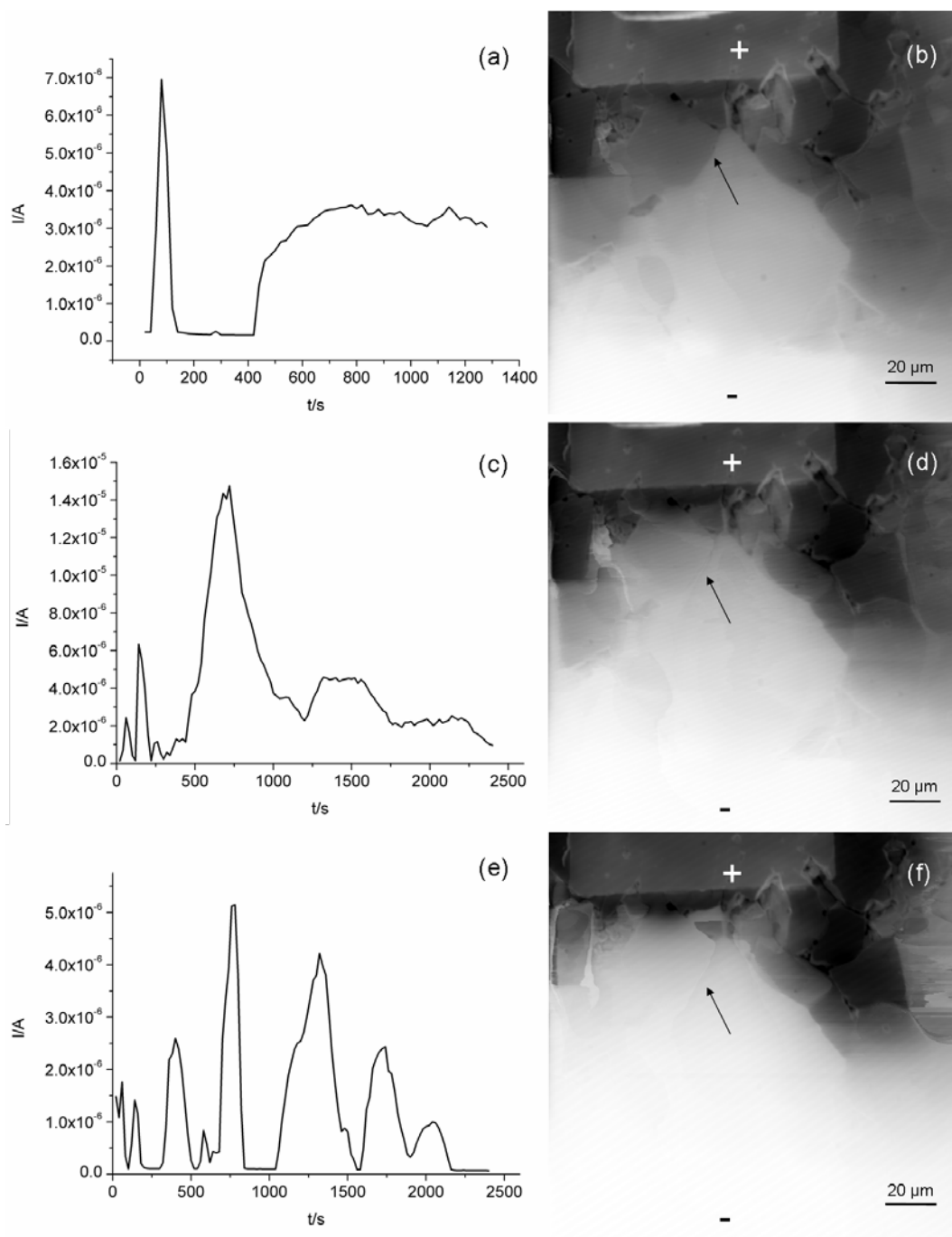
Fig. 4.31: Current plotted against time for subsequent DC experiments in the same area on PZT(Sr/Nb) at 30 V with 100x100 μm^2 Pt electrodes (distance 100 μm, 400°C, $5 \cdot 10^{-4}$ mbar) are depicted in (a), (c) and (e) (arrow marking grain boundary breaking down due to voltage application), while (b), (d) and (f) are the corresponding CM images (10 kV accelaration voltage, 9 nA) obtained after the voltage application.
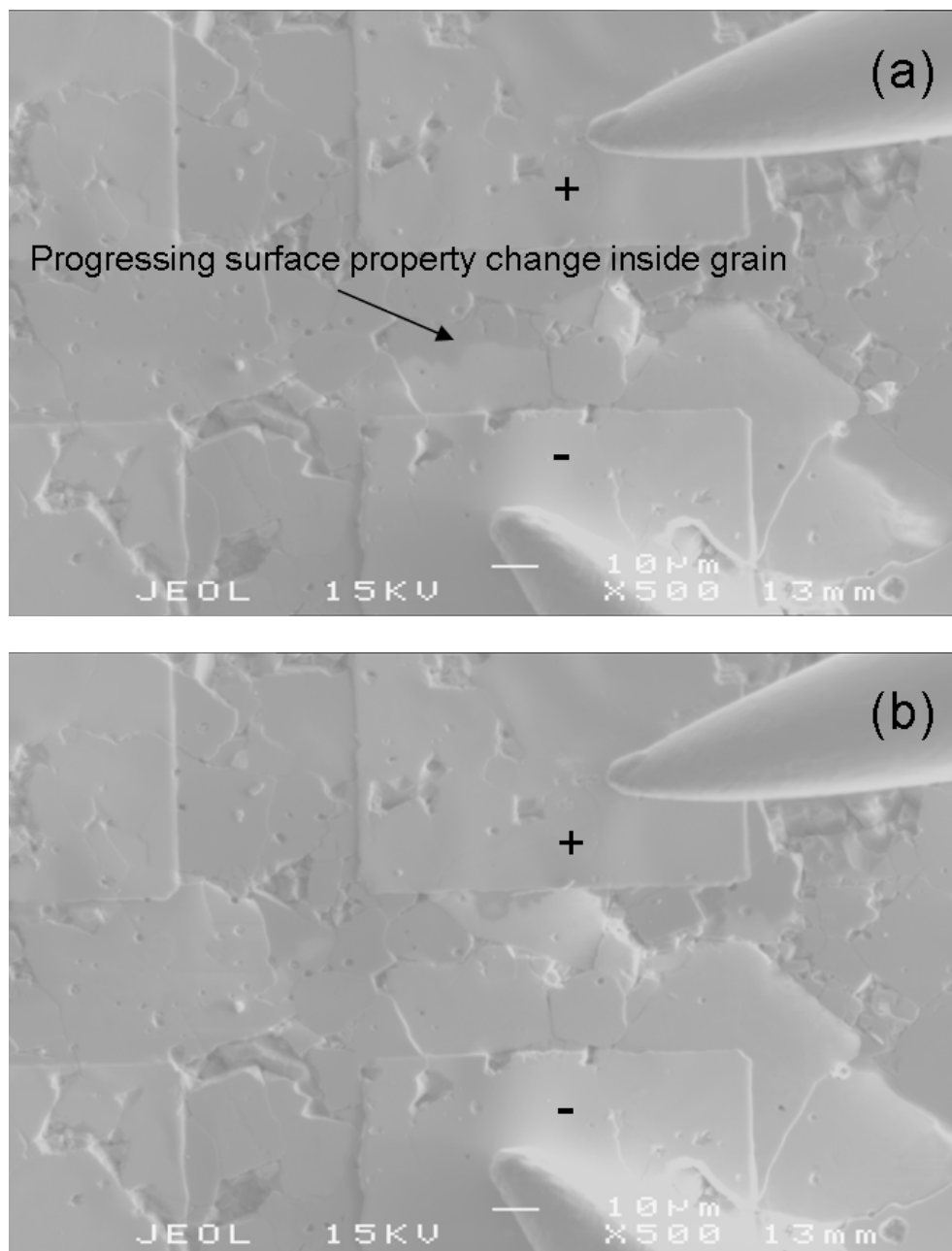
Fig. 4.32: (a) SEM of PZT(Sr/Nb) at 30 V after 5 min with 100x100 μm^2 Pt electrodes (distance 50 μm, 400°C, $5 \cdot 10^{-4}$ mbar); (b) same area after 15 min of field load.

very interesting results. However, if the origin of resistance contrast for the PZTSr/Nb and the PZTNd(Cu) are the resistive grain boundaries the question arises why in most cases only one semi-circle can be observed. Then the grain boundary process should have a similar time constant as the bulk process. Because the obtained results are rather qualitative no comment can be made on how large the resistance at the grain boundaries actually is. Therefore, a small difference in resistance might lead to a contrast in the CM but may hardly influence the impedance mesurements.

5

Results and Discussion: Oxygen Tracer Diffusion Experiments on PZT

5.1 Observation of Grain Boundary Diffusion

The aim of the ^{18}O tracer diffusion experiments was to obtain more information on the oxygen diffusion properties and their contribution to conduction mechanisms. One major focus was put on trying to distinguish between bulk and grain boundary diffusion. Owing to their large grain size PZTSr/Nb samples are particularly advantageous when aiming at visualization of fast grain boundary diffusion but also for evaluating surface diffusion profiles inside a single grain neglecting grain boundary diffusion. Let us first consider some results obtained for ^{18}O diffusion experiments on PZTSr/Nb with large grains (15 μm). Fig. 5.1 (a) shows a typical depth profile image of the ^{18}O intensity after 4 h equilibration in ^{18}O$_2$ at 650°C and integrating the signal in a depth from 900 nm to 1.2 μm. The color code in this figure represents increasing intensity from bottom to top of the color scale. From comparison with the secondary electron (SE) image (Fig. 5.1 (b)) - showing the grain boundaries between individual grains - it becomes evident that there is a high intensity of ^{18}O at the grain boundaries in a depth of 900 nm, while the concentration is low inside the grains. This clearly indicates enhanced grain boundary diffusion at 650°C.

The importance of diffusion along the grain boundaries is even better demonstrated in the cross section image of the same sample (Fig. 5.2 (a)): The diffusion profile extends up to 150 μm into the PZT. This can also be seen in the corresponding profile of the relative ^{18}O concentration
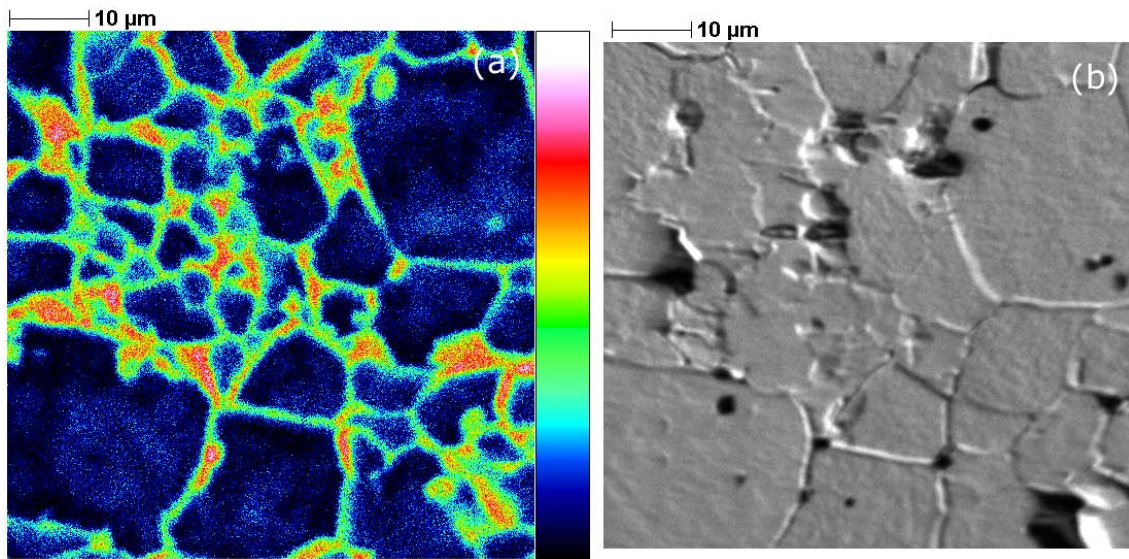
Fig. 5.1: (a) Cumulative ^{18}O image obtained in a depth from 900 nm to 1200 nm of PZTSr/Nb (large grains) annealed at 650°C for 4 h. b) Corresponding SE-image.

(Fig. 5.2 (b)), calculated by integrating the signals of the cross section image along lines parallel to the surface. It has to be kept in mind that the near-surface region is most probably not represented correctly due to roughening of the edge caused during the polishing procedure. For the sample equilibrated at 600°C (Fig. 5.3 (a)) the grain boundary pattern is not visible in the cross section image. The corrected relative concentration of ^{18}O drops to zero immediately after the small surface area with higher concentration (Fig. 5.3 (b)). This suggests that the grain boundary diffusion profile is rather shallow and the diffusion along grain boundaries is therefore expected to be strongly temperature dependent. The corresponding depth profile image (Fig. 5.3 (c)), however, still indicates high ^{18}O intensity at grain boundaries in a depth of 900 nm to 1.1 μm and thus enhanced grain boundary diffusion compared to bulk diffusion. For PZT equilibrated at 500°C, no evidence of fast oxygen grain boundary diffusion is obtained (Fig. 5.4 (a)). However, one should keep in mind that the ion beam used for analysis has a size of about 200 nm for the chosen method. Fast grain boundary diffusion with very little "leakage" into the grain might thus hardly be visible due to the small size of the grain boundary - e.g. a few nm - compared to the measurement spot. A lack of high ^{18}O intensity in scan images at grain boundaries is therefore not necessarily proof for non-existing grain boundary diffusion. How high the concentration would need to be inside a grain boundary to be detected in a cross section or depth profile is still part of ongoing investigations.
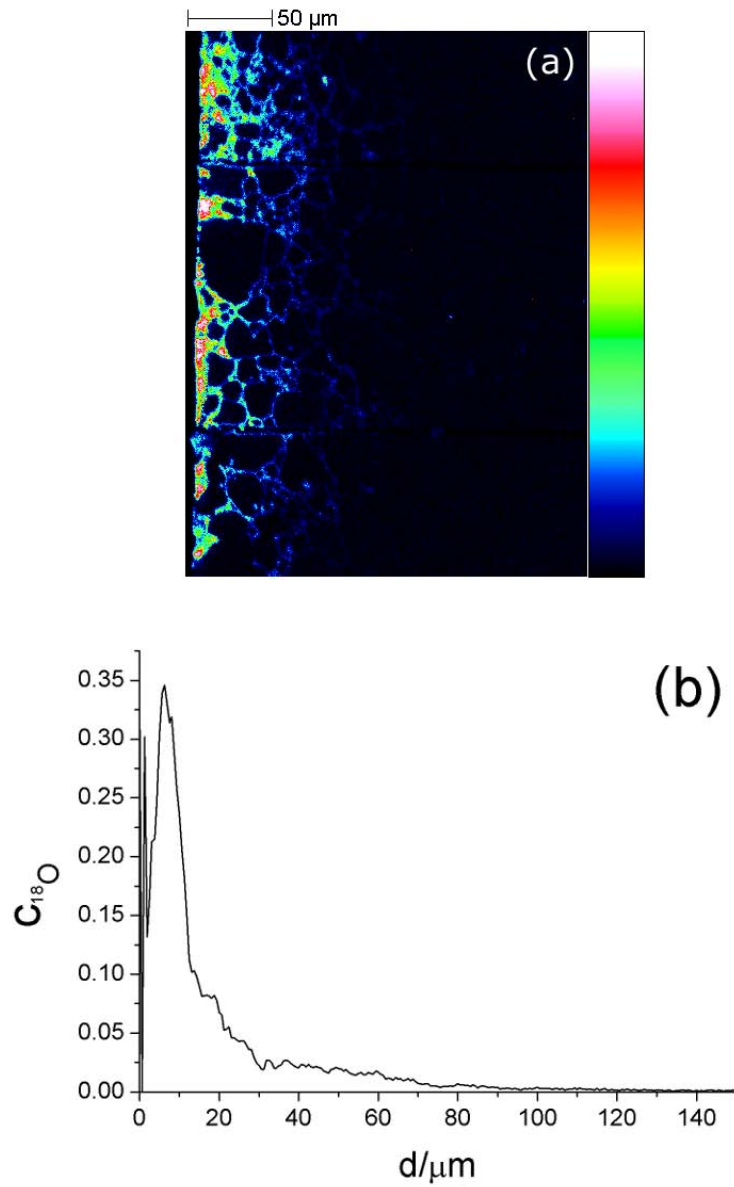
Fig. 5.2: (a) ^{18}O cross section image of PZTSr/Nb (large grains, 650 °C, 4 h). (b) Corresponding ^{18}O concentration profile calculated by integrating along lines parallel to the left side of the cross section image.
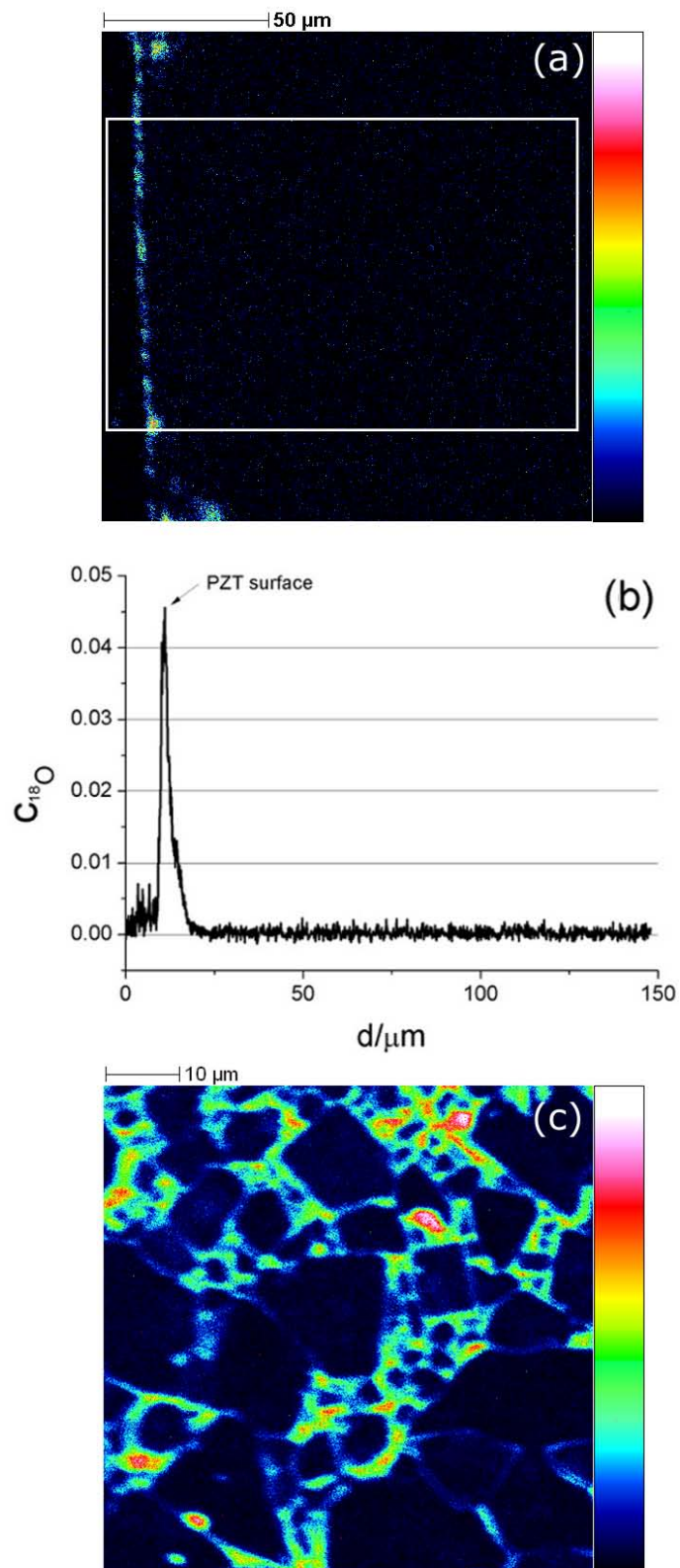
Fig. 5.3: ^{18}O images of PZTSr/Nb doped PZT (large grains, 600 °C, 4 h). (a) ^{18}O cross section image. (b) Corresponding integrated ^{18}O concentration profile within area given by the white box in Fig. 5.3 (a)) (c) Cumulative ^{18}O image from 900 nm to 1100 nm depth.

Focusing on the results for 650°C, the question arises, if quantitative diffusivity data could be obtained from the cross section profile. To calculate the grain boundary diffusion coefficient the method given by WHIPPLE and LECLAIRE [83, 86] is frequently employed in case of experiments determined by type B diffusion kinetics (see Sec. 2.2.5). Quantification of the grain boundary co-
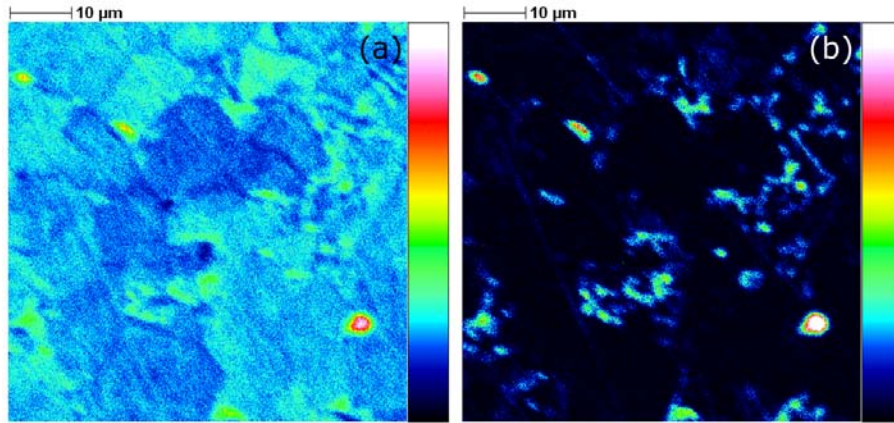
Fig. 5.4: Cumulative ^{18}O-images for PZTSr/Nb (500°C; large grains, 4 h) (a) from surface to 800 nm and (b) from 400 nm to 800 nm.

efficient, according to Eq. 2.40, requires the bulk diffusion coefficient. However, before discussing how this one is obtained in our study, some further aspects are addressed, which might affect the interpretation and quantification of the data. Digital holographic microscopy (DHM) measurements showed no extensive roughening of the surface occurring due the SIMS experiments and therefore no or minor contribution of the so called shadowing effect [153, 197] is expected. For the PZTNd(Ag/Pd), there was only an increase from 3.5 nm to 4.5 nm of the average areal roughness Sa for a crater with a depth of 1 μm compared to the unaffected surface.

A more serious problem for quantifying grain boundary diffusion may arise from the porosity of the samples. In the surface near region of the sample exposed to ^{18}O$_2$ at 500°C (Fig. 5.4 (a)) some ^{18}O intensity is visible inside grains and some small areas show very high intensity, which can be attributed to the pores. In a depth from 400 nm to 800 nm (Fig. 5.4 (a)), however, there is high ^{18}O intensity only close to pore regions. As a result, this intensity has an impact on the depth profile and a tail with slowly decreasing concentration is found (Fig. 5.5). Without the knowledge from the depth profile images that this is only caused by pores, it could be misinterpreted as a result of fast grain boundary diffusion. The rather unusual profile shape at the beginning in Fig. 5.5 will be discussed in the course of the next sections. The question arises, if the porosity
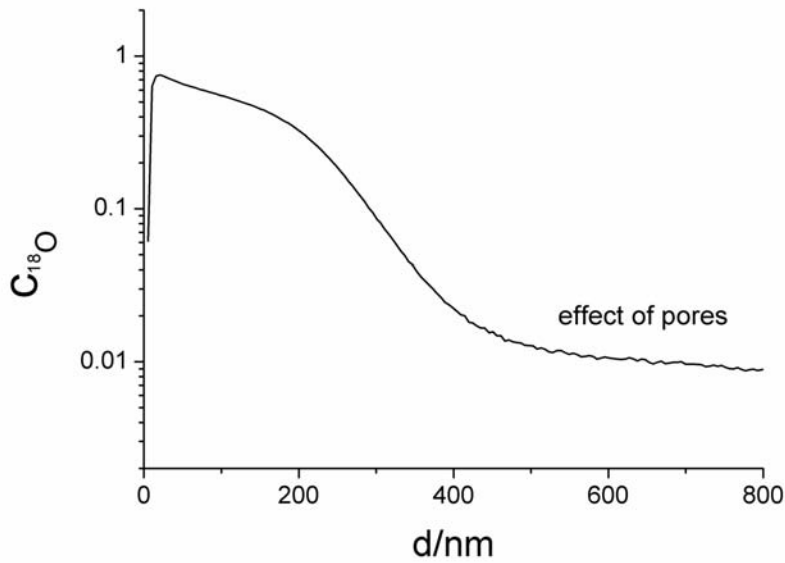
Fig. 5.5: ^{18}O concentration profile for PZTSr/Nb (500 °C; large grains, 4 h) indicating a significant contribution of pores in some depth.

also has an effect on the cross section profiles used in the following for quantifying grain boundary diffusion. The cross section images of the PZT samples (Fig. 5.2 (a), Fig. 5.22 (b), Fig. 5.23 (c) and (d)) clearly illustrate the grain pattern and no indication of an enhanced ^{18}O concentration due to extended open porosity could be found. In the image of the PZTSr/Nb sample annealed in $^{18}O_2$ at 600°C (4 h) (Fig. 5.4 (a)) the ^{18}O intensity is limited to a small surface area. With cracks in the sample or open porosity a similar impact on the cross section profile as on the depth profile should be found. Hence, we conclude that neither open porosity nor cracks affect our cross section profiles. Moreover, despite pores, qualitative information on ^{18}O concentration in grain boundary regions can still be obtained from depth profile images (Fig. 5.1 (a), 5.4 (b)). In the following, the surface diffusion and grain boundary diffusion will be discussed for different samples. Additionally, diffusion coefficients are quantified.

5.2 Surface-Near Tracer Diffusion in PZTSr/Nb: Profile Shapes

Usually the bulk or volume diffusion coefficient of polycrystalline samples is evaluated from the first part of a depth profile, which is dominated by bulk diffusion properties in type B kinetics [170]. In this study we use a different approach. Because of the excellent resolution of

the grain structure in the depth profiling mode of large grained samples, the high lateral resolution of ca. 200 nm and the ability of calculating profiles from defined regions of interest by the ION-TOF software, it was possible to obtain the profiles of the interior of individual grains. An example of an area chosen for analysis is given in Fig. 5.6 (a) (white polygon), while Fig. 5.6 (b) illustrates the section for evaluating grain bulk diffusion in an xz-depiction. Fig. 5.6 (b) also
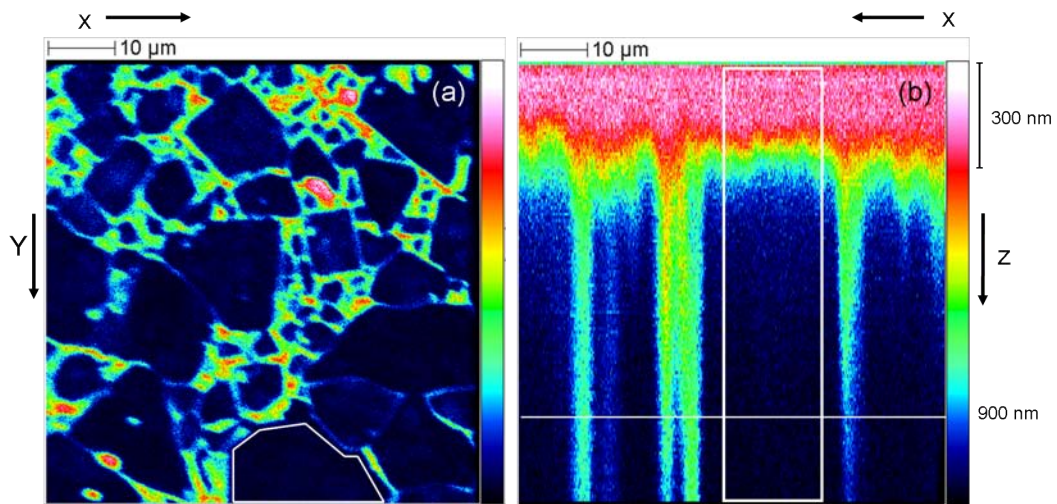
Fig. 5.6: (a) Cumulative ^{18}O image of PZTSr/Nb (600°C, 4 h; large grains; from 900 nm to 1100 nm depth) with the area used for analyzing diffusion in the grain. b) Calculated xz-image of ^{18}O (white box indicating the section for the evaluation of grain diffusion).

again visualizes the fast diffusion paths along the grain boundaries. In this type of analysis the size of the grains should be significantly larger than 5 μm to obtain sufficient or sufficiently high integrated intensity and to exclude an additional contribution from ^{18}O entering the grain via the grain boundaries. Hence, only large grain PZT samples could be investigated by this method.

In Fig. 5.6 (b) it can be seen how smooth the profile extends into the individual grains, which is another evidence for the validity of the approach. For annealing temperatures from 400°C to 650°C depth profiles of grain interior could be obtained for the PZTSr/Nb large grain samples (Fig. 5.7). The sample equilibrated at 400°C seems to exhibit a rather conventional error-function like diffusion profile [79]. However, for higher temperatures a completely different diffusion behavior becomes evident. Between 500°C and 600°C the profile becomes box-shaped with a high concentration of ^{18}O close to the surface and a steep decent at around 300 nm. Below 600°C only little if any ^{18}O is found beyond this "box". This can only be understood by assuming at least two regions with different diffusion coefficients. In the first region - the near-surface region
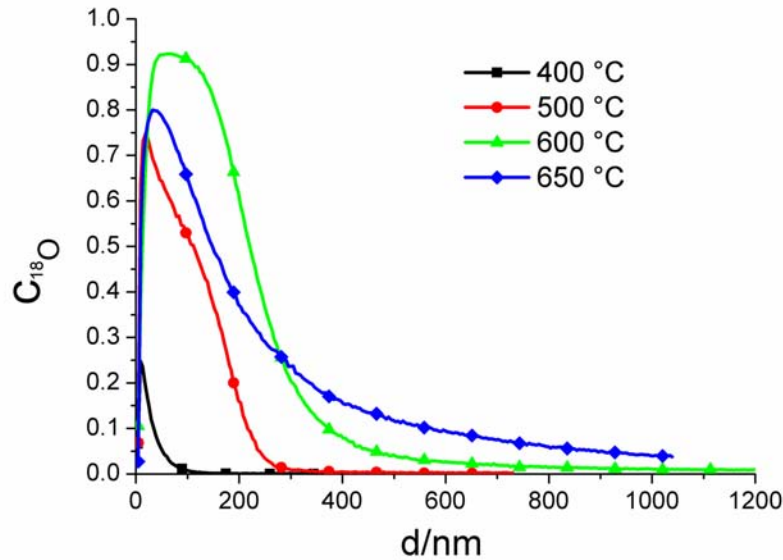
Fig. 5.7: Diffusion profiles of single grains for PZTSr/Nb (large grains) with different annealing temperatures (4 h each); the lines represent measurement data, only one symbol every 20 data points is explicitly shown for indicating temperature.

- the oxide ions are more mobile and hence the vacancy concentration is high. In the second region a low oxygen diffusivity and therefore low vacancy concentration can be assumed. For the most interesting temperature in terms of grain boundary diffusion analysis, i.e. at 650°C, the shape of the profile changes again and the box shape diminishes, while the diffusion profile extends substantially into the second region. The appearance of the surface layer in PZT is highly disadvantageous when looking for the actual bulk diffusion coefficient. Nevertheless, the extended diffusion profile at 650°C (Fig. 5.7) should indeed reflect oxygen diffusion in the bulk into a depth of several hundred nanometers. Note that only minor differences resulted for different pre-annealing times with $t_{pre} = 1/2$ h or $t_{pre} = 17$ h (Fig. 5.8). The latter may be related to slightly different sample properties.

The decrease of the concentration towards the surface particularly for higher temperatures is interpreted as follows: as the samples are cooled in air, the heated PZT can - for a short time span - still exchange oxygen with the ambient atmosphere, in which now $^{16}O_2$ is the dominant isotope. Even the few seconds needed to cool down to room temperature are thus sufficient for ^{16}O to be incorporated into the sample. It has already been discussed in Sec. 2.1.4 that space charge layers can develop at surfaces leading to a depletion or enrichment of the mobile defects
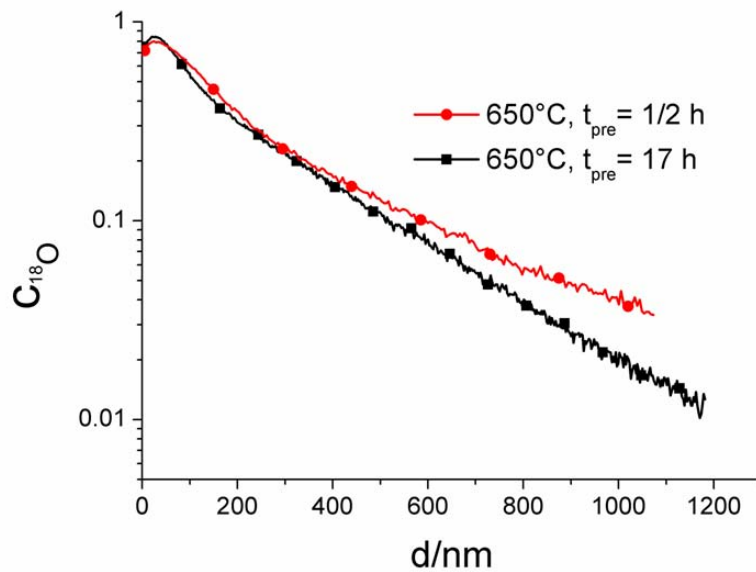
Fig. 5.8: Logarithmic concentration profiles within single grains of PZTSr/Nb (large grains) at 650°C for two different pre-annealing times (one symbol every 20 data points).

in the space charge region to counter balance the effect of the charged surface. This may also lead to a position dependent oxygen tracer diffusion as the vacancy concentration changes with respect to the bulk concentration [63,64]. In the following sections evidence will be provided that indeed a near-surface space charge layer is responsible for the surface tracer diffusion behavior of PZT.

5.3 Impact of Surface and Heat Treatment on the Near-Surface Tracer Concentration Profiles in PZTSr/Nb

To obtain further information on the origin of the unusual profile shape and its temperature dependence several experimental parameters which could have an impact on the surface properties were changed. If a space charge layer was the cause, the box-shaped profile at certain temperatures would either result from oxygen vacancies accumulating beneath the surface or at dislocations possibly induced by the polishing procedure [64, 198]. To exclude the possibility of dislocations as origin of the fast near-surface diffusion, HF-solutions were used to remove PZT material of a polished PZTSr/Nb sample down to a depth larger than the thickness of the unusual profile shape of a few hundred nanometers. The removal of this region was confirmed by

measuring the remaining ^{18}O concentration inside grains compared to the concentration before etching. Fig. 5.9 (a) cleary shows that almost 1 μm of PZT material was removed during the etching process. The profiles resulting from ^{18}O experiments after such an HF-etching procedure are given in Fig. 5.9 (b) for different temperatures. It can be seen that the effect causing the box-shape of the profiles is not diminished; the opposite is rather the case. The profiles extend even further into the material while the shapes remain very similar: Development of a box-shaped profile at 600°C and significant shape change at 650°C. As a result, it is very likely that a dislocation induced space charge layer can be ruled out as the origin of the box-shaped profiles.

A comparison between the concentration profiles from pre-etched and unetched samples after oxygen exchange at 650°C (Fig. 5.10 (a)) shows that the profile changes in the first section due to etching but the slope in the second section remains unchanged. This strongly supports our interpretation that the second process can be attributed to bulk diffusion. In contrast to HF-solution, etching with the HCl-solution did not lead to an observable removal of material. The surface remained clean and polished without a visible etched grain structure. However, etching with HCl-solution does affect the tracer diffusion profile (Fig. 5.10 (b)). From this the conclusion can be drawn that the effect causing the profile shapes strongly depends on the material properties very close to the surface such as electronic or ionic surface states.

To investigate what possible chemical changes are induced by chemical etching ICP-OES measurements of a continously etched (10% HCl) PZTNd(Ag/Pd) surface have been carried out [183]. This way the material, which is removed, can be identified. From the amount of detected cations it becomes clear that the amount of PZT removed from the surface is small and it can be expected that only the first few nanometers are affected by the etching procedure (Fig. 5.11). Nevertheless, it can be seen that the cations are not etched in the stoichiometric proportions. Accordingly, the near-surface properties are definitely altered due to HCl-etching. Whether the signals represents the composition at the surface or this can be attributed to preferential etching of the Pb and Zr from the material cannot be evaluated from these results. Further SIMS measurements similar to those presented in Fig. 5.11 could a least lead to qualitative information on the difference of surface composition with respect to bulk. However, charging of the surface due to the sputter ion beam might also affect these measurements. Nevertheless, a strong correlation between the
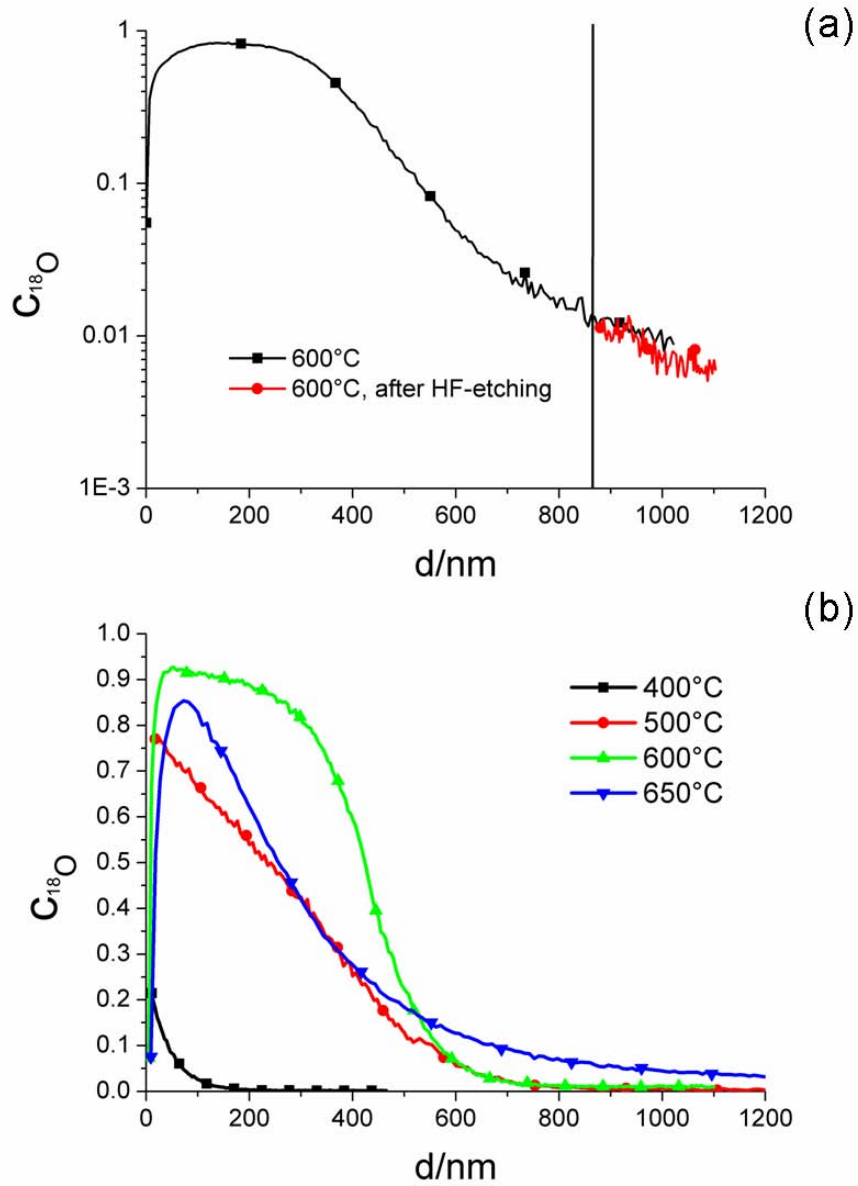
Fig. 5.9: Tracer diffusion profile inside single grain: (a) PZTSr/Nb sample pre-etched with HF-solution and annealed in ^{18}O at 600°C (4 h) (black) in comparison to diffusion profile after further etching for 10 s (red). The latter is shifted on the x-axis to indicate removal of material. (b) PZTSr/Nb (large grains) with different annealing temperatures in ^{18}O$_2$ (4 h) pre-etched with HF-solution (one symbol every 20 data points).
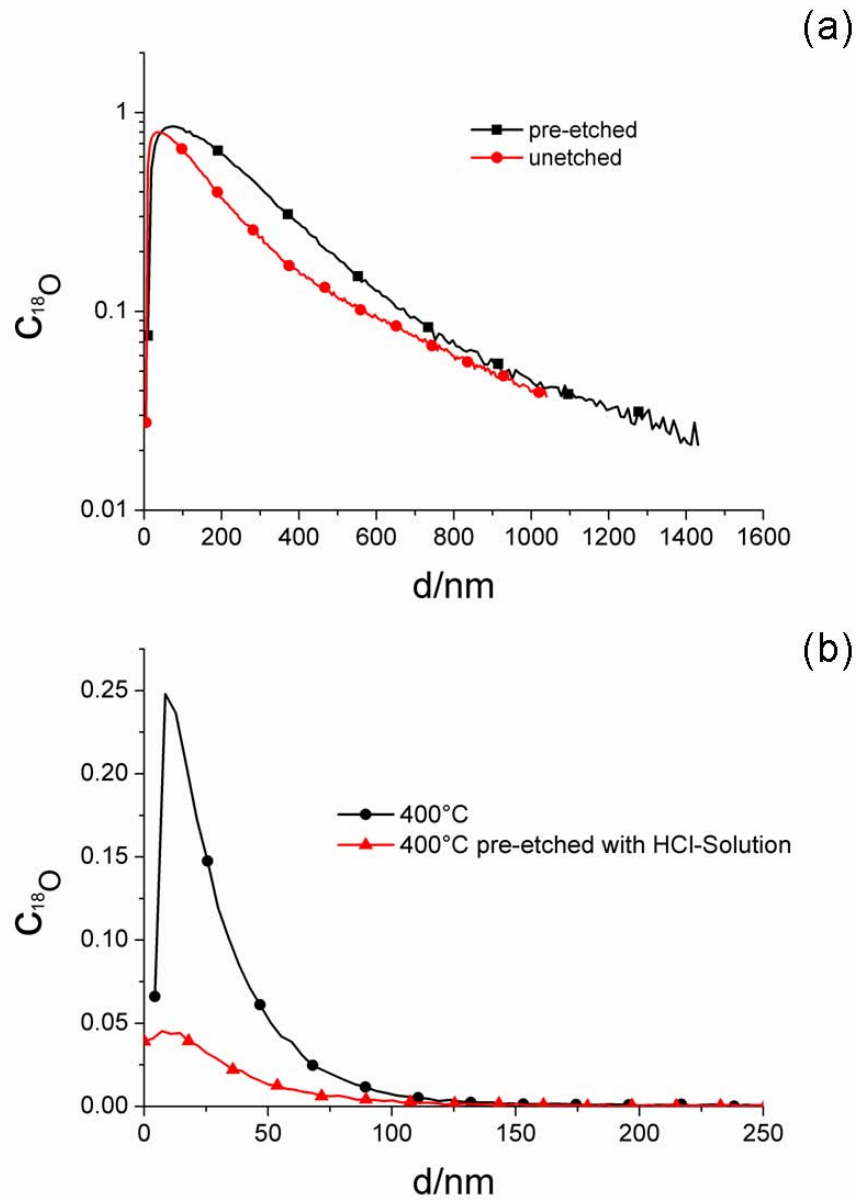
Fig. 5.10: (a) Comparison of unetched and pre-etched PZTSr/Nb samples annealed in $^{18}O_2$ at 650°C (4 h). (b) Unetched PZTSr/Nb sample annealed in $^{18}O_2$ at 400°C (4 h) in comparison to one pre-etched in 10% HCl for 2 min (one symbol every 20 data points).

change in surface cation chemistry and ^{18}O diffusion can be deduced from the above presented results.
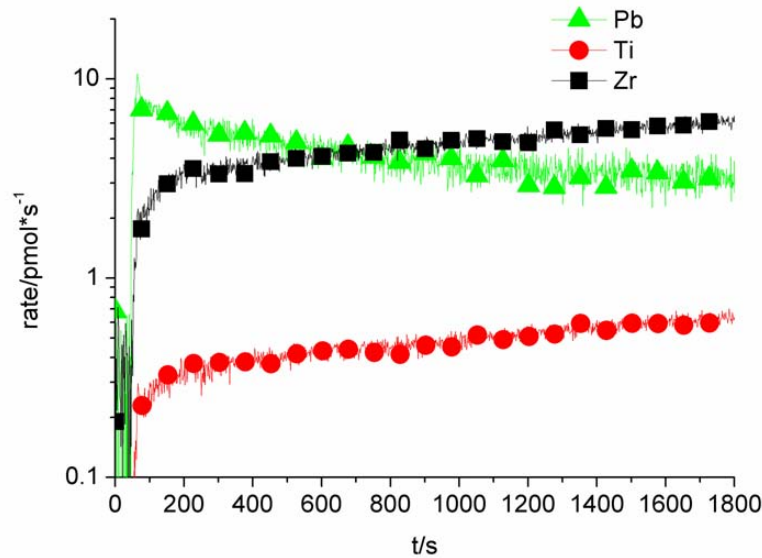
Fig. 5.11: Ecthing rate of cations from PZTNd(Ag/Pd) plotted against etching time with 10%HCl-solution as a result from ICP-OES measurements (symbol every 50 points).

A further aspect, which has to be investigated, is the influence of time and temperature of pre-annealing in $^{16}O_2$ rich gas prior to the tracer exchange experiment. The chemical diffusion can be expected to be much faster than the tracer diffusion [1] so that the healing of higher dimensional defects or slow processes like cation diffusion are the mechanisms that are most likely affected by pre-annealing. Tracer experiments on PZTSr/Nb samples, which have been conducted at the same temperature but with different pre-annealing times and temperature, resulted in modified concentration profiles. This is illustrated in Fig. 5.12 for profiles from tracer experiments at 550°C and 450°C. Even though the pre-annealing conditions influenced the shape of the box-like profile there is no clear trend observable depending on the pre-annealing temperature. For 450°C (Fig. 5.12 (b)) annealing at very similar temperatures (630°C and 650°C) lead to rather different ^{18}O boundary concentrations though decay lengths remained similar. For diffusion at 550°C pre-annealing for 17 h leads to shorter decay lengths in the near-surface regions and again an effect of the annealing temperature. Despite the ambiguity in the trends a very important conclusion can be drawn from these data: The modified ^{18}O tracer diffusion coefficient close to the surface is not caused by coupled diffusion of metal and oxygen vacancies as discussed and

shown for $SrTiO_3$ [32]. Such a cation diffusion front would penetrate into PZT with increasing pre-annealing time and hence the box should continuously broaden with time and increasing temperature, which is not the case.

A certain influence of pre-annealing also on the profiles of tracer experiments at 650°C has already been mentioned (Fig. 5.8). There, the slopes of the bulk tail differ between long term and short term pre-annealed samples but the effect is comparatively minor and could even result from slight differences in the samples. The fact that the profile shape for the PZTSr/Nb changes significantly around 650°C and rapid grain boundary diffusion sets in, leads to the conclusion that a significant change in the defect chemistry of the PZT material close to the surface and possibly also at the grain boundaries takes place at that temperature. The obtained profile shapes rather resemble profiles from tracer exchange experiments with slow near-surface diffusion [64] which should be the opposite of the behavior observed for samples annealed in $^{18}O_2$ below 650°C. The following experiment supports this interpretation: ^{18}O partial pressure of 200 mbar was applied to a PZTSr/Nb sample already at 20°C. During a time span of about 15 min the sample was then heated to 650°C while the $^{18}O_2$ partial pressure was kept constant. As a result, the near-surface part of the tracer diffusion profile extends deeper into the sample than the diffusion profile obtained for $^{18}O_2$ supply only at 650°C, while the two bulk diffusion tails converge (Fig. 5.13). Hence, it is likely that at lower temperatures the material exhibits a near-surface region with fast ^{18}O diffusion up to 600°C and subsequently a conversion of the diffusion characteristics takes place to slow near-surface diffusion typical for 650°C. The change in surface defect chemistry at about 650°C, which leads to the different diffusion properties, can therefore be expected to take place within minutes or even faster.

5.4 ^{18}O Tracer Diffusion in Different Types of PZT

As the grains of the PZTNd(Ag/Pd) samples are much smaller than that of the PZTSr/Nb samples it is not possible to obtain diffusion profiles inside single grains. However, the tracer profile of the near-surface region is expected to be mostly governed by the grain surface properties while the tail in some depth results from grain boundary diffusion (Fig. 5.14). In the near-surface region the profiles found for PZTNd(Ag/Pd) (Fig. 5.14) are similar to those in Fig. 5.7 for single grains of PZTSr/Nb with the same profile shape changes at 650°C. The diffusion tails of the depth profiles at 600°C can be mostly attributed to grain boundary diffusion and is also found for
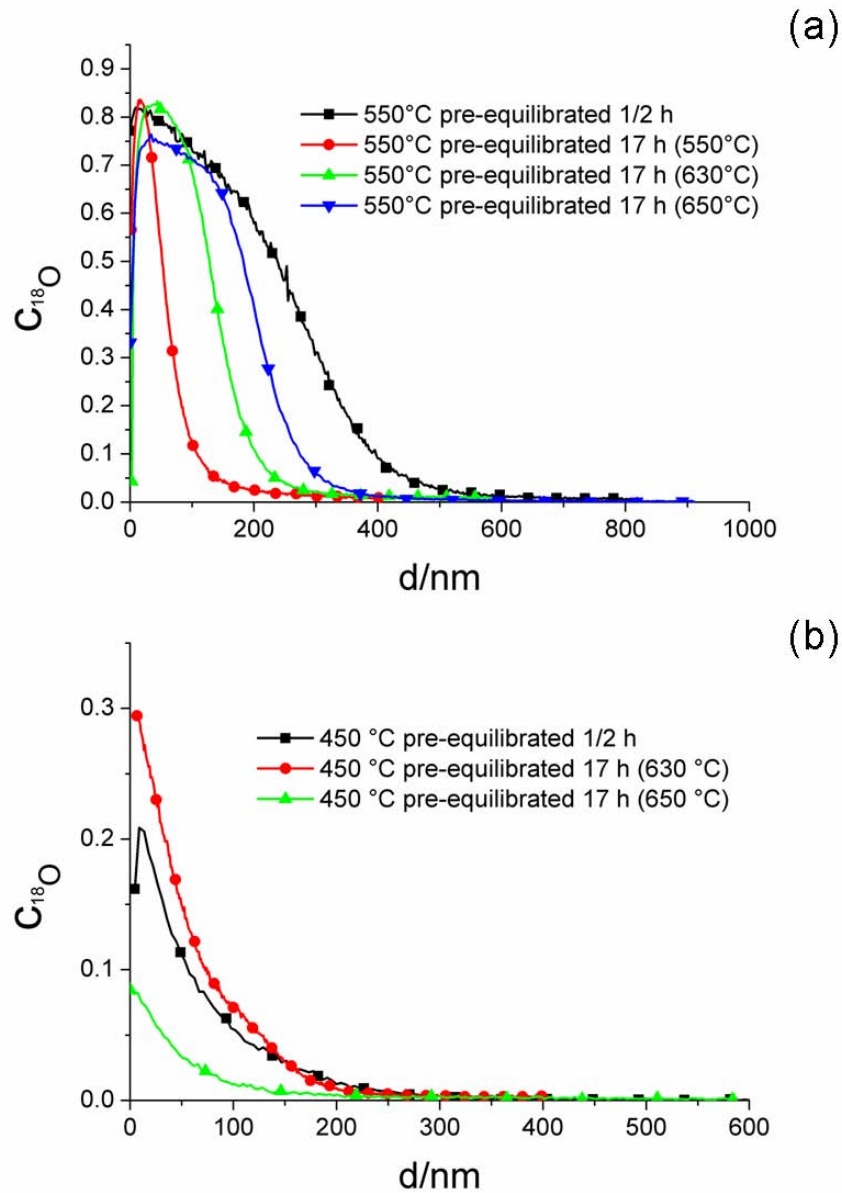
Fig. 5.12: Tracer diffusion profiles inside single grains of PZTSr/Nb samples annealed in $^{18}O_2$ for 4 h with different pre-annealing times in $^{16}O_2$ and different pre-annealing temperatures: (a) 550°C, (b) 450°C (one symbol every 20 data points).
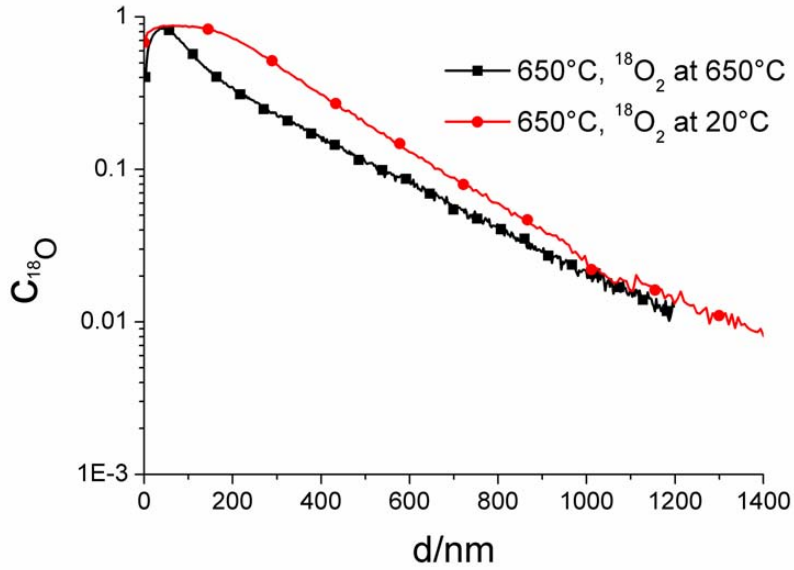
Fig. 5.13: Tracer diffusion profiles within single grains of PZTSr/Nb for different heating rate under $^{18}O_2$ atmosphere (one symbol every 20 data points).

PZTSr/Nb if the whole area is integrated instead of the grain areas only (Fig. 5.6 (a)). At 650°C the tail in the depth profile not only includes grain boundary diffusion but also some extended bulk diffusion. Hence, the profiles do not seem to be strongly influenced by the choice of dopant although a larger series of dopant concentration should be investigated to further verifiy this conclusion. In Ref. [42] also no dependence of the diffusion behavior on the dopant concentration was found. There, however, bulk and grain boundary diffusion was already observed at 250°C, which might be attributed to strongly different defect concentration compared to our study since a pre-annealing step at 723°C in air presumably caused significant stoichiometry changes due to PbO evaporation. In our study, the impact of the production process, especially the sintering step was analyzed by measuring three PZT samples of nominally the same composition but different pre-history. PZTNd(Cu) was sintered in reducing atmosphere and PZTNd(Ag/Pd) in air; both samples were cut from stack pieces of a larger sintering batch. PZTNd was a disc shaped sample sintered in air. In Fig. 5.15 oxygen tracer profiles of these PZT samples annealed in $^{18}O_2$ at 500°C and 600°C are given. The profiles are very different which leads to the conclusion that the preparation procedure, and particularly the oxygen partial pressure, in fact does have a major impact. Reducing sintering caused a vanishing of the box-shape profile. The profile of the PZTNd, on the other hand, shows the largest box effect for tracer experiments conducted
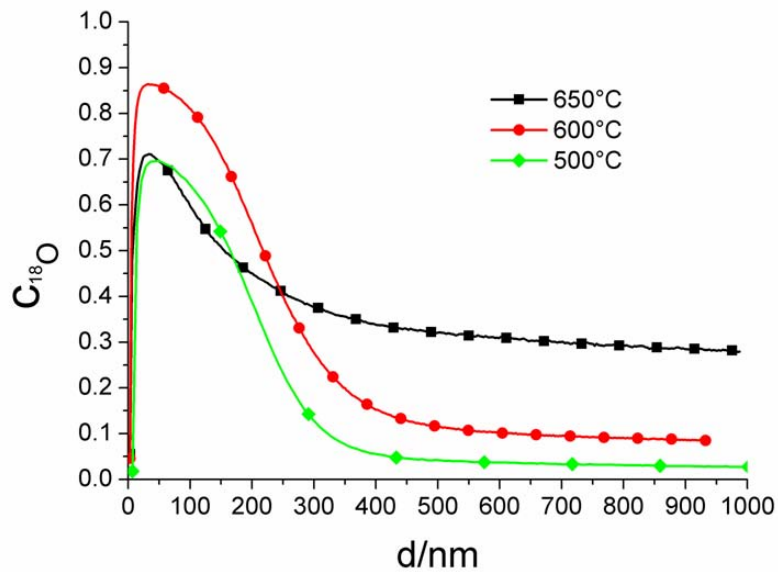
Fig. 5.14: Tracer diffusion profiles for PZTNd(Ag/Pd) at annealed in $^{18}O_2$ (4 h) at different temperatures. (one symbol every 20 data points)

at 600°C. Thus, it cannot be ruled out that the choice of metal electrode in PZT from stacks does also influence the oxygen diffusion properties. Research concerning silver diffusion in PZT could show evidence for very high silver mobility [112, 113]. This results in an incorporation of silver from the Ag/Pd electrodes which influences the defect chemistry and would thus explain the differences found for PZTNd and PZTNd(Ag/Pd) despite the same oxygen partial pressure during sintering. Also in electrical experiments different behavior of these two samples was found (e.g. Sec. 4.2 and 4.3)

5.5 ^{18}O Tracer Diffusion in PZT Under Applied Field

Another opportunity for obtaining further information on the near-surface diffusion properties is the investigation of oxygen tracer migration under applied field. To get a homogeneous distribution and incorporation of oxygen over the whole electrode area, LSC electrodes were chosen due to their excellent mixed electronic/ionic conductivity and oxygen exchange properties [182]. A field of about 130 V/mm was applied to the samples (4 h) as illustrated in Fig. 3.1 (c). The field is still quite low compared to the fields used during poling or operation of a piezoelectric compound [5].
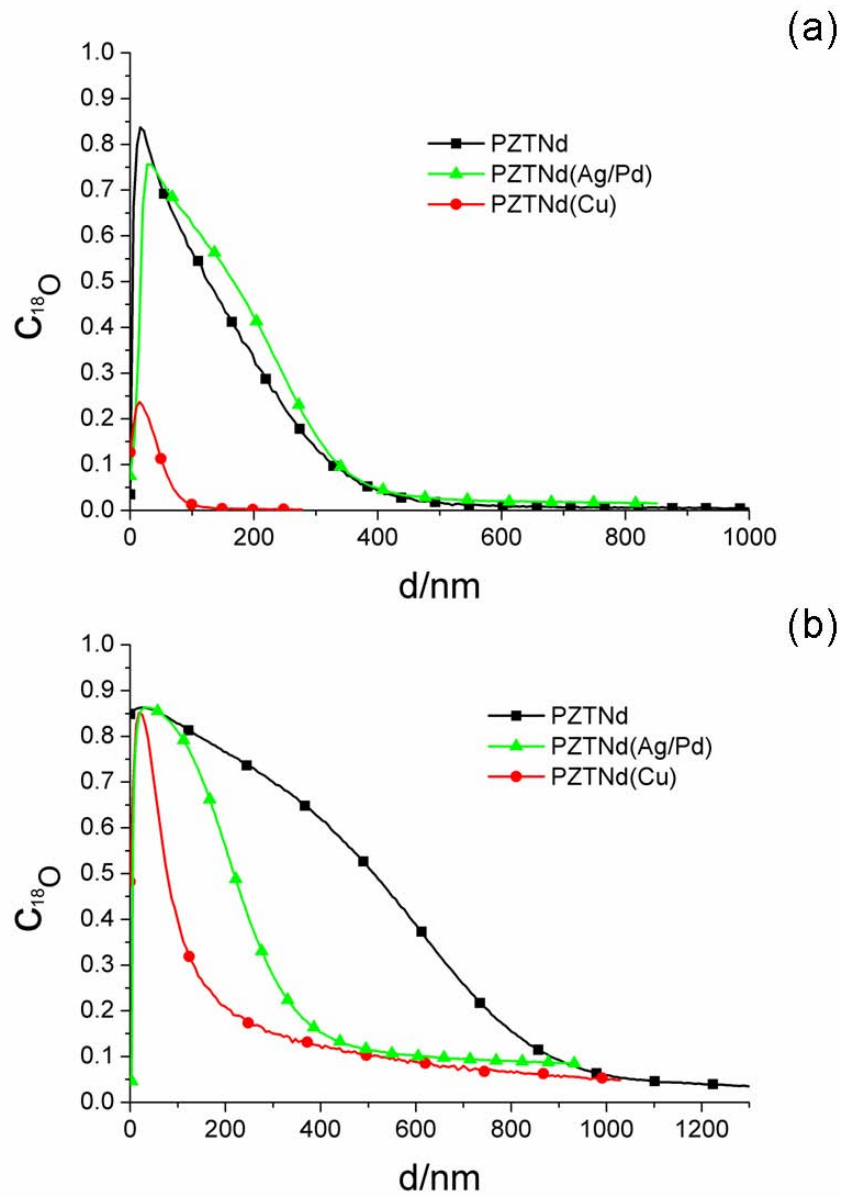
Fig. 5.15: Tracer diffusion profiles for Nd doped PZT from different sources annealed in $^{18}O_2$ (4 h) at (a) 500°C, (b) 600°C (one symbol every 20 data points).
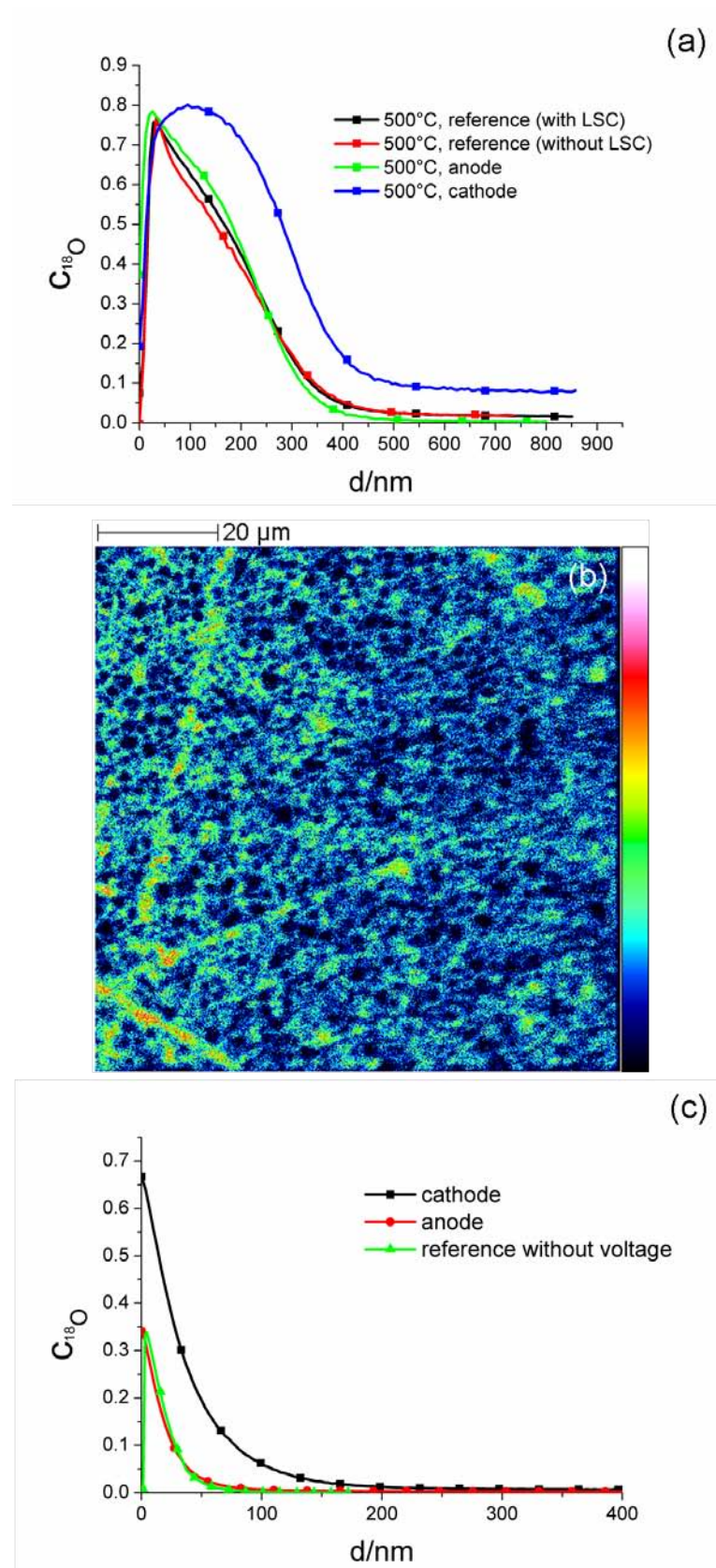
Fig. 5.16: (a) Tracer diffusion profiles in PZTNd(Ag/Pd) after annealing in $^{18}O_2$ for 4 h at 500°C in a field of 130 V/mm and reference samples. b) Cumulative ^{18}O image of the cathode area of the same PZTNd(Ag/Pd) in a depth of 500 to 700 nm. c) Tracer diffusion profiles in PZTNd(Ag/Pd) after annealing in $^{18}O_2$ for 4 h 400°C under a field of 130 V/mm and reference samples (one symbol every 20 data points).

At 500°C (Fig. 5.16 (a)) the oxygen tracer profiles of a reference sample of PZTNd(Ag/Pd) with and without LSC electrode on the surface resemble each other; so it can be assumed that the LSC does not significantly influence the incorporation of the tracer into the PZT. For incorporation under field, the tracer enriched zone is broadened at the cathode compared to the reference profiles and it can be seen that a diffusion tail extends deeply into the sample which can be attributed to grain boundary migration. The latter is concluded from Fig. 5.16 (b), which is a cumulative image of the ^{18}O intensity in a depth from 500 nm to 700 nm. The grain structure is clearly visible by the high intensity of the ^{18}O in the grain boundary regions. At 400°C similar results could be obtained for a PZTNd(Ag/Pd) sample (Fig. 5.16 (c)). However, in that case no grain boundary migration could be observed. Interestingly, the application of voltage does not affect the profiles at the anode.
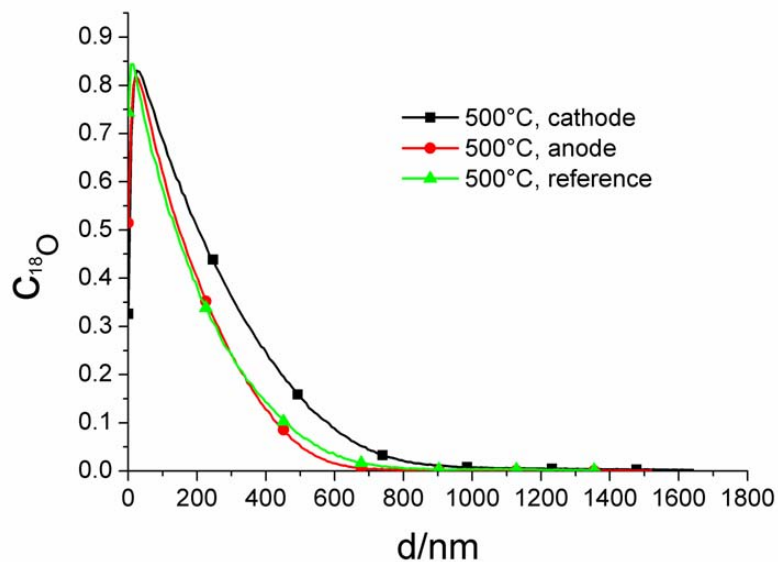
Fig. 5.17: Tracer diffusion profiles in PZTNd after annealing in ^{18}O$_2$ for 4 h at 500°C in a field of 130V/mm and reference sample (one symbol every 20 data points).

The results for tracer experiments on PZTNd (Fig. 5.17) are also similar even though in this case the impact of the field is much lower at 500°C than for PZTNd(Ag/Pd). Interestingly, the PZTNd is more stable in the DC measurements, as well (Sec. 4.3) and there might be a strong correlation between stability under applied voltage and oxygen diffusion. In Fig. 5.18 it can be seen that the conductivity of the PZTNd at 500°C stays even lower than the conductivity value for the experiment on PZTNd(Ag/Pd) at 400°C.

The enhanced ^{18}O concentration in the profile at 400°C can be integrated and substracted from the concentration in the reference sample. Assuming a lattice constant of 4 Å [193] the particle concentration of oxygen is $4.7 \cdot 10^{22}$/cm^3. With the knowledge of the sample dimensions the amount of oxygen tracer ions additionally incorporated due to the applied field can thus be evaluated. From the current recorded during the tracer experiment also the total charge can be calculated and compared to the charge necessary to incorporate the additional oxygen tracer ions. As a result, already 0.8% of the total current would lead to the observed tracer concentration at 400°C if a simple oxygen migration model is assumed. This is an upper estimate of the ionic transference number since enhanced tracer diffusion due to modified vacancy concentrations could further contribute to the larger tracer amount in case of applied field. This would mean that the electronic conductivity is dominant in PZT at 400°C. However, it still does not exclude the possibility that oxygen ions contribute to degradation mechanisms. Moreover this estimation is not possible at 500°C since additional grain boundary diffusion does not allow a simple quantification of the ^{18}O in the corresponding sample (Fig. 5.16 (a)). Especially this enhancement of oxygen migration at 500°C in the grain boundaries is remarkable but still to be understood.

5.6 Mechanistic Interpretation of ^{18}O Tracer Surface Diffusion Profiles

These measurements thus revealed several characteristic results that have to be explained by a model: i) The near-surface region exhibits a different oxygen diffusion coefficient and thus a different vacancy concentration than the bulk. ii) Depending on the temperature, diffusion in this region is faster (typically up to 600°C) or slower (typically 650°C) than the bulk. iii) Etching as well as pre-annealing changes the diffusion properties of this region. iv) Cation diffusion coupled with oxygen vacancy diffusion as well as dislocations can be excluded as origin of this effect. v) An electric field modified the diffusion behavior at the cathode but not at the anode. iv) The sintering procedure strongly affects the profiles. In the following, we show that the assumption of a near-surface space charge layer of varying vacancy concentration might explain these features. In general, space charges at surfaces and grain boundaries lead to spatially varying defect concentrations inside the material to counter balance the effect of an interface charge. The results will be discussed according to the MOTT-SCHOTTKY or GOUY-CHAPMANN
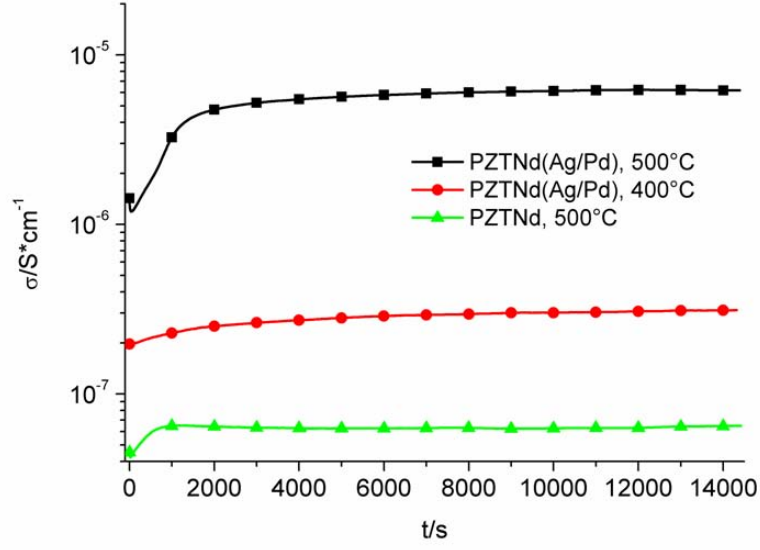
Fig. 5.18: Conductivity variations of PZTNd(Ag/Pd) and PZTNd with LSC electrodes during ^{18}O tracer diffusion experiments with an applied field of 130 V/mm (one symbol every 1000 data points).

case (see Sec. 2.1.4). The tracer diffusion coefficient D depends on the vacancy diffusion coefficient D_v according to [1]:

$$D(x) = D_v f_D c_v(x) \tag{5.1}$$

where f_D is the correlation factor and $c_v(x)$ is the oxygen vacancy concentration depending on the space charge. The spatially varying diffusion coefficient diffusion coefficient can thus be expressed by:

$$D(x) = D \frac{c_v(x)}{c_{v\infty}} \tag{5.2}$$

with the relative vacancy concentration from Eq. 2.8 and 2.10, respectively and the bulk tracer diffusion coefficient D. Accordingly, three fit parameters result, namely D , $\Delta\varphi_0$ and λ (or λ^*). A fourth fit parameter, k, represents the incorporation factor of oxygen from the atmosphere into the sample according to:

$$k(c_{18_O}(0) - c_{18_O}(\infty)) = -D(x)\frac{\partial c}{\partial x} \tag{5.3}$$

where $c_{18_O}(0)$ and $c_{18_O}(\infty)$ are the time dependent concentrations of the tracer at the surface and the concentration in the bulk after reaching equilibrium respectively. Diffusion from a

constant source is thus assumed. Finite difference and finite element calculations were employed to calculate diffusion profiles according to the MOTT-SCHOTTKY and the GOUY-CHAPMANN case. In Fig. 5.19 (a) the profiles of the experiments on PZTSr/Nb samples at 600°C and lower temperatures and the fit results obtained by numerical calculations are shown. Those calculations were carried out assuming an enrichment of oxygen vacancies towards the surface due to a negatively charged surface and a GOUY-CHAPMAN case. The profiles of tracer experiments conducted at temperatures from 400°C to 600°C can be fitted with calculations considering both the MOTT-SCHOTTKY and the GOUY-CHAPMAN case. However, the profiles of samples annealed in $^{18}O_2$ at 650°C for 4 h could only be fitted with calculations considering the GOUY-CHAPMAN condition. Hence, the focus lies on the GOUY-CHAPMAN calculations in the following and the parameters of the fits are given in Tab. 5.1 for annealing temperatures from 400°C to 650°C.

The enrichment of oxygen vacancies at temperatures up to 600°C results in the position dependend diffusion coefficients shown in Fig. 5.19 (b). The tracer diffusion profiles resulting at 650°C for different pre-annealing times (Fig. 5.19 (c)), however, can not be fitted with a calculation considering a negatively charged surface. In this case the latter has to be positively charged, causing a lower tracer diffusion coefficient close to the surface than in the bulk region (Fig. 5.19 (b)). Obviously, the change in surface charge takes place in a rather small temperature range and has to be relatively fast (faster than 1 h) according to the profile in Fig. 5.13.

Tab. 5.1: Fit parameters according to finite element calculations for diffusion experiments on PZTSr/Nb for 4h. (* pre-annealed for 17 h)

	$\Delta\varphi_0$ /V	λ /nm	k /cm $\cdot$ s^{-1}	D /cm$^2 \cdot$ s^{-1}
400°C	-0.13	200	$8.0 \cdot 10^{-11}$	$1.8 \cdot 10^{-17}$
500°C	-0.25	200	$1.8 \cdot 10^{-9}$	$2.5 \cdot 10^{-16}$
600°C	-0.35	180	$1.0 \cdot 10^{-8}$	$1.0 \cdot 10^{-15}$
650°C	0.13	350	$2.0 \cdot 10^{-8}$	$3.9 \cdot 10^{-13}$
650°C*	0.12	300	$1.5 \cdot 10^{-8}$	$2.0 \cdot 10^{-13}$

It should be emphasized that the fit included time consuming numerical finite element calculations of the profile and hence are more reasonable estimates than exact parameters from a non-linear least square minimization. The value for the bulk diffusion coefficient D for experiments conducted at 650°C and a pre-annealing time of 17 h is $2.0 \cdot 10^{-13}$cm^2/s. As expected
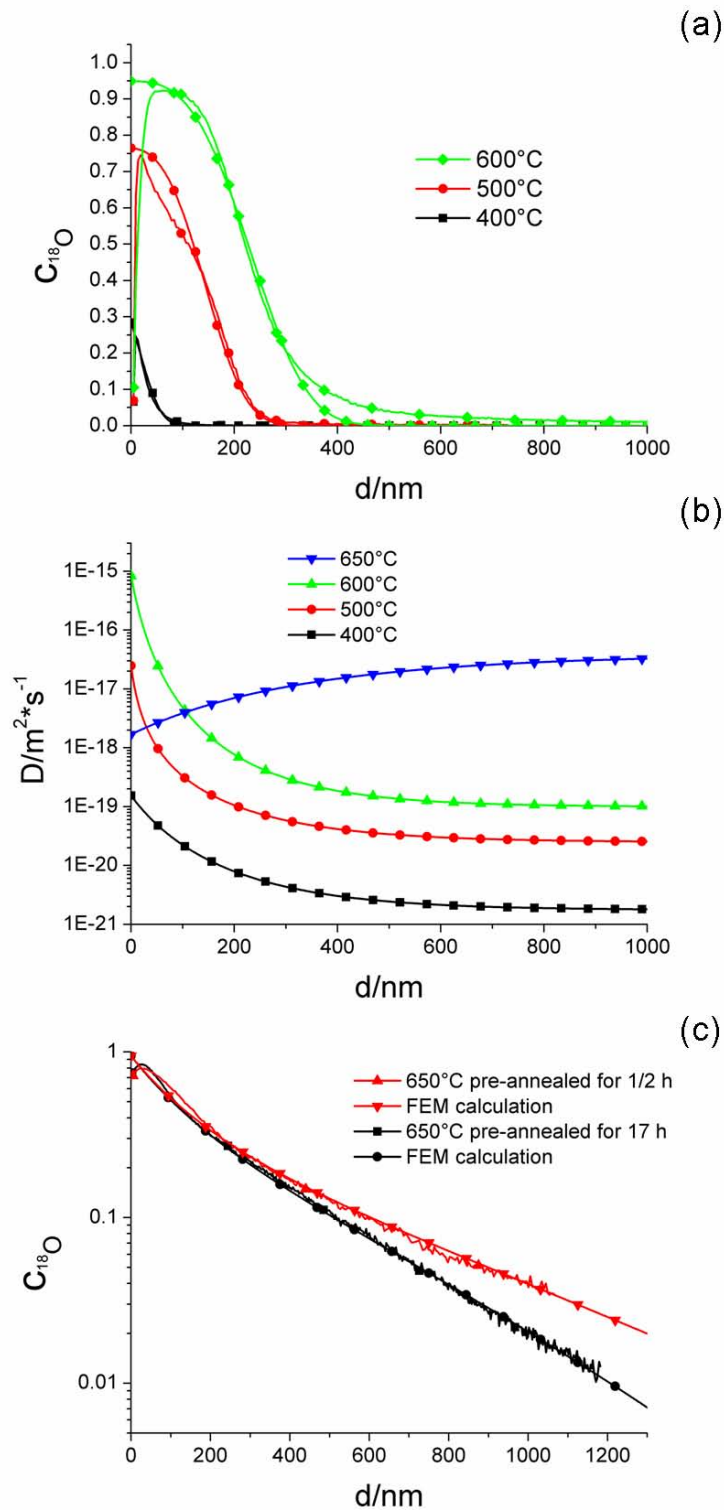
Fig. 5.19: (a) Tracer diffusion profiles of single grains for PZTNdSr/Nb (large grains) with different annealing temperatures in $^{18}O_2$ (4 h) and corresponding Mott-Schottky fits from finite differences calculation (b) Calclulated position dependent diffusion coefficients for profiles given in Fig. 5.19 (a) and (c) (650°C FEM Gouy-Chapman calculation). (c) Tracer diffusion profiles in single grains for PZTNdSr/Nb (large grains) at 650°C in $^{18}O_2$ (4 h) pre-annealed for 1/2 h or 17 h and corresponding Gouy-Chapman fit from FEM calculation.

from the similar profile shapes in Fig. 5.8, the diffusion coefficient for a shorter pre-annealing time (t_{pre}=1/2 h), $3.9 \cdot 10^{-13}$cm^2/s, is only slightly different. The bulk diffusion coefficients increase with temperature from 400°C to 600°C in a reasonable manner. However, there seems to be a larger step between 600°C and 650°C. This can be attributed to the fit procedure because in the calculations for temperatures up to 600°C the focus lay on the first box-shaped part of the profile and no real bulk diffusion could be observed. This could have led to minor errors for the bulk diffusion coefficient values. Nevertheless, an evaluation of an ARRHENIUS-plot of the diffusion coefficients (not shown) resulted in an activation energy $\Delta H^* = 1.6$ eV, i.e. a realistic value. Space charge potentials of about -200 mV are also reasonable [20, 64, 199]. Only the absolute values of DEBYE lengths seem to be large for a highly doped material and there is an unexpected jump in the DEBYE length at 650°C. Taking the permittivity at 500°C of $1.7 \cdot 10^{-10}$ F/cm (obtained from impedance spectra on PZTNd(Ag/Pd) and PZTSr/Nb) the bulk concentration of the majority species causing the GOUY-CHAPMAN space charge can be calculated from Eq. 2.12 and amounts to 0.5 ppm with respect to oxygen sites. This can hardly be the carrier counter-balancing the donor dopant of the order of 1%. Hence, a more complex model has to be assumed.
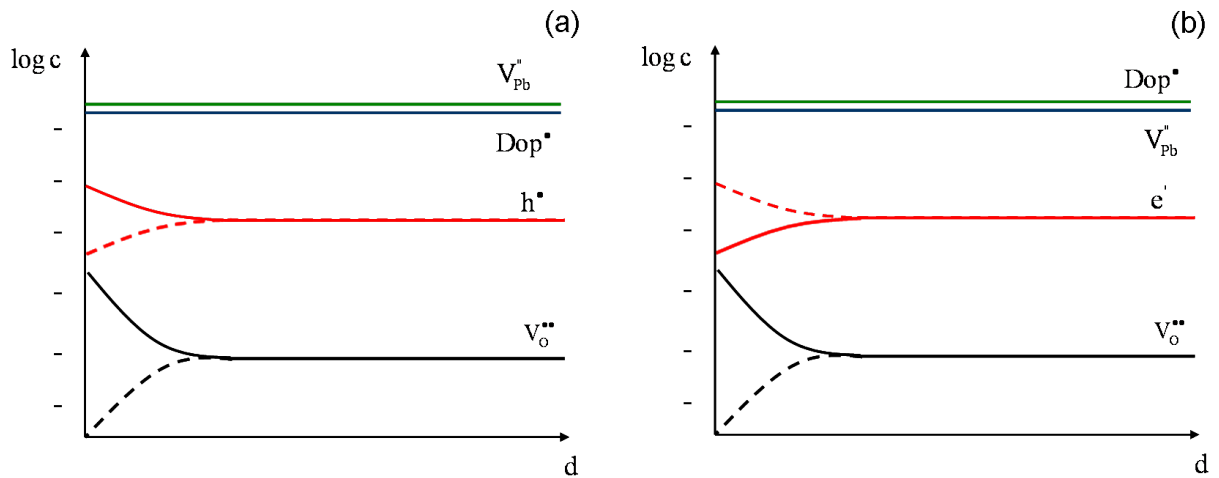
Fig. 5.20: Hypothetical defect chemical relations in donor doped PZT close to the surface (dotted line illustrates modified conditions at and above 650°C) (a) electron compensation (b) hole compensation.

For undoped PZT metal vacancies are created due to the evaporation of PbO during the sintering procedure and these are compensated by holes or oxygen vacancies (see Sec. 2.1.2). The metal vacancies in donor doped PZT, on the other hand, are expected to be mainly compensated by the dopant and the concentration of dopants as well as metal vacancies can be assumed to be frozen-

in at temperatures below 600°C. Hence, they stay constant in the space charge. However, in a first possible scenario it can be assumed that a small amount of metal vacancies is compensated by holes and those are mobile and can be enriched in the space charge. The corresponding negative space charge is quite common in donor doped materials [185, 200]. In such a case the relevant concentration of immobile charge carriers is not the one of metal vacancies but the difference between donor dopant and cation vacancies, i.e. the cation vacancies, which are not ionically compensated. This small amount can easily be of the order of ppm or even lower. An illustration of such a situation is given in Fig. 5.20 (a). As a response to that the concentration of the oxygen vacancies as a minority charge carrier with a bulk concentration even below that of holes increases in the space charge, as well. Hence, indeed a GOUY-CHAPMAN situation with enhanced oxygen vacancy concentration results.

This model would also be valid if the oxygen vacancy concentration is higher than the hole concentration. The above calculated defect concentration then directly represents the oxygen vacancy concentration in the bulk. In that case, a doubly charged carrier compensating the counter defect has to be taken into account according to Eq. 2.9. This leads to a larger DEBYE lengths in the numerical calculations for obtaining the same box thicknesses as in calculations with a defect carrying only one charge. However, for higher temperatures around 650°C, where holes and oxygen vacancies would be depleted, a MOTT-SCHOTTKY case results according to Fig. 5.20 (a). Though, a fit using the MOTT-SCHOTTKY model has not been accomplished for profiles resulting at that temperature. A GOUY-CHAPMAN-type situation is still possible at 650°C if some lead vacancy mobility is assumed and thus accumulation of these may take place close to the surface.

Another possible scenario for donor doped PZT is illustrated in Fig. 5.20 (b). There, the concentrations of donors and vacancies are basically interchanged thus resulting in an electron compensation. A GOUY-CHAPMAN case would be plausible at 650°C for this model. However, a high conductivity of PZT would be expected for electron compensation. Holes could be easily trapped at metal vacancies but none of the present majority defects is expected to trap the electrons. It is generally assumed that holes and oxygen vacancies are the dominant charge carriers [2, 7, 24] but results indicating deeply trapped electrons have also been found [7]. Nevertheless, no conclusive information has been obtained so far. Hence, it is highly necessary to further determine the defect chemical relations in donor doped PZT before additional conclusions can be drawn with

respect to the above mentioned models. It also remains to be explained how or why the surface charge changes above 600°C. This might be due to the onset of PbO evaporation which could easily alter the surface chemistry without changing the defect concentration inside the entire material due to low lead mobility. The modified surface can lead to a different sign of the surface charge and thus to a change of accumulation and depletion for both, holes and oxygen vacancies. The dependence of the diffusion profile on etching by HCl (Fig. 5.9(c)) is further evidence for a space charge change induced by simply altering the surface properties. However, the large step in diffusion coefficient and DEBYE length calculated for temperatures from 600°C to 650°C is still to be understood.

The diffusion behavior under applied field is still a preliminary result and a further extended study of the influence of voltage application is of high importance. Nevertheless, two hypothetical explanations can be provided based on the presented model. Under a high field, a voltage drop could be expected at the cathode and the space charge potential is increased leading to further enrichment of the holes. As a result, oxygen vacancies are also further accumulated and the space charge width is broadened. However, the properties of the anode region are hardly affected by the applied field. A possible explanation for this could be rather given according to the model in Fig. 5.20 (b). In this case, the space charge layer would also be broadened at the cathode. At the anode the electron concentration would increase, which could lead to a smaller voltage drop in that region leaving the oxygen vacancies unaffected by the field. A second effect how field may alter the near-surface diffusion properties is stoichiometry polarization due to limited kinetics of oxygen incorporation at the cathode and oxygen evolution at the anode. Assuming some asymetry in exchange kinetics under positive or negative voltage, an asymetric change of the space charges and thus of the space dependent tracer diffusion coefficient is also possible. This illustrates again how complex the conditions are. From further experiments on the impact of applied field on the near-surface tracer diffusion more information on the defects involved could be obtained.

What also has to be evaluated is why the sintering procedure of the samples has such a large effect on the tracer diffusion profiles. For the PZTNd(Cu) no box-shaped profile was found (Fig. 5.15). The box-shape of the profiles is diminished in this case. The pre-treatment is likely to have a large impact on the oxygen vacancy concentration, so that the reduced atmosphere strongly influences the PZTNd(Cu) properties. The same could be the reason for the non box-shaped

profiles in previous research. As already mentioned, the samples in Ref. [42] were pre-annealed in air at 723°C. This could have led to a high oxygen vacancy concentration due to PbO evaporation although the samples were Nd doped. Also in this case the first part of the profile was attributed to a space charge layer in which oxygen vacancies are depleted. Additionally, it has been found that the space charge only affects the first few nanometers so that λ can be expected to be very small for these samples. Unfortunately, no fit could be obtained for the PZTNd(Cu) samples as only the first part of the profile in Fig. 5.15 (b) for a sample annealed at 600°C in $^{18}O_2$ can be attributed to the near-surface diffusion. In Fig. 5.21 the grain pattern is clearly visible in the ^{18}O image in a depth from 400 nm to 600 nm for the same sample. This means that the tracer grain boundary diffusion has a high impact on the second part of the depth profile which inhibits fitting by numerical calculations. However, a reduction of λ seems reasonable with higher oxygen vacancy concentration in the bulk in this case, as well. In Eq. 2.12 a higher value of c_∞ would result in a smaller DEBYE length and therefore reduce the extend of the space charge layer.
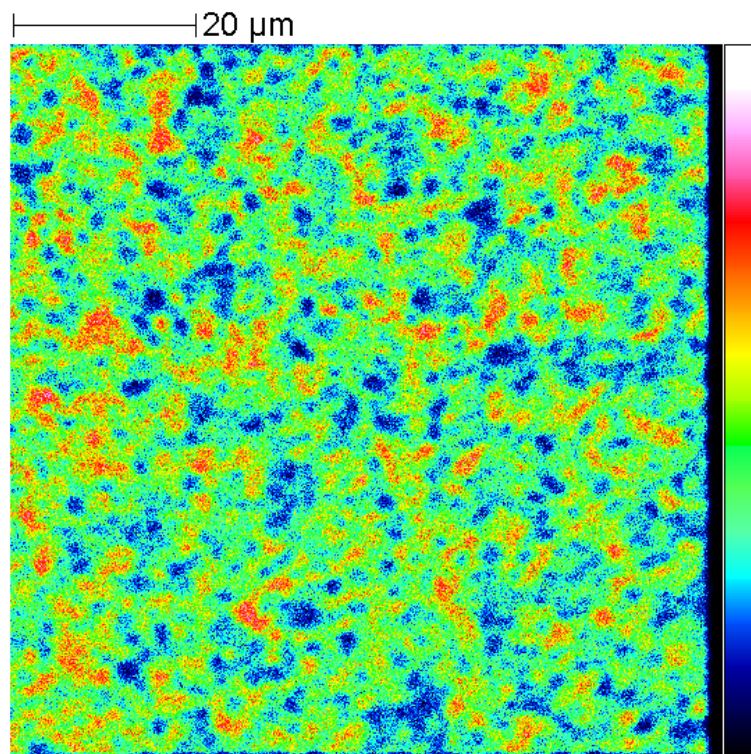
Fig. 5.21: Depth profile image of PZTNd(Cu) annealed in $^{18}O_2$ at 600°C (400 nm to 800 nm).

It has to be further clarified why the near-surface space charge layer becomes vacancy depleted at 650°C while grain boundary diffusion becomes fast at the same temperature. The latter may also

be a space charge effect but different interface states may evolve at surfaces (with presumable PbO evaporation) and at grain boundaries (with possible segregation).

5.7 Evaluation of Surface and Grain Boundary Tracer Diffusion Coefficients for PZTSr/Nb and PZTNd(Ag/Pd)

As it can be seen for the PZTSr/Nb (large grain) samples extended bulk diffusion can only be observed for tracer experiments conducted at 650°C and above (Fig. 5.2). The corresponding plot according to Eq. 2.40 of the integrated concentration for the sample equilibrated in $^{18}O_2$ at 650 °C (Fig. 5.22 (b)) is rather "noisy" even in the region with high ^{18}O concentration. Most probably this is caused by limited statistics due to the large grains. Accordingly, the fewer grains are included in the profile the more pronounced the noise becomes. This is visualized in Fig. 5.22 (c) for the area represented by the white rectangle in Fig. 5.22 (a). As a consequence, a large grained sample is excellent for obtaining valuable cross section images, which clearly visualize and prove that fast grain boundary diffusion had occurred. For a quantitative analysis of integrated profiles, however, a small grained sample is preferable. This is shown for the small grain sample of PZTSr/Nb (Fig. 5.23 (a)) and for PZTNd(Ag/Pd) (Fig. 5.23 (b)). Grain boundary diffusion is less clearly visible in the cross section images (Fig. 5.23 (a) and (b)) but the corresponding integrated profiles are smoother (Fig. 5.23 (c) and (d)). It is worth mentioning that the grain boundary diffusion in the PZTNd(Ag/Pd) becomes visible in the cross section image only at higher temperature (690°C, Fig. 5.23 (b)) compared to 650°C for the PZTSr/Nb samples. At 650°C (not shown) the profile is similar to that of the 600°C PZTSr/Nb sample in Fig. 5.3.

Quantification of the grain boundary coefficient, according to Eq. 2.40, requires the bulk diffusion coefficient. From the measurement within individual grains and fitting with FEM or FD calculations we concluded in Sec. 5.6 that information on the bulk diffusion can be obtained from the profiles of PZTSr/Nb (Fig. 5.19). With the knowledge of the bulk diffusion coefficients the only value missing for the evaluation of the D_{gb} by Eq. 2.40 is the grain boundary thickness δ. Previous research showed a 1-4 nm thick PbO rich secondary phase at the grain boundaries for La doped PZT [201]. We do not have information on whether this is the case for the material investigated in this research. However, regarding results for grain boundary thickness of $SrTiO_3$ without a second phase [65], 2 nm is considered to be a reasonable estimate irrespective of the existence of
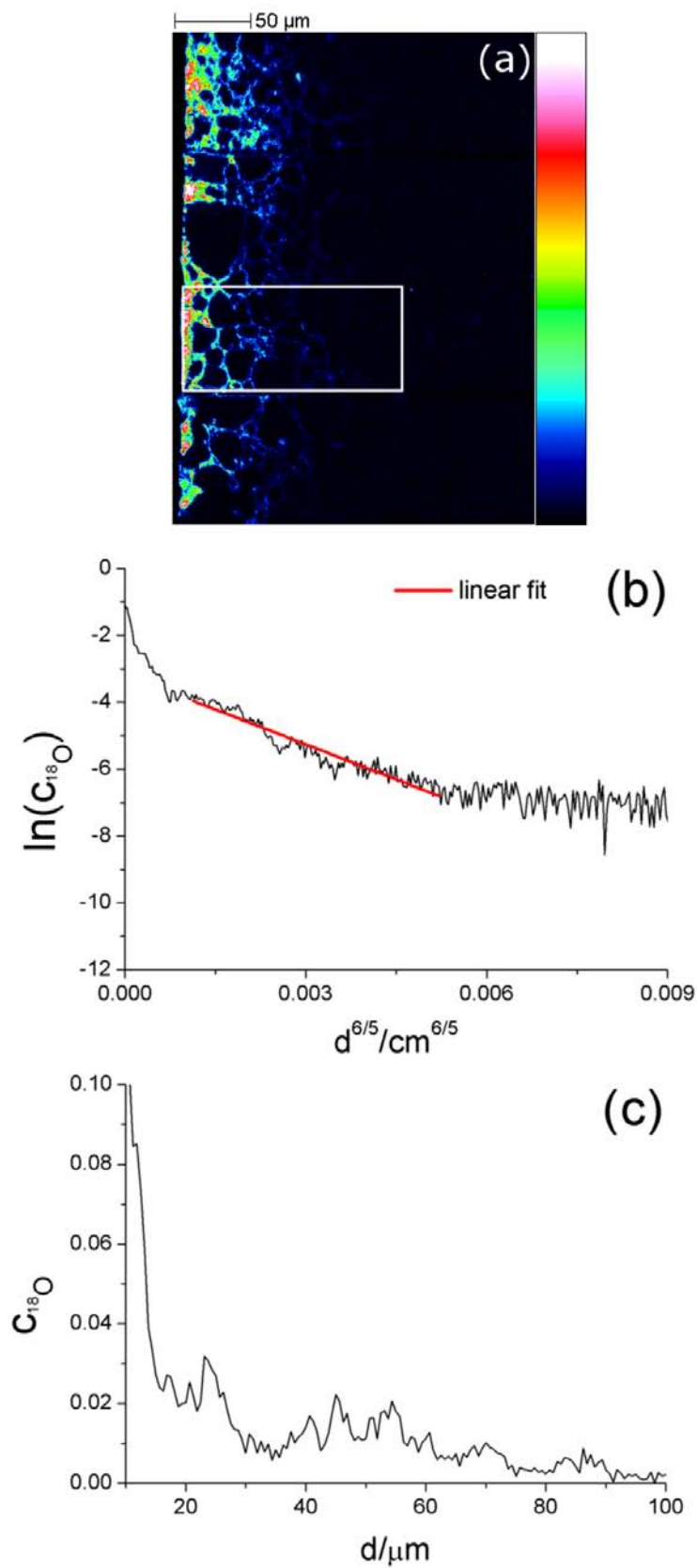
Fig. 5.22: PZTSr/Nb (large grains, 650°C). (a) ^{18}O cross section image. (b) Corresponding integrated ^{18}O concentration profile in a lnc-d$^{6/5}$-plot for grain boundary diffusion coefficient evaluation with a linear fit. c) ^{18}O concentration profile within a smaller area (white box in Fig. 5.22 (a)).
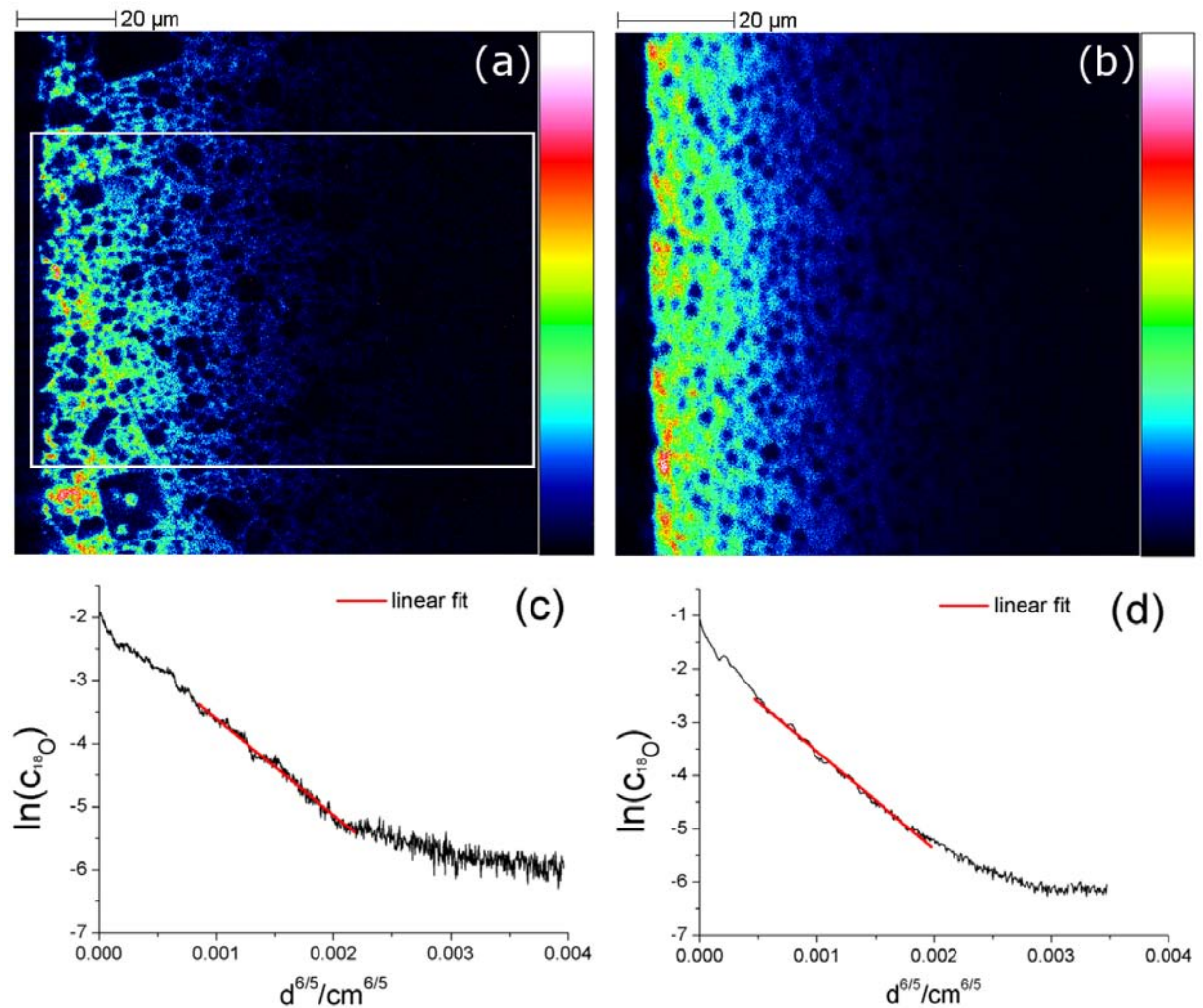
Fig. 5.23: ^{18}O cross section image of (a) PZTSr/Nb (650 °C, 4 h, small grains) and (b) PZTNd(Ag/Pd) (690 °C). (c) ^{18}O concentration profile of PZTSr/Nb (650°C, small grains) with a linear fit; the integration area is given by the white box in Fig. 7a); linear fit in red. (d) ^{18}O concentration profile of PZTNd(Ag/Pd) (690°C) with linear fit; integration area is the entire region in Fig. 5.23 (b).

a secondary phase. Thus, we obtain $D_{gb}(1/2\,h) = 6.2 \cdot 10^{-7} cm^2/s$ at 650°C for the PZTSr/Nb sample ($t_{pre} = 1/2\,h$) with $D(1/2\,h)$ and the slope in Fig. 5.23 (b). For the PZTSr/Nb small grain PZT ($t_{pre} = 17\,h$) the grain boundary diffusion coefficient $D_{gb}(17\,h) = 1.7 \cdot 10^{-7} cm^2/s$ results assuming that the bulk diffusion coefficient $D(17\,h)$ of the large grain sample also applies to smaller grains; profiles within single grains could not be measured for small grain samples. Despite some uncertainties (e.g. the difficulties to approach the true bulk region in a single grain) this data clearly shows that grain boundary diffusion coefficients are about five to six orders of magnitude higher than the bulk diffusion coefficients (Tab. 5.2). This also suggests that PZTSr/Nb has a significant oxide ion conductivity above 600°C. The question arises, how

Tab. 5.2: Calculated bulk and grain boundary diffusion coefficients for PZT at 650°C.(* obtained from large grain sample)

	t_{pre} /h	D /$cm^2 \cdot s^{-1}$	D_{gb} /$cm^2 \cdot s^{-1}$	^2D /$cm^2 \cdot s^{-1}$	$^2D_{gb}$ /$cm^2 \cdot s^{-1}$
PZTSr/Nb (small grains)	17 h	$2.0 \cdot 10^{-13*}$	$1.7 \cdot 10^{-7}$	$3.5 \cdot 10^{-14}$	$5.1 \cdot 10^{-8}$
PZTSr/Nb (large grains)	1/2 h	$3.9 \cdot 10^{-13}$	$6.2 \cdot 10^{-7}$	$2.1 \cdot 10^{-14}$	$1.4 \cdot 10^{-7}$
PZTNd(Ag/Pd)	1/2 h	-	-	$2.4 \cdot 10^{-14}$	$2.7 \cdot 10^{-8}$

large the impact of this oxygen conductivity on the total conductivity might be. The ionic conductivity (either of bulk or grain boundaries) can be calculated from a tracer diffusion coefficient and the NERNST-EINSTEIN equation Eq. 2.19:

$$\sigma = \frac{c_O \cdot q^2}{f_D k_B T} D \qquad (5.4)$$

The correlation factor f_D is usually about 0.69 for a perovskite-type material [202] and the particle concentration c_O was calculated with the lattice constant 4 Å [193]. Both are also assumed to be valid inside the grain boundary. The effective ionic conductivity σ_{eff} includes the contribution of the bulk σ_b and that of the effective grain boundary conductivity $\sigma_{eff,gb}$:

$$\sigma_{eff} = \sigma_b + \sigma_{eff,gb}. \qquad (5.5)$$

Effective conductivities denote conductivity values obtained from a normalization of the resistance to the total sample geometry. The effective grain boundary conductivity can be evaluated from the local grain boundary conductivity σ_{gb} according to:

$$\sigma_{\text{eff,gb}} = \frac{A_{\text{gb}}}{A_{\text{total}}} \sigma_{\text{gb}} \tag{5.6}$$

with A_{gb} and A_{total} denoting the grain boundary area and the total area perpendicular to the flux. With the approximation of a network of cubic grains (brick layer model) and the grain size L_d [203, 204]

$$\frac{A_{\text{gb}}}{A_{\text{total}}} = \frac{2}{L_d}\delta = \lambda_t \delta \tag{5.7}$$

where λ_t is the so called grain boundary trace. Hence, for the calculation of $\sigma_{\text{eff,gb}}$ the equation

$$\sigma = \frac{c_O \cdot 4e^2}{f_D k_B T} \frac{2}{L_d} \delta D_{\text{gb}} \tag{5.8}$$

can be used. δD_{gb} is directly accessible from our experiments, so that no estimation of δ is necessary. Values of the bulk ionic and the effective grain boundary conductivity can be found in Tab. 5.3. It shows that at 650°C the bulk ionic conductivity is of the order of 10^{-7} S/cm and thus also in terms of ionic conductivity grain boundaries dominate by more than two orders of magnitude. The bulk contribution to the effective ionic conductivity is therefore negligible. From

Tab. 5.3: Values of ionic bulk, effective ionic grain boundary and total conductivity for PZT at 650 °C. (* obtained from large grain sample)

	t_{pre} /h	σ_b /S·cm^{-1}	$\sigma_{\text{eff,gb}}$ /S·cm^{-1}	$^2\sigma_b$ /S·cm^{-1}	$^2\sigma_{\text{eff,gb}}$ /S·cm^{-1}	σ_{exp}
PZTSr/Nb (small grains)	17 h	$1.0 \cdot 10^{-7*}$	$4.2 \cdot 10^{-5}$	$1.9 \cdot 10^{-8}$	$1.8 \cdot 10^{-5}$	$2.8 \cdot 10^{-5}$
PZTSr/Nb (large grains)	1/2 h	$2.0 \cdot 10^{-7}$	$8.7 \cdot 10^{-5}$	$1.1 \cdot 10^{-8}$	$2.0 \cdot 10^{-5}$	$4.3 \cdot 10^{-5}$
PZTNd(Ag/Pd)	1/2 h	-	-	$1.2 \cdot 10^{-8}$	$1.5 \cdot 10^{-5}$	$2.6 \cdot 10^{-5}$

the results of impedance measurements of PZT at 650 °C (Fig. 5.24) the experimental effective conductivity can be calculated. For the PZTSr/Nb large grain sample $\sigma_{\text{exp}} = 2.8 \cdot 10^{-5}$ S/cm results, which is rather close to $\sigma_{\text{eff,gb}} = 4.3 \cdot 10^{-5}$ S/cm and therefore also to σ_{eff}. The same agreement is also found for the other samples (Tab. 2). This means that ionic conductivities determined from the oxygen tracer experiments and total conductivities obtained by electrical measurements are very similar, and ionic grain boundary conduction contributes significantly to the total conductivity. However, the accuracy of the data analysis is not high enough to conclude that our PZT samples are predominantly ion conducting. This result also suggests that effective

ion conduction is strongly thermally activated since the upper estimate of the ionic transference number at 400°C of about 1% (Sec. 5.6) is definitely much smaller.

The effective ion conduction is probably caused by the onset of grain boundary diffusion above 600°C since the estimated bulk ionic conductivity is still much smaller than the total one also at 650°C. The conductivity obtained by impedance measurements shows a small time dependency,
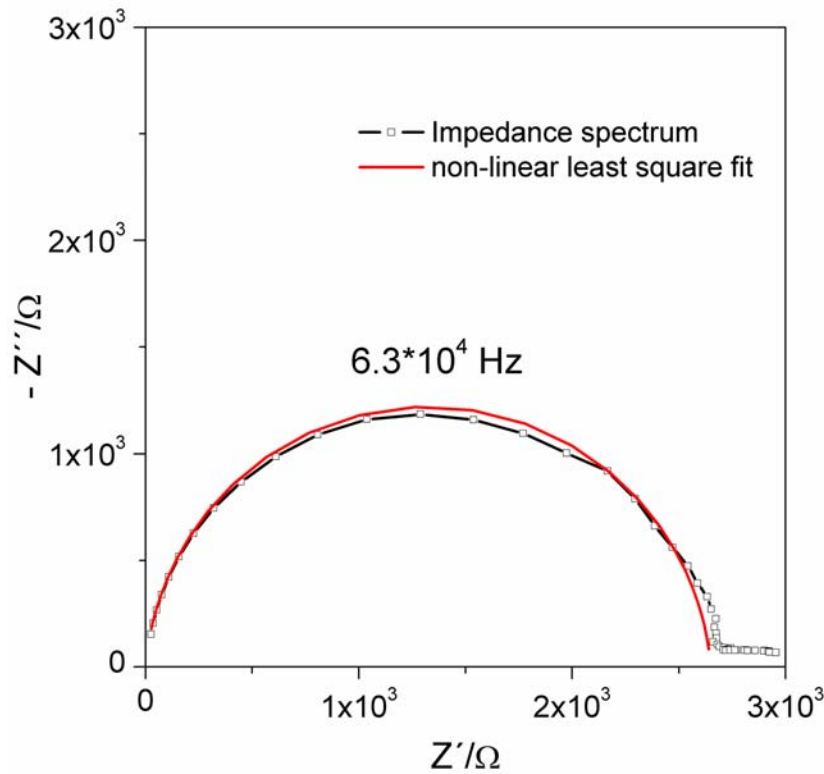
Fig. 5.24: Impedance spectrum of PZTSr/Nb (large grain, measured at 650 °C).

which may reflect defect chemical changes with time. However, in the time frame considered here changes are of the order of a factor two and do not affect our conclusion that a part of the total effective conductivity at 650°C can be attributed to ionic grain boundary transport. To further validate the presented results, another approach introduced by Fielitz et al. [203] was used to determine bulk diffusion coefficients ^2D. Here not only the grain boundary coefficient $^2D_{gb}$ but also ^2D is calculated from the linear tail of a lnc-$d^{6/5}$ plot. When this tail (the linear fit function in Fig. 5.22 (b), 5.23 (c) or (d)) is extrapolated to d = 0, the grain boundary related ^{18}O concentration close to the surface c^0_{gb} is obtained (Tab. 3) and ^2D can be determined from

$$c_{gb}^0 = 0.9 \cdot c_{gas} 2\lambda_t \sqrt{^2Dt} \tag{5.9}$$

where c_{gas} is the gas phase concentration of $^{18}O_2$. It is expected that grain boundary diffusion has a higher impact on the profiles of samples with small grains. Indeed, the highest value of c_{gb}^0 is obtained for the PZTNd(Ag/Pd) sample and the lowest for the PZTSr/Nb with large grains. A major advantage of this method is that it also works for small grain samples and ^2D of the

Tab. 5.4: Relative surface ^{18}O grain boundary concentrations for tracer experiments at 650°C (4 h).

	t_{pre} /h	c_{gb}^0
PZTSr/Nb (small grains)	17 h	0.13
PZTSr/Nb (large grains)	1/2 h	0.04
PZTNd(Ag/Pd)	1/2 h	0.18

PZTNd(Ag/Pd) can also be calculated. The values given in Tab. 5.2 are one order of magnitude lower than the corresponding D values calculated from the depth profiles within single grains but this is still within errors expected for these first data on oxygen diffusion in donor doped PZT. Owing to the square root in Eq. 2.40, the grain boundary diffusion coefficient $^2D_{gb}$ and thus also the effective ionic grain boundary conductivity $^2\sigma_{eff,gb}$ is only moderately affected and this alternative analysis does not alter any conclusion drawn so far. The effective ionic grain boundary conductivity is still of the same order of magnitude as σ_{exp}. According to Fielitz et al. [203] it is also possible to check whether the assumption of type B kinetics is reasonable:

$$36 \cdot \frac{\delta}{L_d} \leq \frac{c_{gb}^0}{c_{gas}} \leq 0.36 \tag{5.10}$$

has to be fulfilled and this is the case for all examples if $\delta \leq 20$ nm . Therefore, the hypothesized type B diffusion kinetics is most likely correct. However, the ratio of $\frac{c_{gb}^0}{c_{gas}} \approx c_{gb}^0$ should also be in a range from 0.02 to 0.1 to have sufficient dynamic range for the evaluation of $^2D_{gb}$ and ^2D at the same time. This applies well for the large grain PZTSr/Nb but the small grain samples are out of that range (Tab. 5.4), which might have led to a decrease in accuracy of these results.

Finally, some remarks are given on the mechanism possibly causing the strongly enhanced grain boundary tracer diffusion or conductivity. Grain boundaries in ionic materials include a core

region, which is structurally different from the bulk and adjacent space charge zones [63]. Both might contribute to fast ion conduction: the core by increased mobility and/or concentration of vacancies and the space charge layer by an increased concentration. In acceptor doped materials, space charge zones often exhibit a depletion of positive charge carriers and grain boundaries become blocking for oxygen vacancies [11, 13, 15]. In such a case the space charge even inhibits "leakage" of ^{18}O from a presumably fast grain boundary core into the bulk. A simple type B analysis according to Eq. 2.40 could then lead to false diffusivities [81]. In a donor doped $BaTiO_3$, however, negative charge carriers are often depleted in space charge zones [22, 62]. This would mean that positive charge carriers and thus also oxygen vacancies are accumulated in the space charge and may enhance the local tracer diffusion coefficient. Hence, fast ion transport along the space charges of grain boundaries would not be surprising in donor doped BT (Sec. 6.1) and also in donor doped PZT. However, Eq. 2.40 does not include the ^{18}O in the fast diffusing zone but only the amount of ^{18}O diffusing into the adjacent bulk, while any fast space charge along grain boundaries would definitely contribute to our integrated profiles. Thus, in case of a fast space charge layer the analysis should be further modified.
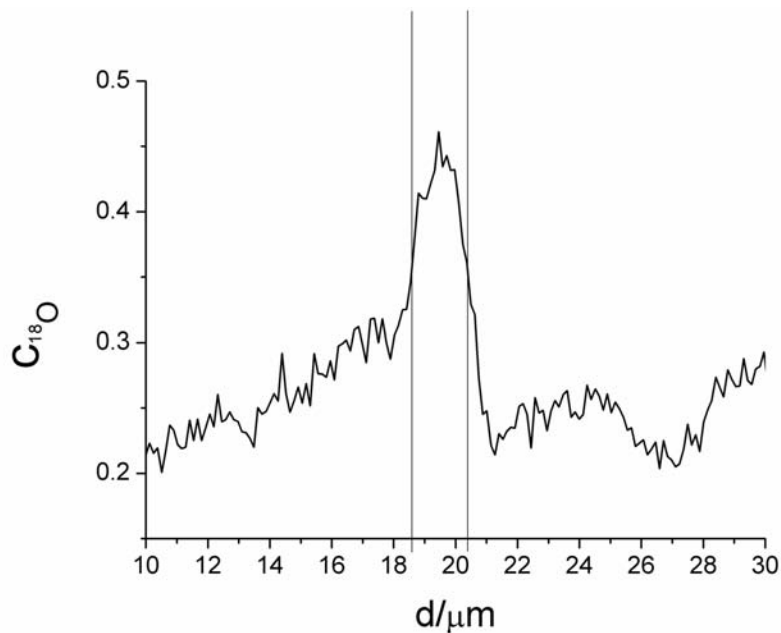
Fig. 5.25: Line profile across a single grain boundary in the cumulative image for a PZTSr/Nb sample (large grain, 650 °C) from 780 nm to 890 nm.

From the line profile across a single grain boundary (Fig. 5.25) a diffusion length of approx. 1 μm into each grain can be deduced. This is in good agreement with the diffusion length, which can

be determined at surfaces for 650°C in Fig. 5.19 (c) (see also Tab. 5.1) and thus again evidence for type B diffusion kinetics, either via a fast grain boundary core or via a vacancy enriched space charge zone. What has to be pointed out is that in case of a fast grain boundary core the local grain boundary conductivity σ_{gb}, which can be calculated from Eq. 5.5 and 5.6 with $\delta = 2$ nm, would be in the range of 10^{-1} S/cm. This means that σ_{gb} would be in the same order of magnitude as the value of the bulk conductivity of yttrium stabilized zirconia (YSZ) at 1000°C [205]. The existence of a PbO rich secondary phase with 1-4 nm thickness in the grain boundary core [201] would result in modified parameters like correlation factor f_D and oxygen particle concentration c_O in Eq. 5.8. However, very pronounced changes of the calculated conductivity σ_{gb} are not expected and hence also in this case enormous oxide ion conduction had to be concluded for the core.

5.8 Simulation of Oxygen Tracer Diffusion in Grain Boundary Space Charge Layers

FEM calculations provide the opportunity to test what kind of profiles result if space charge layers exist at the grain boundary. It is particularly interesting if such a space charge layer could resembles the one responsible for the surface box profiles obtained for temperatures up to 600°C. For this reason, calculations with two 20 μm long, 2 μm thick grains and a 2 nm thick grain boundary have been conducted (see illustrated in Fig. 5.26). These calculations were based on the GOUY-CHAPMAN model similar to the ones used to describe box-shaped near-surface profiles in Sec. 5.6. The grain boundary diffusion coefficient $D_{gb} = 1 \cdot 10^{-7}$ cm^2/s was employed and the values for k and D were taken from Tab. 5.1 for the tracer experiment at 650°C. However, the values of λ and $\Delta\varphi_0$ for the 600°C fit were used to obtain the position dependent diffusion coefficient which leads to a box like shape of the profiles. This diffusion coefficient was then attributed to the space charge next to the grain boundary.

In Fig. 5.27 (a) the ln(c)-d$^{6/5}$-plot of a FEM calculation with the above mentioned parameters and 4 h diffusion time is given. From the corresponding linear fit it should therefore be possible to evaluate D_{gb} when a type B diffusion condition according to HARRISON´s classification [70,85] is valid. Test calculations without taking a space charge layer into account were also carried out (not shown). In these tests, the value used in this simulation for D_{gb} inside the core could be calculated from the linear fit in the ln(c)-d$^{6/5}$-plot and Eq. 2.40. Therefore, the FEM model used for the
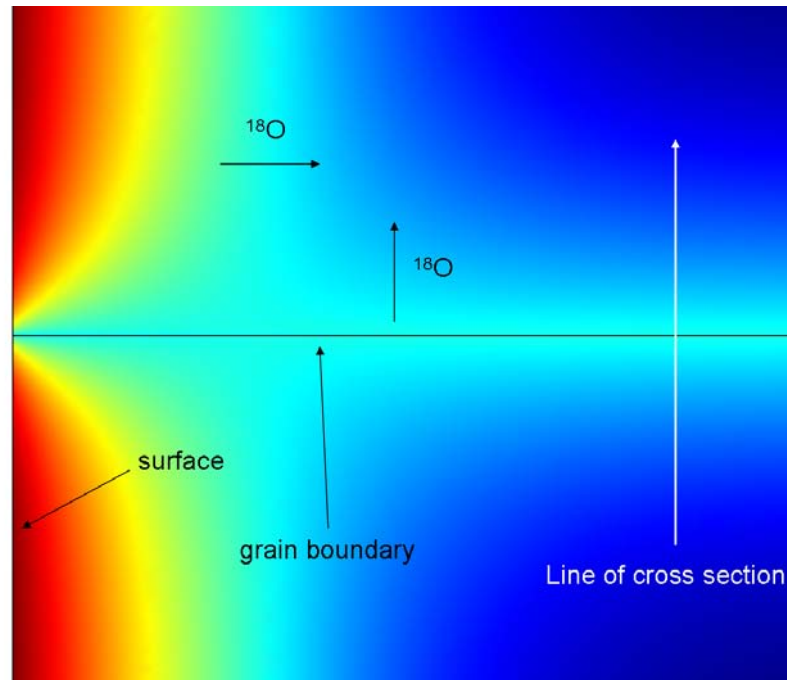
Fig. 5.26: Illustration of a FEM calculation of a type B tracer grain boundary diffusion with two square shaped grains seperated by a 2 nm grain boundary.

simulation is a valid approach to simulate grain boundary diffusion. For the simulation taking a grain boundary space charge layer and a fast grain boundary core into account the value obtained from a $\ln(c)$-$d^{6/5}$-plot is lower than the "real" one. Instead of $D_{gb} = 1 \cdot 10^{-7}$ cm^2/s the value $D_{gb} = 5 \cdot 10^{-8}$ cm^2/s could be evaluated. The slope in the $\ln(c)$-$d^{6/5}$-plot is therefore steeper than it should actually be in the absence of a space charge layer. The increased incorporation of ^{18}O in the space charge layer is the reason for that. In Fig. 5.27 (b) cross section profiles over the grain boundary in two different distances from the surface are given for the calculation with and without space charge layer. The box shape of the profiles can be seen in both space charge layer profiles. The concentration leaking from the grain boundary at 0.5 μm distance into the PZT is higher than for the calculation without the space charge layer. Consequently, this results in a larger concentration gradient in the grain boundary between 0.5 μm and 2.5 μm distance from the surface for the space charge layer calculation. With such a space charge at grain boundaries the assumption of a type B diffusion mechanism is still valid although quantification is inhibited due to the position dependent bulk diffusion coefficient. Nevertheless, it can be seen that the value for D_{gb} obtained from the $\ln(c)$-$d^{6/5}$-plot is still in the order of magnitude of the real value so that the error expecting simple type B diffusion behavior is moderate.
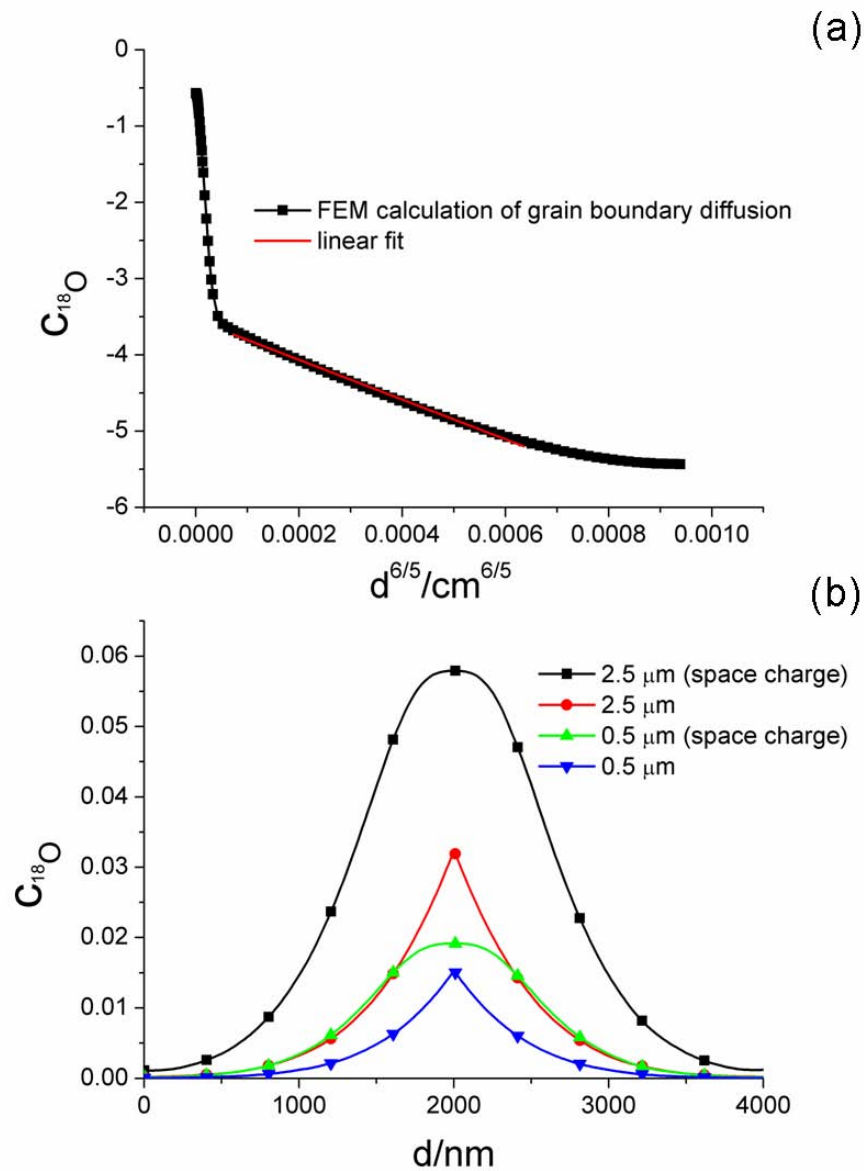
Fig. 5.27: (a) Concentration plot evaluation of grain boundary diffusion coefficient for type B diffusion condition [84]. (b) Cross section concentration profile over the grain boundary as depicted in Fig. 5.26 by the white arrow for 0.5 μm and 2.5 μm distance from the surface of calculations with and without space charge layer.

Although calculations with a depletion layer at the grain boundaries have not been conducted it can be expected that in this case the value for D_{gb} is overestimated [206]. No enhanced tracer concentration could be determined at the grain boundary in calculations with a space charge layer at the grain boundary but without a fast grain boundary core. This basically leads to two possible conclusions considering diffusion mechanisms: 1) If a space charge layer is mainly responsible for fast grain boundary diffusion it has to be different from the one developing at the surface. 2) For a fast grain boundary core and additional space charge layer, similar to the one found for the near-surface region up to 600°C, type B diffusion is still valid. Although, the calculated value for D_{gb} is over- or underestimated depending on the sign of the space charge. Accordingly, the values obtained for D_{gb} from oxygen tracer experiments on PZTSr/Nb and PZTNd(Ag/Pd) at 650°C (Sec. 5.7) should be in the same order of magnitude as the exact value.

5.9 Comparison of Grain Boundary Tracer Diffusion in Different Types of PZT
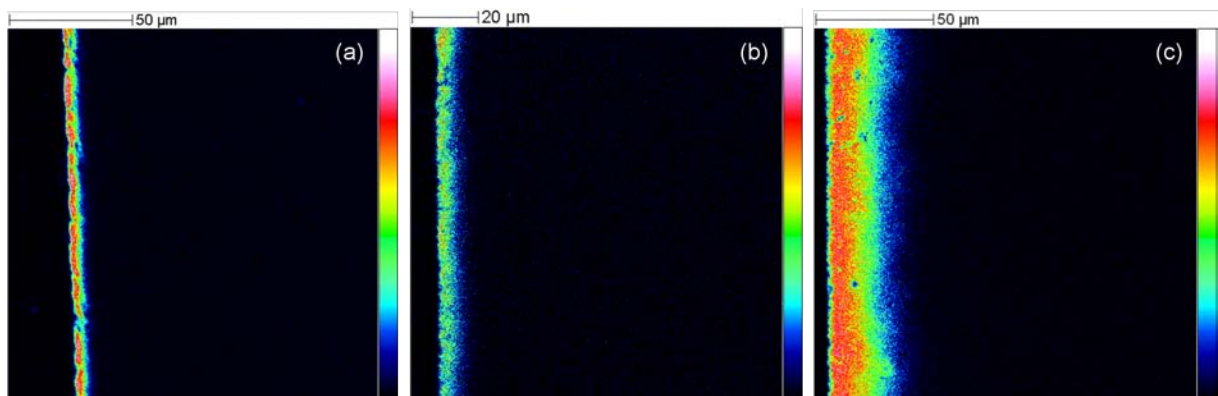
Fig. 5.28: Cross section ^{18}O images from tracer diffusion experiments on PZTNd(Cu) at (a) 750°C; (b) 800°C; (c) 850°C and 4 h annealing time.

The samples showing enhanced grain boundary tracer diffusion at and above 650°C, which have been discussed so far, are samples from actuator stacks with Ag/Pd-inner electrodes and similar pre-treatment. As the near-surface diffusion properties are mainly influenced by the pre-treatment this could be the case for grain boundary diffusion, as well. Therefore, ^{18}O tracer experiments on PZTNd(Cu) and PZTNd have also been conducted for reason of comparison. In Fig. 5.28 the cross section images of the tracer experiments at different temperatures are shown.

It can be clearly seen that even at 800°C (Fig. 5.28 (b)) no extended tracer transport into the depth of the sample occurs. There is just a small line of high intensity indicating that oxygen diffuses less than 10 μm into the sample and no resolution of grain structure can be obtained. This is similar to the results of PZTNd(Ag/Pd) and PZTSr/Nb below 650°C (Fig. 5.3) while PZTNd(Cu) still shows this behavior at 800°C. The profile for the sample annealed in $^{18}O_2$ at
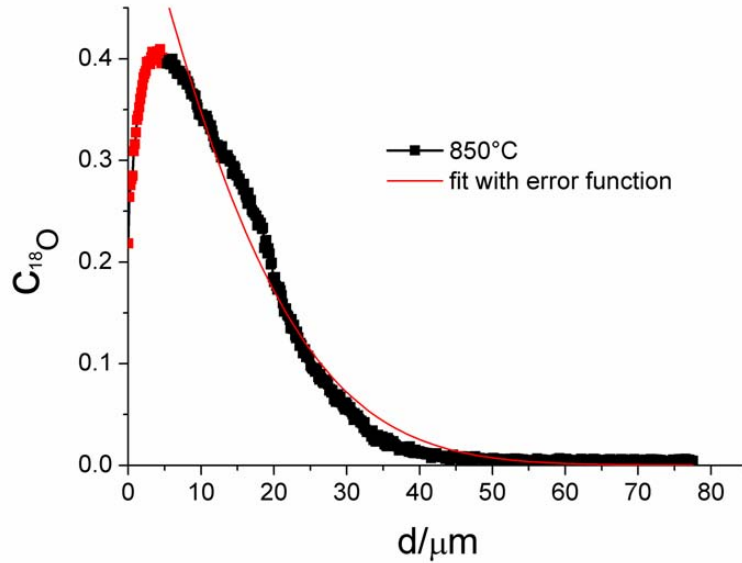
Fig. 5.29: Integrated ^{18}O concentration profile corresponding to Fig. 5.28 (c) of PZTNd(Cu) annealed in $^{18}O_2$ at 850°C annealed for 4 h.

850°C illustrates that the oxygen is transported about 30 μm deep into the material. The ^{18}O concentration profile corresponding to the image given in Fig. 5.28 (c) (Fig. 5.29) does not resemble the grain boundary diffusion profiles obtained for PZTNd(Ag/Pd) or PZTSr/Nb (Fig. 5.22 and 5.23) and it can rather be fitted with an CNLS error function fit regarding diffusion in a semi infinite medium and oxygen surface incorporation from a continious source [79]:

$$c_{^{18}O} = \text{erfc}\left(\frac{x}{2\sqrt{Dt}}\right) - \exp\left(hx + h^2 Dt\right)\text{erfc}\left(\frac{x}{2\sqrt{Dt}} + h\sqrt{Dt}\right) \qquad (5.11)$$

where h=k/D and k is the surface incorporation coefficient according to Eq. 5.3. This gives rise to the assumption that a different diffusion mechanism might explain the profiles of the tracer diffusion experiments on PZTNd(Cu). It basically means that diffusion could be described by type A diffusion mechanism [70] (see Sec. 2.2.5) and the corresponding diffusion coefficient is an effective

diffusion coefficient D_{eff} to which grain boundary and grain bulk diffusion coefficient contribute to. The coefficients resulting from the fit are $D_{eff} = 1.6 \cdot 10^{-10}$ cm^2/s and k $= 1.2 \cdot 10^{-7}$ cm/s. However, from the depth profile image of PZTNd(Cu) annealed in $^{18}O_2$ at 600°C (4 h) it becomes evident that after the first 200 nm grain boundary diffusion is enhanced compared to bulk diffusion because the grain structure with low ^{18}O intensity inside the grains can be clearly identified (Fig. 5.21). In accordance with type A diffusion it is therefore realistic that the small grains are filled with the tracer to a certain degree at 850°C. Although, the grain boundary diffusion could still be faster than bulk diffusion the grain boundary pattern might not be distinguishable by cross section profiling in this case. However, it has to be further investigated what the dominant oxygen diffusion mechanism is and if there are mechanism changes at certain temperatures.

For the PZTNd no extended grain boundary diffusion is visible in the cross section plots even for the sample annealed in $^{18}O_2$ at 850°C. Although also for the PZTNd evidence for grain boundary diffusion could be obtained in depth profile images similar to the one given for PZTNd(Cu) (Fig. 5.21) the diffusion along the grain boundary is obviously slower than for every other PZT material discussed in this thesis.
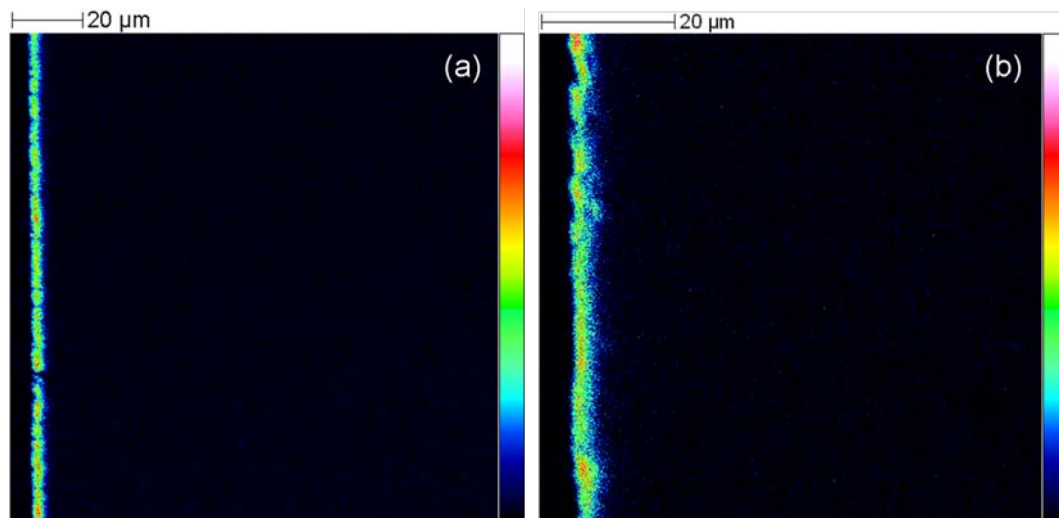
Fig. 5.30: Cross section ^{18}O images from tracer diffusion experiments on PZTNd at (a) 800°C; (b) 850°C annealed for 4 h in $^{18}O_2$.

In Fig. 5.31 (a) it can be seen that diffusion is already very high for undoped PZT samples at 500°C. However, the undoped samples are unfortunately not very dense and prone to developing pores, which could also be sources of ^{18}O if extended porosity is expected. The black areas in Fig. 5.31 (a), for example, represent holes from which ^{18}O could leak into the samples if connected

to ambient atmosphere. Nevertheless, in Fig. 5.31 (b) the concentration profile calculated from the area depicted by the white box in Fig. 5.31 (a) shows a concentration distribution, which could result from a regular diffusion mechanism and the relative concentration in the middle of the sample is already 1%.
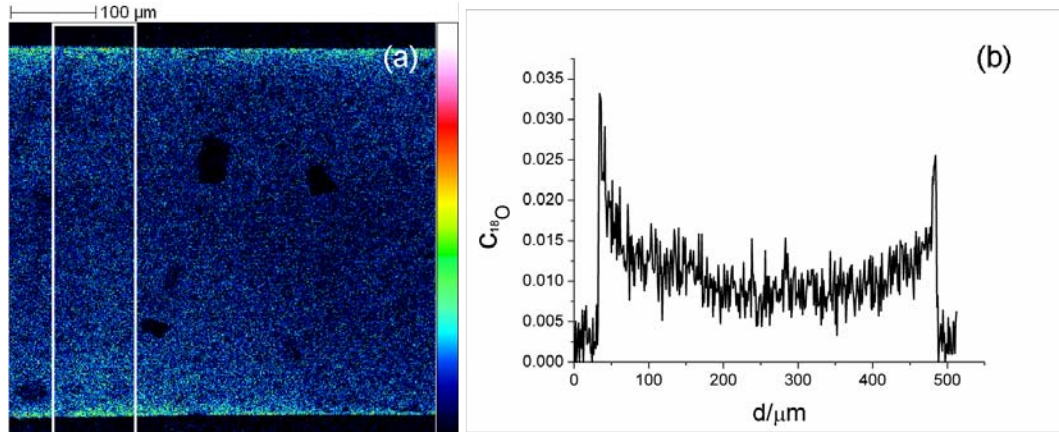
Fig. 5.31: (a) Cross section ^{18}O image from tracer diffusion experiment on undoped PZT at 500°C (4 h) (b) Corresponding plot of relative ^{18}O concentration in the area given by the white rectangle in Fig. 5.31 (a).

From what has been presented so far it can be assumed that the pre-treatment also significantly affects the grain boundary properties. This does not only concern sintering atmosphere but also the electrode choice. Sintering with silver metal electrodes leads to large changes in the electrochemical properties of the PZT material. As it is known from previous research silver is incorporated into the material and could thus act as an additional dopant [46, 47, 112, 113]. The impact on the defect chemistry seems especially high at the grain boundaries as the enhanced grain boundary diffusion in PZTSr/Nb and PZTNd(Ag/Pd) can most likely be attributed to the silver content because the similarly treated PZTNd does not show fast grain boundary diffusion. As Pb and Ag have similar ion radii, Ag is expected replace Pb on the A place of the perovskite crystal structure. In the bulk it would therefore act as an acceptor dopant, which partly or even fully counter-balances the existing donor doping. Hence, the oxygen vacancy concentration would be increased:

$$Ag_2O \rightarrow V_O^{\bullet\bullet} + 2Ag_{Pb}^{'} + O_O^x \Rightarrow Pb_{1-2x}Ag_{2x}(Ti, Zr)O_{3-x}. \tag{5.12}$$
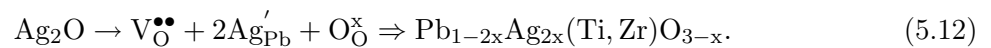
The exact role of silver segregated to grain boundaries is unkown but might also increase the oxygen vacancy concentration therin and therefore cause an enhanced diffusion along this pathway. However, the mechanism of Ag incorporation and transport in PZT still has to be investigated and additional experiments on tracer diffusion properties of the different PZT material are needed to draw further conclusions on the fast diffusion path and the role of Ag in ^{18}O diffusion. Nevertheless, the fact that Ag contributes to oxygen grain boundary diffusion and degradation under high voltage for PZT material is an important outcome of the research presented in this thesis. It can be assumed that there is a correlation between these findings.

In case oxygen transport along grain boundaries contributes to degradation in samples with Ag inner electrodes, it is of great interest whether the oxygen is incorporated into PZT only at the free surface or also via a pathway along the inner electrodes. In the cross section image in Fig. 5.32 it can be seen that no enhanced incorporation of the tracer ion along the inner electrodes occurs. Oxygen is thus not incorporated into the PZT material through the electrodes like it is demonstrated in Sec. 5.5 for oxide electrodes. If degradation is related to oxygen or oxygen vacancy migration mechanisms the properties of the near-surface region could therefore have a large impact.
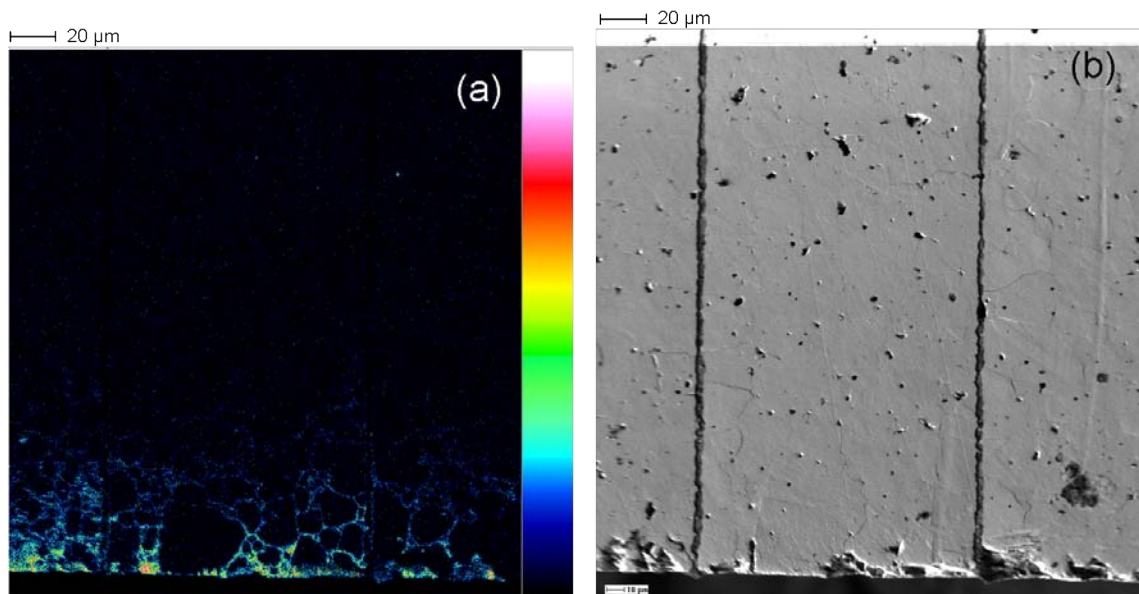
Fig. 5.32: (a) Cross section ^{18}O image from tracer diffusion experiment on PZTSr/Nb with Ag/Pd-inner electrodes at 650°C (4 h) (b) Corresponding SE-image.

5.10 Oxgen Tracer Diffusion Experiments under Applied Field with Surface Electrodes

In order to further investigate the changes in defect chemistry at the surface due an applied field, DC experiments with LSC- and Pt-surface electrodes and simultaneous ^{18}O tracer experiments were carried out according to Fig. 3.1 (d). In Fig. 5.33 ^{18}O images for the experiment on PZTNd(Ag/Pd) at the relatively low temperature of 300°C with 50 V applied for 1 h are given. The intensity inside the LSC at the cathode is obviously higher than at the anode. The
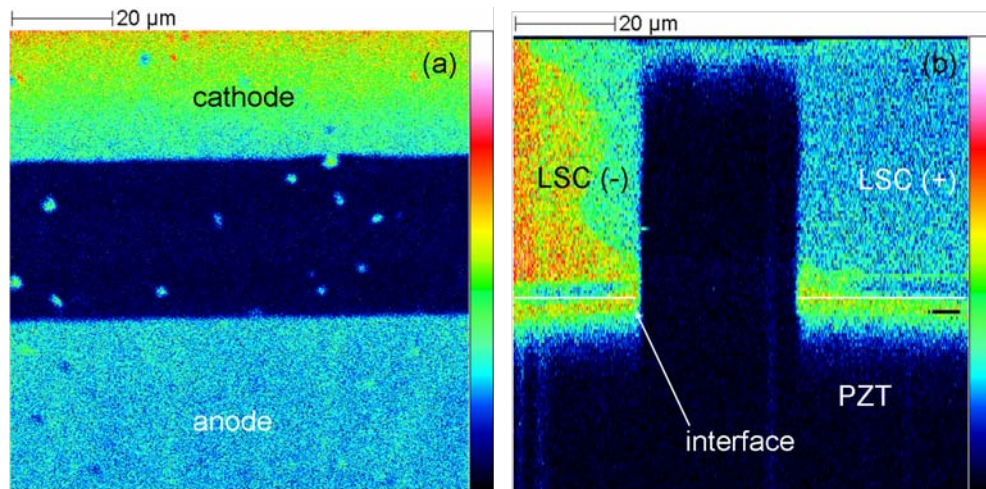
Fig. 5.33: ^{18}O images of tracer experiment on PZTNd(Ag/Pd) with large LSC surface electrodes (300°C, 50 V, 1 h). (a) Culmulative image of depth profile. (b) yz-depiction of depth profile with white line indicating LSC/PZT interface.

middle of the xz-depiction (Fig. 5.33 (b)) represents the free PZT surface between the two LSC electrodes. The LSC/PZT interface is illustrated by the white line and is reached after the LSC layer is removed by the Cs sputter beam. ^{18}O is also incorporated into the anode area of the PZT, which is similar to the bulk voltage experiments in Sec. 5.5. The ^{18}O in the free surface area is homogeneously distributed and no sign of enhanced incorporation of the tracer ion at the cathode can be observed in Fig. 5.33.There are also only minor differences of the relative ^{18}O concentrations in the different areas (Fig. 5.34). However, compared to the reference sample without applied voltage the concentration is increased. Nevertheless, the observable differences in Fig. 5.34 are too preliminary to lead to a conclusion with respect to changes of ^{18}O incorporation due to applied voltage.
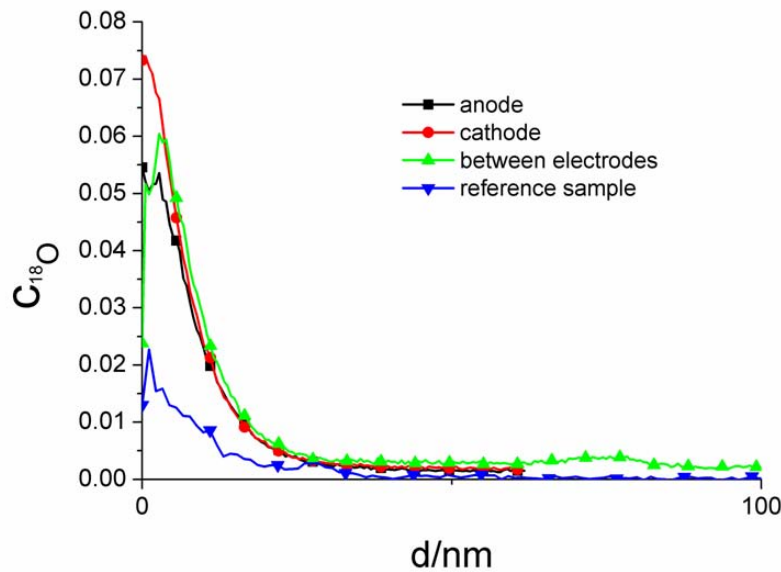
Fig. 5.34: Relative ^{18}O concentration below the cathode, anode and between the electrodes of tracer experiment on PZTNd(Ag/Pd) with large LSC surface electrodes (300°C, 50 V, 1 h) in comparison with a reference sample.

The ^{18}O images of tracer experiment on PZTNd(Ag/Pd) at 400°C with 100 V (4 h) are given in Fig. 5.35. In this case, the SIMS measurement was conducted after removal of the LSC electrodes with a 5% HCl solution. The first dark area in the yz depiction of the depth profile (Fig. 5.35 (b)) results from the Au layer which was deposited on the PZT prior to the measurement to reduce charging effects by the ion beams. The distribution of ^{18}O intensity in the free surface area is not homogenous. Near the cathode the intensity is so high that it results in a long tail in the yz-depiction (Fig. 5.35 (b)). Additionally, the rest of the free surface area also shows high intensity compared to the areas below the electrodes (Fig. 5.35 (a)). This can be even better illustrated in the corresponding plot of the relative tracer concentration (Fig. 5.36). The ^{18}O concentrations inside the free surface area is the highest, which can be seen by the integration of area 1 and 2 in Fig. 5.35 (a). It can also be seen that the concentration in the cathode area of the PZT is a bit higher than at the anode. For area 1 it can be expected that the profile extends much further into the sample as it hardly drops over the first 400 nm in the depth profile. A refence sample has not been investigated in this case. In the ^{18}O images for experiments on PZTNd(Ag/Pd) at 500°C and 100 V (4 h) the effects already observed at lower temperatures become even more pronounced (Fig. 5.37). In this case the free surface area is filled with ^{18}O
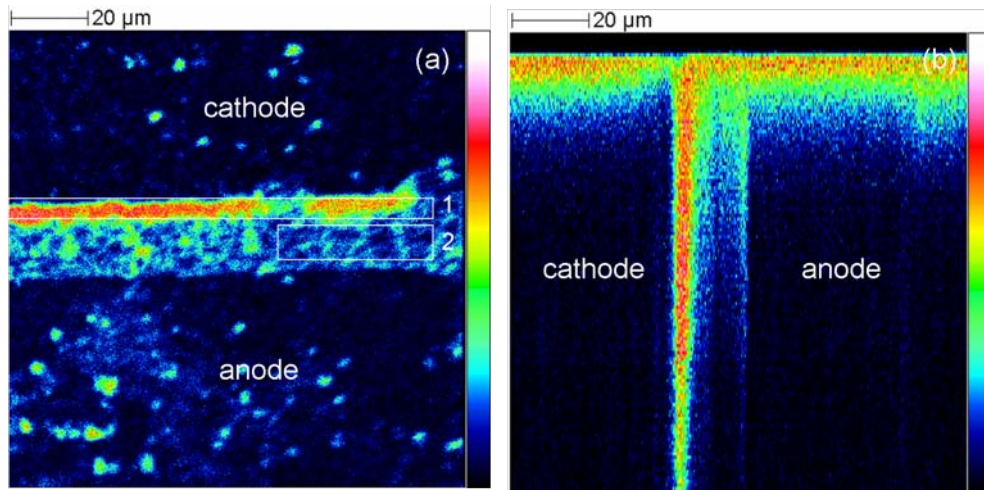
Fig. 5.35: ^{18}O images of tracer experiment on PZTNd(Ag/Pd) with large LSC surface electrodes (400°C, 100 V, 4 h). (a) Culmulative image of depth profile (after removal of LSC layer by etching with 5% HCl solution)(white boxes illustrating areas for concentration evaluation). (b) yz-depiction of depth profile.
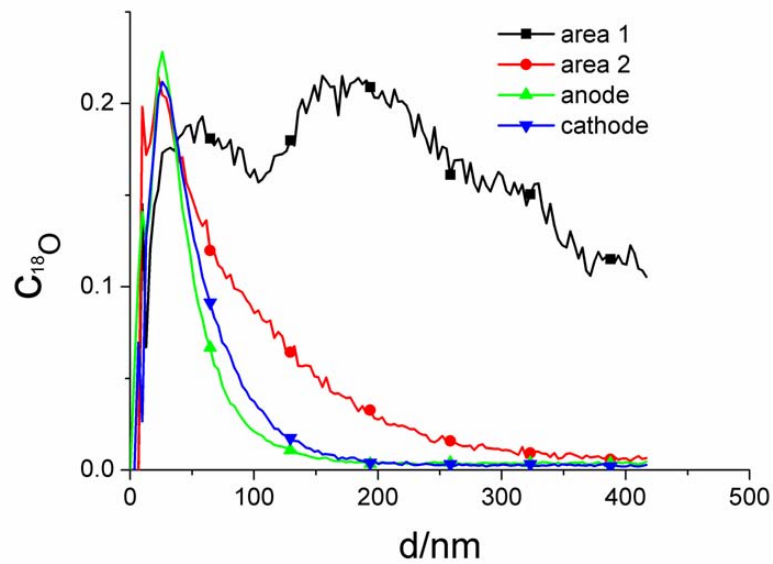
Fig. 5.36: Relative ^{18}O concentrations of tracer experiment on PZTNd(Ag/Pd) with large LSC surface electrodes (400°C, 100 V, 4 h) from different areas of interest (area 1 and 2 are given by the white boxes in Fig. 5.35 (a)).

over the whole depth profile (Fig. 5.37 (a)). The ^{18}O intensity in the cathode area also increases significantly which can be attributed to tracer migration along grain boundaries because the grain pattern is clearly visible in the ^{18}O images in a depth of 600 nm to 900 nm (Fig. 5.37 (b)). In Sec. 5.5 an applied voltage during tracer experiments was also found to enhance oxygen transport at grain boundaries. In the concentration plot (Fig. 5.38) it can be clearly seen that the ^{18}O
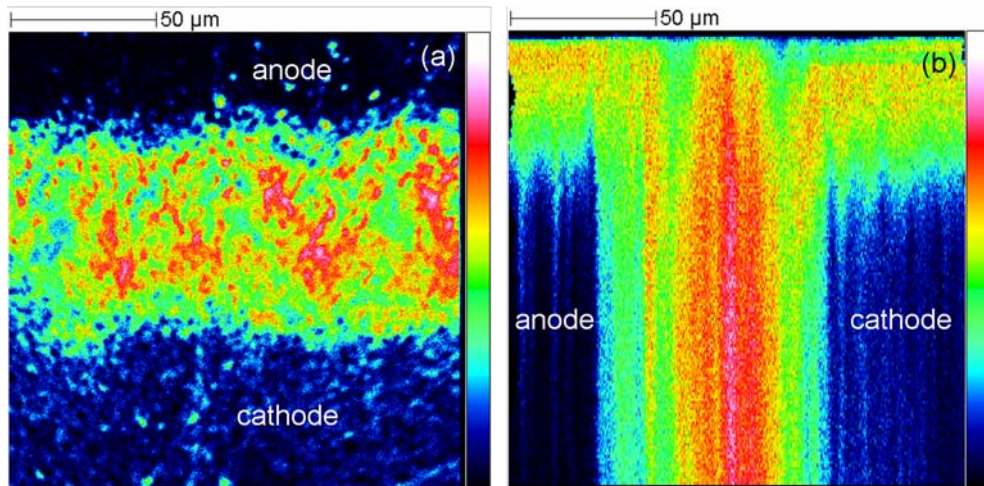
Fig. 5.37: ^{18}O images of tracer experiment on PZTNd(Ag/Pd) with large LSC surface electrodes (500°C, 100 V, 4 h). (a) Culmulative image of depth profile (after removal of LSC layer by etching with 5% HCl solution)(evaluated from 600 to 900 nm). (b) yz-depiction of depth profile.

migrates far into the material in the free surface region and that there is high concentration and a grain boundary tail for the cathode area. The tracer concentration below the anode is almost identical to the one in the reference samples, which is again similar to the results in Sec. 5.5 for the tracer experiments counducted at 500°C and 130 V/mm through the bulk PZT material (Fig. 5.16 (a)). It can be expected that the potential distribution in the sample with the large electrodes is different to the one for the small surface electrodes (see Sec. 4.6). For the large electrodes the geometrical factor $f_{geo} = 0.57$ can also be calculated from FEM simulations (Eq. 4.4).

Although the potential distribution in experiments on the disc shaped PZTNd might deviate from rectangular PZTNd(Ag/Pd) samples, these differences are expected to be quite small. The results for ^{18}O tracer experiments on PZTNd at 500°C and 100 V (4 h) (Fig. 5.39) should be easily comparable to the corresponding experiment on PZTNd(Ag/Pd). The PZTNd sample shows the same behavior as the PZTNd(Ag/Pd) but not to the same extend. By comparing Fig. 5.39 (a) and Fig. 5.37 (a) it becomes clear that the application of voltage has a smaller effect on the
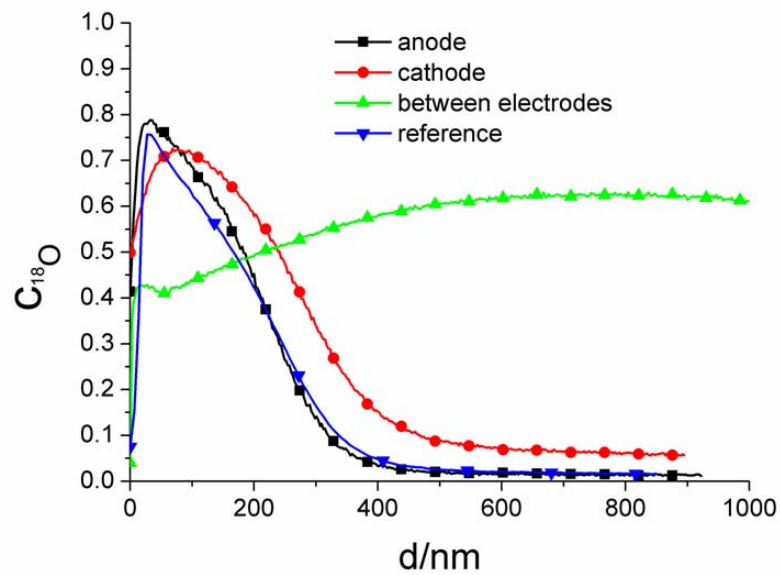
Fig. 5.38: Relative ^{18}O concentrations of tracer experiment on PZTNd(Ag/Pd) with large LSC surface electrodes (500°C, 100 V, 4 h) from different areas of interest and corresponding reference sample (symbol every 10 points).
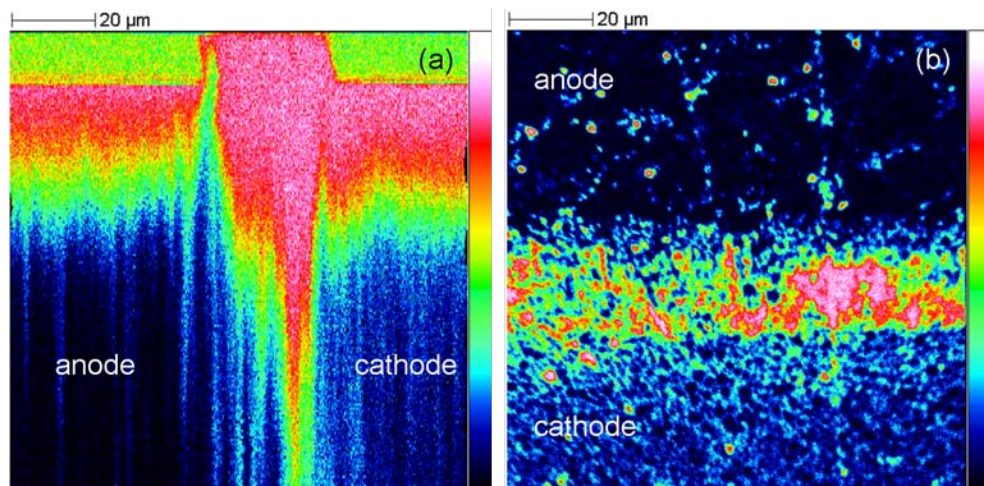
Fig. 5.39: ^{18}O images of tracer experiment on PZTNd with large LSC surface electrodes (500°C, 200 V, 4 h). (a) Culmulative image of depth profile (evaluated from 600 to 900 nm). (b) yz-depiction of depth profile.

tracer migration behavior of the PZTNd. This can also be illustrated by conductivity comparison (Fig. 5.40). The conductivity of the PZTNd is again by far the lowest. The corresponding relative
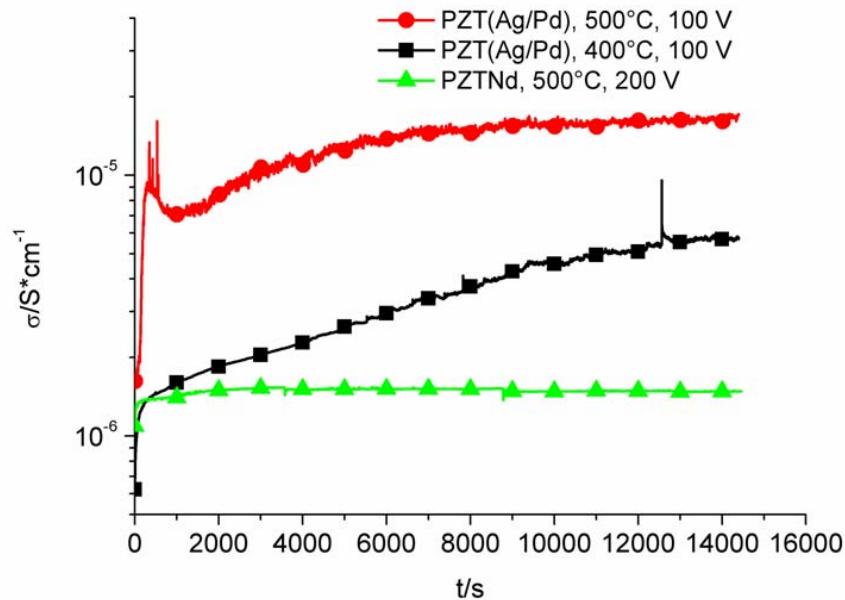
Fig. 5.40: Comparison of conductivities during the large surface electrode experiments on PZTNd and PZTNd(Ag/Pd).

^{18}O concentrations are given in Fig. 5.41. The profiles for the anode and reference area are similar to the one in Fig. 5.15 (a) and the cathode profile is slightly enhanced with respect to them. The profile between the electrodes resembles rather a PZTNd diffusion profile at 600°C (Fig. 5.15 (b)). There is an extended box up to 1 μm for this area with a tail from grain boundary migration. From these LSC surface electrode measurements and the experiments from Sec. 5.5 it can be concluded that the surface and grain boundary properties are changed upon voltage application. The box in the tracer concentration profiles below the cathode and in the free surface area is increased and diffusion along the grain boundaries is enhanced. However, the reason for that still remains unclear and further investigations are needed. Stoichiometric changes caused by oxygen vacancy motion under field might again be highly relevant (see Sec. 5.10). Moreover, there might be a correlation between the changes due to applied field observed during CM (Sec. 4.7) and the near-surface tracer diffusion properties in the area between the LSC electrodes. This might even be related to the Ag-dendrite development on the surface (Sec. 4.3).
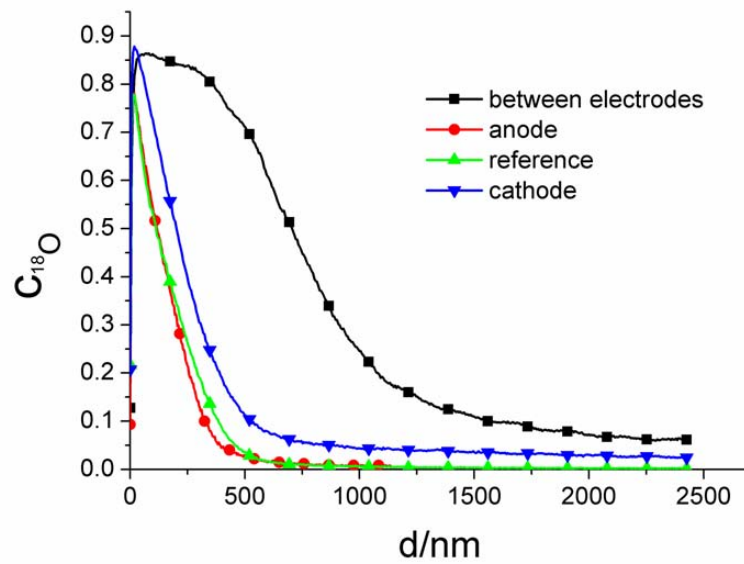
Fig. 5.41: Relative ^{18}O concentrations of tracer experiment on PZTNd with large LSC surface electrodes (500°C, 100 V, 4 h) from different areas of interest.
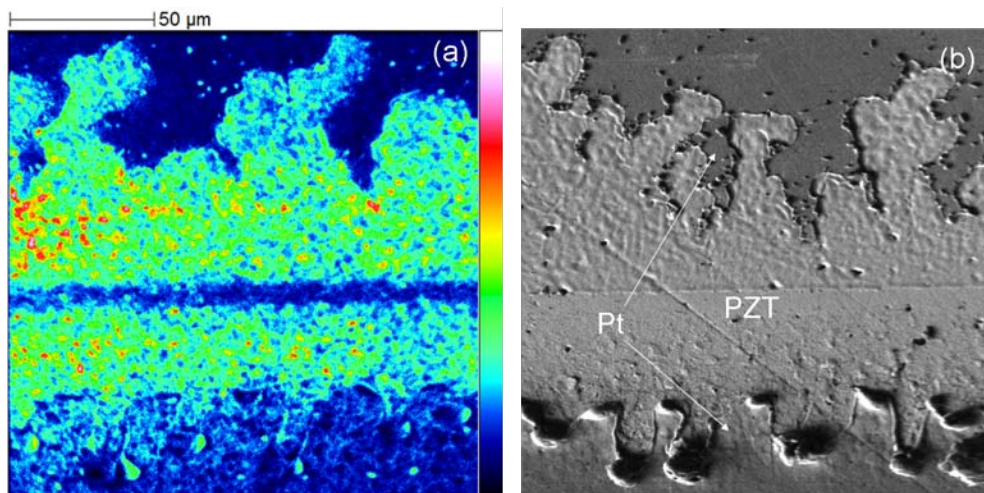
Fig. 5.42: (a) Culmulative image of depth profile of ^{18}O tracer experiment on PZTNd with large Pt surface electrodes (500°C, 100 V, 4 h) (b) Corresponding SE image.

However, in order to get more information and support of the presented theories it is of great interest how metal electrodes and especially Ag electrodes influence ^{18}O tracer experiments with application of voltage. Unfortunately, this has not been accomplished so far as the electrodes show strong degradation on the same time scale as the oxide electrode experiments. In Fig. 5.42 (b) it can be seen that the Pt electrode of an experiment on PZTNd at 500°C and 100 V is partly removed from the surface which can be seen as local breakdown. The enhanced ^{18}O intensity in that area (Fig. 5.42 (b)) might be caused by incorporation of the tracer due to the high temperatures that occur during that breakdown.

However, experiments with 100x100 μm^2 Pt electrodes could give some information. In this case a
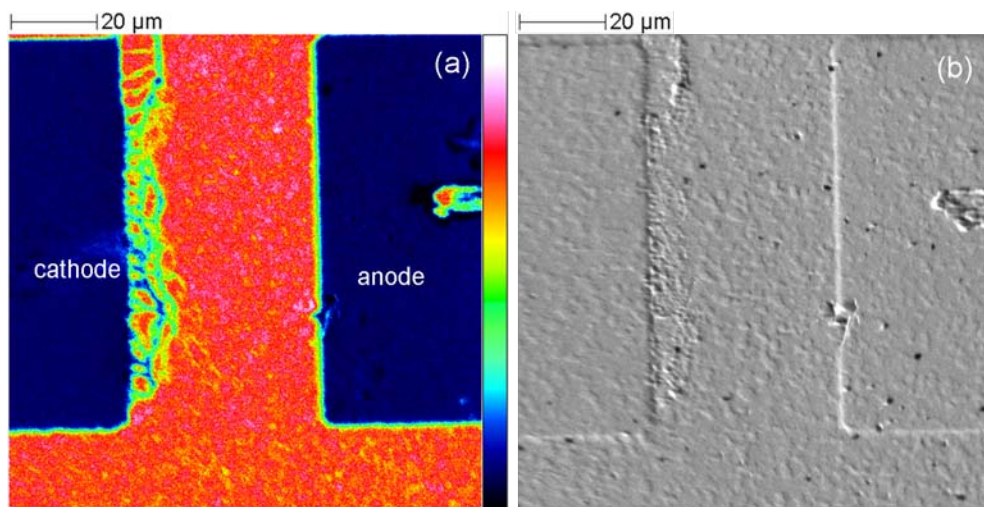
Fig. 5.43: (a) Culmulative image of depth profile of ^{18}O tracer experiment (500°C, 100 V, 4 h) on PZTNd with square Pt surface electrodes (100x100 μm^2, 50 μm distance); a voltage of 100 V was applied after the tracer experiment at 450°C. (b) Corresponding SE image.

^{18}O tracer experiment was conducted at 500°C prior to deposition of the electrodes. Afterwards, 100 V were applied to electrodes with a distance of 50 μm at 450°C. As a result, a tracer deficient area close to the cathode can be seen in the ^{18}O image (Fig. 5.43 (a)). It seems that the tracer deficient pathways resemble grain boundaries but the whole microstructure was altered due to the applied voltage, as it can be seen in the corresponding SE image (Fig. 5.43 (b)). As expected, the intensities of metal oxides with the ^{16}O isotope increase (Fig. 5.44 (a)). The increase of the TiO signal, however, does not only occur due to the higher ^{16}O concentration but also because of the higher Ti signal (Fig. 5.44 (b)). This could either be the result of higher Ti concentration due to Pb evaporation or due to a reduction of this area. Incorporation of electrons could very well increase the ionization probability of the metal anions. However, more experiments

are needed to draw conclusions with respect to the influence metal electrodes. Nevertheless, from the presented results it becomes clear that there is a strong correlation between oxygen migration and degradation and further investigations on the influence of voltage on the oxygen incorporation should be very interesting.
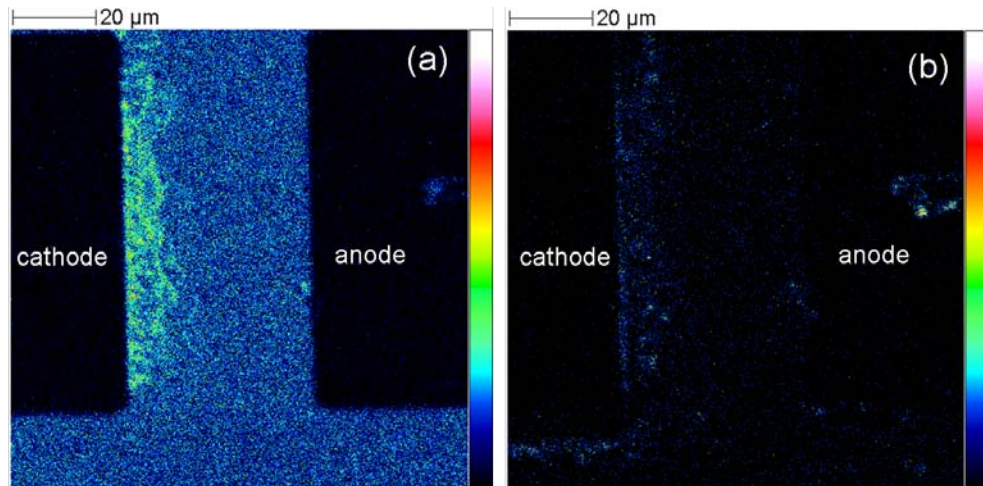
Fig. 5.44: (a) TiO image of tracer experiment (500°C, 4 h) on PZTNd with square Pt surface electrodes (100x100 μm^2, 50 μm distance); a voltage of 100 V was applied after the tracer experiment at 450°C. (b) Corresponding Ti image.

6

Results and Discussion: Oxygen Tracer Diffusion in Donor Doped BT

6.1 Grain Boundary Diffusion
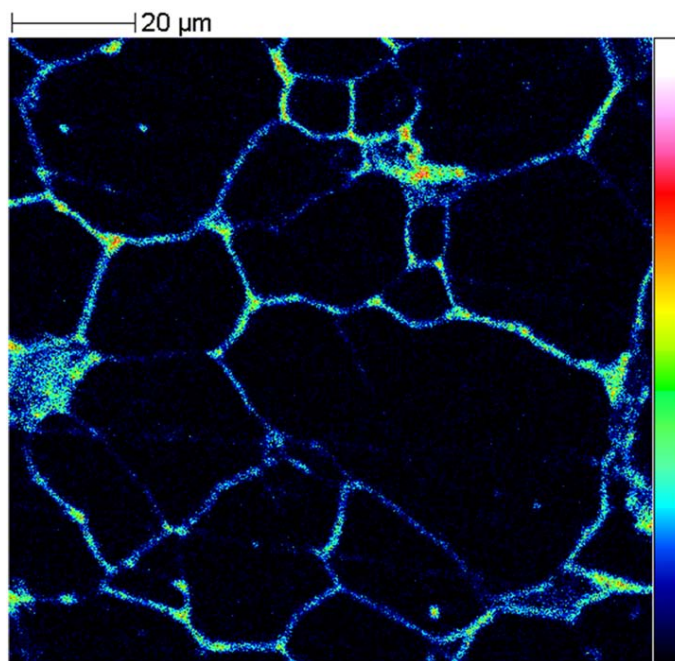
Fig. 6.1: Cumulative ^{18}O image obtained in a depth from 900 nm to 1100 nm of BT sample annealed in ^{18}O$_2$ at 900°C (The color scale represents increasing intensity from bottom to top of the scale).

For the sake of comparison , ^{18}O tracer diffusion experiments were also performed on donor (La) and acceptor (Mn) co-doped BT, which is a material used in PTC resistor devices (Sec. 2.3.4).

A typical ^{18}O distribution image after an $^{18}O/^{16}O$ exchange experiment at 900°C is given in Fig. 6.1. The cumulative data from a depth of from 900 nm to 1100 nm clearly shows strong enhancement of the ^{18}O concentration at grain boundaries and thus fast grain boundary diffusion. Oxygen diffusion deep into the sample can be even better visualized in images obtained on cross sections. Such an image of a sample annealed in $^{18}O_2$ at 900°C is given in Fig. 6.2 (a). The thin layer of higher ^{18}O intensity on the left reflects the surface from which the oxygen diffusion progresses via the grain boundaries deeply into the sample. Fig. 6.2 (b) is an ^{18}O intensity image of the center of the same sample, in which the grain boundary pattern is still visible. Thus, we can conclude that all grain boundaries of the 1.2 mm thick sample are at least partly filled with tracer ions. The same observation was made for samples annealed at temperatures down to 750°C.

At 600°C (Fig. 6.3) no enhanced grain boundary diffusion could be observed. There is still the thin surface layer on the left but no visible grain boundary pattern in the ^{18}O image. However, there are regions of high ^{18}O intensity further away from the surface, which can be attributed to the extended porosity. By comparing Fig. 6.2 (b) and the corresponding secondary electron (SE) image in Fig. 6.2 (c), it becomes clear that the high intensity areas are pore regions. Unfortunately, this shows that the oxygen diffusion does not only occur from the surface into the interior of the sample but also from the voids inside the sample. That leads to grain boundary diffusion originating in different depths and at various angles. Evaluation of grain boundary diffusion coefficients with common methods [83, 84, 86, 203] is therefore not possible. Nevertheless, the images prove unambiguously the existence of fast grain boundary diffusion. A similar behavior has been observed for donor doped PZT material sintered with Ag/Pd-inner electrodes (Sec. 5.1).

6.2 Secondary Phases: Composition and Tracer Diffusion

The origin of the electrical properties of PTC resistors is usually attributed to the formation of SCHOTTKY barriers (depletion layers) at the grain boundaries, which is strongly correlated with the reoxidation process (Sec. 2.3.4). Oxidative annealing at elevated temperatures usually results in an increase of the grain boundary resistivities which may be accompanied by an enhancement of both the SCHOTTKY barrier height and the depletion zone width [20, 61, 62]. It is often discussed that metal vacancy diffusion into the grain during the reoxidation process [21] and
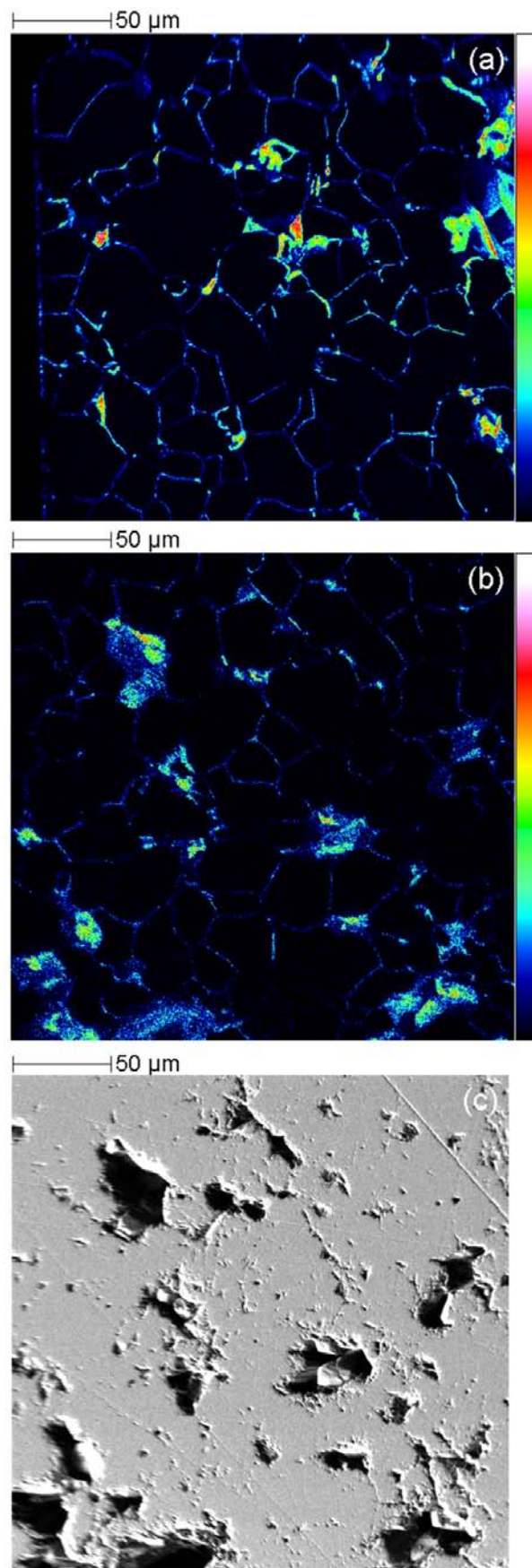
Fig. 6.2: Cross section ^{18}O image of BT sample annealed at 900°C for 4 h (a) from surface (left) to interior of the sample; (b) center of the sample. (c) Corresponding SE image of center area.
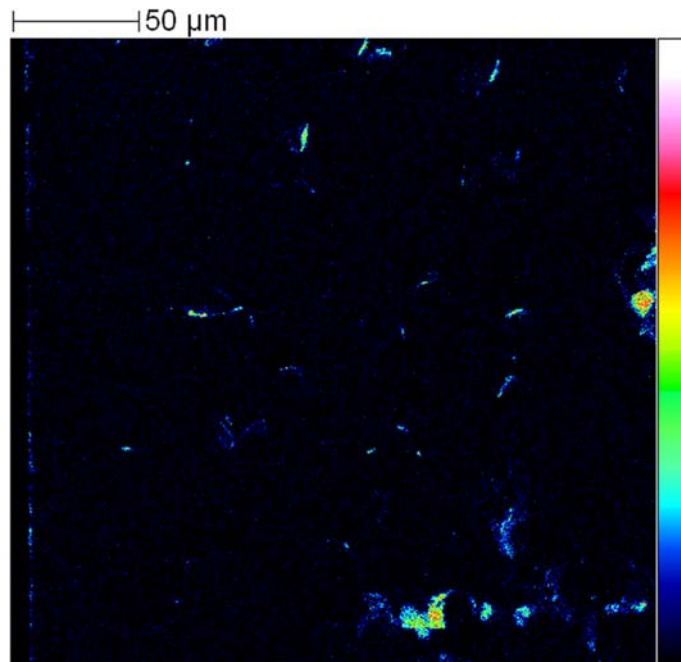
Fig. 6.3: Cross section ^{18}O image BT sample annealed at 600°C (4 h) from surface (left) to interior of the sample.

the development of a secondary phase at the grain boundaries and triple junctions are closely connected [122,123]. There is still some controversy about the predominant mobile metal vacancy species and the composition of the resulting secondary phase [122]. Hence, information on the transport properties and chemical composition of any secondary phase is of great interest. In our study, it is of course likely that a Ti enriched secondary phase develops simply because of the TiO$_2$-excess used as sintering aid in the starting material. Therefore, results on the composition of secondary phases do not necessarily allow mechanistic interpretations of the reoxidation process. Nevertheless, it is interesting to elucidate how the secondary phase contributes to the oxygen diffusion behavior of donor doped barium titanate.

To obtain information on the composition of secondary phases found in our samples, cation ratios of the secondary phase and the bulk material were determined by ToF-SIMS and EDS. Fig. 6.4 (a) shows the Ti-signal of the ToF-SIMS measurement and it can clearly be seen that the areas of high intensity correspond to the secondary phase in the SE-image in Fig. 6.4 (b) . To compare the Ba to the Ti-signal, overlay images of the two ion signals were generated. This is depicted in Fig. 6.4 (c), where the Ba-signal is in red and the Ti-signal in blue colour. The Ti-intensity dominates in the secondary phase, thus indicating Ti enrichment therein. Quantification of the

exact Ba/Ti ratio remains difficult. Due to the matrix effect [153] the intensity of the ion signals in ToF-SIMS measurements is generally not proportional to the corresponding concentration in the material. As the composition of the matrix definitely changes from bulk material to secondary phase, the signals of Ti and Ba may change disproportionally. The qualitative results of this SIMS study were likewise confirmed by EDS measurements. Basically, the composition of the Ti-rich secondary phase may be $Ba_6Ti_{17}O_{40}$ or $BaTi_2O_5$ in accordance with the BaO-TiO_2 phase diagram [207]. Recently, it has been shown by high resolution transmission electron microscopy (HRTEM)-images and TEM/EDS analysis that the secondary phase located at triple junctions is crystalline with the Ti/Ba ratio being close to 3 [200].
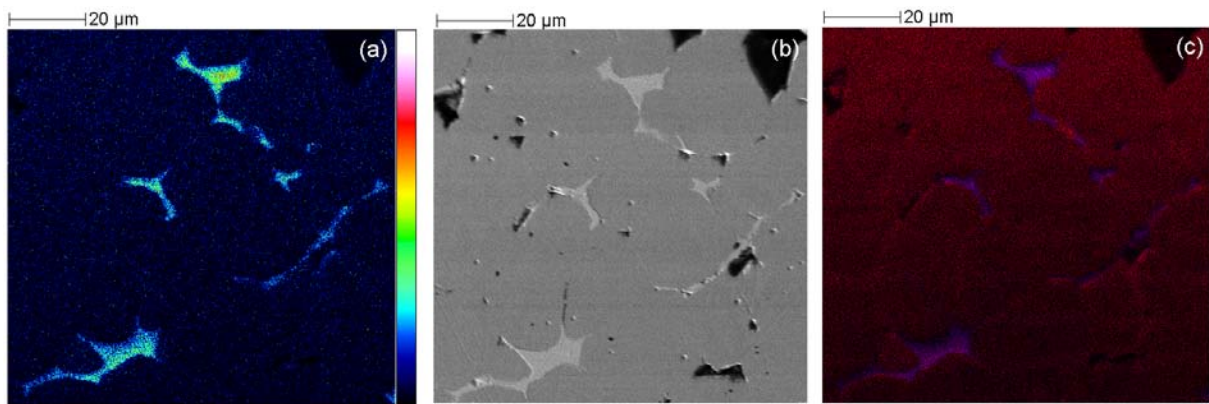
Fig. 6.4: (a) Cumulative Ti image (600°C). (b) Corresponding SE image. (c) Overlay of cumulative Ti and Ba image.

Information on the oxygen diffusion in the secondary phase is again obtained from the ^{18}O tracer experiments. Fig. 6.5 (a) is a cumulative image of ^{18}O intensity in the surface near region from the surface to 600 nm depth obtained during depth profiling of a sample annealed in $^{18}O_2$ at 600°C (4 h). In the major part of the imaged area the tracer is distributed homogeneously (except from some artefacts induced by scratches due to the polishing procedure, which results in the lines of higher intensity). This high surface near ^{18}O tracer concentration inside the grains will be discussed in the next sections. However, there are small areas where no tracer exchange can be observed. These areas correspond to the secondary phases at triple junctions in the SE-image (Fig. 6.5 (b)). With the ION-TOF analysis software it is possible to further evaluate the data obtained by depth profiling with respect to the xz-direction, thereby imaging the distribution of ^{18}O into the depth. Such an image is shown in Fig. 6.5 (c) and it represents the xz-depiction of the region of interest given by the white rectangle in Fig. 6.5 (a). It can be deduced from

Fig. 6.5 (c) that the ^{18}O-tracer exchange occurs in BaTiO$_3$ but hardly any tracer diffuses into the secondary phase.
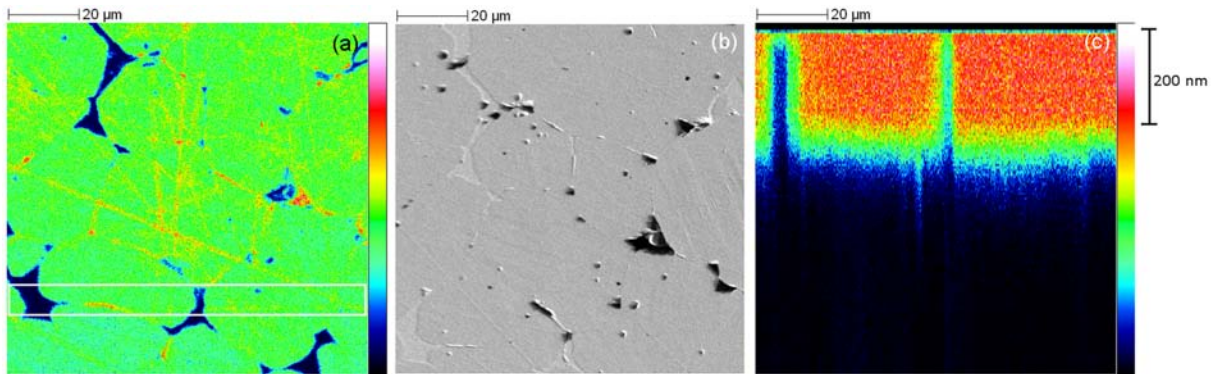
Fig. 6.5: (a) Cumulative ^{18}O image (0-600 nm) of BT annealed at 600°C (4 h). b) Corresponding SE image. c) Calculated xz-image of ^{18}O (white box in Fig. 6.4 (a) indicating the section for the evaluation of grain diffusion).

The impact of the secondary phase on grain boundary diffusion is also of great interest. Fig. 6.6 (a) and (b) are cross section images of ^{18}O and TiO intensities of a sample exposed to ^{18}O$_2$ at 900°C. In this case, the secondary phase corresponds to the high intensity area in the TiO image. The ^{18}O image cleary shows that the tracer enrichment at grain boundaries due to fast diffusion processes is not continous. There are interruptions in the diffusion pathways, which can again be attributed to the secondary phase, as can be seen in the overlay image of the two ion signals (Fig. 6.6 (c)), where the TiO signal is red and the ^{18}O signal is blue. The tracer does not pass through the secondary phase but it rather diffuses along the interface between BaTiO$_3$ and the secondary phase (visible at the left side of the large secondary phase). This agrees well with our findings from surface depth profiling (see Fig. 6.5).

6.3 Diffusion in Single Grains

In Fig. 6.7 the bulk concentration profiles inside single grains of BT samples annealed at different temperatures are given. For annealing temperatures from 600°C to 800°C the profiles are very similar. They appear to be almost box-shaped, which means that there has to be a surface layer, which is filled by the tracer very quickly while diffusion further into the bulk is inhibited. Similar to the experiments on PZT in Sec. 5.2 the short time span the sample is cooled down in an ^{16}O$_2$ rich atmosphere is sufficient for ^{16}O to be incorporated into the sample. This results in a
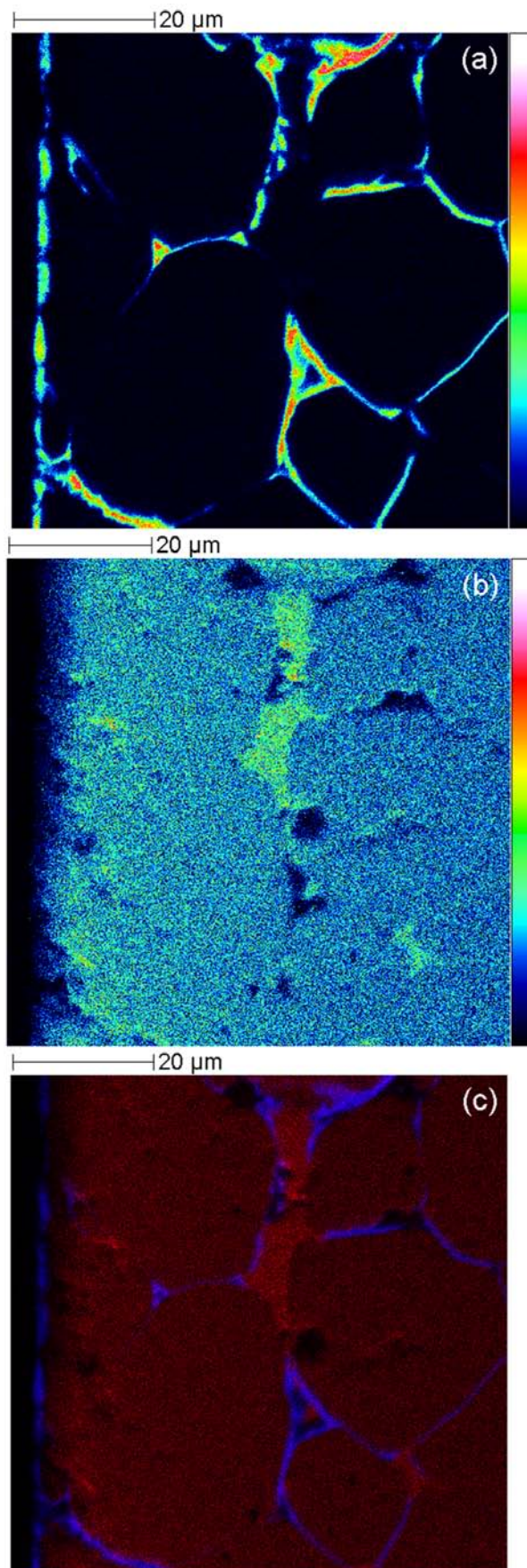
Fig. 6.6: (a) Cross section ^{18}O image of BT sample annealed at 900°C (4 h) from surface (left) to interior of the sample. (b) Corresponding cross section TiO image. (c) Overlay of cross section ^{18}O and TiO image.

maximum of the relative ^{18}O concentration in some depth instead of a box with a concentration value close to one at the surface. The impact of this effect increases with increasing temperature due to faster diffusion. Moreover, some changes seem to take place above 800°C as the box at 900°C extends further into the sample, while below that temperature the profile shape is rather temperature independent. After the first few 100 nm, diffusion in the grains seems to be very slow since hardly any ^{18}O concentration could be measured beyond the "box". Similar profile
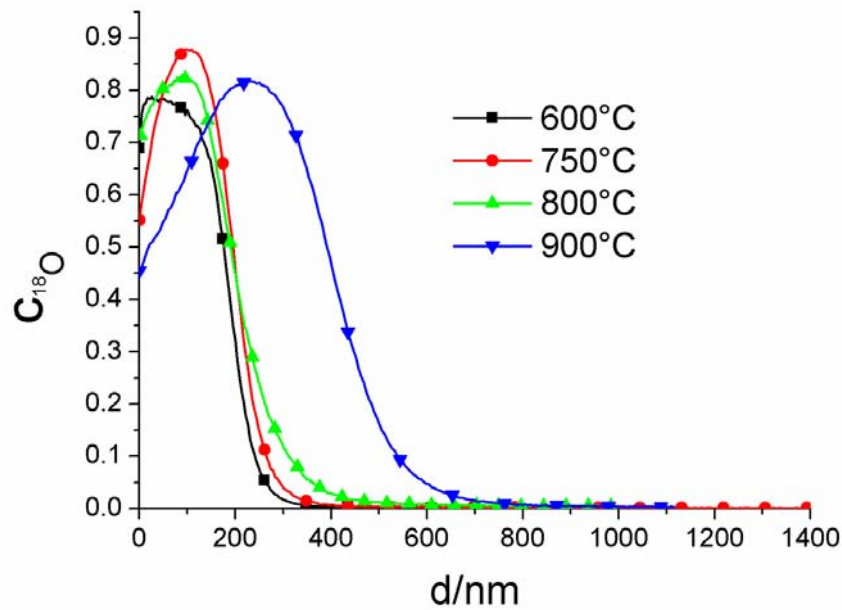
Fig. 6.7: Diffusion profiles inside single grains of BT for different annealing temperatures in ^{18}O$_2$ (4 h each); the lines represent measurement data, only one symbol every 20 data points is shown for indicating temperature.

shapes could also be observed for donor doped PZT sintered in oxidizing atmosphere (see Sec. 5). There, the behavior is attributed to a surface space charge layer with enhanced oxygen vacancy concentration, leading to a position dependent diffusion coefficient. It is realistic to assume that such a surface-near space charge layer with enhanced oxygen vacancy concentration also causes the box like profiles here and that around 900°C defect chemical changes (similar to reoxidation processes during preparation) increase the thickness of this zone.

6.4 Diffusion Pathway Along Grain Boundaries

Considering the presented results, an important question is what the dominant diffusion pathway of oxygen along grain boundaries might be. It was already discussed in Sec. 5.6 that space charge layers are often found at grain boundaries in ceramics, where the mobile charge carriers may be depleted or enriched. Positively charged oxygen vacancies can be expected to be enriched inside space charge layers along the grain boundaries if all mobile negative charge carriers and thus also electrons were depleted. This is exactly in accordance with the Heywang model [22].

Evidence of an interfacial space charge was found for the area close to the surface, see above. The surface properties, of course, do not necessarily represent grain boundary properties and certainly additional investigations are required in order to verify that space charge layers give rise to the observed surface profile shape. Nevertheless, grain boundary and surface states might be similar [64], supporting the assumption of fast oxygen diffusion along space charge layers at the grain boundaries. Further information on the diffusion behavior in grain boundaries was obtained by determining the actual thickness of the grain boundary profile. Line scans over grain boundaries for 900°C, 800°C and 750°C from cross section images are given in Fig. 6.8. For line scans of samples annealed at 750°C and 800°C the thickness measured from the full width at half maximum (FWHM) of the signal is in the range of 700-800 nm while for the 900°C samples it is 1 μm. Thus, the thicknesses of diffusion profiles at grain boundaries are almost exactly twice the surface profile box thicknesses and thus in accordance with two space charge layers at grain boundaries versus one space charge at the surface.

It should be kept in mind though that problems can arise, determining structures smaller than 1 μm in images obtained from ToF-SIMS measurements due to the finite thickness of the primary ion beam (>200 nm). Shifts of the ion beam during measurement, for example, could lead to an exaggerated grain boundary thickness. However, it is generally agreed that even for imaging of challenging organic materials submicron resolution can be achieved [208]. As the presented results are well reproducible with Bi^+ and the higher molecular Bi_3^{++} primary ion beam, they indeed provide further evidence for the suggested ^{18}O diffusion along space charge layers at grain boundaries in donor doped barium titanate.

Moreover, a significant bulk diffusion would be required to account for the measured FWHM values and this bulk diffusion contradicts the results obtained for measurements inside single
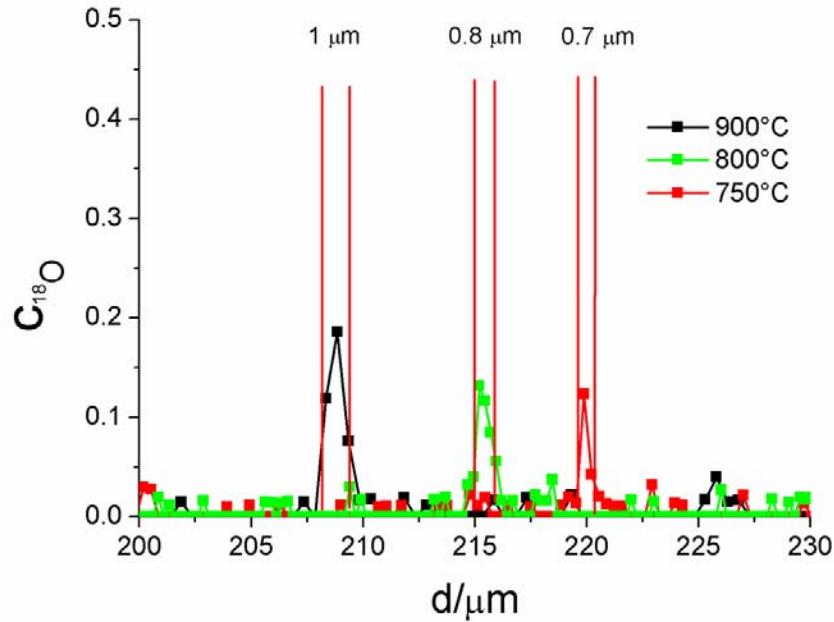
Fig. 6.8: Line profiles across a single grain boundary from cross section images for BT annealed in $^{18}O_2$ at different temperatures (4 h).

grains: A bulk profile beyond the ^{18}O enriched box at the surface could not be determined and this again supports the assumption of oxygen vacancy rich space charge layers along the grain boundaries. However, as mentioned in Sec. 5.8 a type B diffusion mechanism might still be valid although the position dependent bulk diffusion coefficient will lead to errors in the calculation of D_b according to Eq. 2.40.

It should finally be mentioned that significant reoxidation processes may occur at grain boundaries during the pre-annealing for 17 h in air, which most likely affect the interfacial defect chemistry at the highest annealing temperature (900°C, Fig. 6.7). In general, the grain boundary resistivity is enhanced by reoxidation, since the annihilation of oxygen vacancies within the grain boundary core regions and/or creation of cation vacancies diffusing into the grains result in an increase of the space charge layer width. The corresponding extended depletion of electrons may be accompanied by an enrichment of oxygen vacancies [32], visible as a larger FWHM value.

The similarities of the tracer diffusion properties of BT material for PTC and donor doped PZT sintered with Ag/Pd-inner electrodes are intriguing. Development of box-shaped depth profiles and fast grain boundary diffusion has been found for both materials. However, the changes of

the near-surface profile shapes at higher temperatures is very different. For BT the box extends further into the sample (Fig 6.7) while for the PZT the box diminishes and a large tail from bulk diffusion becomes evident in the concentration profiles (Fig. 5.7 and Fig. 5.14). Nevertheless, it can be assumed that similar mechanisms are responsible for the tracer diffusion properties in both materials at lower temperatures. In this case, a near-surface and grain boundary space charge layer is mostly likely involved in the oxygen transport. For further conclusions more investigations on BT and PZT properties are needed and there is still hardly any information on the impact of the Ag-doping on the PZT. This seems to be the crucial parameter facilitating enhanced grain boundary diffusion in donor doped PZT.

Chapter 7

Conclusion

^{18}O tracer diffusion profiles in the near-surface region of PZT exhibit a very pronounced dependence on many parameters, such as temperature, etching and applied field. Already minor alterations can lead to large changes in the tracer profile shapes obtained by ToF-SIMS. Evidence is provided that the near-surface tracer diffusion profiles are strongly correlated with a surface space charge layer. In the investigated donor doped PZT samples this space charge leads to an enrichment of oxygen vacancies at lower temperatures and hence to box-shaped diffusion profiles close to the surface. At about 650°C, however, the shape of the profile changes, which can be attributed to a positive space charge leading to a depletion of oxygen vacancies in the space charge zone. This crossover might be caused by defect chemical changes very close to the surface due to onset of cation motion and/or PbO evaporation. The chemical and thermal pre-treatment of the samples also play a major role in changing near-surface oxygen diffusion properties.

Pre-treatment of the PZT samples has a major impact on the ^{18}O grain boundary diffusion, as well. For the investigated donor doped PZT annealed in ^{18}O$_2$ above 500°C ^{18}O enriched regions in two dimensional images clearly correspond to the grain boundary pattern. For donor doped PZT material sintered with Ag/Pd-inner electrodes it could be shown that very fast grain boundary diffusion is evident at an annealing temperature of 650°C and it is most likely governed by type B kinetics. In this case, the grain boundary pattern was also cleary visible in measurements on cross sections showing tracer diffusion up to 150 μm into the sample. The evaluated grain boundary diffusion coefficient is five to six orders of magnitude higher than the bulk diffusion coefficient and the calculated effective ionic conductivity of the grain boundary contribution is in the same order of magnitude as the total conductivity obtained from impedance measurements. This

means that grain boundary ion conduction may significantly contribute to the total conductivity at 650°C. However, for donor doped PZT without Ag/Pd inner electrodes no extended grain boundary diffusion was observable in the cross section even for annealing temperatures above 800°C. Therefore, doping with Ag, which is incorporated during the sintering process, might contribute to the enhanced grain boundary diffusion in donor doped PZT with Ag/Pd-inner electrodes.

In tracer experiments with applied field on LSC electrodes the tracer concentration at the cathode is increased which might be caused by a field induced change of the space charge potential. Evidence has been found that the field further induces fast grain boundary diffusion. ^{18}O tracer experiments with field applied to LSC surface electrodes also provided evidence for an enhanced box-shaped profile in the free surface area between the electrodes. At higher voltage or temperature this effect is overshadowed by the set-in of fast oxygen grain boundary migration. However, it could be determined that the contribution of ion migration to the overall current at 400°C is 1% at best. This leads to the assumption that electronic conductivity is dominant in PZT and that oxygen transport requires a defect chemical change at higher temperature or activation by application of high voltage.

The change of the properties in the free surface area between the electrode might be related to the effects observed with conductive mode microscopy. It could be shown that upon application of field on Pt-micro electrodes the electrochemical potential of the surface changes with respect to the cathode. Evidence has been found that resistive barriers, which can be attributed to grain boundaries, break down due to the application of voltage, which results in a homogeneous resistivity distribution across the area between the electrodes. However, this could not be resolved by impedance spectroscopy as only one semi-circle was obtained for most of the samples. The difference in resistance could be small enough not to be distinguished by impdance spectroscopy but to be still observable in conductive mode microscopy. By impedance spectroscopy it could nevertheless be shown that annealing at temperatures around 400°C affects the resistance significantly, which is again illustrates that many factors contribute to and influence the conduction mechnisms.

The application of voltage to surface electrodes affects oxygen migration in samples sintered with Ag/Pd-electrodes the most. This material also shows the highest conductivity and lowest stability during the DC experiments. Accordingly, this gives rise to the assumption that there

is a strong correlation between enhanced oxygen migration and resistance degradation of PZT. Furthermore, it could be shown that DC experiments with surface electrodes lead to degradation on much shorter time scales than experiments with inner electrodes, which could mean that the surface is more prone to degradation. However, any of the donor doped PZT samples with Pt-surface electrodes are much more stable than with Ag-surface electrodes, which illustrates that the PZT material properties are not the only factors influencing degradation.

Additionally, with Ag-surface electrodes dendrite development could be observed from the anode to the cathode at temperatures above 300°C irrespective of the PZT material. Hence, it can be assumed that a near-surface process is responsible for this effect, which again might be related to the near-surface property changes observed in the conductive mode microscopy measurements.

It has also been confirmed that oxygen tracer grain boundary diffusion in donor doped barium titanate is very fast at and above 750°C, supporting existing models of fast grain boundary reoxidation. The images of the ^{18}O tracer signals clearly show the diffusion of oxygen along the grain boundaries several tens or even hundreds of microns into the material. Furthermore, it could be shown that the surface-near diffusion behavior in single grains is similar to the ones obtained for PZT, resulting in a box-like shape of the tracer diffusion profile. This can also be attributed to the existence of a surface space charge layer with enhanced oxygen vacancy concentration. Evidence has been provided that space charge layers could likewise be the reason for fast oxygen transport along the grain boundaries of BT and also of PZT. Nevertheless, FEM calculations showed that type B diffusion kinetics could still be valid with a oxygen vacancy enriched space charge layer next to a fast grain boundary core. The secondary phase, which formed during the sintering process in BT, could be determined as Ti-rich. Oxygen diffusion in such a secondary phase is inhibited, which results in an oxygen transport along but not through the phase.

Chapter 8

Outlook

A number of novel aspects regarding oxygen transport and degradation effects in PZT have been obtained and some of the new findings should lead further possibly interesting investigations. Regarding the DC high voltage experiments, investigations with LSC surface electrodes could give further information on the resistance degradation. Using the large surface electrodes this material already showed a high stability compared to the metal electrodes but a direct comparision with the electrode configurations given in Fig. 3.1 is definitely of great interest. The experiments could also be coupled with further ^{18}O tracer experiments where the ^{18}O$_2$ is supplied by a glass capillary onto the surface [209]. This way the experiment can be conducted with microprobe contacts. Additionally, similar ^{18}O tracer experiments with metal electrodes could provide information on the influence of electrode material on tracer diffusion properties.

The influence of doping and pre-treatment should also be investigated extensively. Since now only experiments on PZT material for actuators were conducted. Acceptor doped PZT or PZT far from the morphotropic phase boundary could, for example, be appropriate samples for the next experiments. However, for the tracer diffusion experiments the impact of Ag-doping is especially interesting. By investigating PZT samples with a well known Ag concentration the role of Ag-doping with respect to tracer grain boundary diffusion could be clarified.

To obtain information on the Ag diffusion and migration in PZT, experiments on PZT without initial Ag content should be conducted. By depositing Ag-surface electrodes and annealing at higher temperatures with or without field a Ag-diffusion profile might develop. This could then be measured by electron microprobe analysis. Unfortunately, ToF-SIMS would not be

suitable to obtain an appropriate Ag signal as to many overlapping masses are contributing to the measurement on PZT.

Further tracer diffusion experiments on BT with applied field might be useful to study the similarties with the oxygen tracer migration in PZT. The measurements could easily be compared to the ones obtained for donor doped PZT (Sec. 5.5 and Sec. 5.10) and may provide further evidence for the theories presented in this thesis.

The oxygen partial pressure dependence of resistance degradation of PZT is also something, which could be an interesting topic. In some measurements it has been shown that the resistance as well as the stability of a sample is increased when the experiment is conducted under reduced oxygen partial pressure (Sec. 4.2). However, an extensive investigation is needed to draw proper conclusions from these measurements.

Bibliography

[1] J. Maier, *Physical Chemistry of Ionic Materials: Ions and Electrons in Solids;* John Wiley & Sons, 1 ed., 2004.

[2] B. Jaffe and W. R. Cook, *Piezoelectric Ceramics;* Academic Press Inc.Ltd., 1971.

[3] R. N. Torah, S. P. Beeby, M. J. Tudor, and N. M. White, *J. Electroceram.*, **2007**, *19*, 95–110.

[4] G. Helke and K. Lubitz, *Piezoelectricity - Evolution and Future of Technology;* Springer in Materials Science, 1 ed., 2008.

[5] D. Lupascu and J. Rödel, *Adv. Engin. Mater.*, **2005**, *7*(10), 882–898.

[6] X. J. Lou, *J. Appl. Phys.*, **2009**, *105*, 024101.

[7] M. V. Raymond and D. M. Smith, *J. Chem. Phys. Solids*, **1996**, *57*(10), 1507–1511.

[8] W. L. Warren, D. Dimos, B. A. Tuttle, G. E. Pike, R. W. Schwartz, P. J. Clews, and D. C. McIntyre, *J. Appl. Phys.*, **1995**, *77*, 6695.

[9] Y. A. Genenko and D. C. Lupascu, *Phys. Rev. B*, **2007**, *75*, 184107.

[10] Y. A. Genenko, J. Glaum, O. Hirsch, H. Kungl, M. J. Hoffmann, and T. Granzow, *Phys. Rev. B*, **2009**, *80*, 224109.

[11] R. Waser, T. Baiatu, and K.-H. Härdtl, *J. Am. Ceram. Soc.*, **1990**, *73*, 1645–1653.

[12] S. Rodewald, J. Fleig, and J. Maier, *J. Amer. Ceram. Soc.*, **2000**, *83*(8), 1969–1976.

[13] R. Merkle and J. Maier, *Angew. Chem., Int. Ed.*, **2008**, *47*(21), 3874–3891.

[14] S. Rodewald, J. Fleig, and J. Maier, *J. Am. Ceram. Soc.*, **2001**, *84*, 521–530.

[15] I. Denk, J. Claus, and J. Maier, *J. Electrochem. Soc.*, **1997**, *144*(10), 3526–3536.

[16] J. Daniels, *Philips Res. Repts.*, **1976**, *31*, 505–515.

[17] F. D. Morrison, A. M. Coats, D. C. Sinclair, and A. R. West, *Journal Of Electroceramics*, **2001**, *6*(3), 219–232.

[18] H.-I. Yoo, C.-R. Song, and D.-K. Lee, *J. Electroceram.*, **2002**, *8*, 5.

[19] J. Daniels and K. H. Härdtl, *Philips Res. Repts.*, **1976**, *31*(6), 489.

[20] J. Daniels and R. Wernicke, *Philips Res. Repts.*, **1976**, *31*, 544.

[21] J. Nowotny and M. Rekas, *Ceram. Int.*, **1994**, *20*, 265–275.

[22] W. Heywang, *J. Am. Ceram. Soc.*, **1964**, *47*(10), 484–490.

[23] G. H. Jonker, *Solid State Elec.*, **1964**, *7*, 895–903.

[24] B. A. Boukamp, M. T. N. Pham, D. H. A. Blank, and H. J. M. Bouwmeester, *Solid State Ionics*, **2004**, *170*, 239–254.

[25] A. Pelaiz Barranco, F. Calderon Pinar, O. Perez Martinez, J. De Los Santos Guerra, and I. Gonzalez Carmenate, *J. Europ. Ceram. Soc.*, **1999**, *19*, 2677–2681.

[26] M. F. Zhang, Y. Wang, K. F. Wang, J. S. Zhu, and J.-M. Liu, *J. Appl. Phys.*, **2009**, *105*, 061639.

[27] J.-S. Lee and S.-K. Joo, *Solid State Elec.*, **2002**, *46*, 1651–1657.

[28] A. Hasegawa, S. Fujitsu, K. Koumoto, and H. Yanagida, *Jap. J. Appl. Phys.*, **1991**, *30*(6), 1252–1255.

[29] I. Sakaguchi and H. Haneda, *J. Solid State Chem.*, **1996**, *124*, 195–197.

[30] P.S. Manning, J.D.Sirman, R.A. De Souza, and J.A. Kilner, *Solid State Ionics*, **1997**, *100*, 1–10.

[31] R. H. E. van Dorn, I. C. Fullerton, R. A. de Souza, J. A. Killner, H. J. M. Bouwmeester, and A. J. Burggraaf, *Solid State Ionics*, **1997**, *96*, 1–7.

[32] R. Meyer, R. Waser, J. Heimbold, and G. Borchardt, *Phys. Rev. Lett*, **2003**, *90*, 105901.

[33] M. Dhallu and J. A. Kilner, *J. Fuel Cell Sci Technol.*, **2005**, *2*, 29–33.

[34] P. C. Carman and R. A. W. Haul, *Proc. R. Soc. Lond. A*, **1954**, *222*, 109–118.

[35] R. A. De Souza and M. Martin, *Phys. Stat. Sol.*, **2007**, *4*, 1785.

[36] I. Sakaguchi, K. Matsumoto, T. Ohgaki, Y. Adachi, K. Watanabe, N. Ohashi, and H. Haneda, *J. Ceram. Soc. Jpn.*, **2010**, *118*(5), 362–365.

[37] M. Kessel, R. A. De Souza, H.-I. Yoo, and M. Martin, *Appl. Phys. Lett.*, **2010**, *97*, 021910.

[38] T. Izaki, H. Haneda, A. Watanabe, J. Tanaka, S. Shirasaki, and K. Tsuji, *J. Ceram. Soc. Jpn.*, **1993**, *101*, 113–8.

[39] L. F. Schloss and P. C. McIntyre, *Appl. Phys. Lett.*, **2002**, *81*(17), 3218–3220.

[40] J. S. Cross, K. Kurihara, N. Kamehara, H. Haneda, and I. Sakaguchi, *Appl. Phys. Lett.*, **2005**, *86*, 141909.

[41] R. Wang and P. C. McIntyre, *J. Appl. Phys.*, **2005**, *97*, 023508.

[42] S. Gottschalk, H. Hahn, S. Flege, and A. G. Balogh, *J. Appl. Phys.*, **2008**, *104*, 114106.

[43] O. Auciello, J. F. Scott, and R. Ramesh, *Phys. Today*, **1998**, *51*, 22–27.

[44] A. K. Tagantsev, I. Stolichnov, E. L. Colla, and N. Setter, *J. Appl. Phys.*, **2001**, *90*, 1387.

[45] F. Chen, Q. Z. Liu, H. F. Wang, F. H. Zhang, and W. Wu, *Appl. Phys. Lett.*, **2007**, *90*, 192907.

[46] R. Zuo, L. Li, R. Chen, and Z. Gui, *J. Mater. Sci.*, **2000**, *35*, 5433.

[47] R. Zuo, L. Li, X. Hu, and Z. Gui, *Mat. Lett.*, **2002**, *54*, 185.

[48] M. Okayasu, S. Aoki, and M. Mizuno, *Int. J. Fat.*, **2008**, *1115*.

[49] Niall J. Donnelly and Clive A. Randall, *J. Am. Ceram. Soc*, **2009**, *92*, 405.

[50] A. R. West, *Basic Solid State Chemistry;* John Wiley & Sons, LTD, 2 ed., 1999.

[51] Y.-M. Chiang, D. P. Birnie, and W. David Kingery, *Physical Ceramics: Principles for Ceramics Science and Engineering;* John Wiley & Sons, 1 ed., 1996.

[52] F. A. Kröger, *Chemistry of Imperfect Crystals;* North-Holland, Amsterdam, 1964.

[53] J. Fleig, *Electrical and Electrochemical Investigations of Inhomogeneites in Solid State Ionics;* Universität Ulm, 2002.

[54] Z. Zhang andP. Wu, L. Lu, and C. Shu, *Appl. Phys. Lett.*, **2006**, *88*, 142902.

[55] Z. Zhang, L. Lua, C. Shu, and P. Wu, *Appl. Phys. Lett.*, **2006**, *89*, 152909.

[56] Z. Zhang, P. Wu, K. P. Ong, L. Lu, and C. Shu, *Phys. Rev. B*, **2007**, *76*, 125102.

[57] S. B. Adler, *Chem. Rev.*, **2004**, *104*, 4791.

[58] J. Januschewsky, M. Kubicek, M. Stöger-Pollach, J. Bernardi, and J. Fleig, *ECS Transactions*, **2009**, *25*, 2397.

[59] W. Bao, Q. Chang, R. Yan, and G. Meng, *J. Membr. Sci.*, **2005**, *252*, 175–181.

[60] E. Bucher, W. Sitte, I. Rom, I. Papst, W. Grogger, and F. Hofer, *Solid State Ionics*, **2002**, *152*, 417–421.

[61] M. Gallego and A. R. West, *J. Appl. Phys.*, **2001**, *90*, 394.

[62] W. Preis and W. Sitte, *Solid State Ionics*, **2006**, *177*, 2549–2553.

[63] J. Jamnik and J. Maier, *Ber. Bunsenges. Phys. Chem.*, **1997**, *101*, 23–40.

[64] R. A. De Souza and M. Martin, *Phys. Chem. Chem. Phys.*, **2008**, *10*, 2356–2367.

[65] R. A. De Souza, J. Fleig, J. Maier, O. Kienzle, Z. Zhang, W. Sigle, and M. Rühle, *J. Am. Ceram. Soc.*, **2003**, *86*, 922.

[66] N. D. Browning, J. P. Buban, H. O. Moltaji, S. J. Pennycook, G. Duscher, K. D. Johnson, R. P. Rodrigues, and V. P. Dravid, *Appl. Phys. Lett.*, **1999**, *74*, 2638–2640.

[67] R.A. De Souza, J. Fleig, J. Maier, Z.L. Zhang, W. Sigle, and M. Rühle, *J. Appl. Phys.*, **2005**, *97*, 053502.

[68] X. Guo and R. Waser, *Prog. Mater. Sci.*, **2006**, *51*, 151.

[69] S. Kim, J. Fleig, and J. Maier, *Phys. Chem. Chem. Phys.*, **2003**, *5*, 2268–2273.

[70] H. Mehrer, *Springer Series in Solid State Sciences*, **2007**.

[71] K. Funke, *Prog. Sol. St. Chem.*, **1993**, *22*, 111.

[72] P. Debeye and H. Falkenhagen, *Phys. Z.*, **1928**, *29*, 121.

[73] P. Debeye and H. Falkenhagen, *Phys. Z.*, **1928**, *29*, 401.

[74] T. Frömling; Master's thesis, Philipps Universität Marburg, **2007**.

[75] K. Funke and R. D. Banhatti, *Solid State Ionics*, **2004**, *169*, 1.

[76] K. Funke and R. D. Banhatti, *Solid State Ionics*, **2004**, *175*, 661.

[77] R. Wernicke, *Philips Res. Repts.*, **1976**, *31*, 526.

[78] A. Müller and K. H. Härdtl, *Appl. Phys. A*, **1989**, *49*, 75–82.

[79] J. Crank, *The Mathematics of Diffusion;* Oxford University Press, 2 ed., 1975.

[80] B. Klein, *FEM;* Friedr. Vieweg & Sohn Verlag, 7 ed., 2007.

[81] D. Gryaznov, J. Fleig, and J. Maier, *Solid State Sciences*, **2008**, *10*, 754–760.

[82] J.C. Fisher, *J. Appl. Phys.*, **1951**, *22*, 74.

[83] R. T. P. Whipple, *Phil. Mag.*, **1954**, *45*(371), 1225–1236.

[84] Y. Mishin, C. Herzig, J. Bernadini, and W. Gust, *Int. Mater. Rev.*, **1997**, *42*, 155.

[85] L.G. Harrison, *Trans. Faraday Soc.*, **1961**, *67*, 1191.

[86] A. D. Le Claire, *Br. J. Appl. Phys.*, **1963**, *14*, 351.

[87] A. J. Moulson and J. M. Herbert, *Electroceramics;* John Wiley & Sons Inc., 2 ed., 2003.

[88] R. W. Schwarz, J. Ballato, and G. H. Haertling, *Ceramic Materials for Electronics;* Marcel Dekker, Inc, 3 ed., 2004.

[89] W. Wersing, W. Heywang, H. Beige, and H. Thomann, *Piezoelectricity - Evolution and Future of Technology;* Springer in Materials Science, 1 ed., 2008.

[90] W. Wersing, *Piezoelectricity - Evolution and Future of Technology;* Springer in Materials Science, 2008.

[91] W. Preis and W. Sitte, *Solid State Ionics*, **2008**, *179*, 765.

[92] P. K. Panda, *J. Mater. Sci.*, **2009**, *44*, 5049.

[93] W. Jo, H.-J. Kleebe, and J. Rödel, *J. Appl. Phys.*, **2008**, *103*, 0341071–8.

[94] R. Guo, L. E Cross, S. E. Park, B. Noheda, D. E. Cox, and G. Shirane, *Phys. Rev. Lett.*, **2000**, *84*(23), 5423–5426.

[95] A. Feltz, P. Schmidt-Winkel, M. Schossmann, C. H. Booth, and J. H. Albering, *J. Amer. Ceram. Soc.*, **2007**, *90*, 3959.

[96] N. J. Donnelly and C. A. Randall, *Appl. Phys. Lett.*, **2010**, *96*, 052906–1–3.

[97] N. Balke, T. Granzow, and Jürgen Rödel, *J. Appl. Phys.*, **2008**, *104*, 054120.

[98] C. F. Woellner and J. A. Freire, *J. Chem. Phys.*, **2011**, *134*, 084112.

[99] J. F. Scott, C. A. Araujo, B. M. Melnick, L. D. McMillan, and R. Zuleeg, *J. Appl. Phys.*, **1991**, *70*, 382–388.

[100] D. Dimos, H. N. AlShareef, W. L. Warren, and B. A. Tuttle, *J. Appl. Phys.*, **1996**, *80*(3), 1682–1687.

[101] P. Mokrý, Y. Wang, A. K. Tagantsev, D. Damjanovic, I. Stolichnov, and N. Setter, *Phys. Rev. B*, **2009**, *79*, 054104.

[102] N. Balke, T. Granzow, and J. Rödel, *J. Appl. Phys.*, **2009**, *105*, 104105.

[103] S. Poykko and D. J. Chadi, *Phys. Rev. Lett.*, **1999**, *83*(6), 1231–1234.

[104] D. C. Lupascu and U. Rabe, *Phys. Rev. Lett.*, **2002**, *89*(18), 187601.

[105] Q. Y. Jiang, W. W. Cao, and L. E. Cross, *J. Am. Ceram. Soc.*, **1994**, *77*(1), 211–215.

[106] M. D. Hill, G. S. White, C. S. Hwang, and I. K. Lloyd, *J. Am Ceram. Soc.*, **1996**, *79*(7), 1915–1920.

[107] X. J. Lou, M. Zhang, S. A. T. Redfern, and J. F. Scott, *Phys. Rev. Lett .*, **2006**, *97*(17), 177601.

[108] X. J. Lou, M. Zhang, S. A. T. Redfern, and J. F. Scott, *Phys. Rev. B*, **2007**, *75*, 224104.

[109] D. Zhenga, J. Swingler, and P. M. Weaver, *Sensors and Actuators A: Physical*, **2011**, *167*, 19–24.

[110] I.P. Lipscomb, P.M. Weaver, J. Swingler, and J.W. McBride, *Sensors and Actuators A: Physical*, **2009**, *151*, 179–186.

[111] R. Ramesh, J. Lee, T. Sands, and V. G. Keramidas, *Appl. Phys. Lett.*, **1994**, *64*, 2511–2513.

[112] H. Nagata, H. Haneda, I. Sakaguchi, T. Tanenaka, and J. Tanaka, *J. Ceram. Soc. Jap.*, **1997**, *105*(9), 805–810.

[113] M. V. Slinkina, G. I. Dontsov, and V. M. Zhukovsky, *J. Mat. Sci.*, **1993**, *28*, 5189.

[114] H. M. Naguib and B. K. MacLaurin, *IEEE Trans.*, **1979**, *CHMT-2*, 196–207.

[115] F. Zheng, J. Xu, L. Fang, M. Shen, and X. Wu, *Appl. Phys. Lett.*, **2008**, *93*, 172101.

[116] F. Chen, R. Schafranek, W. Wu, and A. Klein, *J. Phys. D: Appl. Phys.*, **2009**, *42*, 215302.

[117] J. Xu, D. Cao, L. Fang, F. Zheng, and M. Shen andX. Wu, *J. Appl. Phys.*, **2009**, *106*, 113705.

[118] H. Kishi, Y. Mizuno, and H. Chazono, *Jpn. J. Appl. Phys.*, **2003**, *42*, 1–15.

[119] T. B. Wu and J. N. Lin, March , **1994**, *77*(3), 759–764.

[120] B. Huybrechts, K. Ishizaki, and M. Takata, *J. Mater. Sci.*, **1995**, *30*, 2463–2474.

[121] W. Preis andW. Sitte, *Solid State Ionics*, **2006**, *177*, 3093–3098.

[122] C.-E. Lee and H.-I. Yoo, *Solid State Ionics*, **2008**, *179*, 338–346.

[123] H. T. Langhammer, D. Makovec, Y. Pua, H.-P. Abicht, and M. Drofenik, *J. Europ. Ceram. Soc.*, **2006**, *26*, 2899–2907.

[124] S. Shirasaki, M. Tsukioka, H. Yamamura, and H. Oshima, *Solid State Comm.*, **1976**, *19*, 721–724.

[125] S. Shirasaki, H. Haneda, K. Arai, and M. Fujimoto, *J. Mater. Sci.*, **1987**, *22*, 4439–4445.

[126] H.-I. Yoo and C.-E. Lee, *J. Am. Ceram. Soc.*, **2005**, *88*, 617.

[127] W. Preis, *Monatsh Chem*, **2009**, *140*, 1059–1068.

[128] P. A. Tippler, *Physik;* Spectrum Verlag, 1994.

[129] K. H. Rohe, *Elektronik für Physiker;* Teubner Studienbücher, 1983.

[130] H. Lindner, *Taschenbuch für Elektronik und Elektotechnik;* Carl Hanser Verlag, 2004.

[131] E. Barsoukov and J. R. Macdonald, *Impedance Spectroscopy;* Wiley-Interscience, 2005.

[132] I. D. Raistrick, *J. Electrochem. Soc*, **1976**, *123*, 1469.

[133] T. van Dijk and A. J. Burggraaf, *Phys. Stat. Sol.*, **1981**, *63*, 229–40.

[134] J. Fleig and J. Maier, *J. Am. Ceram. Soc.*, **1999**, *82*(12), 3485–3493.

[135] R. N. S. Sodhi, *Analyst*, **2004**, *129*, 483.

[136] J. C. Vickerman and D. Briggs, *ToF-SIMS : Surface Analysis by Mass Spectrometry;* IM Publications LLP, 2001.

[137] L. Van Vaeck, A. Adriaens, and R. Gijbels, *Mass Spec. Rev.*, **1999**, *18*, 41.

[138] D. G. Castner, *Nature*, **2003**, *422*, 129.

[139] R. F. K. Herzog and F. P. Vieböck, *Phys. Rev.*, **1949**, pages 855–856.

[140] D. S. McPhail, *J. Mater. Sci.*, **2006**, *41*, 873–903.

[141] H. Nygren and P. Malmberg, *Trend Biotechnol.*, **2007**, *25*, 599.

[142] I. S. Gilmore and M. P. Seah, *Appl. Surf. Sci.*, **2004**, *231*, 224.

[143] F. Kollmer, *Appl. Surf. Sci.*, **2004**, *231*, 153.

[144] A. Delcorte, *Phys. Chem. Chem. Phys.*, **2005**, *7*, 3395.

[145] R. Kersting, B. Hagenhoff, P. Pijpers, and R. Verleak, *Appl. Surf. Sci.*, **2003**, *203*, 561.

[146] M. L. Pacholski and N. Winograd, *Chem. Rev.*, **1999**, *99*, 2977–3005.

[147] F. Benabdellah, A. Seyer, L. Quinton, D. Touboul, A. Brunelle, and O. Laprévote, *Anal. Bioanal. Chem.*, **2010**, *396*, 151–162.

[148] D.Touboul, F. Kollmer, E. Niehuis A. Brunelle, and O. Laprévote, *J. Am. Soc. Mass Spec.*, **2005**, *16*, 1608.

[149] A. G. Ewing, *Appl. Surf. Sci.*, **2006**, *252*, 6821.

[150] S. Hofmann and J. Y. Wang, *J. Surf. Anal.*, **2002**, *9*(3), 306–309.

[151] S. Rangarajan and B. J. Tyler, *J. Vac. Sci. Technol. A*, **2006**, *24*, 1730.

[152] M. Cwil and P. Konarski, *Vacuum*, **2005**, *78*, 291.

[153] B. Hagenhoff, *Microchem. Acta*, **2000**, *132*, 259–271.

[154] D. Gui, Z.X. Xing, Y.H. Huang, Z.Q. Moa, Y.N. Hua, S.P. Zhao, and L.Z. Cha, *Appl. Surf. Sci.*, **2008**, *255*, 1433–1436.

[155] M. L. Yu and K. Mann, *Phys. Rev. Lett.*, **1986**, *57*, 1476–1479.

[156] M. L. Yu and N. D. Lang, *Phys. Rev. Lett.*, **1983**, *50*, 127.

[157] M. L. Yu, *Phys. Rev. Lett.*, **1978**, *40*, 574.

[158] M. L. Yu and N.D. Lang, *Nuclear Instruments and Methods in Physics Research B*, **1986**, *14*(4-6), 403–413.

[159] T. Grehl; *Improvement in TOF-SIMS Instrumenation for Analytical Application and Fundamental Research;* PhD thesis, Westfälische Wilhelms Universität Münster, **2003**.

[160] Y. Kudriatsev, A. Villegas, S. Gallardo, G. Ramirez, R. Asomoza, and V. Mishurnuy, *Appl. Surf. Sci.*, **2008**, *254*, 4961.

[161] A. M. Belu, D. J. Graham, and D. G. Castner, *Biomaterials*, **2003**, *24*, 3635.

[162] A. Wucher, *Appl. Surf. Sci.*, **2006**, *252*, 6482.

[163] N. Winograd, *Anal. Chem.*, **2005**, page 146.

[164] M. P. Seah, *Surf. Interf. Anal.*, **2007**, *39*, 890.

[165] N. Winograd, Z. Postawa, J. Cheng, C. Szaka, J. Kozole, and B. J. Garrison, *Appl. Surf. Sci.*, **2006**, *252*, 6836.

[166] S. Ninomiya, Y. Nakata, K. Ichiki, T. Seki, T. Aoki, and J. Matsuo, *Nucl. Instr. and Meth. in Phys. Res. B*, **2007**, *256*, 493–496.

[167] Z. Postawa, B. Czerwinski, Marek Szewczyk, E. J. Smiley, N. Winograd, and B. J. Garrison, *Anal. Chem.*, **2003**, *75*, 4402.

[168] K. Iltgen, C. Bendel, A. Benninghoven, and E. Niehuis, *J. Vac. Sci. Technol. A*, **1997**, *15*, 460–464.

[169] J. Claus, M. Leonhardt, and J. Maier, *J. Phys. Chem. Sol.*, **2000**, *61*, 1199–1207.

[170] A. C. Sabioni, M. J. Ramos, and W. B. Ferraz, *Mater. Res.*, **2003**, *6*, 173–178.

[171] G. Knöner, K. Reimann, Ralf Röwer, U. Södervall, and H.-E. Schaefer, *PNAS*, **2003**, *100*, 3870.

[172] J. S. Cross and K. Kurihara, *Appl. Phys. Lett.*, **2005**, *86*, 141909.

[173] A. C. Sabioni, A. M. Daniel, M. J. Ramos, W. B. Ferraz, and F. Jomard, *Mater. Res.*, **2008**, *11*, 221–225.

[174] C. Nivot, C. Legros, B. Lesage, M. Kilo, and C. Argirusis, *Solid State Ionics*, **2009**, *180*, 1040–1044.

[175] E. S. Raj, A. Atkinson, and J. A. Kilner, *Solid State Ionics*, **2009**, *180*, 952–955.

[176] E. S. Raj, J. A. Kilner, and J..T.S. Irvine, *Solid State Ionics*, **2006**, *177*, 1747–1752.

[177] S. Hummelt, S. Flege, and W. Ensinger, *Phys. Status Solidi RRL*, **2010**, *4*(8-9), 203–205.

[178] T. Stephan and A. Benninghoven, *J. Vac. Sci. Technol. A*, **1994**, *12*(2), 405–410.

[179] R.A. De Souza, J. Zehnpfenning, M. Martin, and J. Maier, *Solid State Ionics*, **2005**, *176*, 1465.

[180] A. Schintlmeister; PhD thesis, Technische Universtät Wien, **2011**.

[181] R.A. De Souza and R.J. Chater, *Solid State Ionics*, **2005**, *176*, 1915 –1920.

[182] J. Januschewsky, M. Ahrens, A. K. Opitz, F. Kubel, and J. Fleig, *Adv. Funct. Mater.*, **2009**, *19*, 1–6.

[183] M. Kubicek, A. Limbeck, T. Frömling, H. Hutter, and J. Fleig, *J. Electrochem. Soc.*, **2011**, *158*, B727–B734.

[184] J. D. Russel and C. Leach, *J. Europ. Ceram. Soc.*, **1995**, *15*, 617.

[185] J. Seaton and C. Leach, *J. Europ. Ceram. Soc.*, **2004**, *24*, 1191.

[186] Z. Ling and C. Leach, *J. Mater. Sci*, **1999**, *34*, 6133.

[187] C. Leach, *Interf. Sci.*, **2000**, *8*, 357.

[188] C. Leach, *Act. Mater.*, **2005**, *53*, 237.

[189] P. Hillebrand; Master's thesis, Technische Universität Wien, **2010**.

[190] J. Fleig, *Solid State Ionics*, **2002**, *150*, 181–193.

[191] K. Reichmann, E. Völkl, M. Ahrens, J. Fleig, and J. Votsch, March , **2010**, *45*(6), 1473–1477.

[192] A. Khodorov, S. A. S. Rodrigues, M. Pereira, and M. J. M. Gomes, *J. Appl. Phys.*, **2007**, *102*, 114109.

[193] V. Chaudhari and G. Bichile, *Physica B*, **2010**, *405*, 534.

[194] E. Völkl, P. Hillebrand, and J. Fleig; submitted to J. Electroceram.

[195] J. N. Miller and J. C. Miller, *Statistics and chemometrics for analytical chemistry;* Pearson Education LTD, 5 ed., 2005.

[196] M. Gerstl; Master's thesis, Technische Universität Wien, **2008**.

[197] P. C. Zalm, *Rep. Prog. Phys.*, **1995**, *58*, 1321–1374.

[198] J. Fleig, F. Noll, and J. Maier, *Ber. Bunsenges. Phys. Chem.*, **1996**, *100*, 607–615.

[199] R. A. De Souza, *Phys. Chem. Chem. Phys.*, **2009**, *11*, 9939–9963.

[200] J. Hou, Z. Zhang, W. Preis, W. Sitte, and G. Dehm, *J. Eur. Ceram. Soc.*, **2011**, *31*, 763–771.

[201] M. Hammer and M. J. Hoffmann, *J. Am. Ceram. Soc.*, **1998**, *31*(12), 3277–84.

[202] T. Ishigaki, S.Yamauchi, K. Kishio, J. Mizusaki, and K. Fueki, *J. Solid State Chem.*, **1988**, *73*(1), 179–187.

[203] P. Fielitz, G. Borchardt, M. Schmücker, and H. Schneider, *Solid State Ionics*, **2003**, *160*, 75–83.

[204] J. Maier, *Ber. Bunsenges. Phys. Chem.*, **1986**, *90*, 26–33.

[205] J.-H. Park and R. N. Blumenthal, *J. Electrochem. Soc.*, **1989**, *136*(10), 2867–2876.

[206] D. Gryaznov, J. Fleig, and J. Maier, *Solid State Ionics*, **2006**, *177*, 1583–1586.

[207] S. Lee, C. A. Randall, and Z.-K. Liu, *J. Am. Ceram. Soc.*, **2007**, *90*, 2589–2594.

[208] A. Gunnarsson, F. Kollmer, S. Sohn, F. Höök, and P. Sjövall, *Anal. Chem.*, **2010**, *82*, 2426–2433.

[209] A. K. Opitz, A. Schintlmeister, H. Hutter, and J. Fleig, *Phys. Chem. Chem. Phys.*, **2010**, *12*, 12734–12745.

List of Abbreviations

AC	alternating current
BT	barium titanate
CM	conductive mode microscopy
CPE	constant phase element
CNLS	complex non-linear least square
DC	direct current
DHM	Digital Holographic Microscopy
EBIC	electron beam induced current
EDS	energy dispersive x-ray spectroscopy
FEM	finite element method
FD	finite differences
HRTEM	high resolution transmission electron microscopy
ICP	inductive coupled plasma
LSC	lanthanum strontium cobaltate
MLCC	multilayer ceramic capacitor
MPB	morphotropic phase boundary
OES	optical emission spectroscopy
PZT	lead zirconate titanate
RSF	relative sensitvity factor
PLD	pulsed laser deposition
PTC	positive temperature coefficient
SE	secondary electron

SEM	scanning electron microscopy
TEM	transmission electron microscopy
SCLC	space charge limited current
SOFC	solid oxide fuel cell
SIMS	secondary ion mass spectrometry
ToF	time of flight
YSZ	yttrium stabilized zirconate

List of Symbols

A	area
d	thickness/distance
ω	angular frequency
t	time
C	capacitance
L	inductance
R	resistance
R_{gb}	grain boundary resistancs
f_{geo}	geometrical factor
L_e	electrode length
i_n	normal current density
Z	impedance
M	modulus
I	current
U	voltage
D_S	self-diffusion coefficient
D_v	vacancy diffusion coefficient
D	bulk tracer diffusion coefficient
D_{gb}	grain boundary tracer diffusion coefficient
k	incorporation coefficient
σ	conductivity
σ_b	bulk conductivity

σ_{gb}	grain boundary conductivity
σ_{eff}	effective conductivity
λ_{t}	grain boundary trace
$\Delta \mathrm{x}_0$	particle jump distance
τ	jump rate
u	mobility
$\mathrm{f}_{\mathrm{d(c)}}$	correction factor of diffusion
δ	grain boundary thickness
s	segregation coefficient
L_{d}	grain size
$\mathrm{t}_{\mathrm{pre}}$	preannealing time
T	Temperature
ϵ	permittivity
ϵ_0	permittivity of vacuum
ϵ_{r}	relative permittivity
c	concentration
c_{s}	source concentration
c_{b}	natural abundance of $^{18}\mathrm{O}$
$\mathrm{c}_{\mathrm{gas}}$	gas phase concentration of $^{18}\mathrm{O}$
$\mathrm{c}^{*}_{^{18}\mathrm{O}}$	relative $^{18}\mathrm{O}$ concentration
$\mathrm{c}_{^{18}\mathrm{O}}$	relative $^{18}\mathrm{O}$ concentration taking c_{b} into account
$\mathrm{c}^{0}_{\mathrm{gb}}$	grain boundary related $^{18}\mathrm{O}$ concentration close to the surface
z	charge number
k_{B}	BOLTZMANN constant
e	elementary charge
φ	electric potential
q	charge
m	mass
Q	charge density
λ	DEBYE length
G	free energy
H	free enthalpy

S	entropy
j	particle flux density
i	electrical current density
F	FARADAY constant
T_c	CURIE temperature
P_r	remnant polarization
P_s	maximum polarization
T_{ij}	stress
S_{ij}	strain
E_i	electric field
D_i	displacement
d_{ij}	piezoelectric constant
s_{ij}	elastic compliance
a_{O_2}	oxygen activity
c_d	bulk donor density
c_{gb}	trapped charge per area in grain boundary acceptor states
I_m	secondary ion current
I_p	primary ion flux
Y_m	sputter yield
U_I	ionization potential
ϕ	work function
α	ionization probability
θ_m	fractional concentration of species m
η	transmission of SIMS analysis system
N	number of SIMS ionization pulses
I_{exp}	secondary ion intensity from experiment
I_{corr}	corrected secondary ion intensity
$^S\sigma$	standard deviation

List of Figures

List of Tables

Acknowledgements

Angaben zur Person

Nachname(n) / Vorname(n)	**Frömling, Till**
Adresse(n)	Anemonenweg 14, D-51069 Kln
Staatsangehörigkeit(en)	deutsch
Geburtsdatum	19. August 1981 in Sigmaringen

Ausbildung

• 04/2008-06/2011	Doktorarbeit in der Arbeitsgruppe von Prof. Dr. Fleig an der Technischen Universität Wien im Christian-Doppler Laboratorium für Ferroische Materialien Thema: "Oxide Ion Transport in Lead Zirconate Titanate (PZT)"
• 10/2007 • 03/2007	Abschluss des Studiums als Diplom-Chemiker an der Philipps Universität Marburg Diplomarbeit in der Arbeitsgruppe von Prof. Dr. Roling Thema: "Charakterisierung von festen und flüssigen Lithiumelektrolyten auf Basis ionischer Flüssigkeiten."
• 10/2005-04/2006	Auslandssemester am Imperial College in London Forschungsprojekt in den Arbeitsgruppen von Prof. Dr. Welton und Dr. Hunt Thema: "Investigation on coordinating effects of ionic liquids on Ni(II)-complexes"
• 10/2002	Beginn des Studiums an der Philipps Universität in Marburg Fachrichtung Chemie (Diplom)
• 2001-2002	Zivildienst bei der Arbeiterwohlfahrt, Münster
• bis 2001	Annette-v.-Droste-Hülshoff-Gymnasium, Münster Leistungskurse: Chemie, Mathematik Grundkurse: Englisch, Wirtschaftswissenschaften Abschluss: Abitur

Praktika

• 06/2002-07/2002	Praktikum am LUFA (Untersuchungszentrum der Landwirtschaftskammer) in Münster
• 12/2007-03/2008	Praktikum bei der Evonik Degussa GmbH im Bereich Lithium-Akkumulatorforschung

Tätigkeiten neben dem Studium

• 2002-2007	Mitglied der aktiven Fachschaft des Fachbereichs Chemie an der Universität Marburg
• 07/2004-07/2005	Gewähltes Mitglied des Fachschaftsrates
• 2003-2007	Mitglied der Kommission zur Einführung der neuen Studiengänge
• 2005-2006	Verantwortlicher für die Einführung und Durchführung der Lehrevaluierung am Fachbereich Chemie